

The Feasibility of Integrating Self-Powered Internet of Things Nodes in Indoor Conditions

By
Gethin Thomas

Submitted to Swansea University in fulfilment of the requirement for
the degree of Doctor of Philosophy



Swansea University
Prifysgol Abertawe

Swansea University
2023

Copyright: The Author, Gethin Thomas, 2023.

Distributed under the terms of a Creative Commons Attribution Non
Commercial 4.0 License (CC BY-NC 4.0).

The Feasibility of Integrating Self-Powered IoT Nodes in Indoor Conditions

Gethin Thomas

Abstract

The internet of thing (IoT), also called internet of everything or industrial internet embeds intelligence into our environment, with 75.44 billion IoT connected devices projected to be worldwide by 2025. Many of these smart devices will be used in indoor environments, raising the question of how much energy can be harvested under environmental ambient conditions to support IoT nodes.

This thesis explores the best technology for optimised power harvesting, concluding that dye sensitised solar cells (DSSCs) provide the greatest design flexibility and performance when implemented in indoor applications, having the aesthetic qualities prioritised by users. The work investigates the optimal type of electrolyte and active area size of a monolithic DSSC for low light conditions, mainly changing the iodine concentration of the triiodide electrolyte.

A new method of integrating a monolithic DSSC as an energy harvester and self-power their interactive features was achieved in this work. This involved monitoring the photocurrent output of asymmetrical patterned monolithic DSSCs, using machine learning to recognise simple linear directional hand gestures, achieving an accuracy prediction of 98%. The patterned active area of this cell was also optimised through computer modelling the photocurrent outputs, increasing the prediction accuracy of additional directional hand gestures.

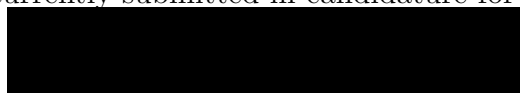
Several different designs and prototypes are also presented in this work, demonstrating the importance of collaborating in the field of human computer interaction with material science. DSSCs were used to self-power different IoT node applications, which included a novel self-powered method of displaying a Moiré pattern through an electromagnetic actuator, at very low light intensities.

This thesis demonstrates that DSSCs are the ideal choice for IoT node integration in indoor conditions, having the capabilities to provide the aesthetic qualities and performance characteristics to power interactive technologies, as well as provide a mean of interactive control.

Declaration and Statements

This work has not previously been accepted in substance for any degree and is not being concurrently submitted in candidature for any degree.

Signed



Date28/06/2023.....

This thesis is the result of my own investigations, except where otherwise stated. Other sources are acknowledged by footnotes giving explicit references. A bibliography is appended.

Signed



Date28/06/2023.....

I hereby give consent for my thesis, if accepted, to be available for photocopying and for inter-library loan, and for the title and summary to be made available to outside organisations.

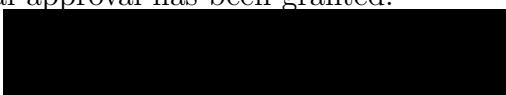
Signed



Date28/06/2023.....

The University's ethical procedures have been followed and, where appropriate, that ethical approval has been granted.

Signed



Date28/06/2023.....

Contents

1	Literature Review	16
1.1	Basics of Internet of Things (IoT)	16
1.1.1	Architectural IoT Layout	17
1.1.2	IoT Applications	18
1.1.3	Present issues with IoT systems	22
1.1.4	Solution	26
1.2	Indoor Energy Harvesting	27
1.2.1	Introduction	27
1.3	Energy Harvesting Techniques from Ambient Sources	29
1.3.1	Ambient Radio Frequency (RF) Energy Harvesting	29
1.3.2	Thermoelectric Energy Harvesting	34
1.3.3	Photovoltaic (PV)	39
1.4	Energy Harvesting Techniques from Mechanical Sources	46
1.4.1	Piezoelectric Energy Harvesting	47
1.4.2	Triboelectric Energy Harvesting	50
1.5	Hybrid energy harvesting (HEH)	52
1.5.1	Indoor light and RF energy	52
1.5.2	Indoor light and mechanical energy	53
1.5.3	Indoor light and thermal energy sources	53
1.5.4	Thermal and mechanical energy sources	53
1.6	Energy Harvesting Techniques' Conclusion	54
1.6.1	Evaluate and compare different harvesting sources using Pugh matrix	54
1.7	Indoor PV Cell Comparison	56
1.7.1	Dye Sensitised Solar Cell (DSSC) Background	59
1.8	Overarching Summary: Focus and layout of study	62
2	Experimental Methods	77
2.1	Materials	77
2.2	Cell Fabrication Process	78
2.2.1	Working Electrode (WE) Substrate	79

2.2.2	Mesoporous TiO ₂ deposition and annealing	79
2.2.3	Counter Electrode (CE) Substrate	80
2.2.4	Assembly of DSSC	81
2.3	Solar Cell Characterisation Techniques	82
2.3.1	Light simulators	82
2.3.2	Optical Characterisation	83
3	Investigation into the optimal type of transparent monolithic DSSC for a visually appealing interface and performance for indoor IoT nodes	86
3.1	Introduction	86
3.1.1	Background	86
3.1.2	Related Work	88
3.1.3	Summary	90
3.2	Materials and methods	91
3.2.1	Control variables	91
3.2.2	Independent variables	91
3.2.3	Dependent variables	93
3.3	Comparing different DSSC compositions (1 cm ² active area) at dif- ferent light intensities	93
3.3.1	Results and discussion	93
3.4	Performance of remaining DSSCs with different active area sizes . . .	105
3.4.1	Results and discussion	105
3.5	Conclusion	119
4	Integrating a Monolithic DSSC for Hand Gesture Recognition	125
4.1	Introduction	125
4.1.1	Background	125
4.1.2	Related work	126
4.1.3	Summary	127
4.2	Materials and methods	128
4.2.1	DSSC design	128
4.2.2	DSSC fabrication	129
4.2.3	Gesture Data collection	129
4.3	Gesture Detection Using Thresholding	132
4.3.1	Method	132
4.3.2	Results and discussion	134
4.4	Gesture detection using machine learning (ML)	135
4.4.1	Data Pre-Processing	136
4.4.2	Gesture Recognition Results and Discussion	145

4.5	Additional Gestures with Machine Learning	149
4.5.1	Results and discussion	150
4.6	Conclusion	152
5	Optimising the Active Area Pattern of a Monolithic DSSC for Hand Gesture Recognition	156
5.1	Introduction	156
5.2	Computational modelling of different patterns for gesture optimisation	157
5.2.1	Computer model set-up	157
5.2.2	Active area optimisation	160
5.2.3	Results and discussion	165
5.3	Invisible gesture detection	173
5.3.1	Introduction	173
5.3.2	Results and discussion	175
5.4	Alternative low power data collection method	178
5.4.1	Set-up	178
5.4.2	Results and discussion	180
5.5	Conclusion	182
6	Human Computer Interaction Prototyping and Contribution	185
6.1	PV-Pix: Deformable smart messaging material prototypes	186
6.1.1	FabricOn prototypes	186
6.1.2	TiltTile module prototype	187
6.2	Light-based concept prototypes	190
6.2.1	SolarPix prototype designs	190
6.2.2	Self-powered Moiré pattern shadow motion (ShadMo)	192
6.3	Conclusion	206
7	Conclusion	210
7.1	Future prospects	212
	Appendices	216
A	Initial Pattern Exploration and Optimisation	216
A.1	Initial Pattern Exploration	216
A.2	Optimisation	222
B	Additional results from 5 mM (HM) electrolyte area void change	230
C	Additional Results from Optimised and FTO etched Cells	232
C.1	Trained Model Results of the 3 Optimised Cells	232

C.2	Trained Model Results for Etched FTO Cell	233
C.3	Low Power Alternative Method	233

Acknowledgements

Yn gyntaf, rydw i eisiau dweud diolch i 'm goruchwyliwr academiaidd yr Athro Matt Carnie, am eu harweiniad a'i gymorth yn ystod y prosiect hwn. Diolch arbennig hefyd i Adam Pockett a Suzanne Thomas am roi amser nhw fyny i hyfforddi yn yr labs ar nodwyddau offerynnau, ac i gadw fi i ddatblygu trwy'r blynyddoedd dwethaf. Hefyd, eisiau dweud diolch i'r tîm M2A am y gefnogaeth amhrisiadwy, a'r swyddfa A208 am y cwmni hyfryd dros y tair blynedd diwethaf.

I orffen, rydw i eisiau dweud diolch i fy ffrindiau a fy nheulu, hebddo, fyddai byth wedi gallu cwblhau'r gwaith yma. Diolch mam a dad am eich cefnogaeth a'r amser chi wedi rhoi mewn i gadw fy hunan ar y trywydd iawn. Diolch enfawr i fy nghariad Heledd, am fod mor ddealladwy gyda fy absenoldeb ar amser, a rhoi'r egni ychwanegol i fi gallu gorffen y prosiect yma, gravity.

List of Tables

1.1	Emerging low-power communication technologies	26
1.2	Pugh matrix ranking each ambient and mechanical energy harvesting source	56
1.3	Performance of different PV cell technologies under ambient lighting .	57
2.1	DSSC materials and solvents	78
3.1	Advantages and disadvantages of each electrolyte tested	120
4.1	Confusion Matrix Using Threshold Detection	134
4.2	Trained model accuracy for wavelet and statistical features	146
4.3	Evaluated accuracy from each trained model classifier type	147
4.4	Confusion Matrix of best evaluated model	148
4.5	Trained model accuracy for selected wavelet features without DTW .	149
4.6	Evaluated accuracy from each trained model classifier type without DTW technique	149
4.7	Trained model accuracy for 8 gestures	151
4.8	Evaluated accuracy from the best trained model classifier type	151
4.9	Confusion Matrix of best evaluated model for 8 Gestures	152
5.1	Justification for the use of different electrolytes in various Chapters .	166
5.2	Trained model accuracy for pattern 1 (14.08 cm^2)	167
5.3	Trained model accuracy for pattern 2 (16.25 cm^2)	168
5.4	Trained model accuracy for pattern 3 (17.24 cm^2)	168
5.5	Confusion Matrix of best evaluated model from pattern 3 (17.24 cm^2)	169
5.6	Evaluated trained model accuracy for etched FTO DSSC	176
5.7	Confusion Matrix of best evaluated model with 100% accuracy . . .	176
5.8	Evaluated trained model accuracy for low power alternative data cap- turing method	181
5.9	Confusion matrix of best evaluated model with 80% accuracy	181

List of Figures

1.1	Basic architecture of an IoT system	18
1.2	Applications of IoT	18
1.3	Taxonomy of indoor energy harvesting techniques. Adapted from [32][36]	27
1.4	RF energy harvesting layout. Adapted from [50][51]	29
1.5	Equivalent single diode circuit for a PV module [68]	39
1.6	Configuration of the RF and Solar hybrid energy harvester [25]	52
1.7	Molecular structures of different DSSC sensitizers. Adapted from [107] [83] [90] [108]	58
1.8	Diagram of a DSSC, including the energy levels and its working mech- anism (numbers in circles refer to stages)	60
2.1	2700 K light spectrum at 10000 Lux	83
3.1	Different layouts of a DSSC on an IoT display	88
3.2	1cm^2 active area DSSCs at one sun	94
3.3	1cm^2 active area DSSCs at 10,000 Lux	96
3.4	1cm^2 active area DSSCs at 1000 Lux	97
3.5	1cm^2 active area DSSCs at 100 Lux	98
3.6	Transmittance spectrum for each type of electrolyte	99
3.7	Shows that both the full concentration (numbered) and half concen- tration (lettered) of copper redox have dried	100
3.8	Zombie cell comparison at one sun	101
3.9	Zombie cell comparison at 10,000 Lux	102
3.10	Zombie cell comparison at 1000 Lux	103
3.11	Zombie cell comparison at 100 Lux	104
3.12	DSSC comparison at 1 cm^2	106
3.13	DSSC comparison at 4 cm^2	108
3.14	DSSC comparison at 16 cm^2	109
3.15	DSSC comparison at 64 cm^2	111
3.16	Open-circuit voltage at different active area sizes	113

3.17	Short-circuit current density at different active area sizes	114
3.18	Power density at different active area sizes	116
3.19	Fill factor at different active area sizes	117
3.20	Absolute Power at different active area sizes	119
4.1	Photodiode layout for IoT node applications. Adapted from [4][5] . .	126
4.2	SolarGest layout and stored gestures used. Adapted from [2]	127
4.3	Schematic of initial DSSC testing	128
4.4	Photocurrent when individually covering from largest to smallest area	129
4.5	Asymmetrical pattern design	129
4.6	Gesture data collection rig	130
4.7	Gesture capture using LabVIEW	131
4.8	Sketches of the 4 hand gestures performed over the DSSC. The second row shows the photocurrent response for each gesture at 1000 Lux . .	131
4.9	First Trough detection for each gesture photocurrent	133
4.10	Comparing photocurrent signals under different light intensities . . .	135
4.11	Flowchart of the machine learning process	136
4.12	Amplitude alignment using Z-score transformation	138
4.13	DTW technique using a reference curve	139
4.14	Alterations to the pre-processing technique	140
4.15	Statistical Features Ranked Through One-Way ANOVA	142
4.16	FFT analysis of a single photocurrent signal	143
4.17	DWT detail coefficients up to level 6 with approximation coefficients level 6	144
4.18	Sketches of the 4 additional hand gestures performed over the DSSC. The second row shows the photocurrent response for each gesture at 1000 Lux	150
5.1	Example of the Model in LabVIEW, with a bar width ratio of 0.2 . .	157
5.2	Right Swipe Gesture model output using different width bar sizes compared to DSSC measured data at 1000 Lux	158
5.3	Comparing all eight gesture photocurrent outputs with the model outputs at a width bar ratio of 0.8	159
5.4	Adaption designs from the original flower pattern using same active area	161
5.5	Design idea 6	162
5.6	Idea Pattern 16	162
5.7	Step. 4	163
5.8	Geometry restriction	164
5.9	Step. 13	164

5.10	Step. 20	165
5.11	Fabricated 3 Cells from the optimised steps progression in Appendix A.2	167
5.12	DSSC design pattern comparison	170
5.13	Changing the electrolyte area around a 1 cm^2 active area	171
5.14	50 mM (HM) DSSC performance characteristics of changing the elec- trolyte area around a 1 cm^2 active area	172
5.15	Re-design of pattern 3, showing the constraints	173
5.16	Re-designed detailed pattern on a DSSC	173
5.17	Masking the active area before etching	174
5.18	Final fabricated appearance of the etched FTO DSSC	175
5.19	Photocurrent signal output for Etched FTO DSSC	175
5.20	Etched DSSC performance characteristics compared to pattern design 3 and the original flower pattern DSSC	177
5.21	Schematic diagram of ADS1115 Set-up	179
5.22	Comparing capture rate speeds of the ADS1115 with the Right swipe	180
6.1	Exploded view of the rendered FabricOn design	186
6.2	Rendered operation of the FabricOn	187
6.3	Working example of the FabricOn in open state	187
6.4	Initial prototype of the TiltTile module	188
6.5	Working example of the initial prototype	189
6.6	Final optimised concept design of the TiltTile	190
6.7	Rendered design of the SolarPix	191
6.8	Back view of the SolarPIx	191
6.9	Side view of SolarPix, with the addition of DSSCs	192
6.10	Base layer moving under the revealing layer	193
6.11	Demonstrating the effect of the base layer under the revealing layer at different linear movements	193
6.12	Initial rendered design of the Moiré pattern mount	194
6.13	Moiré pattern of a beating heart using acetate sheets	195
6.14	Rendered schematic design of the second iteration with an actuator and DSSC	196
6.15	Resultant fabrication of DSSC with Moiré line for revealing layer . . .	197
6.16	Assembled Moiré pattern design using a DSSC as the revealing layer .	197
6.17	Example of a solar dancing flower [7] showing the inside mechanic. The arrows in orange represent the motion direction	198
6.18	Design alteration of the revealing layer for radial movement by the base layer	199

6.19	Design alteration of the base layer for radial movement	200
6.20	Motion of the base layer underneath the revealing layer, showing dif- ferent segments of the butterfly	201
6.21	Disfigured pattern when the base layer is positioned lower behind the revealing layer	201
6.22	Labelled set-up of the pendulum Moiré pattern	202
6.23	Performance characteristics of the DSSC (revealing layer)	203
6.24	Current consumption of the microcontroller	204
6.25	Current consumption after the cold start of the microcontroller	204
6.26	Moiré pattern powered through a low powered pendulum mechanism	205

Abbreviations

AC	Alternating current
ADC	Analogue-to-digital converter
ADL	Applications on monitoring the activities of daily life
AI	Artificial intelligence
BL	Blocking layer
BLE	Bluetooth low energy
CAD	Computer aided design
CE	Counter electrode
CPS	Cyber-physical systems
DAQ	Data acquisition device
DC	Direct current
DI	De-ionised
DSSC	Dye sensitised solar cell
DTW	Dynamic time warping
DWT	Discrete wavelet transform
EV	Electric vehicle
FF	Fill factor
FL	Fluorescent
FTO	Fluorine-doped tin oxide
GSM	Global system for mobile communication
HCI	Human computer interaction
HCL	Hydrochloric acid

HEH	Hybrid energy harvesting
HF	High frequency
HM	Homemade
I_{SC}	Short-circuit current
IoMT	Internet of medical things
IoT	Internet of things
IPA	Isopropanol
J_{SC}	Short-circuit current density
LED	Light-emitting diode
LF	Low frequency
LIB	Lithium-ion battery
LoRa	Long range radio
LUMO	Lowest unoccupied molecular orbital
M2M	Machine-to-machine
ML	Machine learning
MPP	Maximum power point
MPPT	Maximum power point tracking
NIR	Near infrared range
OPV	Organic solar cells
PCE	Power conversion efficiency
PEDOT	Poly(3,4-ethylenedioxythiophene)
PIEG	Piezoelectric generators
PSC	perovskite solar cell
PV	Photovoltaic
PYEG	Pyroelectric generators
RF	Radio frequency
RFID	Radio frequency identification
SG	Smart grid

TCO	Transparent conducting oxides
TEG	Thermoelectric generators
TENG	Triboelectric nanogenerators
Ubicomp	Ubiquitous computing
UHF	Ultra-High frequency
UI	User interface
V_{OC}	Open-circuit voltage
WE	Working electrode
WLED	White light-emitting diode
WS	Wearable sensors
WSN	Wireless sensor network
Zigbee	Zonal intercommunication global-standard

Chapter 1

Literature Review

This thesis explores the practicality of incorporating internet of things (IoT) devices in indoor settings. The following section delves into a comprehensive examination of IoT, shedding light on its significance and the typical architectural configuration of an IoT device within indoor environments. The subsequent section investigates recent applications of indoor IoT, spanning from residential to utility contexts, culminating in an examination of the hurdles associated with the integration of IoT devices in indoor conditions.

1.1 Basics of Internet of Things (IoT)

There has been unprecedented rise in the number of IoT devices all over the world, with a projected 75 billion connected devices in 2025 [1]. The IoT ecosystem is expected to grow to an incredible one trillion by 2035 [2], with a substantial amount being placed in indoor environments.

IoT can be defined as a combination of Wireless Sensor Network (WSN) technologies with communicating – actuating network, being either through a public or private network [3][4]. WSN is a network of nodes, considered as remote sensing, which measure and monitor the environmental conditions [3][5]. Machine-to-machine (M2M) and cyber-physical systems (CPS) have also said to be integral components of the term IoT [4]. M2M can be viewed as a system that allows effective communication between machines, having no or limited human intervention, with WSNs being its supplement. Contrastingly, CPS being an evolved format of M2M, they possess the additional intelligence that delves deeper into the network. By doing so, they are controlling, analysing, and communicating across multiple domains [6].

Ubiquitous computing (UbiComp) can be considered as machines that integrate technology into everyday life, having a human-to-machine (H2M) interaction, associated

through the internet via smart communication technologies. In contrast, IoT is labelled as an IP-based connectivity of devices, systems and services that goes beyond the level of H2M and M2M, being associated over the internet [7][8][9].

IoT has evolved the internet into a network of interconnected objects, with the desired functionality of the device being controlled remotely, providing facilities for information transfer, analytics, applications, and communications. It enables businesses and individuals with the capacity to collect, analyse, and act upon real-time data from a vast array of connected devices, which enhances operational efficiency, reduces costs, and streamlines processes [3][4].

1.1.1 Architectural IoT Layout

A basic and conventional architectural layout for an IoT system is considered as the three-layered architecture, consisting of perception, network and application layers [3][10][11].

- Perception Layer: This is described as the physical layer, where the integrated sensors collect physical parameters, such as data; sending it to the network layer.
- Network Layer: This is responsible in connecting (wired or wireless) to other servers and network devices, processing and transmitting the sensor data.
- Application Layer: This provides specific services for the user, with an easily accessible and designable platform for different applications. It also sends the data back through the network layer to the perception layer.

For a finer aspect of IoT, a five-layered architecture is also considered. With the previous three layers having the same functionality, transport and middleware layers are added. Both the three and five-layered architecture are presented in Figure 1.1.

- Transport Layer: This manages the IoT communication, transferring the data through a network (ZigBee, Bluetooth, WiFi, 4G/5G, LTE, VSAT, LoRaWAN, NB-IoT, Wightles, etc.) from the perception layer to the processing aspect of the network layer.
- Middleware Layer: This software layer allows ease of input and output communication for software developers, giving flexibility between the hardware and the applications. Global Sensor Networks is an example of an open-source middleware platform, allowing users to develop and deploy a sensor service [12].

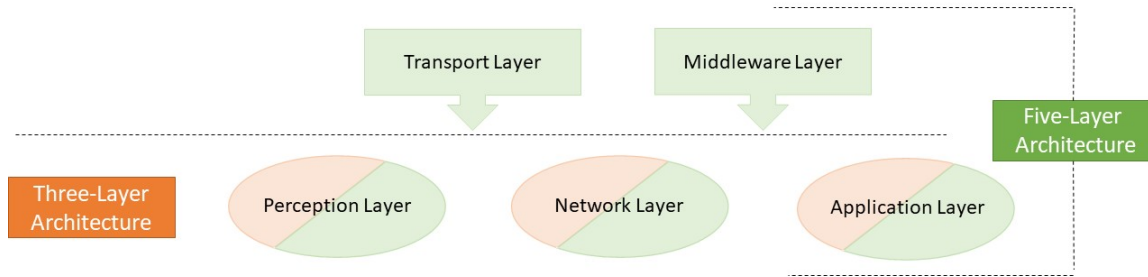


Figure 1.1: Basic architecture of an IoT system

1.1.2 IoT Applications

As previously mentioned, IoT devices are expected to grow to 75 billion connected devices in 2025 [1], having the potential to cover the social, environmental, and economic impacts. IoT is now being used in a wide range of applications, and can be categorised into 4 titles Personal and Home, Enterprise, Utilities and Mobile, as seen in Figure 1.2 below [9][12][13][14].

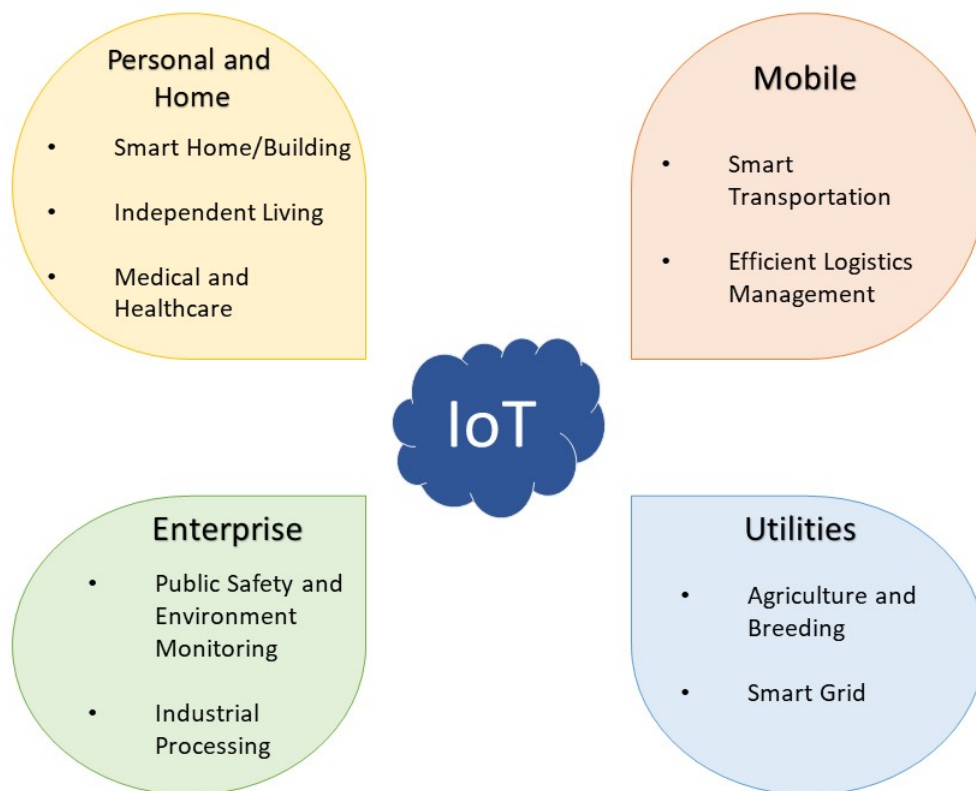


Figure 1.2: Applications of IoT

Each IoT application category is considered in further detail below. In doing so, emphasis is placed on a recent technique, review or contribution being cited for each application as used in mainly indoor conditions.

1.1.2.1 Personal and Home

Smart Home/ Building

Smart homes and buildings combine the use of electronic devices such as heating and lighting with wireless communication technology, which can be controlled remotely from the user's computer, tablet, or smartphone. It has allowed homes and buildings to become more energy-efficient and help consumers with their everyday needs.

There are many different aspects of smart home/buildings, with Gazis *et al.* [15] presenting a prevailing part being home security. The article listed low power sensors that could be integrated in home security, for motion, gas, moisture, and temperature detection, highlighting the need for an overall low powered communication technology to achieve the production of large WSNs.

An energy management approach for smart buildings and homes is mentioned in a paper by Mir *et al.* [16], that sets out to familiarise the factors to energy management. This is to provide the objective of reducing the energy consumption in the household, reducing the greenhouse gas emissions but to also utilise the resources efficiently for the 'Smart Grid'. Consequently, this supports the need for future IoT development to explore ways to manage energy consumption.

Independent Living

This involves supporting elderly people in their day-to-day routine by including a home monitoring system, allowing for an 'independent and safe lifestyle' [9].

Wearable Sensors (WS) have been mentioned by Baig *et al.* [17] as an effective tool for supporting the daily life for older adults by detecting and minimising falls. Baig *et al.* reviewed several articles involving some applications on monitoring the activities of daily life (ADL) and others detecting and preventing falls. The main findings from the review discovered the importance of the design and development of the system for an end-user acceptability. Many complications also arise from applications struggling with the power/storage consumption and the processing and transmission of data. This implies that future IoT development is needed in order to address the power/storage consumption and data usage issues.

Medical and Healthcare

This is also often called the Internet of Medical Things (IoMT), being an ubiquitous healthcare system, connecting and uploading several types of medical equipment data to the servers.

Ashfaq *et al.* [18] provides a detailed review of different IoMT devices, being mostly deployed for home-based healthcare. The extensive applications reviewed and analysed include remote health monitoring, disease prediction, human behaviour prediction, automatic insulin injection, intelligent medicine box, mental health monitoring, non-invasive e-medical care, sleep monitoring, fall detection, seizure detection, and stress and anxiety monitoring. It was concluded that machine learning and edge computing had the most significant impact on the IoT-based smart healthcare, with room for further improvements with respect to these areas.

1.1.2.2 Enterprise

Public Safety and Environment Monitoring

This involves devices that can monitor the parameter changes in the environment, allowing for real time tracking and observation of different conditions, including fisheries, forests, air quality, weather conditions, endangered species protection and other natural habitats.

Marques *et al.* [19] whilst presenting an extensive review on the air quality monitoring IoT systems in indoor environments, noted that humans spend more than 90% of their time indoors, with the primary health risks being the indoor air and environmental (thermal comfort, acoustics, and lighting) quality. The analysed literature by Marques *et al.* found that there are still limitations for indoor air quality systems, with respect to the accuracy of the sensors, communication, and the energy consumption of the monitoring systems.

Industrial Processing

The industrial domain has had a large growth with IoT, with complexity and functionality requirements of equipment being intense; and tracking the machinery performance and predictive maintenance becoming popular [9].

A momentous component of Industry 4.0 is from the introduction of IoT, mentioned by Khan *et al.* [20]. Industry 4.0 being the fourth industrial revolution, involves

advanced computing devices and logistics. The article mentions the increased manufacturing efficiency with the addition of IoT, reduces human error. The best approach for predictive maintenance has also been discovered through using IoT.

1.1.2.3 Utilities

Agriculture and Breeding

The change from conceptional farming to using modernising concepts has allowed for changes in agricultural development under real time data, with regards to realities of climate change [9].

An article by Martini *et al.* [21] proposed a computational model that supports farmers with improvement, warnings and alerts with respect to cultivation problems involving indoor crops. The focused indoor agriculture model is called IndoorPlant, giving recommendations for cultivation improvements. Other work by Yang *et al.* [22] resulted in an environmental collector (temperature, humidity, illumination intensity and air) using IoT nodes in indoor farms that allows for data to be periodically sent to the cloud. The data then provides information and guidance for plant cultivation for the users.

Smart Grid (SG)

Technology has allowed two-way communication between the generation site to the customer; providing efficiency and flexibility to the energy grid. The energy load and demand can be altered, depending on the real-time data transmitted through the IoT, which can also redirect distribution and detect blackouts [9][13].

Mehmood *et al.* [23] describes an underlying issue with using IoT alongside SG, with a bottleneck effect from the IoT to the cloud, due the enormous amount of data that the sensors have to collect; imposing stress on the communication network. The authors further emphasise that using Edge Computing to overcome these issues by providing data processing and storage resources at the edge of the IoT system, leads to a reduction in the latency and network load for the real-time applications.

1.1.2.4 Mobile

Smart Transportation and Efficient Logistics Management

By applying the principle of Mobile Ad-hoc Network (MANET), Vehicular Ad-hoc Network (VSNET) was created, allowing for information to be relayed between cars. This can increase transportation efficiencies, improving road safety. Traffic management has also evolved, having an interconnection of devices to prevent traffic jams and accidents. IoT can also be integrated into monitoring transported items and planning efficiently.

Jan *et al.* [24] produced an improved method of analysing large amounts of real-time data, processed by Hadoop and Spark. This allowed users to receive real time information following a vigorous data transportation process, providing status of the road traffic information for the user to adopt and decide which route is best to take.

1.1.3 Present issues with IoT systems

There are challenges facing IoT systems, which can be detrimental from small scale issues (users) to large scale (utilities) use. These arise in security, which can affect consumer privacy and data. Energy consumption is another challenge, with storage and size being a major concern for self-powered devices [12] [25].

With WSNs being a key feature for IoT, having the capabilities of gathering the environmental information whilst also performing actions and data analysis, they are now considered inseparable to each other [26]. Therefore, the communication and sensing aspects (perception layer) of WSNs/IoTs will now be referred to as IoT nodes, being the key parameters of collecting, processing, and transmitting the relevant data between each node, and to the internet.

1.1.3.1 Security

Security attacks are an issue facing indoor IoT ecosystems, with insecurities and incapacities of defending from attackers being a major concern. A security attack can be defined as an illegal action by an intruder which accesses sensitive and personal information through the network by making changes. This can allow the attacker to monitor and take control of different smart homes devices remotely, affecting the IoT device's performance whilst also collecting information for a malicious purpose

[3][4][27]. Privacy is also important for user's trust, especially health related data; meaning that safeguarding sensitive personal information is imperative, especially with IoMT applications [18].

There are security challenges for the whole of the IoT architecture, that being the three-layered or the five-layered architectural layout. Each layer should therefore have its own security protocol with additional security that protects the entire IoT system, crossing each layer [28].

The perception layer has the largest number of issues with security attacks compared to the network and application layers, as IoT nodes have limited memory, processing capabilities and heterogeneity; meaning that standard and existing security protocols are too complicated for the IoT nodes. This allows intruders to gain an easier access to the IoT ecosystem, being an attractive architectural layer to gain sensitive data and personal information gathered from the IoT nodes [16][26][29].

The main security issues that arise in the perception layer are listed below:

- Eavesdropping: This is when an attacker intercepts the communication between different IoT nodes, taking confidential data. The issue becomes more of a problem when there are multiple nodes transmitting to each other [27][30];
- Sniffing: A sniffing application can be placed by the attacker, being a malicious sensor/device, forcing entry into the system and collecting private information[27];
- Booting: During a boot process, especially with edge devices (this being the entry point into the network), there are minimal security mechanisms, resulting in the attacker taking advantage of this weakness [27];
- Node Capturing: The attacker can create a gate by replacing a network node with one of their compromised sensors, giving entry into the system. This technique is usually implemented when deployed nodes are in an unattended environment [31];
- Side Channel: Side channel information can be obtained from the encrypted system, through the cryptographic algorithm. By exploiting the power usage, execution timing, and electromagnetic field, information might be obtained to gain access to the system [27][28].

Connecting IoT nodes to a trustworthy network prevents security issues such as sniffing. It is suggested by Touqeer *et al.* [27] not to connect to unmonitored

public WiFi places, which could be created by an attacker, with malicious nodes. They also recommended the use of leakage-resilient, public-key encryption scheme, meaning that even if some data bits are lost, it guarantees the confidentiality of information. A domain-based solution called fog computing has also emerged as an energy management system of processing data, by either processing at the local edge or sent to the cloud for storage. This has allowed for a faster processing of information, with improved reliability and security [16].

1.1.3.2 Storage

The autonomous operation for powering IoT nodes is one of the biggest critical issues that is preventing the growth of indoor IoT ecosystems [3][18][26][32][33][34]. Primary and secondary batteries are the most used energy sources for IoT nodes; primary being a ‘single use’ power supply, such as alkaline, whilst secondary refers to batteries that can be rechargeable, such as lithium-ion. The issue arises with the lifetime (Equation 1.1) of these power supply. The finite capacity will eventually cause the batteries to deplete, causing many complications with replacing and maintaining the IoT nodes, especially if placed in inaccessible areas. This limits the ideal set-up for these IoT nodes due to the maintenance operation difficulties. Batteries also discharge when not in use due to current leak, with rechargeable batteries having internal inefficiencies; reducing the performance after each recharging cycle, limiting the numbers of charge-discharge cycles and hence resulting in not surpassing 80% deep-discharge [26][35][36][37].

$$\text{Battery Lifetime (Years)} = \frac{C}{I_L * 24 * 365} * \eta \quad (1.1)$$

The primary battery can be calculated with a capacity of C to power the system. η indicates the usable capacity (assumed discharge down to 20% of its full capacity). The I_L is the average load current [38].

(Say if a system with 3-Ah battery capacity and 113 μA of average load current, then $3/(113 \times 10^{-6} * 24 * 365) * 0.8 = 2.4$ years of battery lifetime, which doesn’t include the additional current leakage issues).

Lithium based batteries are popular with portable devices due to their high specific capacity and energy density, with lithium-ion batteries (LIBs) having the largest contribution of rechargeable battery type [39]. A rapid growth of LIBs have come from the development of electric vehicles (EVs), with 10 million units globally pro-

duced in 2020, with an expected growth of EVs to 225 million in 2030 [40].

The environmental and economic sustainability impact in the rise of using LIBs has drawn some challenges, due to the toxicity, acidification, and the resource depletion of raw materials (lithium, cobalt, nickel, or manganese) used in LIBs manufacturing [35]. There has been recent work in recycling retired LIBs, to save some of the non-renewable resources and the reduction emissions of greenhouse gases. However, whilst there are several active research studies involving laboratory scale recycling, there are limited life cycle assessments (assessment of environmental impacts of products) of rechargeable batteries, with urgency for more commercial scale processes for regeneration or recovery of the materials required [35][39][40].

An alternative energy storage technology is to use supercapacitors (or known as ultracapacitors), which can provide an interim power supply to the IoT nodes. Supercapacitors are environmentally friendlier than LIBs, providing a larger power density (supplied per unit mass), unlimited cycle life, and shorter recharge times. However, LIBs still provide a much higher energy density (energy stored per unit mass) compared to supercapacitors with a higher self-discharge rate [26][36][41].

1.1.3.3 Energy Consumption

The energy consumption of IoT nodes varies depending on the application, as different sensor systems and communication technologies have a range of power requirements. The communication system consumes most of the energy compared to other subsystems, hindering the life expectancy, with the greatest dissipation in power occurring during the transmission of data. A widely used key feature in power reduction is for the communication subsystem to enter sleep mode, disabling all subsystems temporarily [32][36].

Several low power communication technologies have recently emerged for indoor IoT applications, with Table 1.1 below (see page 26) showing some of the low power transceivers available. Each type of wireless communication technology is designed and optimised for a particular environment of the placed IoT nodes, meaning a careful consideration is required for the optimal performance of the whole WSNs. The emerging indoor low-powered wireless technology types include, Radio frequency identification (RFID), Bluetooth low energy (BLE), Zonal intercommunication global-standard (Zigbee), Sigfox, Long range radio (LoRa) and cellular [18][34].

There has been a recent impact with the introduction of using transceivers with a sub-GHz networking such as LoRa, SigFox, IEEE 802.15.4, and DASH7; providing a longer communication range with lower power consumption compared to technologies using the 2.4 GHz band, such as BLE and WiFi. The longer distance is due to physical matter not absorbing as much of the lower radio frequencies. However, the drawback is slower transmission speed, with a short-range device (SRD) regulation being placed, restricting the devices with the availability, and allowed radio spectrum. The unlicensed frequency band in the European region is ranged between 863 to 870 MHz [42].

Table 1.1 Emerging low-power communication technologies

Model Name		Supply Voltage	Power Consumption			Max Data Rate	Nominal Range	Ref
			Transmit	Receive	Sleep			
LLCC68 (LoRa)		1.8 V to 3.7 V	45 mA	4.6 mA	600 nA	300 Kbs (FSK)	Several Km	[43]
RYZ012 - BLE (2.4 – GHz)		1.8 V to 3.6 V	4.8 mA	5.3 mA	0.4 μ A (without SRAM retention)	125-500 kbps for Long Range	10 m-100 m	[44][45]
ST: S2-LP (Sub 1GHz band)		1.8 V to 3.6 V	11 mA (@+10 dBm)	7 mA	700 nA	500 kbps	Several Km	[41][45]
nRF9160 -Cellular IoT (100 bytes/hour with GPS)	LTE-M	3.0 V to 5.5 V	Average = 42.67 μ A (sleep = 2.7 μ A)			300-375 kbps	“up to 4x”	[46][47]
	NB-IoT		Average = 62.46 μ A (sleep = 2.7 μ A)			127-169 kbps	“up to 7x”	

1.1.4 Solution

IoT ecosystem has become prevalent, embedding intelligence into our environment. Being part of smart homes devices to modernising the methods for indoor agriculture, the IoT ecosystem has become an important tool for real-time data analysis, supporting social, environmental, and economic impacts.

However, due to the large increase in IoT nodes, it has resulted in security and power consumptions issues. With security being a significant issue, ensuring sufficient input power to the IoT nodes would allow for more powerful memory and processing capabilities to tackle the security challenges. Whilst the power consumption of microcontroller and communication technologies have made a substantial progress in reducing the energy consumption, fully relying on primary or secondary batteries to power the nodes is economically and environmentally unsustainable.

A promising solution in providing sufficient power is to harvest indoor energy. This would result in prolonging the lifespan of these devices, key in reducing the complexities of replacing batteries in inaccessible areas, having a greater economic appeal and technical viability for security. This could either be to aid the battery life of the IoT nodes, storing the energy harvested, or preferably work battery-less [36]. Subsequent Section (1.2) describes the available techniques for indoor energy harvesting, presenting the recent progress, benefits, and limitations of each technique.

1.2 Indoor Energy Harvesting

1.2.1 Introduction

Renewable or ‘freely’ available energy can be obtained from mechanisms that generate power from the environment. Energy harvesting can be divided into two categories: large energy harvesting modules for terrestrial power generation (kW to MW), and smaller harvesting modules to power IoT nodes and portable electronics (μW to mW) [48]. Section 1.2 will therefore focus on the micro-energy harvesting technologies (indoor environment), which again can be categorised into two harvesting sources: ambient (readily available energy in the indoor environment) and external (mechanical or human energy) sources [32]. In an IoT context, ambient energy is considered naturally occurring in the device’s environment, whilst external sources are described as energy supplied that is not necessarily part of the device’s immediate environment. The available indoor energy harvesting techniques are shown in Figure 1.3

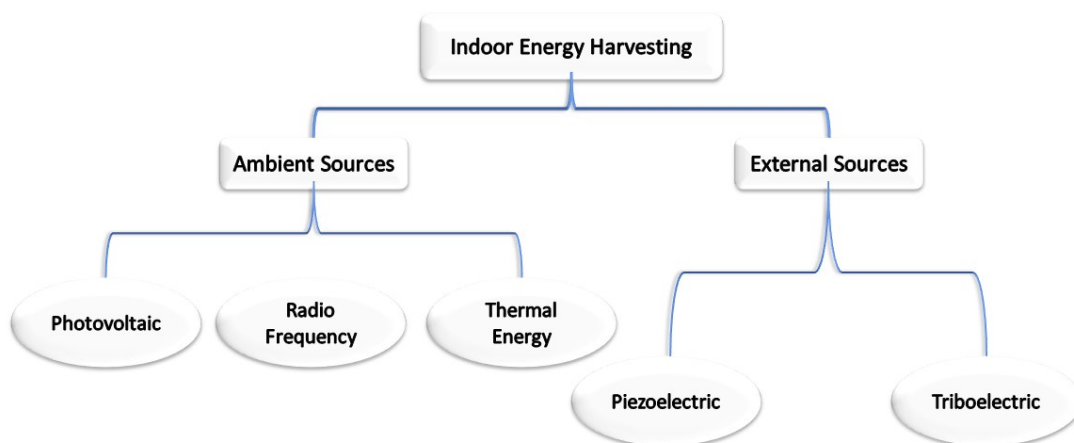


Figure 1.3: Taxonomy of indoor energy harvesting techniques. Adapted from [32][36]

1.2.1.1 Parameters

Pecunia *et al.* [36] lists several parameters that should be considered when selecting the best suited indoor energy harvesting techniques. These include:

Energy Reliability - Depending on the application, IoT nodes might need to rely on the predictability and controllability of the energy source; allowing to forecast the amount of energy but to also potentially change the energy levels supplied by the end-user of the IoT.

Environmental Sustainability - Similar to considerations with the use of different energy sources such as LIBs, it is important to take into account the environmental impacts, including the base materials, manufacturing process, use, and the decomposition of the energy harvester mechanism.

Cost - Low-cost is beneficial for the energy harvesting mechanism, with the likelihood of having the same amount of modules as the IoT nodes itself, it is key to keeping the overall price to a minimum.

Durability - It is important that the energy harvester can sufficiently last a long time, enabling the IoT nodes to deliver their nominal performance, but depending on the mechanism, to also increase the lifetime of the nodes.

Deployability - The functionality should be considered, where there is flexibility in the range of applications the energy harvester mechanism can be applied. This includes operating in a diverse energy level output and the ease of installation at different locations.

Efficiency - The overall power from the energy harvester should be sufficient to operate the IoT nodes/ support the energy source. Improved power conversion efficiency (PCE) from the mechanism would result in an opportunity to reduce the energy harvester size and the IoT node's overall footprint. The PCE is defined in Equation 1.2 below, where P_{in} is the amount of power from the energy source that reaches the energy harvester, and P_{out} being the resultant power output.

$$PCE = \frac{P_{out}}{P_{in}} \quad (1.2)$$

1.3 Energy Harvesting Techniques from Ambient Sources

1.3.1 Ambient Radio Frequency (RF) Energy Harvesting

There are several RF sources available in the ambient environment, having the possibility of converting the electromagnetic waves into electricity. These include static (continuous power), such as radio and TV stations, and dynamic sources (intermittent power), such as cellular systems and WiFi. The frequency spectrum is between 3 KHz and 300 GHz [26].

There are also some other non-ambient RF sources, which can be emitted purposefully for RF harvesting, acting as a dedicated energy source. This does provide some predictability, offering the IoT nodes the freedom to be placed in inaccessible locations with reliability of gaining the energy source, prolonging the lifetime from the harvested energy. However, these transmitters require continuous grid-based power, high deployment cost, and limited output power due to regulations being placed with concerns to health and safety [49].

1.3.1.1 Process overview

The key element in a RF energy harvester is the rectenna, which is the combination of an antenna and the rectifier circuit, seen in Figure 1.4 below.

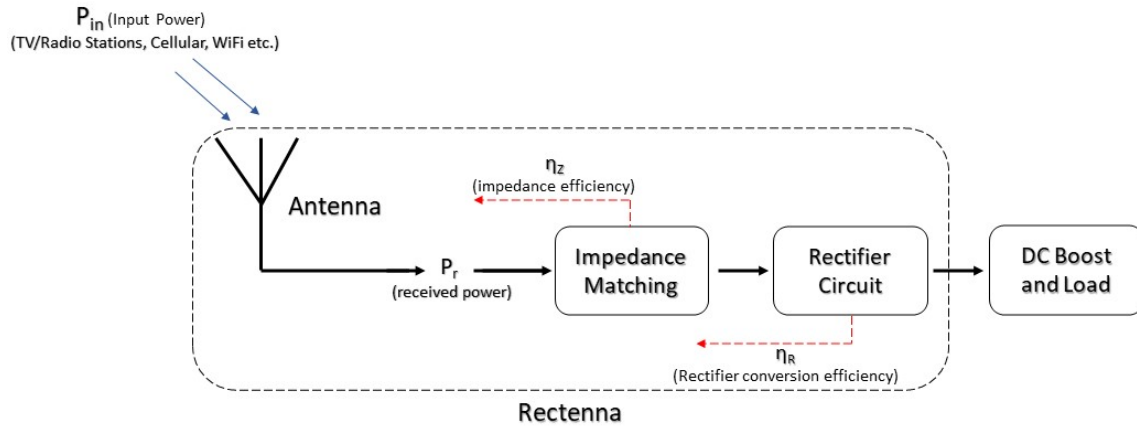


Figure 1.4: RF energy harvesting layout. Adapted from [50][51]

Antenna

The antenna detects the RF energy, sending it to the RF rectifier circuit through the

impedance matching. Multiple antennas will increase the amount of RF collected compared to a single antenna system [25].

$$P_r = \frac{P_t G_t G_r \lambda^2}{(4\pi d)^2} \quad (1.3)$$

There are many factors that can alter the received power P_r from the antenna, as seen in Equation 1.3 above, following Friis' theorem. These include the distance between the RF source and the receiver antenna, performance of the antenna and the operating frequency. The gains of receiver and transmitter antennas are denoted by G_t and G_r respectively; P_t being the transmitted power; λ is the wavelength (= speed of light/frequency), and d is the far-field distance [52][53].

Impedance Mismatching

Due to the high impedance of the diode (part of the rectifier circuit), signal reflection can occur, resulting in some RF power being reflected back towards the antenna, causing a loss in energy conversion efficiency. The impedance mismatching configuration includes inductors and capacitors which minimise the reflected power loss, transferring most of the captured power to the rectifier circuit [51][54].

The efficiency of the impedance mismatching η_Z , can be seen in Equation 1.4 below [50]:

$$\eta_Z = 1 - |\Gamma|^2 \quad (1.4)$$

Where the reflection coefficient Γ , can be defined in Equation 1.5. The input impedance of the rectifying circuit and antenna are represented by Z_L and Z_R respectively [50][51].

$$\Gamma = \frac{Z_L - Z_R^*}{Z_L + Z_R} \quad (1.5)$$

Rectifier Circuit

The rectifier circuit is an important aspect and a central component of RF energy harvesting, converting the harvested RF signal collected from the antenna (small magnitude of a high-frequency voltage) to a DC load (steady voltage with a defined value) [52]. Schottky diodes are mainly used for rectifier circuits, as they can meet the high frequency operations and low drop voltage, with several rectifier topologies available (such as single or multiple-stage circuit), depending on the required output voltage. However, the fundamental thermal limit has been reached with the

Schottky diodes, with poor conversion efficiency when RF incident power is low [51][54]. A solution to this is to use diode connected complementary metal oxide semiconductor (CMOS) transistors, offering an integrated circuit rectifier; however issues arise with the processing complexities including high costs [51].

Other promising diodes have now become an alternative option to Schottky diodes, including backward tunnel (Esaki) diodes, which have surpassed the current responsivity thermal limit; spin diodes and metal-insulator-metal (MIM) diodes [54][55].

1.3.1.2 Resultant efficiency of RF Energy Harvester

The overall PCE of RF to DC of the whole rectenna can be expressed in Equation 1.6, taking into account the efficiency loss at each section, involving the antenna, impedance mismatching and the rectifier circuit [55].

$$PCE_{RF-DC} = \frac{1}{4} P_r R_I^2 \eta_Z^2 R_j \left[\frac{1}{1 + (\frac{f}{f_c})^2 (1 + \frac{R_s}{R_j})} \right]^2 \quad (1.6)$$

Where R_I is the current responsivity, R_J and R_s are the nonlinear junction and parasitic resistance (of the rectifier) respectively, with f and f_c being the frequency and cut-off frequency.

1.3.1.3 Radio Frequency Identification (RFID)

A prominent example of a basic RF energy harvester is RFID [56], being an important low energy wireless component; regarded as one of the main pillars of IoT applications [57]. They can be said to be an automatic identification device, enabling to locate a tagged object for automatic detection. They consist of a tag (transponder), a reader and an antenna. Like barcode, but with the capability of reading and writing data, whereas in contrast, barcodes only read data in the line of sight without sending to other devices. RFID technology works with the tag receiving electromagnetic waves from the reader working at 2.4 GHz. The tag then sends a response, which involves data installed in the form of product serial number back to the reader via an electromagnetic wave [32][58].

RFID tags which are implemented with IoT nodes tend to be passive [59], meaning that they don't include a source of energy storage such as a battery, relying on the reader to provide power through electronic emission energy. They are suitable for a wide range of applications as they are smaller and easier to install [60]; whilst an active tag carries a battery, giving power to their circuit. Therefore, the tag does

not have to rely on the reader as the source of energy, increasing the read distance, accuracy, and complexity of data [58].

RFID technology uses the LF (low frequency), HF (high frequency) and UHF (ultra-high frequency) operation, with higher the frequency, the greater the distance of detection. Due to the limited power consumption of passive tags, embedding an analogue-to-digital converter with sensors including a reasonable operating range has been difficult to deliver [61]. Depending on the antenna size and the mounted surface of the passive tags, the communication range using UHF varies from 1 *m* to approximately 15 *m*, with 30 *m* being also achieved with metal mountable tags [60].

Whilst there are many benefits for using RFID for data communication, including the adaptation of RFID sensors with extremely low power usage; overall, the read range can be low, also requiring an RFID reader to provide the energy requirements (for passive tags). This is similar to dedicated energy source with ambient RF energy harvesters [59].

1.3.1.4 Overview of Applications

Whilst there have been many applications and research based on dedicated transmitters for RF energy harvesting [50][53][62][63], the additional power consumption (from the grid) required to power these dedicated transmitters is unsustainable, with also a potentially hazardous risk to health. Due to this, only ambient RF energy harvesting should be considered [36].

However, the reasoning behind switching to dedicated transmitters has been due to the low RF ambient energy source. Visser *et al.* [50] mentions that using ambient energy is unfeasible, iterating that between 25 – 100 *m* from a Global system for Mobile Communication (GSM) 900 base station, the expected power density was estimated to be in the range of $10^{-2} - 3 \times 10^{-1} \mu W/cm^2$, meaning that 330 to 1000 *cm*² area antenna is required to harvest 100 μW , without including the efficiency losses. Raj *et al.* [49] also mentions the impracticality of harvesting ambient RF power due to only providing around 1 $\mu W/cm^2$ in energy source.

On the other hand, there have been some promising diode technologies arising, that have surpassed the limited Schottky diode for an improved low-power transceiver [54]. Other developments have included flexible rectennas fabricated using flexible semiconductors, allowing RF harvesters to be integrated into smaller spaces and arbitrary shapes. There have been limitations with the transport properties of the flexible semiconductors; however through use of novel material, the range frequency

of 10 GHz has been achieved [55]. With an input RF power of -0.7 dBm , the ambient power harvested from the 2.4 GHz Wi-Fi, achieved an output of $48.4\text{ }\mu\text{W}$ at a transmitted distance of 1 m , from a MoS2 enabled flexible rectenna [64].

Currently one of the main issues is the considerable drop when the incoming signal is below -12 dBm , with no power harvested at -35 dBm [52]. Chiu *et al.* [65] attempts to mitigate this issue by combining multi-banded ($900, 1800$ and 2100 MHz) and dual-polarized multiple antennas in order to harvest the low ambient RF power density. In doing so, a cold start time (operational time it takes to harvest energy from no stored initial energy in the system) of 6 hours, and a warm start time (taken to harvest energy from an operational management system to enough energy to collect and transmit data) of 15 minutes is achieved, for RF power levels of -28.6 dBm at 950 MHz (sensing temperature, pressure and humidity, with wireless transmission). While it does not mention the amount of energy harvested, a device was created, being $34 \times 34\text{ cm}^2$ big placed 50 m away from the base station by a window.

1.3.1.5 Strengths and limitations of ambient radio frequency energy harvesting

1.3.1.5.1 Strengths

- Good reliability of RF ambient energy source, which can harvest energy to IoT nodes day and night.
- Different radio frequency ranges can be harvested, from cellular to Wi-Fi (2.4 GHz).
- Flexible rectennas have been achieved, allowing RF harvesters to be integrated into IoT nodes with smaller spaces and arbitrary shapes [55].

1.3.1.5.2 Limitations

- The available ambient power source of the RF signal is low, which could be an issue to sufficiently power IoT nodes.
- It has an overall low efficiency, especially when the input energy is below -30 dBm , with the density being inversely proportional to distance [26][65].
- Indoor object can scatter, absorb, and reflect the RF source, affecting the strength of the electromagnetic waves reaching the RF energy harvesters [36].

1.3.2 Thermoelectric Energy Harvesting

In indoor conditions, heat sources can be found in the form of waste heat, such as ovens, radiators, boilers, and air conditioners. Harvesting heat from the human body is also a feasible energy source to power IoT nodes [36][66].

1.3.2.1 Thermoelectric Generators (TEGs)

1.3.2.1.1 Process overview

Consideration of utilising the spatial-temperature gradient [26], thermoelectric generators (TEGs) consist of a p-type semiconductor and an n-type semiconductor, interposed between two ceramic layers to support the module. This forms a thermocouple, each one placed electrically in series and thermally in parallel [36][67].

Depending on the heat flow direction, there are three thermocouple arrangements of TEGs. These include: lateral heat flow transfer through lateral thermocouple arrangement; vertical heat flow transfer through vertical thermocouples arrangement; and vertical heat flow transfer through lateral thermocouples arrangement [66].

The thermoelectric generators (TEGs) are based on the Seebeck effect, being the diffusion of electrons and holes through p-and-n-type semiconductors, by a temperature gradient. If the temperature gradient is maintained between the semiconductors end faces, from the hot end to cold, carriers will diffuse, resulting in an electromotive force (V_{Thermo}) [36][68]. The output voltage (V_{Thermo}) can be seen in the Equation 1.7 below, determined by the Seebeck coefficient (α) [69].

$$V_{Thermo} = \alpha \Delta T \quad (1.7)$$

Where ΔT is the temperature gradient being $\Delta T = T_H - T_C$. T_H is the temperature of the thermal energy that is generated from the heat source, with T_C being the release of the heat sink temperature to the surrounding ambient air [68]. Therefore, the maximum obtainable power from the TEG, for different thermal gradients results in varied output voltage [68].

The region of the Seebeck coefficient for a typical thermoelectric material is between 200 - 300 $\mu V K^{-1}$, meaning that a TEG requires thousands of thermocouples to provide a voltage of $\approx 1 V$, in ambient conditions. A typical ambient temperature difference is said to be $\approx 10 K$ [36].

The thermoelectric material's value of merit ZT , being dimensionless, is used to determine the performance. It is a well-known standard of comparing thermoelectric

generators, expressed in Equation 1.8 below as [69]:

$$ZT = \frac{\sigma \alpha^2 T}{K_e + K_I} \quad (1.8)$$

K_e and K_I are defined as the electronic and lattice contributed thermal conductivity respectively, and σ is the electrical conductivity [69]. T is the average absolute temperature, defined below as [36]:

$$T = \frac{(T_H + T_L)}{2} \quad (1.9)$$

This demonstrates that the best performance is from a high Seebeck coefficient and electrical conductivity (for an increase in output voltage and internal resistance reduction), with a low thermal conductivity (provide a considerable temperature difference) [70][67].

The power conversion efficiency (PCE) of a TEG can be defined as [36][66]:

$$PCE_{TEG} = \frac{T_H - T_L}{T_H} \frac{\sqrt{1 + ZT} - 1}{\sqrt{1 + ZT} + \frac{T_L}{T_H}} \quad (1.10)$$

where the first term of this equation is the Carnot efficiency. The other section is the ratio between the heat flow and electrical power produced through the TEG module [67].

1.3.2.1.2 Overview of Applications

Flexible planar and vertical TEGs have been achieved to self-power IoT nodes (for smart building monitoring) [71] [72], being placed around heat pipes. With a temperature difference of 127 K, Iezzi *et.al.* [71] achieved an output power of 308 mW through using an industrial pipe; whereas Kim *et.al.* [72] achieved a power density output of 1.72 mWcm⁻², with a heat pipe being at 70 °C.

There are various applications exploiting the sustainable energy from body heat [26]. Some of these include wearables for sports and fitness, health monitoring, and tracking systems. Depending on the body activities, it is said that the temperature gradient is around 13 °C between the body and ambient air [66].

Zhang *et al.* [73] transmitted electrocardiogram (ECG), electromyogram (EMG), and electroencephalogram (EEG) data through a battery-less body sensor node, powered by a thermoelectric generator. This was achieved by designing a very low total chip power of 19 μW (TX duty-cycled at 0.013%), with the capabilities of having a very low input voltage of 30 mV. However, this does require a RF pulse

kick (-10 dBM) to allow the internal oscillator and control logic to turn on, which require 600 mV , after this, the chip can sustain the voltage from the TEG voltage output.

Furthermore, Bao *et al.* [74] developed a flexible wearable TEG with an optimised cooling-enhanced electrode, being only 3 mm in thickness. With an experimental volunteer wearing the device, whilst sitting indoors, the device achieved an output of $30.25 \mu\text{Wcm}^{-2}$ with a voltage of 60 mV .

Bi_2Te_3 - based inorganic materials have been adopted for TEGs in ambient conditions ($< 150 \text{ }^\circ\text{C}$) [67], providing a ZT of ≈ 1 , with a power density of $< 60 \mu\text{Wcm}^{-2}$ in wearable applications. There are some environmental challenges using these inorganic materials, relying on scarce and toxic elements, with a high-energy intensive fabrication method. Organic polymers have also been tested, however with a lower ZT values between $0.2 - 0.45$, to provide TEGs that are mechanically flexible [36].

Other thermoelectric materials that have reached a ZT of around 1 also include PbTe and CoSb_3 for intermediate temperature range ($150 - 500 \text{ }^\circ\text{C}$) [67]. The main issues of improving the thermoelectric material's value of merit ZT , is the dependency of the Seebeck coefficient and electrical conductivity. With an increase of Seebeck coefficient leads to the decrease of electrical conductivity due to a decrease in carrier concentration [66].

1.3.2.1.3 Strengths and limitations of thermoelectric generators

1.3.2.1.3.1 Strengths

- No moving parts and noise free [36].
- Design simplicity, long lifetime, and no unnecessary maintenance [66].
- Recycling waste heat energy.

1.3.2.1.3.2 Limitations

- Each thermocouple has a low voltage output, requiring the voltage to be increased to power the IoT node.
- Limited temperature gradient in ambient conditions, resulting in a potential of insufficient energy harvested to the IoT nodes.

- A good thermal contact is necessary with the heat source and sink available; required for an efficient TEG, meaning they can only power dedicated IoT nodes in the vicinity of the heat source [36].

1.3.2.2 Pyroelectric Generators (PYEGs)

1.3.2.2.1 Process overview

Considered as utilising the temporal variation in temperature [26], pyroelectric effect is the spontaneous polarisation change through a continuous change in temperature, containing materials that are a class of non-centrosymmetric polar crystals [75]. Piezoelectric properties are included in pyroelectric materials, resulting in a secondary effect from the thermal expansion with temperature change. Therefore, at constant stress conditions (to prevent the secondary effect), the pyroelectric coefficient, P_{pyro} , is [69]:

$$p_{pyro} = \frac{d\rho}{dT} \quad (1.11)$$

where T is temperature, and ρ being the spontaneous polarisation. The voltage output can be calculated as:

$$V = \frac{p_{pyro}}{\epsilon} h \Delta T \quad (1.12)$$

In the polarization direction, the permittivity of the pyroelectric material is denoted by ϵ , with h being the thickness [75]. When heated, meaning that $dT/dt > 0$, a disturbance in the dipole alignment is caused by the thermal vibrations, changing the spontaneous polarization. This results in bound charge carriers separating, and accumulating at the electrode surface. The change in the spontaneous polarization also happens when cooling, with dipoles realigning themselves. The corresponding electric current flow when the pyroelectric capacitive structure is connected to the load is [76] [77]:

$$I = \frac{dQ}{dt} = p_{pyro} A \frac{dT}{dt} \quad (1.13)$$

The induced charge is Q , and A is the surface area. The capacitance of the pyroelectric generator is represented as:

$$C = \epsilon \frac{A}{h} \quad (1.14)$$

The energy stored in the pyroelectric material can be stated below as [76]:

$$E = \frac{1}{2} CV^2 = \frac{1}{2} \frac{p_{pyro}^2}{\epsilon} Ah (\Delta T)^2 \quad (1.15)$$

The large and fast change in temperature is important for an increased energy conversion. This is seen by the equations showing that the change in temperature difference (ΔT) and with time (dT/dt) are proportional to the output current and voltage [75].

1.3.2.2.2 Overview of Applications

Lee *et al.* [75] enhanced the pyroelectric conversion, using a pyroelectric material of polyvinylidene difluoride and an absorbing electrode being tosylate-doped poly(3,4-ethylenedioxythiophene) (PEDOT:Tos). This achieved a power density of 449.0 nW/cm^2 when irradiated by 1200 nm NIR light with 100 mW/cm^2 intensity, having a frequency of 33 mHz . The output voltage is considerably large, outputting a peak voltage of 74.6 V , however with small AC currents. The AC voltage output will have to be converted to DC voltage (requiring a rectifier circuit) for IoT node applications.

Whilst there have been other work done using pyroelectric generators [76], very few studies have been conducted in indoor conditions. This is mainly because of the limited amount of power that can be harvested due to the lack of ability of the generators to induce high frequency temperature fluctuations [78].

1.3.2.2.3 Strengths and limitations of pyroelectric generators

1.3.2.2.3.1 Strengths

- Large AC voltage output required to power IoT nodes [75].
- Easy to fabricate [76].
- Desirable when there are no temperature gradients [77].

1.3.2.2.3.2 Limitations

- Lack of ability to induce high frequency temperature fluctuations.
- Outputting an AC voltage.
- The pyroelectric material produces high specific heat resulting in less electrical dipolar energy and more energy absorbed [77].
- Low efficiency of charge extraction cycles [78].
- Inability to induce high frequency temperature fluctuations [76].

1.3.3 Photovoltaic (PV)

Clean and affordable solar energy has great potential in outdoor conditions, being an attractive energy to harvest for IoT nodes [32]. Contrastingly, the energy source in indoor conditions is different, where the main light sources typically are white light-emitting diode (WLED) and fluorescent (FL) [36]. These light energy sources are a great potential in indoor energy harvesting for IoT nodes. In homes, the reliability of the light sources can be predicted, however with a lower light intensity compared to outdoors. Other beneficial locations such as industrial buildings, stadiums, and hospitals may provide more consistent lighting [32].

1.3.3.1 Process overview

Typically, when a PV cell absorbs a light energy source; electron-hole pairs are converted through the semiconductor electrical junction device. The photovoltaic effect involves the external voltage and electric current outputs causing the charges to travel towards the electrodes sandwiching the semiconductor, to the attached load [32][36].

A single diode electrical circuit, as seen below in Figure 1.5, can be considered as an equivalent PV model. The PV cell acts like a current source with a voltage limiter at low light intensity [79]. The second diode is omitted following Shockley theory, where recombination in the space-charge zone is neglected [80].

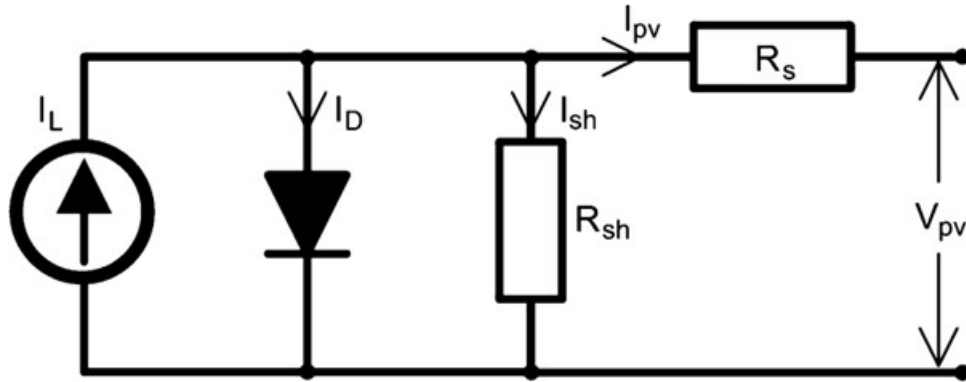


Figure 1.5: Equivalent single diode circuit for a PV module [68]

Considering a single diode electrical circuit, the current density output from PV cell can be expressed as J_{PV} , in Equation 1.16. The components of parasitic resistances are also included, being the shunt and series resistance; having the capabilities of degrading the cell, impacting on the current-voltage (I-V) curve [81].

$$J_{PV} = J_L - J_0 \left[\exp \left(\frac{q(V + JAR_s)}{nkT} \right) - 1 \right] - \frac{V + JAR_s}{R_{sh}} \quad (1.16)$$

Where J_L is the photo-generated current density, J_o is the dark/reverse saturation current density of the p-n diodes, R_s and R_{sh} are the series and shunt cell resistances respectively, and A is the cell area. The number of PV cells in series is represented by n , and V is the output terminal voltage of the PV cell [38][80][82].

In general circumstances, the shunt resistance R_{sh} , is infinite [68], resulting in the output current density, with a four parameter model, being defined as:

$$J_{PV} = J_L - J_0 \left[\exp \left(\frac{q(V + JAR_s)}{nkT} \right) - 1 \right] \quad (1.17)$$

The junction terminal thermal voltage V_t , can be defined as:

$$V_t = \frac{kT_c}{q} \quad (1.18)$$

The charge of the electrons is defined by q ; k is the Boltzmann's constant, and the cell temperature is T_c . By considering that the light generated current is equal to the short circuit current, the ambient temperature is defined by T_c [82].

The fill factor FF , can be calculated in conjunction with open-circuit V_{oc} , and closed-circuit I_{sc} , which is the maximum voltage and current from a solar cell. The fill factor is the ratio of the maximum power (MP) from the solar cell to the product of open and closed circuit, shown below as:

$$FF = \frac{V_{MP} I_{MP}}{V_{OC} I_{SC}} \frac{P_{MP}}{V_{OC} I_{SC}} \quad (1.19)$$

The power conversion efficiency (PCE) of a cell can be calculated as a fraction of intensity of incident light (I_0) converted into electricity, where J_{sc} is the short-circuit photocurrent density [83], as:

$$PCE = J_{SC} V_{OC} \frac{FF}{I_0} \quad (1.20)$$

Shockley and Queisser can be considered as the most popular method of calculating the maximum power conversion using solar. The method considers PV cells as one photon giving one electron, 40.8% under maximal concentrated solar light (46,200 suns) and 31% as maximum under one sun for a given band gap. First generation solar cells are silicon with second generation solar cells representing a thin film solar cells, which are less material intensive and more cost effective than the first generation. Second generation include thin film crystalline (Si), amorphous silicon

(a - Si), copper indium gallium diselenide (CIGS) and cadmium telluride (CdTe). Less commercially advanced PV systems are called the third generation PV. These include organic thin film solar cells and dye-sensitized solar cells. Other emerging material which have good photoluminescence quantum yield and defect tolerance are perovskite solar cells [84][85].

The effects that led to the Shockley and Queisser limit included: thermalization losses that occur, when photons have energy much higher than the bandgap; the non-usage of the photons; and when the energy is below the bandgap. Several approaches have been proposed to overcome this effect, which involve hot carrier cells, up/down convertors, multiple excitonic charge-carriers generation and multi-junction (tandem type) solar cells [84].

The primary loss mechanisms are listed as: transparency; thermalization; optical; recombination; and resistive losses. Optical losses occur when the metal contacts and the incident surface reflect photons away from the active area. Recombination losses are considered as the annihilation of photogenerated electron-hole pairs prior to carrier collection, occurring within the perimeter, surface, or the bulk of the device [81].

1.3.3.1.1 Indoor light conditions

There is an incredible lack of standardisation when it comes to estimating the indoor performance of PV cells, having no universally accepted standard for indoor integrated irradiance and spectral quality. Consequently, this leads to several different layouts when it comes to measuring the performance and fabrication of PV cells, including: use of non-calibrated power and Lux meters; cell sizes and layout; illumination sources; and masking of the cells [34].

Indoor artificial light intensities are much less compared to outdoor conditions, being approximated to be three orders of magnitude lower than solar light, with a typical indoor irradiance level of 10 W/m^2 ($0.001 \text{ W/cm}^2 = 1 \text{ mW/cm}^2$) [32] [36]. Illuminance is used to relate the intensity of how light is perceived by people, and not power, being analogous to irradiance (W/m^2). Indoor intensity is said to be between 200 and 2,000 Lux, with full solar irradiation being around 100,000 – 110,000 Lux. [38][68][83]. In outdoor conditions, $\approx 50 \%$ of the power captured from the terrestrial solar spectrum is in the near-infrared wavelength range, meaning that the optimum bandgap is between 1.1 - 1.4 eV. However, indoor light sources are only in the visible wavelength range, meaning that the optimum bandgap for indoor PV

is between 1.9 - 2.0 eV [36].

In indoor conditions, transparency losses can be considered negligible, due to the limited number of photons having energy higher than the bandgap. The recombination losses in indoor conditions can become dominant, being used to determine the conversion efficiency of the PV cell. The contact and series resistance losses are also said to be ‘insignificant’ in indoor conditions, however, under extremely low illumination, the shunt resistance can be detrimental, degrading the overall performance and fill-factor of the PV cells [36][81].

By taking the parasitic resistance components for a PV shown in the Equation 1.16 (see page 40), and neglecting the series resistance, where the measurements are when the shunt resistance is dominant, it can be simplified to Equation 1.21 [81].

$$J_{SC} - J_0 \left[\exp \left(\frac{q(V + JAR_s)}{nkT} \right) - 1 \right] = \frac{V_{OC}}{AR_{sh}} \quad (1.21)$$

During very dim conditions, this results in a linear relation, with the J_{SC} becoming dominant:

$$J_{SC} = \frac{V_{OC}}{AR_{sh}} \quad (1.22)$$

1.3.3.1.2 Maximum Power Point Tracking (MPPT)

To have an efficient use of the power output of photovoltaics, MPPT is used to reach the best yield of power. The maximum power point (MPP) varies depending on the light intensity, because of the non-linearity of the diodes. Achieving the ideal power output of the cell through calculations is not possible due to external environmental parameters required (incoming light and temperature) and the unachievable calculation power required by the IoT nodes. Therefore, MPPT uses trial and error to find the maximum power output, with several methods available in complexity, energy, and time demand. Some of these include [86]:

Optimal Fixed Voltage: By characterising (before the real application) the PV under similar conditions of deployment, the optimal operation point can be found, fixing the output voltage. This is not the most accurate method, as any change from the predetermined environmental conditions will deviate from the fixed MPP. This method can be considered as the simplest and default method of MPPT [86].

Measuring the environmental conditions: By using sensors integrated within

the IoT node to measure the environmental conditions, the optimal values of current and voltage can be taken from a stored data library to find the MPP at different conditions. Therefore, it requires additional power requirements to measure the environmental conditions, and a large environmental data set for a more accurate MPPT. The benefit of using this method is that the PV cells do not have to be disconnected from the IoT nodes for power measurement [86].

Ratio Approximation: There are similarities (at different environmental conditions) between the ratio of the current at MPP and the short-circuit current, being also the same for the voltage at MPP and the open-circuit voltage. The ratio equations are:

$$K_V \approx \frac{V_{MPP}}{V_{OC}} \quad (1.23)$$

for the voltage, or:

$$K_I \approx \frac{I_{MPP}}{I_{SC}} \quad (1.24)$$

for the current. The MPP can therefore be derived by using the pre-determined ratios for either current or voltage with the measured short circuit or the open-circuit voltage respectively. Whilst not being very accurate in finding the MPP, with the PV required to be disconnected from the circuit to be measured, this overall method is easily usable [79][86].

Perturb and observe: Whilst the real MPP will never be retained, this method measures the output power of the PV cell, by moving in one direction by a defined voltage step size. Therefore, at each time the power is measured, and is increasing, the system will continue in the same direction to find its true MPP. The direction will change if the power decreases from one step to the next. This method is very popular due to its simplicity (no high hardware demands) and with good accuracy [86]. However, issues arise when there is a sudden change in light conditions. If the energy source increases, the system will continue in the direction of the increased power but could be diverging from the true optimal working point. The misalignment is only corrected when there is stable energy source [86].

Incremental conductance: By calculating the conductance for a defined time step, following Equation 1.25:

$$\frac{dI}{dV} = \frac{I}{V} \quad (1.25)$$

the position of the MPP on the curve in relation to the measured position can be easily determined with accuracy through the progress of the power over the voltage calculated, being on, after or before the MPP; seen below as:

$$\begin{aligned}\frac{dI}{dV} &= -\frac{I}{V} \left(\frac{dP}{dV} = 0 \right) \\ \frac{dI}{dV} &> -\frac{I}{V} \left(\frac{dP}{dV} > 0 \right) \\ \frac{dI}{dV} &< -\frac{I}{V} \left(\frac{dP}{dV} < 0 \right)\end{aligned}\tag{1.26}$$

Artificial Intelligence (AI) methods: By using AI methods such as fuzzy logic, the MPP steps' progression can be varied to allow small error and fast convergence. Additionally, neural network can be performed which trains a network using a substantial number of environmental conditions and output data, to then predict the MPP location at a given time. These methods are becoming easier to implement with the increasing resources of modern microcontrollers. However, they initially require a large dataset, and a high computational power [86].

1.3.3.2 Overview of Applications

Due to the narrow band distribution of the light source in indoor conditions (such as LED), and the reduced thermalisation losses; the maximum possible efficiency that an indoor PV cell can achieve is 52%, with a band gap of 1.5 – 2.0 eV [34].

With the narrow band gap and the narrowed incident light spectrum, one of the dominant PV types using silicon only achieves around 8% in indoor conditions, with amorphous silicon achieving slightly better efficiencies to 10 % due to its wider band gap of 1.6 eV. Thin-film (second generation) material has also had commercial success, such as CdTe and CIGS. However, the efficiencies at low light are decreased due to suffering from low shunt resistance. III-V light harvesters (such as GaAs) have improved efficiencies over 20% due to the wider band gap compositions [34].

It appears that the current, best fabricated indoor PV cell, being below an active area of 1 cm², with a masked area of 0.2 cm² was with a perovskite cell, achieving an efficiency of 38.2% (142.8 μWcm⁻²) at a light intensity of a 1000 Lux [87]. In comparison, Zhang *et al.* [88], used DSSCs to achieve the best performing cell above an active area of 1 cm², reaching 34.5% (output power of 109.8 μWcm⁻²) at a 1000 Lux and 32.4 % at 200 Lux from DSSCs.

Wearable devices (such as an effective tool for supporting the daily life for older adults) have had an 18% growth rate per year, being mostly battery powered. This has resulted in devices needing to be recharged frequently and thereby not satisfying the user's experience. The proposed SensorTile wearable node [89] was designed for indoor and outdoor with an Artificial Intelligent application, from an ANN algorithm to ensure correct operation in different environments. The energy harvester had a 90% accuracy MPPT algorithm, with a low start-up voltage of 75 mV. A third-generation organic photovoltaic device was used due to its flexibility and customisation freedom, involving harmless materials that could be disposed through recycling.

At a 1000 Lux, Michaels *et al.* [90] achieved to power IoT nodes and a base station, using DSSCs, with a $Cu^{II/I}(tmby)_2$ redox mediator and the XY1 and L1 sensitizers. The capabilities observed included wireless communication of the data and sensing. The DSSCs were also used to power an IoT device, involving a Raspberry Pi Zero, training an artificial neural network through machine learning, on an IoT device. This neural network was then used to infer information.

1.3.3.3 Strengths and limitations of PV energy harvesting

1.3.3.3.1 Strengths

- Able to provide sufficient amount of power from the low-intensity illumination of indoor environments [25].
- Indoor photovoltaics do not have to be in the immediate vicinity of the energy source [36].
- Predictable periods of indoor light availability, resulting in a high energy reliability; having the potential to accurately estimate the incoming energy [36][86].
- Avoids complications with outdoor conditions such as the operating temperature; not varying as much in indoor conditions, resulting in constant storage elements' characteristics. (battery self-discharge rate roughly doubles with every 10 °C in ambient temperature) [38].
- Limited variation in level of irradiation, temperature, and humidity [90].
- The PV optimal power point to the IoT nodes does not change with the time of day, as the incident radiation stays the same [38].

- Avoids using mechanical parts, resulting in no unexpected failures and maintenance [38].
- Able to provide high output power from the high-intensity illumination of indoor environments [25].

1.3.3.3.2 Limitations

- There is no guarantee that there will be instantaneous power harvested; with conditions such as indoor lights being turned off could cause the power demand not being met (meaning that an energy storage component is required) [49] [38].
- Building a system without energy storage will require the light to be continuously on to power the IoT nodes, or required to go into sleep mode until there is a light source [38].
- Some argue that utilising an MPPT circuit will only add additional costs and power consumptions, explaining that the overall increase in power output of the system due to MPPT will not be as much compared to the consumption power required [38].
- Cleaning the dust accumulation must be periodically scheduled, with careful position of the PV cells, to harvest sufficient power to the IoT nodes [38].

1.4 Energy Harvesting Techniques from Mechanical Sources

Mechanical vibration and pressure can be considered as an accessible ambient energy source to power IoT nodes. The actuation or moving part can be found in different types of surroundings, being in the form of: airflow (air conditioning systems, ventilation and heating); ambient vibrations (walking, home and industrial appliances); and body motion (mounted on human body, such as smart wearables) [26][36].

Whilst there are several generator technologies that harvest vibrational energy, including electrostatic and electromagnetic generators, piezoelectric and triboelectric generators yield the highest energy density [91][92]. Consequently, this Section will give an overview of these two mechanical harvesting techniques.

1.4.1 Piezoelectric Energy Harvesting

Piezoelectric energy harvesters or also known as piezoelectric generators (PIEGs), produce electrical charge from the piezoelectrical material when under mechanical stress [36][93]. The mechanical stress can be described as an actuator, requiring the generator to be in the vicinity of the energy source, to produce sufficient power to the IoT nodes. The overall conversion efficiency is lost if inadequate mechanical contact is made with the actuator [36].

1.4.1.1 Process overview

A basic piezoelectric generator consists of two electrodes with a piezoelectric material placed in between. When a mechanical stress is applied, dipoles which are present in the piezoelectric material are varied. The piezoelectric effect leads to a voltage across the opposite faces, as a result of the charge density variations at the surfaces. The energy output of PIEG is typically an alternating current and voltage [36][92].

There are several modes of operation using PIEGs, with the most common modes being the transverse, longitudinal and shear [92]. The amount of energy in a stored piezoelectric material can be considered as equal to the energy stored in a capacitor [93], being:

$$E_C = \frac{1}{2}CV^2 \quad (1.27)$$

where V is the produced voltage, and C is the capacitance. In one dimensional condition, the strain S , and the electrical displacement field D , during mechanical stress can be defined respectively as [94]:

$$S = s^E T + d^t E \quad (1.28)$$

$$D = dT + \varepsilon^T E \quad (1.29)$$

where: s is the elastic compliance (as a proportionality coefficient); E is the electrical field; ε is the permittivity of the material; the mechanical stress is T ; d is the direct piezoelectric charge coefficient; ε^T is the permittivity of the material under constant stress; s^E is the compliance under constant electrical field; and d^t is the matrix for reverse piezoelectric effect [94]. The three-dimensional piezoelectric effect is described in further detail by Ilyas *et al.* [93].

With electrodes attached to the thickness axis, the V_{OC} output from a piezoelectric material can be given as [94]:

$$V_{OC} = \frac{I_3 \sigma_m(I_3)}{\varepsilon_{33}} \quad (1.30)$$

Where the thickness of the piezoelectric material is defined by I_3 ; $\sigma_m(I_3)$ is the density of piezoelectric charges on the surface of the material; and ε_{33} represents permittivity of the piezoelectric material [94].

When the resonant stress matches with the natural frequency of the piezoelectric generator, the maximum power is generated [36]. The energy conversion for a cantilever beam type piezoelectric energy harvester can be expressed as [95]:

$$\eta = \frac{\left(\frac{1}{2} \frac{k_p^2}{1-k_p^2}\right)}{\left(\frac{1}{Q_m} + \frac{1}{2} \frac{k_p^2}{1-k_p^2}\right)} \quad (1.31)$$

Q_m is the piezoelectric mechanical quality factor, and K_p is the electromechanical coupling factor.

1.4.1.2 Overview of Applications

Integrating piezoelectric generators alongside human movements, in the case of wearables, has been the most popular application use. These include: attaching PIEGs on parts of the shoe; rucksack straps; woven into textiles; implantable electronics, such as cardioverter-defibrillators; and blood pressure sensors. There has also been a substantial amount of non-indoor applications involving PIEGs, such as harvesting mechanical energy from: moving vehicles on roads; high-speed railway; and falling raindrops and wind [94].

Ceramic based on $Pb(Zr, Ti)O_3$ (lead zirconate titanate, PZT) is said to be a dominant class of piezoelectric material, having a high piezoelectricity and energy density, producing 560×10^{-12} C electrical charge when 1 Newton force is applied [93][96]. However, as the material consists of lead, there is a risk of releasing lead into the environment during the material's life cycle. Conversely, other lead free alternatives have been produced, with materials based on $(K, Na)NbO_3$ (potassium sodium niobate, KNN). However, they also have an environmental burden due to the use of niobium pentoxide, with respect to the extraction of the raw material [36]. Other environmentally friendlier materials have included polyvinylidene fluoride (PVDF), which can be flexible, facile processing, biocompatible, and being able to withstand structural fatigue. Despite these benefits, they however do not have lower piezoelectric activity performance than other materials [36][93].

It is stated by Pecunia *et al.* [36] that the average power density range from piezo-electric generators in indoor conditions is between 100 nWcm^{-3} - 900 Wcm^{-3} .

As comprehensively reviewed by Sharma *et al.* [92], an interesting application using PIEGs, is to integrate them into tiles and floors, facilitating the harvesting of energy from human movement indoors. There are several different layouts for harvesting energy through tiles, such as cantilever, curve, and array/stacked type. A cantilever type PIEG, self-powered floor tile was achieved by Kim *et al.* [95] to wirelessly transmit a signal to a switch module in order to turn on a light when a person of average weight ($50 - 80 \text{ kg}$) stepped on the tile. The output voltage achieved was 42 V with a current output of $52 \text{ }\mu\text{A}$. The issues that arise with PIEG tiles are the broad range of the frequency and amplitude from human involvement [92].

1.4.1.3 Strengths and limitations of piezoelectric energy harvesting

1.4.1.3.1 Strengths

- Architecturally simplistic, having minimal moving parts, and being a scalable technique [26][93].
- They can be compact and flexible, and therefore ideal to be integrated with IoT nodes [93].

1.4.1.3.2 Limitations

- Required to be in the vicinity of the actuator, thereby being an unpredictable source of energy, and limiting the location of where the IoT nodes can be placed [36].
- Require high frequency to generate enough energy to power the IoT nodes [93].
- There is a limited amount of material selection available, with a resultant low output current to power the IoT nodes [93].
- To integrate PIEGs in some application such as floor tiles, would require extensive work, resulting in high cost installation [92].
- An AC to DC converter circuit is required due to the battery requiring DC voltage [92], as well as requiring a diode bridge rectifier to convert AC – DC [91].

1.4.2 Triboelectric Energy Harvesting

Another technique which converts mechanical energy into electricity is through triboelectric nanogenerators (TENGs), which do this through the combination of triboelectrification and electrostatic induction [97].

1.4.2.1 Process overview

The power output of TENGs depends on the external mechanical force applied that brings two materials in contact (with presence of friction) with each other, either through bending or pressure. When in contact, the charges are induced (triboelectrification) on the surfaces resulting in an electric potential being created (electrostatic induction) when the external force is released, separating the charged surfaces. This causes a charge flow through the external load, and when in a continuous cycle, an AC output can be achieved [36][97].

The output current from the TENG, can be described as a capacitor with varying capacitance. Therefore, the output current can be given by [97]:

$$I = \frac{dQ}{dt} = A \frac{d\sigma_{tr}}{dt} \quad (1.32)$$

with Q being the charge, A is the area, and σ_{tr} is the amount of transferred charge accumulated on the electrodes. The output voltage can be expressed as [97]:

$$V = -\frac{1}{C(z)}Q + V_{OC}(z) \quad (1.33)$$

where C is the capacitance between the distance z of the two materials [97]. The maximum energy output E_m , is calculated using:

$$E_m = \frac{1}{2}Q_{SC,max}(V_{OC,max} + V'_{max}) \quad (1.34)$$

At short circuit conditions, the maximum transferred charge is defined by $Q_{SC,max}$. The figure of merits (FOM), especially FOM_p (figure of merit performance) can be considered as a method of characterising the performance of TENGs, being a combination of structural (FOM_S) and material (FOM_M) [97].

$$FOM_P = FOM_S.FOM_M = \frac{2\varepsilon_0}{\sigma^2 A} \frac{E_m}{x_{max}} . \sigma^2 = \frac{2\varepsilon_0}{A} \frac{E_m}{x_{max}} \quad (1.35)$$

A , being the triboelectrification area of TENG, ε_0 is the permittivity of vacuum, and x_{max} is the maximum displacement [97].

1.4.2.2 Overview of Applications

The power densities range of TENGs is between 400 nWcm^{-2} - 50 mWcm^{-2} [36]. However, the reported power densities up to 50 mW/cm^2 are said by Raj *et al.* [49] to be misleading due to the power sources not being continuously available.

The most used materials for net positive charge are nylon and metals, whilst polytetrafluoroethylene (PTFE) and silicone are the commonly used materials for a negative triboelectric charge. The manufacturing of TENGs is considerably simple, involving low energy-demand manufacturing methods and high-throughput, due to the simplicity of the materials used. A key challenge is to match the resonance between the source and the TENG, ensuring optimal vibration levels [49].

TENGs have been used in the healthcare sector, monitoring human wellness and activity. This is due to the natural triboelectrification of the human body, with the superior performance at low frequencies. Similar to piezoelectric, their self-powered applications are mostly concentrated with wearables and biomechanical harvesting [97].

1.4.2.3 Strengths and limitations of triboelectric energy harvesting

1.4.2.3.1 Strengths

- It can be enabled with broad application scenarios, and expanded to different working modes, depending on the IoT node application [97].
- High efficiency from low operation frequency [97].
- Low cost, light weight and several different materials available, to achieve flexibility in integrating with IoT nodes [97].

1.4.2.3.2 Limitations

- Required to be in the vicinity of the actuator, thereby being an unpredictable source of energy, and limiting the location of where the IoT nodes can be placed, similar to the limitations with PIEGs [36].
- An AC to DC converter circuit is required due to the battery requiring DC voltage [92], as well as requiring a diode bridge rectifier to convert AC – DC [91].
- The durability of the surface structure could be an issue, especially for sliding mode TENGs [97].

1.5 Hybrid energy harvesting (HEH)

Due to the drawbacks of having a single source for some energy harvesting techniques (such as the availability of ambient power sources), HEH is an approach which include multiple energy sources to minimise the energy supply and extend operational lifetime, adding diversity [25][68].

Issues (such as different voltage power outputs) arise when trying to combine several energy sources together, with required complex and multiple power management integrated circuits (PMIC). These procedures are required to manage different electrical properties such as capacity, polarity, impedance, and frequency. Additionally, overall size and cost can also increase with higher power losses [69][98]. The following sub-sections draw on recent studies on combining different energy harvesting techniques (as previously mentioned in the literature review), to power IoT nodes in indoor applications, as well as mitigating the issues (i.e. limitations) as reported above.

1.5.1 Indoor light and RF energy

By integrating a transparent antenna on a solar cell, a compact indoor HEH was achieved by Zhang *et al.* [25]. This consisted of a 2.4-GHZ-ISM band, transparent multiport dual-polarized patch antenna, and an efficient rectifier and amorphous silicon solar cell panel (8 cells connected in series – model: KYYG-B150150) [25]. The area of the whole hybrid prototype is 150 x 150 mm, with the configuration shown in Figure 1.6 (see below). With a 72.4% antenna efficiency, and RF – DC rectifier conversion efficiency of 53.2% at input power of -10 dBm, the RF harvester can achieve an additional 4.8% to 45.8% of power to the system, with the input RF energy source varying from 13.30 to 52.96 mW/m² respectively. At 360 Lux, the solar module obtains 1.68 mW of power [25].

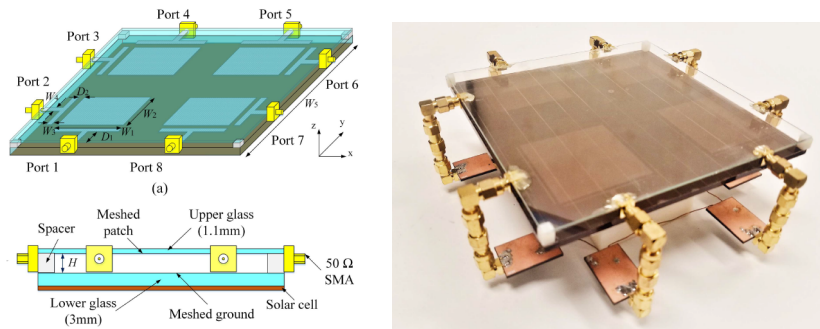


Figure 1.6: Configuration of the RF and Solar hybrid energy harvester [25]

1.5.2 Indoor light and mechanical energy

A single power conditioning circuit was fabricated by Yu *et al.* [98], to harvest both available light and vibration energy. A MEMS piezoelectric cantilever arrays generator ($11 \times 12.4 \text{ mm}^2$) was used alongside an amorphous-silicon (a-Si) solar module ($4.8 \times 2.0 \text{ cm}^2$). Under light intensity of 200 Lux, and vibration frequency of 234.5 Hz , the complete energy harvesting system (input power from PV module and PIEGs to output) achieved 76.7% efficiency.

The first hybrid combination including TENG and PV was achieved by Jung *et al.* [99], targeting indoor human activities to power IoT nodes. A PM6:IT4F-based non-fullerene bulk heterojunction (BHJ) OPV was used as the PV cell, with a 50 mm^2 active area, at a 1000 Lux, with the cell outputs being $301.2 \mu\text{Wcm}^{-2}$. The TENG (width = 5.5 cm , depth = 5.5 cm , height = 1.0 cm) consisted of CU balls being the positive triboelectric material and polydimethylsiloxane (PDMS) matrix acting as the negative. The yield power of the TENG exceeded $3 \mu\text{W}$, with an average charge up to 1.5 nC , at a walking speed of $\approx 4.0 \text{ ms}^{-1}$.

1.5.3 Indoor light and thermal energy sources

In this case, Tan *et al.* [68] achieved to combine indoor ambient light and thermal energy, to extend the lifetime of an IoT node. By using the optimal fixed voltage method for MPPT and avoiding using individual power management circuits for each energy source, the system's form factor, power losses and cost are reduced. A SC-01 amorphous type solar module (16.5 cm^2) was used under indoor fluorescent lighting conditions, and the TEG was made up of 5200 thermocouples with each one having a Seebeck's coefficient, α , of 0.21 mVK^{-1} . At an average thermal gradient of 10 K , and light intensity of 1010 Lux, the power output achieved was $621 \mu\text{W}$, with a boost converter efficiency of 90%.

1.5.4 Thermal and mechanical energy sources

As previously mentioned in Section 1.3.2.2.1, pyroelectric materials have piezoelectric properties that enable the simple combination of both techniques to harvest the temperature variation energy as well as the mechanical energy source, when under any form of strain.

Wang *et al.* [100] achieved the production of a one-structure HEH from thermal and mechanical energy sources, by triboelectric, piezoelectric and pyroelectric ef-

fects. The triboelectric layer consisted of a PVDF nanowires–poly(dimethylsiloxane) (PDMS) composite film, with both piezoelectric and pyroelectric layers made from a polarised PVDF film. Whilst this structure is designed for outdoor applications, with a recommended temperature change of 11 K , the paper demonstrated the feasibility of integrating different energy sources together.

1.6 Energy Harvesting Techniques' Conclusion

In summary, the literature review presents a systematic, comparative study into the potential of indoor energy harvesting techniques, to sufficiently power IoT nodes. Several ambient and mechanical indoor energy sources have been reviewed, including radio frequency, thermoelectric, pyroelectric, photovoltaic, piezoelectric, and triboelectric harvesting. Additionally, some recent applications involving a mixture of these harvesters (hybrid energy) were also considered, demonstrating the flexibility on what can be achieved in indoor conditions.

1.6.1 Evaluate and compare different harvesting sources using Pugh matrix

1.6.1.1 Pugh matrix methodology

The Pugh matrix is a decision-making tool, in this case used to evaluate and compare different energy harvesting techniques based on multiple criteria, attempting to address the problem of which technique is most suitable for indoor conditions. The criteria are selected based on the parameters mentioned in Section 1.2.1.1, created by Pecunia *et al.* [36]. The relative importance for each criterion has been assigned equal weighting (value of 1) in the matrix, as there is no clear justification for giving one criterion more weight than another. The baseline is taken as the original template, being an IoT node without any additional energy harvesters; thus, the score value is assessed around the baseline (value of 0). The following Pugh matrix has been employed in Table 1.2 below, ranking each harvester technique from best = 1 to worst = 5, for each of the criteria.

The evaluation scoring of different indoor energy harvesting techniques for each criterion is mentioned in more detail below, following the review outcomes of different energy harvesting techniques in Section 1.3 – 1.4.

Energy Reliability: With the scoring for all techniques being in the positive, due to harvesting more energy than the baseline, PV and RF sources are more

predictable than other techniques, with light conditions also having the capabilities of being controllable (scoring 2). Mechanical and temperature-based harvesting sources have more of a sense of randomness when it comes to reliability of the energy source (scoring 1).

Environmental Sustainability: The impact of the environmental sustainability of IoT nodes will only benefit from using no energy storage, due to the introduction of an energy harvester. However, this Section will only consider the addition of an energy harvester with no change to the IoT node. PV, RF and TENG scores 0 (see Table 1.2), due to the fabrication process utilising a low-energy process, with the availability of using non-toxic materials. Whilst this should still score below the baseline (as it adds more material to the IoT node), the involvement of promoting renewable energy and prolonging the lifespan of the IoT node balances the scoring. PYEG and PIEG have similar fabrication methods, with some types using toxic and raw materials. TEG also has a high energy-intensive fabrication method resulting in a lower score mark of -1.

Cost: The cost for each harvesting technique will increase the IoT node compared to the baseline, resulting in a negative scoring. Depending on the size and deployability, some techniques might be slightly cheaper to install such as RF and triboelectric due to their simplicity in fabrication, however, not enough to be equal to the cost of the baseline.

Durability: All harvesting techniques cannot be used everywhere compared to the baseline IoT node. However, the mechanical and thermal harvesters are more limited in the location they can be placed (scoring -2) compared to PV and RF (scoring -1), not needing to be placed in the immediate vicinity of the energy source.

Efficiency: In this case, the power density (W/cm^2) is considered as the scoring method, with the best three scoring 2, and the lowest three scoring 1. Depending on the input energy source power, RF has the lowest power output density, with the mechanical energy harvesters (TENG and PIEG) and PV having the highest energy density output.

1.6.1.2 Pugh matrix results and conclusion

Table 1.2 Pugh matrix ranking each ambient and mechanical energy harvesting source

Criteria	Importance Weighting	Baseline	Ambient Sources				Mechanical Sources	
			RF	TEG	PYEG	PV	PIEG	TENG
Energy Reliability	1	0	2	1	1	2	1	1
Environmental Sustainability	1	0	0	-1	-1	0	-1	0
Cost	1	0	-1	-1	-1	-1	-1	-1
Durability	1	0	1	1	1	1	1	1
Deployability	1	0	-1	-2	-2	-1	-2	-2
Efficiency	1	0	1	1	1	2	2	2
Net Score			2	-1	-1	3	0	1
Rank			2	5	5	1	4	3

(+2) = Much Improved
(+1) = Improved
(0) = Equal to
(-1) = Worse
(-2) = Much Worse

Note: RF= Radio Frequency, TEG = Thermoelectric Generator, PYEG = Pyroelectric Generator

PV = Photovoltaic, PIEG = Piezoelectric Generator, TENG = Triboelectric Nanogenerator.

Table 1.2 shows that the best indoor energy harvesting technique is from using ambient light conditions with a PV harvester. Radio Frequency was ranked second with Triboelectric nanogenerators coming third. The interpretation behind the Pugh matrix scoring is as follows:

In conclusion, the outcome from the Pugh matrix, as presented in Table 1.2, shows that the best technique for indoor energy harvesting is PV. Consequently, this will be further investigated in the following chapters of this thesis, to establish the capabilities of what PV can achieve alongside IoT nodes. The Pugh matrix demonstrates that the importance for a good energy harvester comes from techniques with a reliable energy source (being predicable and controllable), and a good deployability, where both RF and PV surpassed. The main reasoning as to why RF didn't rank above PV was due to its low power density.

1.7 Indoor PV Cell Comparison

To give an indication as to which type of PV cell is best for indoor conditions, Table 1.3 below shows the recent types of PV cells that have performed well in indoor conditions, at different low light intensities.

Table 1.3 Performance of different PV cell technologies under ambient lighting

Type of PV Cell	Composition	Light Source	Light Intensity (<i>Lux</i>)	Area (<i>cm</i> ²)	V _{oc} (<i>mV</i>)	J _{sc} (<i>μAcm</i> ⁻²)	Power Density (<i>μWcm</i> ⁻²)	FF	PCE (%)	Year	Ref
DSSC	Sensitizer: D35 and XY1	Osram 930	1000	2.80	797	138.0	88.5	0.80	28.90	2017	[83]
			200	2.80	-	-	15.6	-	-		
	Sensitizer: XY1 and Y123		1000	2.80	878	149.3	101.2	0.77	31.80	2018	[101]
			500		850	74.3	47.1	0.75	30.80		
			200	808	29.6	17.5	0.72	27.50			
			1000	879	124.7	84.0	0.77	26.40			
			500	824	60.2	36.6	0.74	23.00			
			200	767	24.2	13.4	0.72	21.10			
	Sensitizer: XY1 and L1		1000	0.25	910	147.0	103.0	0.77	34.00	2020	[102]
			500		880	73.4	50.0	0.77	32.70		
			200	840	29.0	19.0	0.78	31.40			
			1000	3.20	910	142.0	100.3	0.78	33.20		
	Sensitizer: MS5+XY1		1000	2.80	900	142.0	92.5	0.73	30.60	2021	[88]
			500		980	138.2	109.8	0.82	34.50		
			200		950	63.9	51.4	0.85	32.30		
			200	920	27.1	20.6	0.83	32.40			
PSC	ETL : PCBM/[BMIM]BF4	Fluorescent lamp (Osram L18W/827)	1000	0.09	870	150.0	97.9	75.00	35.20	2018	[103]
			500		690	70.0	35.7	74.00	25.70		
			200		580	14.0	5.4	66.00	19.50		
			1000	4.00	840	108.0	64.4	71.00	23.20		
	HTMa – P2 (MA0.91FA0.09) Pb(I0.094Br0.06)	LED 5000k	1000	0.20	960	188.0	142.0	78.70	38.20	2021	[87]
OPV	SVA time (2) BTR:PC71BM	fluorescent lamps (Osram L18W/827)	1000	0.15	791	133.1	78.2	75.20	28.10	2018	[104]
	Active Layer: PM6:Y6-O ETL: PDI-NO	3,000 K LED	1650	0.08	840	241.0	155.7	0.76	31.01	2020	[105]
			860		820	126.0	79.1	0.76	30.20		
			170		770	25.0	14.5	0.74	27.97		
Active Layer: TPD-3 F: IT-4F	TL84 fluorescent	1000	5.95	750	66.9	48.5	0.65	26.20	2020	[106]	
Flexi GaAs	Alta Devices	Osram Warm White 827	1000	mini module -	940	99.0	74.5	0.80	21.00	2017	[83]
			200	50 <i>cm</i> ²	870	20.1	13.1	0.75	18.60		

Note: DSSC = Dye sensitised Solar Cell, PSC = Perovskite Solar Cell, OPV - Organic photovoltaic, GaAs = Gallium Arsenide,

ETL = Electron Transport Layers, HTM = Hole Transporting Material, (-) = not specified.

Figure 1.7 below shows the molecular structures of the different DSSC sensitizers mentioned in Table 1.3.

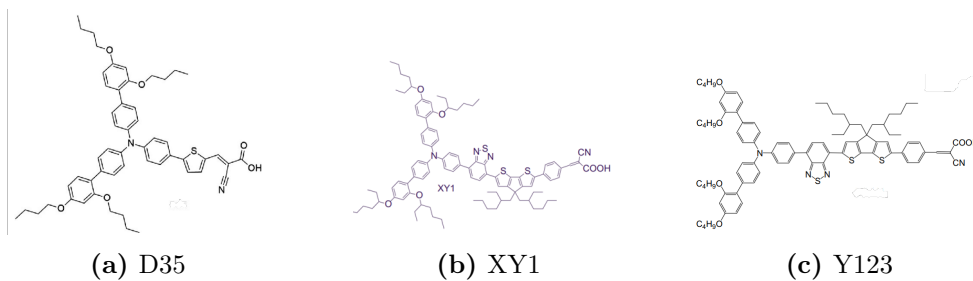




Figure 1.7: Molecular structures of different DSSC sensitizers. Adapted from [107] [83] [90] [108]

From Table 1.3, there are now several different types of cells that can achieve a high-performance level in indoor conditions, ranging from a light intensity of 1000 to 200 Lux. It appears that the best performance technology at indoor illumination was achieved by Opoku *et al.* [87], with an impressive conversion efficiency of 38.2% at a light intensity of 1000 Lux. This was from a perovskite solar cell (PSC), however, with a small active area of 0.2 cm^2 .

The best performing cell technology above an active area of 1 cm^2 was from dye sensitised solar cells (DSSCs). Zhang *et al.* fabricated DSSCs with an active area of 2.8 cm^2 , reaching 34.5% efficiency at a light intensity of 1000 Lux. This cell also achieved the best conversion efficiency under the lowest light intensity measured, of 200 Lux, with an efficiency of 32.4% [88]. Organic solar cells (OPV) offer another interesting approach, which in 2020 achieved the best indoor efficiency of 30.2%, under a light intensity of 860 Lux [105], but again like perovskite cells, the active area used was very small at 0.08 cm^2 .

Larger monolithic PV cells have also been explored under low light conditions, with the largest active area size of 20.25 cm^2 from a DSSC, being measured at both 1000 and 200 Lux, attaining 26.4% and 21.1% respectively [101]. An 8 cm^2 DSSC was also fabricated with the same redox mediator of Cu(II/I)(tmby) but with a sensitizer using a combination of XY1 and L1, having an efficiency of 30.6%. A 5.95 cm^2 OPV was also fabricated by Liao *et al.* [106], with efficiency up to 26.2%.

However, by improving the efficiency of different types of PV cells, the sustainable development has not fully been considered. The toxic lead content which is used in the fabrication of perovskite cells is still a major issue, hindering the integration of these devices into indoor electronic applications [109]. This is due to the adverse effects (such as impaired nerve conduction and encephalopathy) lead can cause to human health, when exposed to the environment. Many countries now have legislations in place to minimise and eliminate lead contamination, by having strict

regulations on the production and recycling of lead [110]. Integrating lead-based products in household would have to follow and manage a rigorous life cycle of the product, in order to prevent any contamination into the environment, which would pose as a hindrance to consumers [110].

Both OPV and DSSC have many similar characteristics other than its high efficiencies in indoor light, including low cost, non-toxic material, colourful, transparency, and their flexibility [109][111]. However, DSSCs have been shown to have a simpler and easier fabrication method, especially based on evidence for larger active area solar cells, such as the 20.25 cm^2 [101], being a very attractive and appealing device during IoT node design.

DSSC also have the required design flexibility, making it preferable over other PV technologies. The significance is that DSSCs can be incorporated into indoor spaces in aesthetically pleasing ways, making them less obtrusive, through customisable form factors and transparency. This is also the case compared to other IoT energy sources such as TEG and RF, as DSSCs are more versatile in terms of energy sources, having been optimised for low light indoor conditions. DSSCs also provide continuous and renewable source of energy, compared to batteries, having limited capacity and require periodic replacement or recharging. The design flexibility enables DSSCs to be customised and tailored for specific indoor IoT nodes, having the capabilities to blend seamlessly with the indoor environment. Therefore, DSSCs will be further explored to maximise its potential in indoor smart devices; whilst integrating with IoT nodes.

1.7.1 Dye Sensitised Solar Cell (DSSC) Background

In 1991, DSSCs were invented by Grätzel and O'Regon, developing a new third-generation PV [112]. The basic and most standard composition of a DSSC is a sandwich cell, consisting of four main components: the semiconductor electrode (photoanode or working electrode), dye sensitizer (being metal coordination complexes or organic), redox electrolyte, and a counter electrode (CE).

TiO_2 is the most employed material for the semiconductor electrode, having very minimal contributions to the absorption of the light, due to its wide band gap. The TiO_2 therefore adsorbs dye molecules through the mesoporous layers, which absorbs the light at wavelengths in the range of 920 nm to 380 nm , depending on the selected dye. The incident photons are converted into photoelectrons by the dye molecules,

through a process called photo-oxidation. Many other alternative metal oxides have been explored, including ZnO and SnO_2 [111][113].

A schematic diagram of a general sandwich DSSC is shown in Figure 1.8, with a (iodide/triiodide) I^-/I_3^- redox electrolyte being used to describe how the reduction process is achieved. However, whilst I^-/I_3^- is one of the most common electrolytes used, there are several other electrolytes that can be used, including cobalt and copper redox mediators.

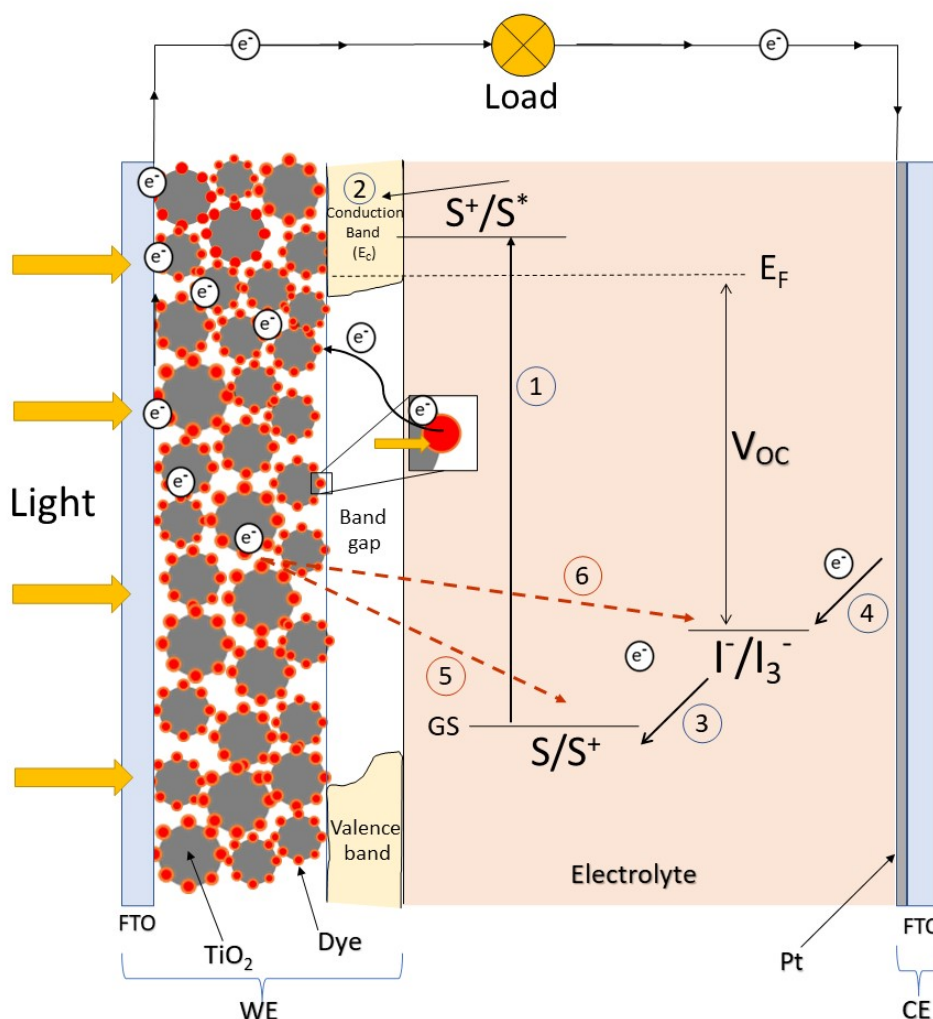


Figure 1.8: Diagram of a DSSC, including the energy levels and its working mechanism (numbers in circles refer to stages)

When illuminated, photons are absorbed into the dye molecule, exciting the electrons from the ground state (S) to an excited state (S^*) (Step 1 in Figure 1.8). The excited electrons are injected into the conduction band of the TiO_2 , transported by electronic drift-diffusion to the transparent conducting oxides (TCO) layer, which

tends to be fluorine-doped tin oxide (FTO) on the glass substrate (Step 2 in Figure 1.8 and Equation 1.36).



The redox mediator, in this case I^-/I_3^- , performs two important steps: it can donate an electron from the iodide to regenerate the oxidised dye (S^+) molecules (Step 3 in Figure 1.8 and Equation 1.39).



It also transfers the triiodide through diffusion to the CE, consisting of the FTO glass and a catalyst, in this case it's platinum (Pt); however other materials such as carbon or a conducting polymer can be used. Iodide is regenerated by the reduction of triiodide on the cathode ((Step 4 in Figure 1.8 and Equation 1.38).



Some additional steps also occur that can impact the performance of the cells, involving the recombination of the electrons before it reaches the TCO. The excited electrons can recombine with the oxidized dye (Step 5 in Figure 1.8), or even recombine with the oxidized redox mediator (Step 6 in Figure 1.8) [84][85][111][113].

The ground-state energy level, GS, on the diagram (Figure 1.8) is the HOMO (highest occupied molecular orbital); thus when a photon strikes, the dye molecule is excited (S^*) from the HOMO to the lowest unoccupied molecular orbital (LUMO), subsequently creating electrons and holes [114].

The potential difference between the working electrode (WE) and the CE is the voltage output of the cell. When no current is flowing, being under open-circuit conditions, the potential of the CE is equal to the potential of the redox electrolyte. The Fermi level (E_F) of the semiconductor is equal to the WE, which is given by:

$$E_F = E_C - \frac{K_B T}{e} \ln \frac{n_c}{N_C} \quad (1.39)$$

Where E_C is the conduction band level of the TiO_2 , Boltzmann constant is K_B , e is the elementary charge, T the absolute temperature, n_c is the electron density of the conduction band, and N_C is the effective density at the bottom of the conduction band [111].

1.7.1.1 Environmental impact of integrating DSSCs into IoT nodes

As previously mentioned in Section 1.1.3.2, the use of LIBs to solely power IoT nodes has drawn some environmental challenges, due to the toxicity, acidification, and resource depletion of raw material, such as lithium and cobalt, with limited life cycle assessments of rechargeable batteries.

Compared to batteries, DSSCs have the advantage of generating clean, renewable energy during their operational life, offsetting some of the environmental costs associated with their production, such as being energy-intensive during fabrication. Using recycled materials to build DSSCs have been previously achieved by recovering conductive glass (FTO) and TiO_2 layer from old cells [115]. Another important factor to consider is increasing the longevity of DSSCs before recycling. For liquid-state electrolyte, one the main reasons for a short lifetime is from the electrolyte drying out, which can be resolved by refilling the cells with more electrolyte [115].

Alternatively, a more desirable option is to use solid-state electrolytes, which drastically increase the lifetime of the DSSCs. A recent promising solid-state DSSC structure was initially achieved by Freitag *et al.* [116] in 2015, called ‘zombie’ cells. These cells are initially fabricated as a liquid-state DSSC; however, the copper complex electrolyte is allowed to dry slowly for a couple of days (by providing a small gap on the side of the DSSC sealant), forming a solid hole transport material. Zombie cells have also been successful using iodide/triiodide redox couple, incorporated with a faster drying method by Sutton *et al.* [117].

1.8 Overarching Summary: Focus and layout of study

As the aim of this PhD study is to investigate the feasibility of integrating energy harvesting technology in indoor conditions, the literature review has explored and justified the best technology and parameters for optimised power harvesting, and in doing so the thesis sets out to establish the capabilities of what PV can achieve alongside IoT nodes. In light of this focus, the thesis has been organised as follows:

Chapter 2: provides an overview of the basic experimental methods, as applied in each subsequent Chapter.

Chapter 3: is devoted to the characterisation and modification potentials of DSSCs in indoor applications.

Chapters 4 & 5: details the preliminary design opportunity and computational optimisation respectively, using hand gesture recognition integrated with a monolithic DSSC.

Chapter 6: delves into the application opportunities and prototypes for IoT nodes, specifically suited for human computer interaction.

Bibliography

1. Internet of Things (IoT) connected devices installed base worldwide from 2015 to 2025. 2016. Available from: <https://www.statista.com/statistics/471264/iot-number-of-connected-devices-worldwide/> [Accessed on: 2020 Apr 15]
2. Sparks P. The route to a trillion devices. White Paper, ARM 2017
3. Gubbi J, Buyya R, Marusic S, and Palaniswami M. Internet of Things (IoT): A vision, architectural elements, and future directions. *Future Generation Computer Systems* 2013; 29:1645–60. DOI: <https://doi.org/10.1016/j.future.2013.01.010>. Available from: <http://www.sciencedirect.com/science/article/pii/S0167739X13000241>
4. Khan MA and Salah K. IoT security: Review, blockchain solutions, and open challenges. *Future Generation Computer Systems* 2018; 82:395–411. DOI: 10.1016/j.future.2017.11.022
5. Kocakulak M and Butun I. An overview of Wireless Sensor Networks towards internet of things. *2017 IEEE 7th Annual Computing and Communication Workshop and Conference (CCWC)*. 2017 :1–6. DOI: 10.1109/CCWC.2017.7868374
6. Wan J, Chen M, Xia F, Di L, and Zhou K. From machine-to-machine communications towards cyber-physical systems. *Computer Science and Information Systems* 2013; 10:1105–28
7. Weiser M, Gold R, and Brown JS. The origins of ubiquitous computing research at PARC in the late 1980s. *IBM Systems Journal* 1999; 38:693–6. DOI: 10.1147/sj.384.0693
8. Fysarakis K, Askoxylakis I, Soultatos O, Papaefstathiou I, Manifavas C, and Katos V. Which IoT Protocol? Comparing Standardized Approaches over a Common M2M Application. *2016 IEEE Global Communications Conference (GLOBECOM)*. 2016 :1–7. DOI: 10.1109/GLOCOM.2016.7842383

9. Khanna A and Kaur S. Internet of Things (IoT), Applications and Challenges: A Comprehensive Review. *Wireless Personal Communications* 2020; 114:1687–762. DOI: 10.1007/S11277-020-07446-4/TABLES/27. Available from: <https://link.springer.com/article/10.1007/s11277-020-07446-4>
10. Al-Qaseemi SA, Almulhim HA, Almulhim MF, and Chaudhry SR. IoT architecture challenges and issues: Lack of standardization. *2016 Future technologies conference (FTC)*. IEEE. 2016 :731–8
11. Jabraeil Jamali MA, Bahrami B, Heidari A, Allahverdizadeh P, and Norouzi F. IoT Architecture. *Towards the Internet of Things: Architectures, Security, and Applications*. Cham: Springer International Publishing, 2020 :9–31. DOI: 10.1007/978-3-030-18468-1_2. Available from: https://doi.org/10.1007/978-3-030-18468-1_2
12. Lee I and Lee K. The Internet of Things (IoT): Applications, investments, and challenges for enterprises. *Business Horizons* 2015; 58:431–40. DOI: <https://doi.org/10.1016/j.bushor.2015.03.008>. Available from: <http://www.sciencedirect.com/science/article/pii/S0007681315000373>
13. TechTarget. Top 8 IoT applications and examples in business. Available from: <https://www.techtarget.com/iotagenda/tip/Top-8-IoT-applications-and-examples-in-business> [Accessed on: 2022 Nov 14]
14. Asghari P, Rahmani AM, and Javadi HHS. Internet of Things applications: A systematic review. *Computer Networks* 2019; 148:241–61
15. Gazis A, Katsiri E, and Assistant T. Mini Review Author Details Smart Home IoT Sensors: Principles and Applications A Review of Low-Cost and Low-Power Solutions. *International Journal on Engineering Technologies and Informatics* 2021; 2. DOI: 10.51626/ijeti.2021.02.00007. Available from: <https://skeenapublishers.com/terms-conditions>
16. Mir U, Abbasi U, Mir T, Kanwal S, and Alamri S. Energy Management in Smart Buildings and Homes: Current Approaches, a Hypothetical Solution, and Open Issues and Challenges. *IEEE Access* 2021; 9:94132–48. DOI: 10.1109/ACCESS.2021.3092304
17. Baig MM, Afifi S, GholamHosseini H, and Mirza F. A systematic review of wearable sensors and IoT-based monitoring applications for older adults—a focus on ageing population and independent living. *Journal of medical systems* 2019; 43:1–11

18. Ashfaq Z, Rafay A, Mumtaz R, Zaidi SMH, Saleem H, Zaidi SAR, Mumtaz S, and Haque A. A review of enabling technologies for internet of medical things (IOMT) ecosystem. *Ain Shams Engineering Journal* 2022; 13:101660
19. Marques G, Saini J, Dutta M, Singh PK, and Hong WC. Indoor air quality monitoring systems for enhanced living environments: A review toward sustainable smart cities. *Sustainability* 2020; 12:4024
20. Khan IH and Javaid M. Role of Internet of Things (IoT) in adoption of Industry 4.0. *Journal of Industrial Integration and Management* 2022; 7:515–33
21. Martini BG, Helfer GA, Barbosa JLV, Modolo RCE, Silva MR da, Figueiredo RM de, Mendes AS, Silva LA, and Leithardt VRQ. IndoorPlant: A Model for Intelligent Services in Indoor Agriculture Based on Context Histories. *Sensors* 2021, Vol. 21, Page 1631 2021; 21:1631. DOI: 10.3390/S21051631. Available from: <https://www.mdpi.com/1424-8220/21/5/1631/htm%20https://www.mdpi.com/1424-8220/21/5/1631>
22. Yang J, Liu M, Lu J, Miao Y, Hossain MA, and Alhamid MF. Botanical internet of things: Toward smart indoor farming by connecting people, plant, data and clouds. *Mobile Networks and Applications* 2018; 23:188–202
23. Mehmood MY, Oad A, Abrar M, Munir HM, Hasan SF, Muqeet HAU, and Golilarz NA. Edge Computing for IoT-Enabled Smart Grid. *Security and Communication Networks* 2021; 2021. DOI: 10.1155/2021/5524025
24. Jan B, Farman H, Khan M, Talha M, and Din IU. Designing a Smart Transportation System: An Internet of Things and Big Data Approach. *IEEE Wireless Communications* 2019; 26:73–9. DOI: 10.1109/MWC.2019.1800512
25. Zhang Y, Shen S, Chiu CY, and Murch R. Hybrid rf-solar energy harvesting systems utilizing transparent multiport micromeshed antennas. *IEEE Transactions on Microwave Theory and Techniques* 2019; 67:4534–46. DOI: 10.1109/TMTT.2019.2930507
26. Sanislav T, Mois GD, Zeadally S, and Folea SC. Energy Harvesting Techniques for Internet of Things (IoT). *IEEE Access* 2021; 9:39530–49. DOI: 10.1109/ACCESS.2021.3064066
27. Touqeer H, Zaman S, Amin R, Hussain M, Al-Turjman F, and Bilal M. Smart home security: challenges, issues and solutions at different IoT layers. *The Journal of Supercomputing* 2021; 77:14053–89
28. Khattak HA, Shah MA, Khan S, Ali I, and Imran M. Perception layer security in Internet of Things. *Future Generation Computer Systems* 2019; 100:144–64

29. Gurunath R, Agarwal M, Nandi A, and Samanta D. An Overview: Security Issue in IoT Network. *2018 2nd International Conference on I-SMAC (IoT in Social, Mobile, Analytics and Cloud) (I-SMAC)* *I-SMAC (IoT in Social, Mobile, Analytics and Cloud) (I-SMAC), 2018 2nd International Conference on.* 2018 :104–7. DOI: 10.1109/I-SMAC.2018.8653728
30. Anajemba JH, Iwendi C, Razzak I, Ansere JA, and Okpalaoguchi IM. A Counter-Eavesdropping Technique for Optimized Privacy of Wireless Industrial IoT Communications. *IEEE Transactions on Industrial Informatics* 2022; 18:6445–54. DOI: 10.1109/TII.2021.3140109
31. Wang C, Wang D, Tu Y, Xu G, and Wang H. Understanding Node Capture Attacks in User Authentication Schemes for Wireless Sensor Networks. *IEEE Transactions on Dependable and Secure Computing* 2022; 19:507–23. DOI: 10.1109/TDSC.2020.2974220
32. Shaikh FK and Zeadally S. Energy harvesting in wireless sensor networks: A comprehensive review. 2016. DOI: 10.1016/j.rser.2015.11.010
33. Adila AS, Husam A, and Husi G. Towards the self-powered Internet of Things (IoT) by energy harvesting: Trends and technologies for green IoT. *2018 2nd International Symposium on Small-scale Intelligent Manufacturing Systems (SIMS).* 2018 :1–5. DOI: 10.1109/SIMS.2018.8355305
34. Mathews I, Kantareddy SN, Buonassisi T, and Peters IM. Technology and Market Perspective for Indoor Photovoltaic Cells. *Joule* 2019; 3:1415–26. DOI: <https://doi.org/10.1016/j.joule.2019.03.026>. Available from: <https://www.sciencedirect.com/science/article/pii/S2542435119301667>
35. Peters JF, Baumann M, Zimmermann B, Braun J, and Weil M. The environmental impact of Li-Ion batteries and the role of key parameters – A review. *Renewable and Sustainable Energy Reviews* 2017; 67:491–506. DOI: <https://doi.org/10.1016/j.rser.2016.08.039>. Available from: <https://www.sciencedirect.com/science/article/pii/S1364032116304713>
36. Pecunia V, Occhipinti LG, and Hoye RLZ. Emerging indoor photovoltaic technologies for sustainable internet of things. *Advanced Energy Materials* 2021; 11:2100698
37. Tiliute DE. Battery Management in Wireless Sensor Networks. *Elektronika ir Elektrotechnika* 2007; 76:9–12. Available from: <http://eejournal.ktu.lt/index.php/elt/article/view/10706>
38. Nasiri A, Zabalawi SA, and Mandic G. Indoor power harvesting using photovoltaic cells for low-power applications. *IEEE Transactions on Industrial Electronics* 2009; 56:4502–9

39. Yang Y, Okonkwo EG, Huang G, Xu S, Sun W, and He Y. On the sustainability of lithium ion battery industry – A review and perspective. *Energy Storage Materials* 2021; 36:186–212. DOI: <https://doi.org/10.1016/j.ensm.2020.12.019>. Available from: <https://www.sciencedirect.com/science/article/pii/S2405829720304827>
40. Tian G, Yuan G, Aleksandrov A, Zhang T, Li Z, Fathollahi-Fard AM, and Ivanov M. Recycling of spent Lithium-ion Batteries: A comprehensive review for identification of main challenges and future research trends. *Sustainable Energy Technologies and Assessments* 2022; 53:102447. DOI: <https://doi.org/10.1016/j.seta.2022.102447>. Available from: <https://www.sciencedirect.com/science/article/pii/S2213138822004994>
41. STMicroelectronics. Ultra-low power, high performance, sub-1GHz transceiver. Available from: <https://www.st.com/en/wireless-connectivity/s2-1p.html> [Accessed on: 2023 Jan 11]
42. Saelens M, Hoebeke J, Shahid A, and Poorter ED. Impact of EU duty cycle and transmission power limitations for sub-GHz LPWAN SRDs: an overview and future challenges. *EURASIP Journal on Wireless Communications and Networking* 2019; 2019:219. DOI: 10.1186/s13638-019-1502-5. Available from: <https://doi.org/10.1186/s13638-019-1502-5>
43. LoRa Core for Smart Home, LoRa Transceiver — Semtech. Available from: <https://www.semtech.com/products/wireless-rf/lora-connect/1lcc68#documentation> [Accessed on: 2023 Jan 12]
44. RenesasElectronicsCorporation. Renesas Introduces Bluetooth Low Energy Module for Ultra-Low Power IoT Applications — Renesas. Available from: <https://www.renesas.com/us/en/about/press-room/renesas-introduces-bluetooth-low-energy-module-ultra-low-power-iot-applications> [Accessed on: 2023 Jan 11]
45. Daviteq. What Is Sub-GHz Wireless Communication? Available from: <https://www.daviteq.com/blog/en/what-is-sub-ghz-wireless-communication/> [Accessed on: 2023 Jan 11]
46. NordicSemiconductor. Low power cellular IoT. Available from: <https://www.nordicsemi.com/Products/Low-power-cellular-IoT/What-is-cellular-IoT?lang=en#infotabs> [Accessed on: 2023 Jan 11]
47. NordicSemiconductor. Online Power Profiler for LTE. Available from: <https://devzone.nordicsemi.com/power/w/opp/3/online-power-profiler-for-lte>

48. Fraas LM and Partain LD. Solar cells and their applications. Vol. 236. John Wiley and Sons, 2010
49. Raj A and Steingart D. Review—Power Sources for the Internet of Things. *Journal of The Electrochemical Society* 2018; 165:B3130–B3136. DOI: 10.1149/2.0181808jes. Available from: <https://iopscience.iop.org/article/10.1149/2.0181808jes>
50. Visser HJ and Vullers RJM. RF Energy Harvesting and Transport for Wireless Sensor Network Applications: Principles and Requirements. DOI: 10.1109/JPROC.2013.2250891
51. Chaour I, Fakhfakh A, and Kanoun O. Radio frequency power transfer for wireless sensors in indoor applications. *Technology, Components and System Design*. Ed. by Kanoun O. Berlin, Boston: De Gruyter Oldenbourg, 2019 :181–96. DOI: doi:10.1515/9783110445053-011. Available from: <https://doi.org/10.1515/9783110445053-011>
52. Charalampidis G, Papadakis A, and Samarakou M. Power estimation of RF energy harvesters. *Energy Procedia* 2019; 157:892–900. DOI: 10.1016/J.EGYPRO.2018.11.255
53. Nariman M, Shirinfar F, Toda AP, Pamarti S, Rofougaran A, and Flaviis FD. A Compact 60-GHz Wireless Power Transfer System. *IEEE Transactions on Microwave Theory and Techniques* 2016; 64:2664–77
54. Hemour S and Wu K. Radio-Frequency Rectifier for Electromagnetic Energy Harvesting: Development Path and Future Outlook. DOI: 10.1109/JPROC.2014.2358691. Available from: http://www.ieee.org/publications_standards/publications/rights/index.html
55. Zhang X, Grajal J, López-Vallejo M, McVay E, and Palacios T. Opportunities and Challenges of Ambient Radio-Frequency Energy Harvesting. *Joule* 2020; 4:1148–52. DOI: 10.1016/J.JOULE.2020.05.006
56. Aman AHM, Shaari N, and Ibrahim R. Internet of things energy system: Smart applications, technology advancement, and open issues. *International Journal of Energy Research* 2021; 45:8389–419
57. Alsharif MH, Kim S, and Kuruo N. Energy Harvesting Techniques for Wireless Sensor Networks/Radio-Frequency Identification: A Review. 2019. DOI: 10.3390/sym11070865. Available from: www.mdpi.com/journal/symmetry
58. Dewi LM. Rfid: Theory, Implementation and Critics. *Bina Ekonomi* 2010; 14

59. Landaluce H, Arjona L, Perallos A, Falcone F, Angulo I, and Muralter F. A review of IoT sensing applications and challenges using RFID and wireless sensor networks. *Sensors* 2020; 20:2495
60. Abdulghafor R, Turaev S, Almohamedh H, Alabdan R, Almutairi B, Almutairi A, and Almotairi S. Recent Advances in Passive UHF-RFID Tag Antenna Design for Improved Read Range in Product Packaging Applications: A Comprehensive Review. *IEEE Access* 2021; 9:63611–35. DOI: 10.1109/ACCESS.2021.3074339
61. Costa F, Genovesi S, Borgese M, Michel A, Dicandia FA, and Manara G. A review of RFID sensors, the new frontier of internet of things. *Sensors* 2021; 21:3138
62. Eltresy NA, Dardeer OM, Al-Habal A, Elhariri E, Abotaleb AM, Elsheakh DN, Khattab A, Taie SA, Mostafa H, Elsadek HA, and Abdallah EA. Smart Home IoT System by Using RF Energy Harvesting. *Journal of Sensors* 2020; 2020. Ed. by Wu Q:8828479. DOI: 10.1155/2020/8828479. Available from: <https://doi.org/10.1155/2020/8828479>
63. Lenssen KMH, Stofmeel L, Van Delden M, Vullers RJM, Visser HJ, and Pop V. Zero Energy E-Skin. *Proc. of the International Display Workshop*. 2010
64. Zhang X, Grajal J, Vazquez-Roy JL, Radhakrishna U, Wang X, Chern W, Zhou L, Lin Y, Shen PC, Ji X, et al. Two-dimensional MoS₂-enabled flexible rectenna for Wi-Fi-band wireless energy harvesting. *Nature* 2019; 566:368–72
65. Chiu MT, Chiu CY, Ng C, Wong LO, Shen S, and Murch R. An Ambient RF Powered Wireless Sensor System. *IEEE Open Journal of Antennas and Propagation* 2022; 3:1382–93
66. Jaziri N, Boughamoura A, Müller J, Mezghani B, Tounsi F, and Ismail M. A comprehensive review of Thermoelectric Generators: Technologies and common applications. *Energy Reports* 2020; 6:264–87. DOI: <https://doi.org/10.1016/j.egyrs.2019.12.011>. Available from: <https://www.sciencedirect.com/science/article/pii/S2352484719306997>
67. Zoui MA, Bentouba S, Stocholm JG, and Bourouis M. A Review on Thermoelectric Generators: Progress and Applications. *Energies* 2020; 13. DOI: 10.3390/en13143606. Available from: <https://www.mdpi.com/1996-1073/13/14/3606>
68. Tan YK and Panda SK. Energy Harvesting From Hybrid Indoor Ambient Light and Thermal Energy Sources for Enhanced Performance of Wireless Sensor Nodes. *IEEE Transactions on Industrial Electronics* 2011; 58:4424–35. DOI: 10.1109/TIE.2010.2102321

69. Ryu H, Yoon HJ, and Kim SW. Hybrid energy harvesters: toward sustainable energy harvesting. *Advanced Materials* 2019; 31:1802898
70. Wang J, Xiao F, and Zhao H. Thermoelectric, piezoelectric and photovoltaic harvesting technologies for pavement engineering. *Renewable and Sustainable Energy Reviews* 2021; 151:111522. DOI: 10.1016/J.RSER.2021.111522
71. Iezzi B, Ankireddy K, Twiddy J, Losego MD, and Jur JS. Printed, metallic thermoelectric generators integrated with pipe insulation for powering wireless sensors. *Applied Energy* 2017; 208:758–65. DOI: <https://doi.org/10.1016/j.apenergy.2017.09.073>. Available from: <https://www.sciencedirect.com/science/article/pii/S0306261917313557>
72. Kim YJ, Gu HM, Kim CS, Choi H, Lee G, Kim S, Yi KK, Lee SG, and Cho BJ. High-performance self-powered wireless sensor node driven by a flexible thermoelectric generator. *Energy* 2018; 162:526–33. DOI: <https://doi.org/10.1016/j.energy.2018.08.064>. Available from: <https://www.sciencedirect.com/science/article/pii/S0360544218315962>
73. Zhang Y, Zhang F, Shakhsheer Y, Silver JD, Klinefelter A, Nagaraju M, Boley J, Pandey J, Shrivastava A, Carlson EJ, et al. A batteryless 19 μ W MICS/ISM-Band energy harvesting body sensor node SoC for ExG applications. *IEEE Journal of Solid-State Circuits* 2012; 48:199–213
74. Bao S, Zhu W, Yu Y, Liang L, and Deng Y. Wearable Thermoelectric Generator with Cooling-Enhanced Electrode Design for High-Efficient Human Body Heat Harvesting. *ACS Applied Engineering Materials* 2023; 1:660–8. DOI: 10.1021/acsaenm.2c00167. Available from: <https://doi.org/10.1021/acsaenm.2c00167>
75. Lee J, Kim HJ, Ko YJ, Baek JY, Shin G, Jeon JG, Lee JH, Kim JH, Jung JH, and Kang TJ. Enhanced pyroelectric conversion of thermal radiation energy: Energy harvesting and non-contact proximity sensor. *Nano Energy* 2022; 97:107178. DOI: <https://doi.org/10.1016/j.nanoen.2022.107178>. Available from: <https://www.sciencedirect.com/science/article/pii/S2211285522002592>
76. Thakre A, Kumar A, Song HC, Jeong DY, and Ryu J. Pyroelectric Energy Conversion and Its Applications—Flexible Energy Harvesters and Sensors. *Sensors* 2019; 19. DOI: 10.3390/s19092170. Available from: <https://www.mdpi.com/1424-8220/19/9/2170>

77. Pandya S, Velarde G, Zhang L, Wilbur JD, Smith A, Hanrahan B, Dames C, and Martin LW. New approach to waste-heat energy harvesting: pyroelectric energy conversion. *NPG Asia Materials* 2019; 11:26. DOI: 10.1038/s41427-019-0125-y. Available from: <https://doi.org/10.1038/s41427-019-0125-y>
78. Bowen CR, Taylor J, Le Boulbar E, Zabek D, Chauhan A, and Vaish R. Pyroelectric materials and devices for energy harvesting applications. 2014; 7:3817–4148. DOI: 10.1039/c4ee01759e. Available from: www.rsc.org/ees
79. Hua Yu, Qiuqing Yue, and Hanzhong Wu. Power management and energy harvesting for indoor photovoltaic cells system. *2011 Second International Conference on Mechanic Automation and Control Engineering*. 2011 Jul :521–4. DOI: 10.1109/MACE.2011.5986975
80. Celik AN and Acikgoz N. Modelling and experimental verification of the operating current of mono-crystalline photovoltaic modules using four- and five-parameter models. *Applied Energy* 2007; 84:1–15. DOI: <https://doi.org/10.1016/j.apenergy.2006.04.007>. Available from: <http://www.sciencedirect.com/science/article/pii/S0306261906000511>
81. Teran AS, Moon E, Lim W, Kim G, Lee I, Blaauw D, and Phillips JD. Energy Harvesting for GaAs Photovoltaics under Low-Flux Indoor Lighting Conditions. *IEEE Transactions on Electron Devices* 2016 Jul; 63:2820–5. DOI: 10.1109/TED.2016.2569079
82. Tekin N, Erdem HE, and Gungor VC. Analyzing lifetime of energy harvesting wireless multimedia sensor nodes in industrial environments. *Computer Standards and Interfaces* 2018; 58:109–17. DOI: <https://doi.org/10.1016/j.csi.2017.12.005>. Available from: <https://www.sciencedirect.com/science/article/pii/S0920548917301502>
83. Freitag M, Teuscher J, Saygili Y, Zhang X, Giordano F, Liska P, Hua J, Zakeeruddin SM, Moser JE, Grätzel M, et al. Dye-sensitized solar cells for efficient power generation under ambient lighting. *Nature Photonics* 2017; 11:372
84. Kalyanasundaram K. Dye-sensitized solar cells. EPFL press, 2010
85. Mahmood A. Recent research progress on quasi-solid-state electrolytes for dye-sensitized solar cells. 2015 Nov. DOI: 10.1016/j.jechem.2015.10.018
86. Viehweger C. Solar energy harvesting for wireless sensor systems. *Technology, Components and System Design*. Ed. by Kanoun O. Berlin, Boston: De Gruyter Oldenbourg, 2019 :37–44. DOI: doi:10.1515/9783110445053-002. Available from: <https://doi.org/10.1515/9783110445053-002>

87. Opoku H, Kim YH, Lee JH, Ahn H, Lee JJ, Baek SW, and Jo JW. A tailored graft-type polymer as a dopant-free hole transport material in indoor perovskite photovoltaics. *Journal of Materials Chemistry A* 2021 Jul; 9:15294–300. DOI: 10.1039/D1TA03577K. Available from: <https://pubs.rsc.org/en/content/articlehtml/2021/ta/d1ta03577k>
<https://pubs.rsc.org/en/content/articlelanding/2021/ta/d1ta03577k>
88. Zhang D, Stojanovic M, Ren Y, Cao Y, Eickemeyer FT, Socie E, Vlachopoulos N, Moser JE, Zakeeruddin SM, Hagfeldt A, et al. A molecular photosensitizer achieves a Voc of 1.24 V enabling highly efficient and stable dye-sensitized solar cells with copper (II/I)-based electrolyte. *Nature communications* 2021; 12:1–10
89. Nicosia A, Pau D, Giacalone D, Plebani E, Bosco A, and Iacchetti A. Efficient light harvesting for accurate neural classification of human activities. *2018 IEEE International Conference on Consumer Electronics, ICCE 2018*. Vol. 2018-Janua. Institute of Electrical and Electronics Engineers Inc., 2018 Mar :1–4. DOI: 10.1109/ICCE.2018.8326103
90. Michaels H, Rinderle M, Freitag R, Benesperi I, Edvinsson T, Socher R, Gagliardi A, and Freitag M. Dye-sensitized solar cells under ambient light powering machine learning: towards autonomous smart sensors for the internet of things. *Chem. Sci.* 2020; 11:2895–906. DOI: 10.1039/C9SC06145B. Available from: <http://dx.doi.org/10.1039/C9SC06145B>
91. Sarker MR, Julai S, Sabri MFM, Said SM, Islam MM, and Tahir M. Review of piezoelectric energy harvesting system and application of optimization techniques to enhance the performance of the harvesting system. *Sensors and Actuators A: Physical* 2019; 300:111634. DOI: <https://doi.org/10.1016/j.sna.2019.111634>. Available from: <https://www.sciencedirect.com/science/article/pii/S0924424719312816>
92. Sharma S, Kiran R, Azad P, and Vaish R. A review of piezoelectric energy harvesting tiles: Available designs and future perspective. *Energy Conversion and Management* 2022; 254:115272. DOI: <https://doi.org/10.1016/j.enconman.2022.115272>. Available from: <https://www.sciencedirect.com/science/article/pii/S0196890422000681>
93. Ilyas MA. Piezoelectric energy harvesting : methods, progress, and challenges. New York: New York: Momentum Press, 2018
94. Shepelin NA, Glushenkov AM, Lussini VC, Fox PJ, Dicinoski GW, Shapter JG, and Ellis AV. New developments in composites, copolymer technologies and processing techniques for flexible fluoropolymer piezoelectric gener-

- ators for efficient energy harvesting. *Energy & Environmental Science* 2019; 12:1143–76
95. Kim KB, Cho JY, Jabbar H, Ahn JH, Hong SD, Woo SB, and Sung TH. Optimized composite piezoelectric energy harvesting floor tile for smart home energy management. *Energy Conversion and Management* 2018; 171:31–7. DOI: <https://doi.org/10.1016/j.enconman.2018.05.031>. Available from: <https://www.sciencedirect.com/science/article/pii/S0196890418305089>
 96. Shreeshayana R, Raghavendra L, and Manjunath VG. Piezoelectric energy harvesting using PZT in floor tile design. *Int. J. Adv. Res. Electr. Electron. Instrum. Eng* 2017; 6:8872–9
 97. Wu C, Wang AC, Ding W, Guo H, and Wang ZL. Triboelectric nanogenerator: a foundation of the energy for the new era. *Advanced Energy Materials* 2019; 9:1802906
 98. Yu H, Yue Q, Zhou J, and Wang W. A Hybrid Indoor Ambient Light and Vibration Energy Harvester for Wireless Sensor Nodes. *Sensors* 2014; 14:8740–55. DOI: 10.3390/s140508740. Available from: <https://www.mdpi.com/1424-8220/14/5/8740>
 99. Jung S, Oh J, Yang UJ, Lee SM, Lee J, Jeong M, Cho Y, Kim S, Baik JM, and Yang C. 3D Cu ball-based hybrid triboelectric nanogenerator with non-fullerene organic photovoltaic cells for self-powering indoor electronics. *Nano Energy* 2020; 77:105271. DOI: <https://doi.org/10.1016/j.nanoen.2020.105271>. Available from: <https://www.sciencedirect.com/science/article/pii/S221128552030848X>
 100. Wang S, Wang ZL, and Yang YA. A one-structure-based hybridized nanogenerator for scavenging mechanical and thermal energies by triboelectric–piezoelectric–pyroelectric effects. *Advanced Materials* 2016; 28:2881–7
 101. Cao Y, Liu Y, Zakeeruddin SM, Hagfeldt A, and Grätzel M. Direct contact of selective charge extraction layers enables high-efficiency molecular photovoltaics. *Joule* 2018; 2:1108–17
 102. Michaels H, Rinderle M, Freitag R, Benesperi I, Edvinsson T, Socher R, Gagliardi A, and Freitag M. Dye-sensitized solar cells under ambient light powering machine learning: towards autonomous smart sensors for the internet of things. *Chemical Science* 2020 Mar; 11:2895–906. DOI: 10.1039/C9SC06145B. Available from: <https://pubs.rsc.org/en/content/articlehtml/2020/sc/c9sc06145b> <https://pubs.rsc.org/en/content/articlelanding/2020/sc/c9sc06145b>

103. Li M, Zhao C, Wang ZK, Zhang CC, Lee HK, Pockett A, Barbé J, Tsoi WC, Yang YG, Carnie MJ, Gao XY, Yang WX, Durrant JR, Liao LS, and Jain SM. Interface Modification by Ionic Liquid: A Promising Candidate for Indoor Light Harvesting and Stability Improvement of Planar Perovskite Solar Cells. *Advanced Energy Materials* 2018 Aug; 8:1801509. DOI: 10.1002/AENM.201801509. Available from: <https://onlinelibrary.wiley.com/doi/full/10.1002/aenm.201801509> <https://onlinelibrary.wiley.com/doi/abs/10.1002/aenm.201801509> <https://onlinelibrary.wiley.com/doi/10.1002/aenm.201801509>
104. Lee HKH, Wu J, Barbé J, Jain SM, Wood S, Speller EM, Li Z, Castro FA, Durrant JR, and Tsoi WC. Organic photovoltaic cells—promising indoor light harvesters for self-sustainable electronics. *Journal of Materials Chemistry A* 2018; 6:5618–26
105. Ma LK, Chen Y, Chow PCY, Zhang G, Huang J, Ma C, Zhang J, Yin H, Hong Cheung AM, Wong KS, So SK, and Yan H. High-Efficiency Indoor Organic Photovoltaics with a Band-Aligned Interlayer. *Joule* 2020; 4:1486–500. DOI: <https://doi.org/10.1016/j.joule.2020.05.010>. Available from: <https://www.sciencedirect.com/science/article/pii/S2542435120302282>
106. Liao CY, Chen Y, Lee CC, Wang G, Teng NW, Lee CH, Li WL, Chen YK, Li CH, Ho HL, Tan PHS, Wang B, Huang YC, Young RM, Wasielewski MR, Marks TJ, Chang YM, and Facchetti A. Processing Strategies for an Organic Photovoltaic Module with over 10% Efficiency. *Joule* 2020; 4:189–206. DOI: <https://doi.org/10.1016/j.joule.2019.11.006>. Available from: <https://www.sciencedirect.com/science/article/pii/S2542435119305367>
107. Bettucci O, Saavedra V, Bandara T, Furlani M, Abrahamsson M, Mellander BE, and Zani L. Organic dye-sensitized solar cells containing alkaline iodide-based gel polymer electrolytes: Influence of cation size. *Physical Chemistry Chemical Physics* 2017; 20. DOI: 10.1039/C7CP07544H
108. Housecroft CE and Constable EC. Solar energy conversion using first row d-block metal coordination compound sensitizers and redox mediators. *Chemical Science* 2022; 13:1225–62
109. Xie L, Song W, Ge J, Tang B, Zhang X, Wu T, and Ge Z. Recent progress of organic photovoltaics for indoor energy harvesting. *Nano Energy* 2021; 82:105770
110. Ren M, Qian X, Chen Y, Wang T, and Zhao Y. Potential lead toxicity and leakage issues on lead halide perovskite photovoltaics. *Journal of Hazardous Materials* 2022; 426:127848. DOI: <https://doi.org/10.1016/j.jhazmat>

- 2021.127848. Available from: <https://www.sciencedirect.com/science/article/pii/S030438942102817X>
111. Muñoz-García AB, Benesperi I, Boschloo G, Concepcion JJ, Delcamp JH, Gibson EA, Meyer GJ, Pavone M, Pettersson H, Hagfeldt A, and Freitag M. Dye-sensitized solar cells strike back. *Chemical Society Reviews* 2021 Nov; 50:12450–550. DOI: 10.1039/D0CS01336F. Available from: <https://pubs.rsc.org/en/content/articlehtml/2021/cs/d0cs01336f>
<https://pubs.rsc.org/en/content/articlelanding/2021/cs/d0cs01336f>
 112. O'regan B and Grätzel M. A low-cost, high-efficiency solar cell based on dye-sensitized colloidal TiO₂ films. *nature* 1991; 353:737–40
 113. Saeed MA, Yoo K, Kang HC, Shim JW, and Lee JJ. Recent developments in dye-sensitized photovoltaic cells under ambient illumination. *Dyes and Pigments* 2021 Oct; 194:109626. DOI: 10.1016/J.DYEPIG.2021.109626
 114. Devadiga D, Selvakumar M, Shetty P, and Santosh MS. Dye-Sensitized Solar Cell for Indoor Applications: A Mini-Review. *Journal of Electronic Materials* 2021 Jun; 50:3187–206. DOI: 10.1007/S11664-021-08854-3/TABLES/1. Available from: <https://link.springer.com/article/10.1007/s11664-021-08854-3>
 115. Schoden F, Dotter M, Knefelkamp D, Blachowicz T, and Schwenzfeier Helkamp E. Review of state of the art recycling methods in the context of dye sensitized solar cells. *Energies* 2021; 14:3741
 116. High-efficiency dye-sensitized solar cells with molecular copper phenanthroline as solid hole conductor. *Energy and Environmental Science* 2015 Sep; 8:2634–7. DOI: 10.1039/c5ee01204j
 117. Sutton M, Lei B, Michaels H, Freitag M, and Robertson N. Rapid and Facile Fabrication of Polyiodide Solid-State Dye-Sensitized Solar Cells Using Ambient Air Drying. *ACS Applied Materials & Interfaces* 2022; 14:43456–62. DOI: 10.1021/acsami.2c14299. Available from: <https://doi.org/10.1021/acsami.2c14299>

Chapter 2

Experimental Methods

In this Chapter, the main experimental methods for dye sensitised solar cells (DSSCs) are discussed, highlighting details on materials, fabrication methods, and the characterisation techniques employed.

2.1 Materials

Unless otherwise stated, sandwich type DSSCs are fabricated; produced on fluorine doped tin oxide (FTO) coated glass substrates from XOP Glass, being TEC 15 (12-15 ohm/sq) with a thickness of 2.2 mm. TiO_2 is the employed material for the semiconductor electrode, also called the working electrode (WE), with two different Solaronix type pastes being used, Ti-Nanoxide T/SP (transparent), and Ti-Nanoxide D/SP (opaque).

Several different materials have been explored for use as dyes, redox mediators, sealants, and counter electrodes, which affects the electrical properties and appearance of the device. The main materials used in this thesis are listed in Table 2.1 (see page 78), with additional electrolyte solutions (redox mediator) discussed in further detail in Chapter 3.

Table 2.1 DSSC materials and solvents

Material	Manufacturer	Description	Role
N719	Solaronix	Ruthenizer 535-bisTBA	Dye
XY1:L1	Dyename	1:1 Ratio	Dye
Mosalyte TDE-02	Solaronix	iodine:ionic liquid (1:240)	Redox Mediator
Cu(II/I)(tmby)	Dyename	CuI(tmby)2TFSI: 0.2 M CuII(tmby)2(TFSI)2: 0.06 M	Redox Mediator
Surlyn	Solaronix	Meltonix - 25 μ m thick	Sealant
Light Cure Adhesive	ThreeBond	Product Code: TB3035B	Sealant
Chloroplatinic acid	Sigma-Aldrich	hydrate, assay: 99.9%	CE
PEDOT	Sigma-Aldrich	3,4-Ethylenedioxythiophene(assay: 97%) Sodium dodecyl sulfate(assay: \geq 99.0%)	CE
Titanium diisopropoxide bis(acetylacetonate)	Sigma-Aldrich	75 wt. % in isopropanol	Blocking Layer
4-tert-Butylpyridine	Sigma-Aldrich	assay: 98%	Additive
Bis(trifluoromethane)sulfonimide lithium salt	Sigma-Aldrich	99.95% trace metal basis	Additive
Chenodeoxycholic acid	Sigma-Aldrich	anionic	Additive
Chloroform	Sigma-Aldrich	anhydrous, assay: \geq 99%	Solvent
Ethanol	Sigma-Aldrich	anhydrous, assay: \geq 99.0%	Solvent
Acetonitrile	Sigma-Aldrich	anhydrous, assay: 99.8%	Solvent
IPA	Sigma-Aldrich	extra pure	Solvent

Note: CE = Counter electrode, IPA = Isopropanol

2.2 Cell Fabrication Process

All solutions were prepared in a sterile laboratory, and if required, sonicated to dissolve the additives precisely. Materials were weighed using a laboratory balance, being placed on a glass weighing boat; rinsed with the required solvents to ensure accuracy.

2.2.0.1 Substrate Cleaning

The FTO glass substrates are prepared as follow: using a solution of Hellmanex® (2% in de-ionised (DI) water), the FTO side and glass side is scrubbed with a medium bristle toothbrush. After careful scrubbing, the substrate is rinsed with DI water. The substrate is then soaked in acetone and isopropanol (IPA) respectively, drying with a nitrogen gun.

Originally, additional steps would be included; the substrates are to sonicate at 60 °C for 10 minutes in Hellmanex, then acetone and IPA. However, due to investigating

into large active area sizes of DSSCs, this process cannot take place due to the size restrictions and the limited availability of large substrate holders. Therefore, to maintain repeatability with different active areas, this step is removed from the substrate cleaning process.

2.2.1 Working Electrode (WE) Substrate

2.2.1.1 Blocking Layer (BL) Spray Deposition

The clean WE FTO substrate is placed on a hotplate, heating to 300 °C. A solution of titanium diisopropoxide bis(acetylacetonate) is diluted with IPA, in a 1:9 volume ratio. The spray gun is filled with this diluted solution. At a constant and appropriate height and spray gun settings, the solution is sprayed at 10 second intervals, with 15 spray cycles.

It is vital that a compact BL is evenly distributed across the whole substrate, prior to TiO_2 deposition. This has an important role of reducing/ suppressing the charge recombination (or back transfer of electrons) between the conductive substrate (FTO) and the electrolyte. This has a significant impact on the PCE of DSSCs under low light conditions [1][2].

2.2.2 Mesoporous TiO_2 deposition and annealing

The initial transparent TiO_2 (Ti-Nanoxide T/SP) layer is deposited on the BL, through a screen-printing technique. The screen is placed 5 mm above the base of the screen printer, with the substrate placed on the base. The TiO_2 paste is placed on the screen; a squeegee is used to run the paste through the holes of the screen. The initial run is to ensure that the paste has filled the screen mesh, making sure that not too much force is applied. More paste is then applied on the screen, with the second run applying enough force to draw the TiO_2 through the mesh onto the substrate using the squeegee. Several screens are used with different active areas (cross sectional area of the TiO_2 layer). Each screen is manufactured from MCI Precision Screens, with the product code and mesh details of, 245 43-80, 45°, 13m.

If an opaque layer is required, the substrate is placed on the hot plate at 100 °C until the Ti-Nanoxide T/SP is dried. The screen is then thoroughly cleaned using fibre-free blue roll and ethanol. The opaque TiO_2 (Ti-Nanoxide D/SP) paste is then placed on the screen, following the same process as before.

The substrate is covered for a few minutes before being placed on the hot plate set

at 70 °C. The TiO_2 layer is then annealed at 500 °C for 30 minutes with a 30-minute ramp time (time taken to reach the final preset temperature). Once cooled, substrates are placed in a dye bath containing the chosen dye solution, and left to dye in a dark environment overnight. Best results are achieved when the substrates are immersed in dye solution before they have fully cooled down; around 100 °C.

2.2.3 Counter Electrode (CE) Substrate

Before cleaning and depositing a catalyst material onto the CE substrate, holes are drilled to allow filling of the electrolyte. The substrate is immersed in water, and drilled using a 1 mm diameter tungsten drill bit, on the FTO side. Depending on the size of the active area, additional holes are drilled to fully fill the cavity of the DSSC.

Platinum (Pt), or PEDOT is used as the counter electrode material, which requires different techniques to deposit onto the substrate. Pt is used alongside I^-/I^{-3} redox mediators, whilst PEDOT CE is used with copper redox mediators.

2.2.3.1 Pt deposition

To deposit the Pt layer, the substrate is initially cleaned and then placed onto the spin coater, with the particulates being removed using the nitrogen gun. 5 mM of Chloroplatinic acid in IPA is deposited in the centre of the FTO side of the substrate. The solution is spread across the surface of the FTO, using a pipette tip and surface tension; attentive of not damaging the surface by contacting the pipette tip onto the substrate.

A 30 s spin is set at an acceleration of 200 ms^{-2} , and at 1000 RPM. After the spin cycle is complete, the CE substrate is placed onto a hotplate set at 70 °C and annealed at 400 °C for 15 minutes with a 15-minute ramp time.

2.2.3.2 PEDOT deposition

An aqueous solution consisting of 0.01 M of 3,4-ethylenedioxythiophene and 0.1 M of sodium dodecyl sulfate (assay: $\geq 99.0\%$) is electropolymerized [3] onto the substrate, forming a Poly(3,4-ethylenedioxythiophene) (PEDOT) layer. This is achieved through the chronopotentiometry setting of the Zahner. The current applied to the electrodes varies the thickness of the PEDOT layer, with the current having different values depending on the desired cross-sectional area deposition of the PEDOT.

2.2.4 Assembly of DSSC

The WE and CE substrates are assembled, making sure that they are dust free and the FTO sides are facing each other. The hole (or holes, depending on active area size) in the CE is aligned with the active area on the WE substrate. The sealing method depends on the composition of the CE and redox mediator used.

2.2.4.1 Sealing cells

I^-/I^{-3} redox mediator and Pt CE - A Surlyn gasket is cut to the desired area using a laser cutter, being placed in between the two substrates, carefully aligning with the active area of the WE. A t-shirt press set to 120 °C and at a desired pressure, pushes the two substrates together, melting the Surlyn for 30 s. The cell is allowed to cool, and then sealed again from the other side.

Copper redox mediator and PEDOT CE - This composition is assembled using a UV-curing glue (TB3035B, Threebond), set using the CS2010 High Power UV curing LED system (Thorlabs). The glue is placed around the edges of both the substrates, cured using the LED system.

2.2.4.2 Electrolyte filling

The electrolyte is injected into the predrilled hole. If the active area is small, only one hole is required. To force the electrolyte into the cell, it is placed in a vacuum desiccator, which removes the air from inside the cell. Once air is fully removed, the valve is opened, releasing the air back into the desiccator. This forces the electrolyte (sitting above the hole) into the cell.

If the active area of the cell is larger than 4 cm², several predrilled holes are introduced at each corner of the active area. The electrolyte is injected into half of the predrilled holes, which naturally fills the cell through capillary action. The excess electrolyte is wiped with ethanol, to clean the surface of the glass.

The holes are covered depending on the original method of sealing the cells. If Surlyn is initially used, a small Surlyn square is placed above the hole, and a circular cover glass on top. A soldering iron at 330 °C is gently placed on the cover glass, melting the Surlyn. Otherwise, the UV curing glue is placed inside the hole, cured using the high-power LED system.

2.2.4.3 Ultrasonic soldering

To increase the conductivity at the contact points (to measure the cell) for DSSCs, an ultrasonic soldering iron is used to apply solder on the FTO substrate, being on the working and counter electrode. Care is taken to ensure that no solder is applied too close to the overlapping sections of the sandwiched DSSC, otherwise, will cause shorting.

2.3 Solar Cell Characterisation Techniques

2.3.1 Light simulators

The J-V curve of a solar cell is measured through a light simulator, which is an important tool to discover its performance. The equations can be found in Section 1.3.3.1, which discusses the cell fill factor and cell efficiency. Two different types of light sources are tested on the DSSC, one being equivalent to 1 sun, and the other characterising the performance at low light intensities. These methods are discussed in further detail below.

2.3.1.1 Solar Simulator

A G2V Pico class AAA LED solar simulator was used to measure the DSSC at one sun, alongside the Keithley SMU. The maximum area of the DSSC that can be placed under the solar simulator is $2.5\text{ cm} \times 2.5\text{ cm}$. Initially, the simulator is calibrated using a quartz reference cell, with no need of a KG5 filter. This is due to a good spectral match of the LED simulator in near infrared range (NIR), compared to other standard solar simulators that use a Xenon arc lamp.

All measurements occurred with the DSSC situated on the adjustable bed without a metal mask; calibrated at a height (distance from end of the lens tube) of 4.5 cm . The cells were measured in a reverse sweep direction, with a pre-sweep delay of 10 s , step voltage of 5 mV , and a step measurement delay of 50 ms .

2.3.1.2 Low light simulator

An enclosed low light simulator was used to measure the performance of DSSCs in indoor conditions, by providing a diffused LED light source with a colour temperature of 2700 K (see spectrum in Figure 2.1). This system uses the Keithley SMU and Thorlabs power supply, measured in a reverse sweep direction. The LED array is calibrated using the Ocean Insight spectrophotometer, which is set-up to measure

the photometry in Lux values through the ‘OceanView’ software.

The measurement values differ depending on the light intensity output. At lower light intensities, it is important that the J-V curves are measured correctly, with the curve passing through 0 current. An incomplete J-V curve results in an incorrect V_{OC} , which can happen in very low light intensities due to DSSCs having a slow rise to steady state V_{OC} . The V_{OC} delay and V_{OC} tolerance should therefore be increased, to mitigate this issue before measuring.

Larger DSSCs are able to be measured using the low light simulator, as a consequence of the array of LEDs in an enclosed box. This cannot be achieved using the solar simulator, due to their smaller light beam area, and as they are not enclosed from ambient lighting. This does mean that larger DSSCs cannot be tested under one sun, but at the highest light intensity output of the LED array of the low light simulator, being 10,000 Lux.

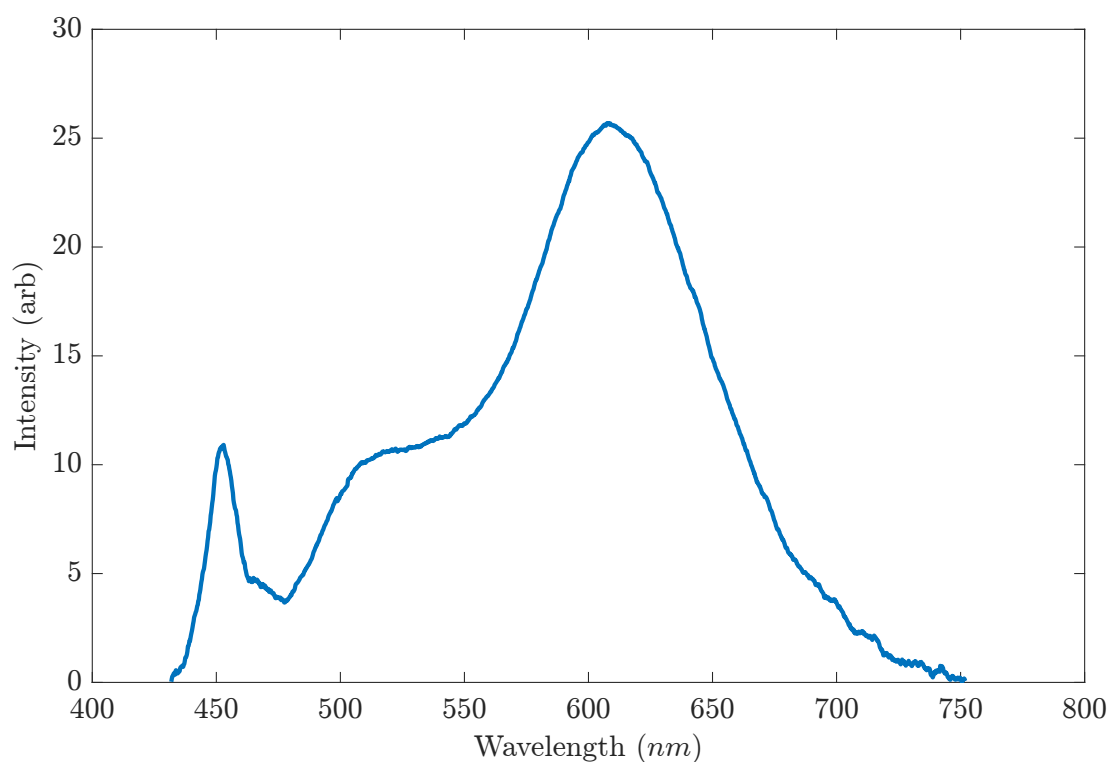


Figure 2.1: 2700 K light spectrum at 10000 Lux

2.3.2 Optical Characterisation

2.3.2.1 UV-Vis-NIR Spectrophotometry

The transparency and absorption spectra of the incident light through different layers of a DSSC can be achieved with the Perkin Elmer Lambda 750 UV-Vis-NIR

spectrophotometer. The instrument uses two different light sources, being deuterium and tungsten halogen, to provide short and long wavelengths to the sample. The deuterium lamp covers the UV spectrum, with the spectrophotometer switching to the tungsten halogen lamp (for the visible region) around $300\text{ nm} - 350\text{ nm}$ [4]. Before taking measurements of different layers of the DSSC, the instrument undergoes a calibration of 100% transmission and 0% (dark state) spectra, for increased accuracy.

Bibliography

1. Saeed MA, Yoo K, Kang HC, Shim JW, and Lee JJ. Recent developments in dye-sensitized photovoltaic cells under ambient illumination. *Dyes and Pigments* 2021; 194:109626. DOI: <https://doi.org/10.1016/j.dyepig.2021.109626>. Available from: <https://www.sciencedirect.com/science/article/pii/S0143720821004927>
2. Hart JN, Menzies D, Cheng YB, Simon GP, and Spiccia L. TiO₂ sol-gel blocking layers for dye-sensitized solar cells. *Comptes Rendus Chimie* 2006; 9:622–6. DOI: <https://doi.org/10.1016/j.crci.2005.02.052>. Available from: <https://www.sciencedirect.com/science/article/pii/S1631074805002936>
3. Leon A de and Advincula RC. Chapter 11 - Conducting Polymers with Superhydrophobic Effects as Anticorrosion Coating. *Intelligent Coatings for Corrosion Control*. Ed. by Tiwari A, Rawlins J, and Hihara LH. Boston: Butterworth-Heinemann, 2015 :409–30. DOI: <https://doi.org/10.1016/B978-0-12-411467-8.00011-8>. Available from: <https://www.sciencedirect.com/science/article/pii/B9780124114678000118>
4. SHIMADZU. Light sources for Spectrophotometers. Available from: https://www.shimadzu.com/an/service-support/technical-support/uv/essential_knowledge/lightsources.html

Chapter 3

Investigation into the optimal type of transparent monolithic DSSC for a visually appealing interface and performance for indoor IoT nodes

3.1 Introduction

3.1.1 Background

As computers became widespread, Human Computer Interaction (HCI) research started taking place, studying the interaction between users and computers, concentrating mainly on the physical, psychological, and theoretical aspects. HCI is a multi-disciplinary field, mainly consisting of psychology and cognitive science, ergonomics, sociology, computer science, engineering, business, and finally graphic design [1].

An optimal HCI design can be described as a desired fit between the user, the machine, and its application [2]; with the main requirements being concentrated around the user, it is important that the overall appearance and performance of the IoT nodes can be optimised, having a good interaction with a computer system, through a user interface (UI). An increasingly important feature is the appearance of the UI, needing to be eye-catching and attractive [3]. HCI not only improves the user experience but also promotes a broader adoption of IoT in everyday life, emphasising on user-centric and user-friendly design. By using HCI, new technologies have arisen to consider the needs of various demographic groups, including individuals

with disabilities and the elderly [4]. A study by Bissoli *et al.* [4], assisted people with physical disabilities, to pursue daily activities at home, by integrating a new assistive system based on eye tracking, to control different indoor equipment, through IoT.

Following the literature review in Chapter 1, some energy harvesting techniques can be used within the machine or smart device, meaning that the user does not visually see the harvester. This can be beneficial, as the harvester does not have to be aesthetically pleasing for the user, resulting in no additional modifications. These mainly include energy harvesters that use RF, Thermal, and Mechanical energy sources. However, after ranking each technique through the Pugh Matrix, shown in Table 1.2 (see page 56), PV cells outperformed the other harvesting techniques, having the capabilities of being reliable, controllable, and possessing high energy density output in indoor environments. Nonetheless, by integrating PV cells with IoT nodes, would result in the harvesting light technology to be visible to the user.

Chapter 1 concluded that the design flexibility and performance of DSSCs in indoor conditions outperforms other types of PV. Whilst recent research has shown the performance improvements in indoor conditions of DSSCs [5][6][7][8], there has been limited work concentrating on combining the visual appearance of the light energy harvester and IoT nodes with the user in mind; as further discussed in the related work outlined in Section 3.1.2 below (see page 88).

This Chapter concentrates on the user interface as the primary factor, and not purely based on the performance of the DSSC. Whilst the user interface does change with regards to the IoT application, a baseline approach has been considered across smart devices which involve interacting with the user, and in doing so eliminating any IoT nodes that are for background indoor environmental requirements. The applications in mind are situated primarily with the interaction of the user to the IoT node, with many types mentioned in Chapter 1; some of these include wearables, smart meters, smart thermostats, and other automated systems which require user interaction. All these types of IoT node applications mentioned have one thing in common, the display screen, which allows a natural interaction (being the user interface) with the user.

For DSSCs to be integrated with these types of IoT node applications, the most common and applicable method is to place the cell in front of the screen, to capture the required indoor light to harvest energy, and minimise the IoT node footprint. Therefore, a transparent monolithic DSSC is required to allow the user to see the

display behind the harvester, but also allow full potential of the display, which can be hindered if a DSSC module is used; as the active area will be divided, being clearly visible to the user. There are two feasible methods of achieving this: having the full DSSC covering the display (Figure 3.1a); or alternatively having a border around the display that includes both the dye and electrolyte, with the centre only containing the electrolyte, which potentially allows further transparency to see the display behind (Figure 3.1b). Although containing the electrolyte within the framed active area offers a possibility, it does however complicate the sealing process of the cell, as well as being visible to the user.

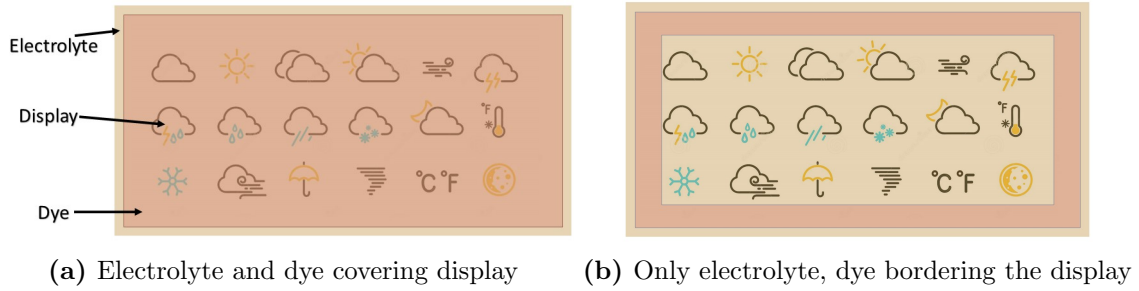


Figure 3.1: Different layouts of a DSSC on an IoT display

3.1.2 Related Work

3.1.2.1 Transparent appearance

There are two aspects to consider; if layout from Figure 3.1a is used, then the transparency of both the dye and electrolyte is important. However, if Figure 3.1b layout is applied, then there is no requirement for the dye to be transparent, only the electrolyte. Previous work on the transparency improvements of dyes and electrolytes for DSSCs are mentioned further below:

3.1.2.1.1 Transparent Devices

Integrating DSSCs into building and greenhouse windows has had a substantial amount of research, to improve the transparency of the dyes [9][10][11][12][13]. There are two main ways of creating a transparent dye film:

1. By decreasing the thickness of the semiconductor material (TiO_2 in this case), reduces the amount of dye that can attach onto the TiO_2 film. Several different film thicknesses were investigated by Selvaraj *et al.* [9], concluding that whilst the transparency of the cell increased with the reduction in thickness (tested to $3.5 \mu m$), the PCE of the cell decreased, when under an illumination of 1000

W/m² (AM 1.5G). This is due to the reduced dye particles attached to the TiO_2 , absorbing less light. It was also found that increasing the titania layer above 10 μm also decreased the performance of the DSSC, due to the increase in electron diffusion length.

2. An alternative is to bypass the eye sensitive region (500-600 nm), which allows the DSSC to become highly transparent but also maintains a high PCE in outdoor conditions [11][14]. An optimised outdoor transparent DSSC was achieved by Zhang *et al.* [11] by mixing two different dyes based in the UV and the NIR, being low in the eye sensitive region. The dyes used were Y1 and HSQ5, achieving an efficiency of 3.66% with a light transmittance of 60.3% (in the high-eye-sensitivity region (500–600 nm)), at 1 sun. However, this technique is not suitable for indoor conditions, due to most of the irradiance of a 3000 K (used as the indoor light simulator) spectrum being high in the region of 500-600 nm . Avoiding the absorbance of this region, would drastically decrease the PCE of the DSSC.

3.1.2.1.2 Electrolytes

In a general DSSC composition, the dye affects the transparency more than the electrolyte. This means that there is limited work done in trying to improve the transparency of the electrolyte solution. However, one of the most common and studied electrolyte used within DSSCs is the I_3^-/I^- redox couple, having been optimised for indoor conditions, with good transmission.

Several papers have delved into decreasing the iodine concentration of the I_3^-/I^- redox couple, for indoor conditions [15] [16] [17] [18] [19]. Under low light, the electron recombination at the semiconductor, dye, and the redox mediator can be lowered by the reduction of Iodine in the I_3^-/I^- electrolyte. The colour of the electrolyte also becomes lighter, allowing for more light absorption through the dye. Overall, this approach improves the PCE at lower light conditions, without any loss in dye regeneration (due to low input light intensity), but also increases the transparency of the electrolyte [20].

Like the Iodine reduction, this outcome was also achieved with lowering the concentration of the Cu(II) redox mediator; decreasing the interfacial charge recombination [6][8]. This also could increase the transmittance of the electrolyte.

3.1.2.2 Altering the active area size

Whilst there have been several studies on different indoor tested DSSC modules and monolithic sizes, being rigid [6][7], and flexible; most active area sizes reported in DSSC literature are below 1 cm^2 , with Saeed *et al.* [18] highlighting the importance of scaling up DSSCs for understanding the usage in practical applications. This review [18] does also explore the work done on larger active areas, which tend to be modules. However, research on establishing the optimised active area size of a monolithic DSSC in indoor conditions has not previously been fully explored.

3.1.3 Summary

Whilst the transmission of the dye can be increased with the reduction in the thickness of TiO_2 , there is less understanding as to which type of electrolyte preferable. Two key criterion's are analysed when deciding which electrolyte is best for indoor conditions, being the transparency and performance output of the DSSC. Increased optical transparency would allow integration of DSSCs in applications where aesthetic and visual appeal are important, but also implies more effective light absorption and improved overall performance. Higher DSSC efficiency implies an improved energy conversion, being a more competitive alternative to other types of DSSCs. There is also limited work being done on fully understanding what active area size increase a monolithic DSSC can achieve in indoor conditions, whilst maintaining its performance.

Following Chapter 1, it is evident that the best type of redox mediator is Cu(II/I)(tmby) , for opaque DSSCs. Therefore, a characteristic comparison of different concentrations of commercial and lab-made I_3^-/I^- electrolyte, and different concentrations of Cu(II/I)(tmby) , would be sufficient to find the most appropriate type of electrolyte for an indoor transparent DSSC.

The aim of this Chapter will therefore investigate the following research questions listed below:

- What type of transparent monolithic DSSC is best for indoor conditions, being feasibly assembled and suitable for integration with a display behind that leads to a balance of a good indoor power harvester and a visually appealing UI?
- What is the best maximum/ optimal active area size, and type of monolithic DSSC in low light intensity conditions?

3.2 Materials and methods

The overall, general fabrication methods and materials are stated in Chapter 2, with additional information for this Chapter mentioned below:

3.2.1 Control variables

The thickness layer of the TiO_2 paste (Ti Nanoxide T/SP) remains constant throughout this Chapter. This is achieved by using the same type of screen-printing mesh and setup to draw the paste onto the substrate, giving an average thickness of $6\ \mu m$.

Depending on the type of DSSC fabricated, being either with the I_3^-/I^- or the Copper redox, the control variables are mentioned below:

3.2.1.1 I_3^-/I^- based DSSC

Dye: $0.5\ mM$ of Ruthenizer 535-bisTBA (commonly known as N719) in ethanol.

Counter Electrode: $5\ mM$ of chloroplatinic acid in IPA.

3.2.1.2 Copper-based DSSC

Dye: XY1:L1 in a ratio of 1:1. The solution for each dye is prepared as follows:

- $0.1\ mM$ of XY1 with $1\ mM$ chenodeoxycholic acid in chloroform/ethanol 3:7
- $0.5\ mM$ of L1 in acetonitrile

Counter Electrode: PEDOT an aqueous solution consisting of $0.01\ M$ of 3,4-ethylenedioxythiophene and $0.1\ M$ of sodium dodecyl sulfate.

3.2.2 Independent variables

3.2.2.1 Electrolyte

Different types of I_3^-/I^- and copper electrolytes are investigated in this Chapter, some being ‘homemade’ (fabricated in the laboratory), and others bought commercially.

3.2.2.1.1 I_3^-/I^-

Homemade (HM): A solution of electrolyte was created using the materials listed below, with a high ($50\ mM$) and low ($5\ mM$) iodine concentration, in acetonitrile.

- $0.6\ M$ 1-methyl-3-n-propylimidazolium iodide (Sigma-Adrich: $\geq 98.0\%$)
- $0.1\ M$ lithium iodide (Sigma-Adrich: 99.9% trace metals basis)

- 50 *mM* or 5 *mM* iodine (Sigma-Adrich $\geq 99.99\%$ trace metals basis)
- 0.5 *M* 4-tert-butylpyridine

Commercial: Other pre-made I_3^-/I^- electrolytes were also tested, having high and low iodine concentrations. Some of the listed electrolytes are optimised for indoor conditions (low light intensity).

- Mosalyte TDE-025 (Solaronix - iodine / ionic liquid (1/240))
- Idolyte Z-50 (Solaronix – 50 *mM* redox concentration, solvent: 3-methoxypropionitrile)
- Idolyte AN-50 (Solaronix - 50 *mM* redox concentration, solvent: acetonitrile)

3.2.2.1.2 Cu(II/I)(tmby)

The copper redox was prepared in acetonitrile, with two different electrolyte solutions fabricated; one having the correct acetonitrile measurements (full concentration), and the other having double the volume of acetonitrile, diluting the solution and thereby halving the concentration of the redox mediator (half concentration). This latter fabrication was performed in an attempt to increase transmission of the solution. The electrolytes were prepared as follows:

- CuI(tmby)₂TFSI: 0.2 *M*
- CuII(tmby)₂(TFSI)₂: 0.06 *M*
- 0.1 *M* lithium bis(trifluoromethanesulfonyl)imide
- 0.6 *M* 4-tert-butylpyridine

3.2.2.2 Active area size

The different active area sizes of the DSSC are listed below; screen printed with different mesh slot sizes to provide the accurate required area of the semiconductor.

- 1 *cm*² (1 *cm* x 1 *cm*)
- 4 *cm*² (2 *cm* x 2 *cm*)
- 16 *cm*² (4 *cm* x 4 *cm*)
- 64 *cm*² (8 *cm* x 8 *cm*)

3.2.3 Dependent variables

3.2.3.1 1 cm² DSSCs

They are tested under one sun and low light intensities, ranging from 10,000 Lux to a 100 Lux, gathering the J-V curve for each type of DSSC. This outputs the open-circuit voltage (V_{OC}), short-circuit current density (J_{SC}), fill factor (FF), and the photoelectric conversion efficiency (PCE).

3.2.3.2 Larger active area DSSCs

Only the low light simulator is used to measure the J-V curves for each active area size, due to the small light exposure area from the solar simulator. Again, measuring with a light intensity range of 10,000 Lux to 100 Lux.

3.3 Comparing different DSSC compositions (1 cm² active area) at different light intensities

3.3.1 Results and discussion

Eight 1 cm² DSSCs were tested for each type of electrolyte, under 1 sun and in low light conditions (10,000, 1000 and 100 Lux). The results include the open-circuit voltage (V_{OC}), short-circuit current density (J_{SC}), and the fill factor (FF), being the overall summary data from each J-V curve output. The photoelectric conversion efficiency (PCE) of each cell is also included to summarise the efficiency conversion between the input power (from the light source) and output power (from the DSSC). The results are plotted using the whisker and box plots at each light intensity.

The whisker and box plots use two times the interquartile range, meaning anything beyond the whiskers are displayed as an outlier; represented as a dot. The top end and lowest end of the whisker is the maximum and minimum value respectively, from the set of values. The box contains a horizontal line, representing the median value from the dataset. The area above and below this line is the 75th percentile and 25th percentile respectively.

3.3.1.1 At one sun

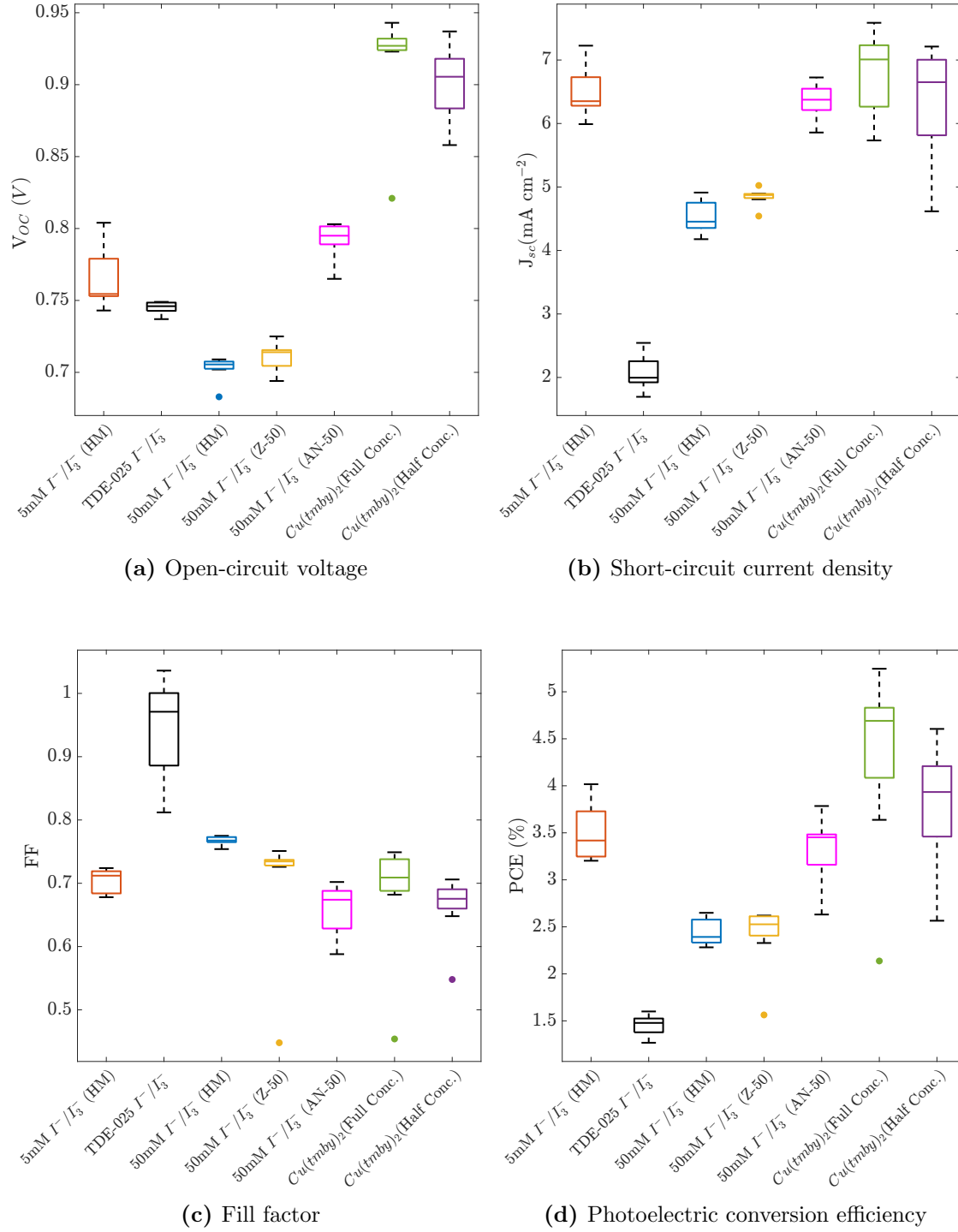
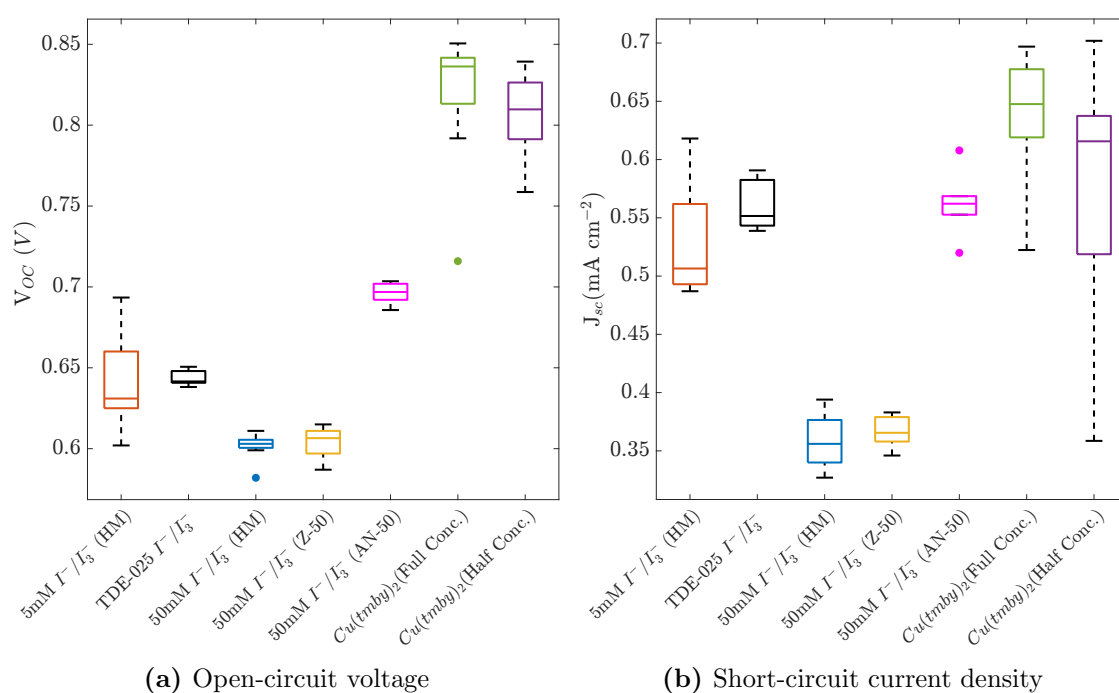


Figure 3.2: 1cm^2 active area DSSCs at one sun

At a light intensity of 1 sun, Figure 3.2 shows clearly that the full concentration copper electrolyte (and dye XY1:L1) outperforms the other types of cells, with a PCE reaching over 5% due to its high V_{OC} output (see Figure 3.2a and Figure 3.2d). The half copper concentration performs slightly worse, with the mosalyte TDE-025 underperforming, only reaching a PCE of approximately 1.6%. This is due to the

low J_{SC} (median $\approx 2 \text{ mA cm}^{-2}$) output and unreasonable fill factor values (≥ 1), meaning that the cell has high parasitic resistances, being mainly caused by series resistance. The FF for the other cell types behaves well, achieving over 0.7. The short-circuit current density, J_{SC} , of the 5 *mM* HM electrolyte and AN-50, perform considerably like the J_{SC} output of the copper DSSCs, however with a lower V_{OC} , achieves a PCE of around 4%.

3.3.1.2 At 10,000 Lux



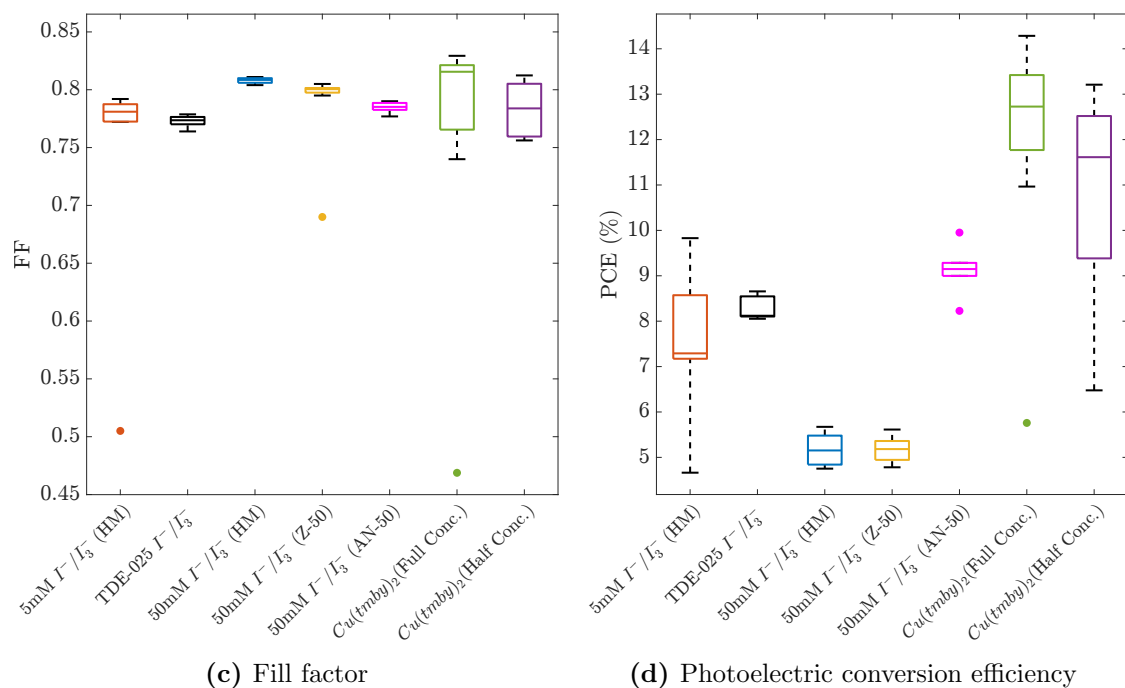


Figure 3.3: 1cm^2 active area DSSCs at 10,000 Lux

As the light intensity decreases to 10,000 Lux (being approximately tenth of the sun's intensity), the J_{SC} and V_{OC} (see Figure 3.3a and Figure 3.3b) of all cell types (except for the J_{SC} of the mosalyte TDE-025) decrease. With reduced input power, the TDE-025 electrolyte has less resistance, and performs accordingly. The fill factor and PCE however, have increased for all cell types (except the FF of the TDE-025), with the full concentration copper redox achieving a maximum efficiency of over 14%. The performance of the 5 *mM* HM and AN-50 electrolytes are again similar with a PCE of around an average of 8%, whereas both the 50 *mM* HM and Z-50 only achieve a PCE of approximately 5%.

3.3.1.3 At 1000 Lux

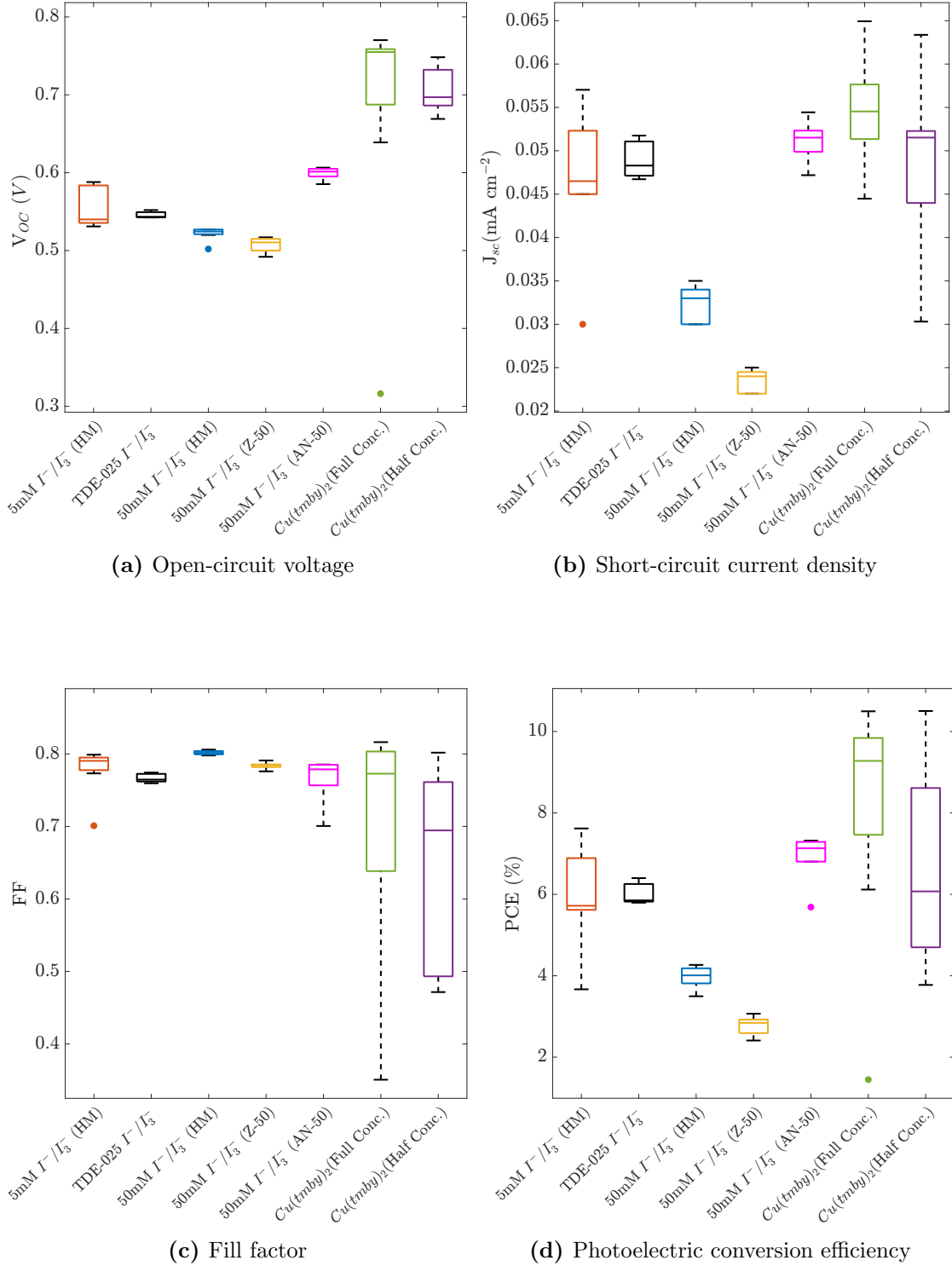


Figure 3.4: 1cm 2 active area DSSCs at 1000 Lux

The results at a 1000 Lux have a similar trend when at a light intensity of 10000 Lux, with similar FF values, the V_{OC} and J_{SC} of all DSSC types decrease. The PCE also decreases, with the full copper concentration electrolyte still outperforming the

other types, with a median of over 9%.

3.3.1.4 At 100 Lux

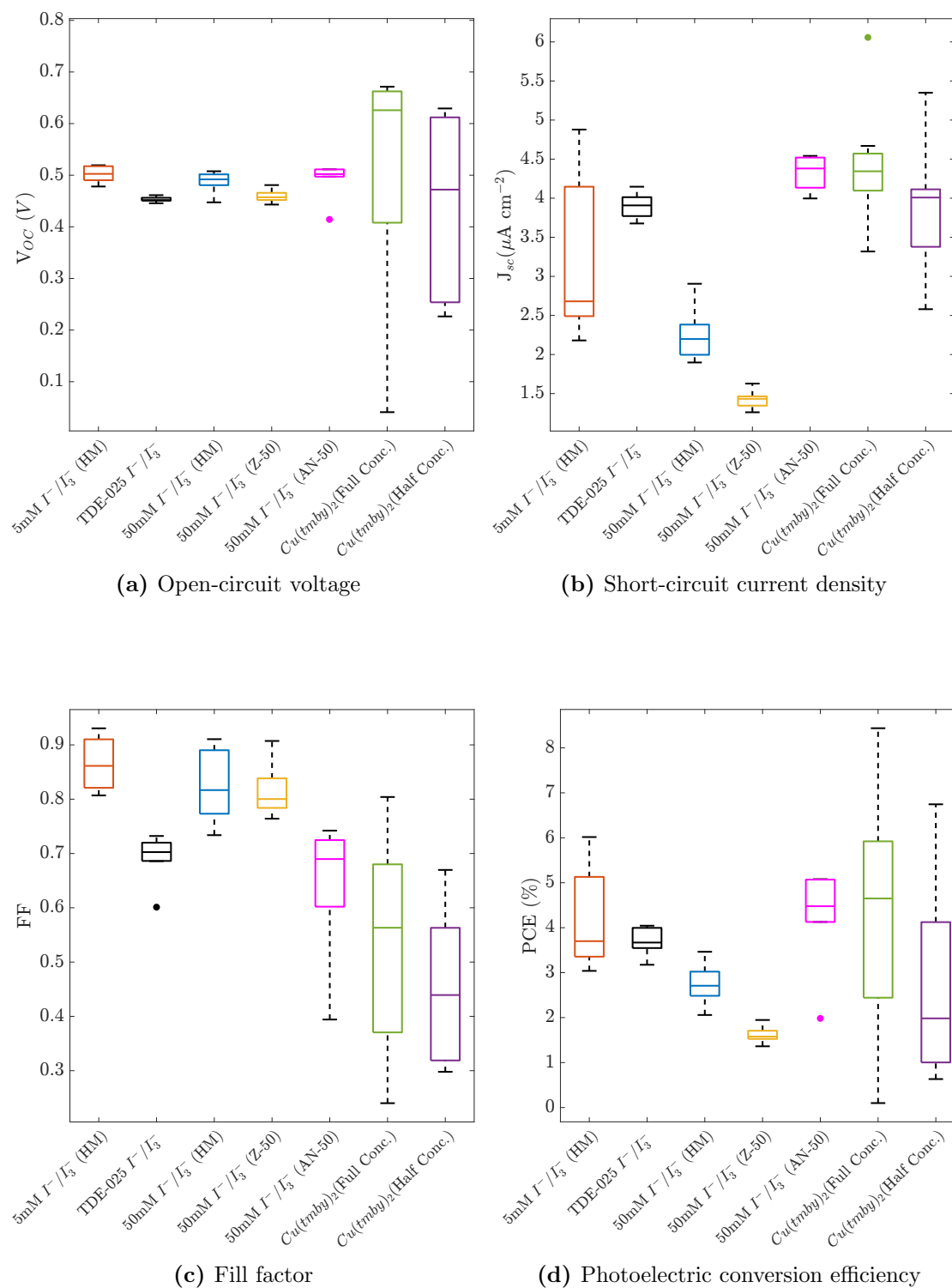


Figure 3.5: $1cm^2$ active area DSSCs at 100 Lux

The V_{OC} decreases as the light intensity is reduced to a 100 Lux can be seen to be larger with the copper redox electrolytes, compared to the I_3^-/I^- types. The V_{OC} of all I_3^-/I^- types are very similar to the half copper concentration output, of 0.5 V, with the full concentration achieving slightly larger V_{OC} of over 0.65 V. The FF has also decreased for the copper electrolyte DSSCs, with the 5 mM HM electrolyte achieving over 0.9. Overall, at a very low light level of a 100 Lux, the PCE of the 5 mM HM, AN-50 and the full copper concentration are very similar, achieving a PCE of 5% (see Figure 3.5d).

3.3.1.5 Transmittance spectra of incident light through different layers of DSSC

The transmittance spectrum for each type of electrolyte are measured, to compare how transparent the electrolytes are for use, as detailed in Figure 3.1b. This is achieved by placing the electrode between two pieces of substrate, without any additional layers introduced (such as the BL, dye, and the counter electrode). This is filled using the same process mentioned in Section 2.2.4.2, depending on the DSSC type (being either Surlyn or UV curing glue).

The assembled piece is placed inside the UV-Vis-NIR spectrophotometer, finding the transmittance at each wavelength, between the range of 700 nm to 300 nm. The transmission spectra for each electrolyte are presented in Figure 3.6, with a base comparison of an air sample and an FTO glass substrate.

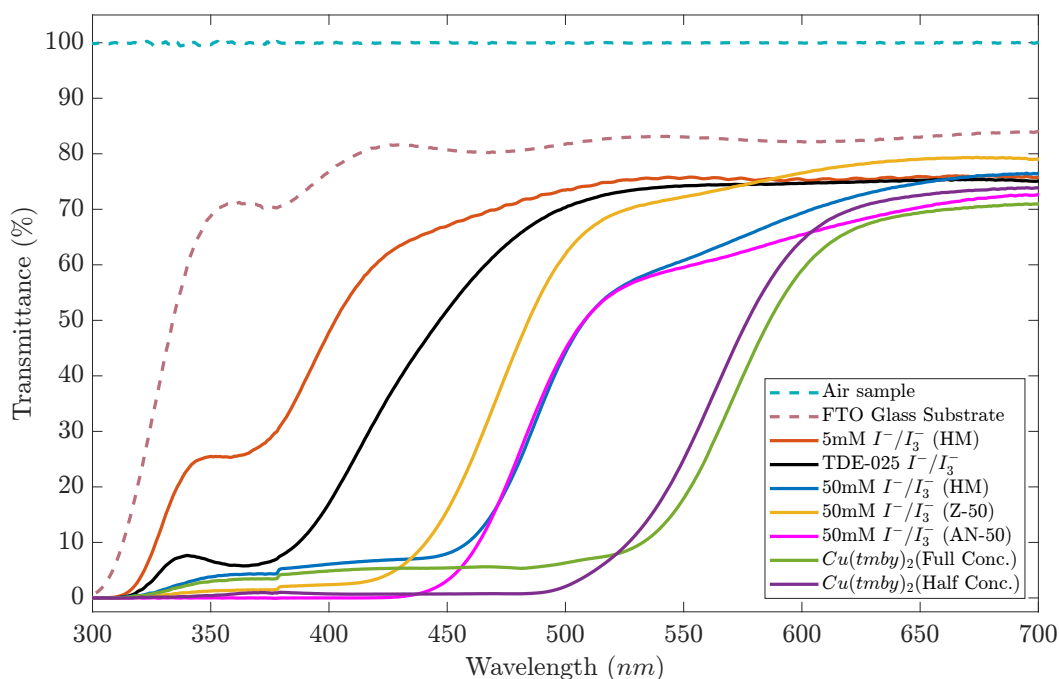


Figure 3.6: Transmittance spectrum for each type of electrolyte

The most transparent electrolyte is the 5 *mM*, having the highest transmittance value throughout each wavelength reading. The area under the transmittance between 300-700 *nm* for 5 *mM* (HM) electrolyte is 2.38×10^4 %-nm. Comparing this with copper (full conc.), having a value of 1.01×10^4 %-nm, demonstrates how much more transparent the 5mM electrolyte is. It was also noticed that halving the concentration of the copper redox only has a slight increase in transmission improvement, whilst reducing the Iodine from 50 *mM* HM to 5 *mM* HM largely improves the transmission of the electrolyte.

3.3.1.6 Zombie Cell comparison

After two weeks from the original fabrication of the DSSCs, liquid based redox mediators such as I_3^-/I^- will remain as liquid and will not work if the electrolyte leaks from a damaged cover slip on the hole or from an improper seal between the counter and working electrode.

However, copper based redox mediators are fabricated with UV curing glue, which eventually does allow some gaps to appear between the electrodes, resulting in the slow drying of the redox mediator. The drying of the liquid copper redox mediator forms a solid hole transport material (called zombie cells), seen in Figure 3.7, which means that after drying, there is no possibility for the electrolyte to leak, prolonging the life of the DSSC. The performance before and after drying is compared at different light intensities.

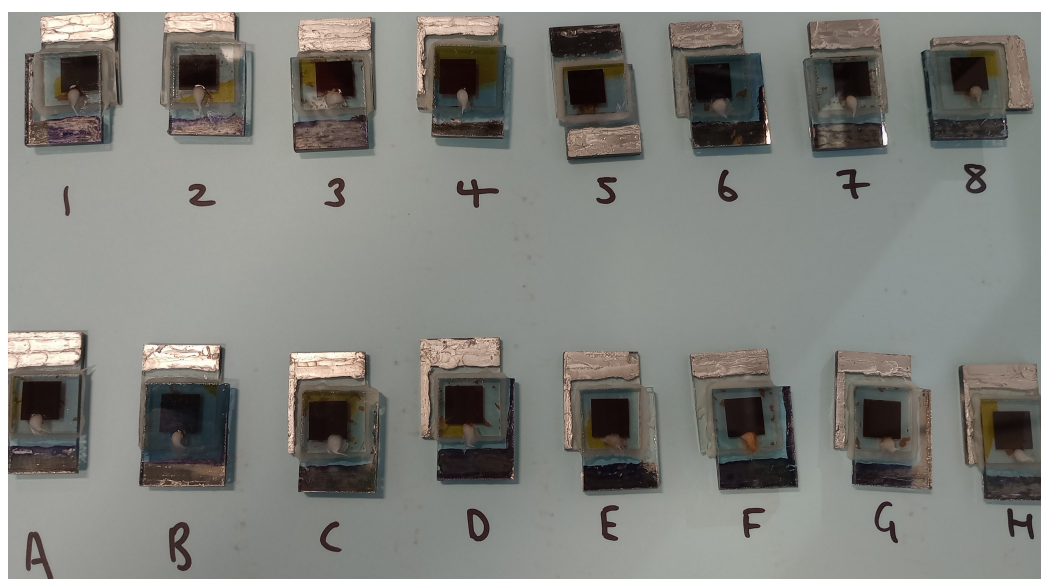
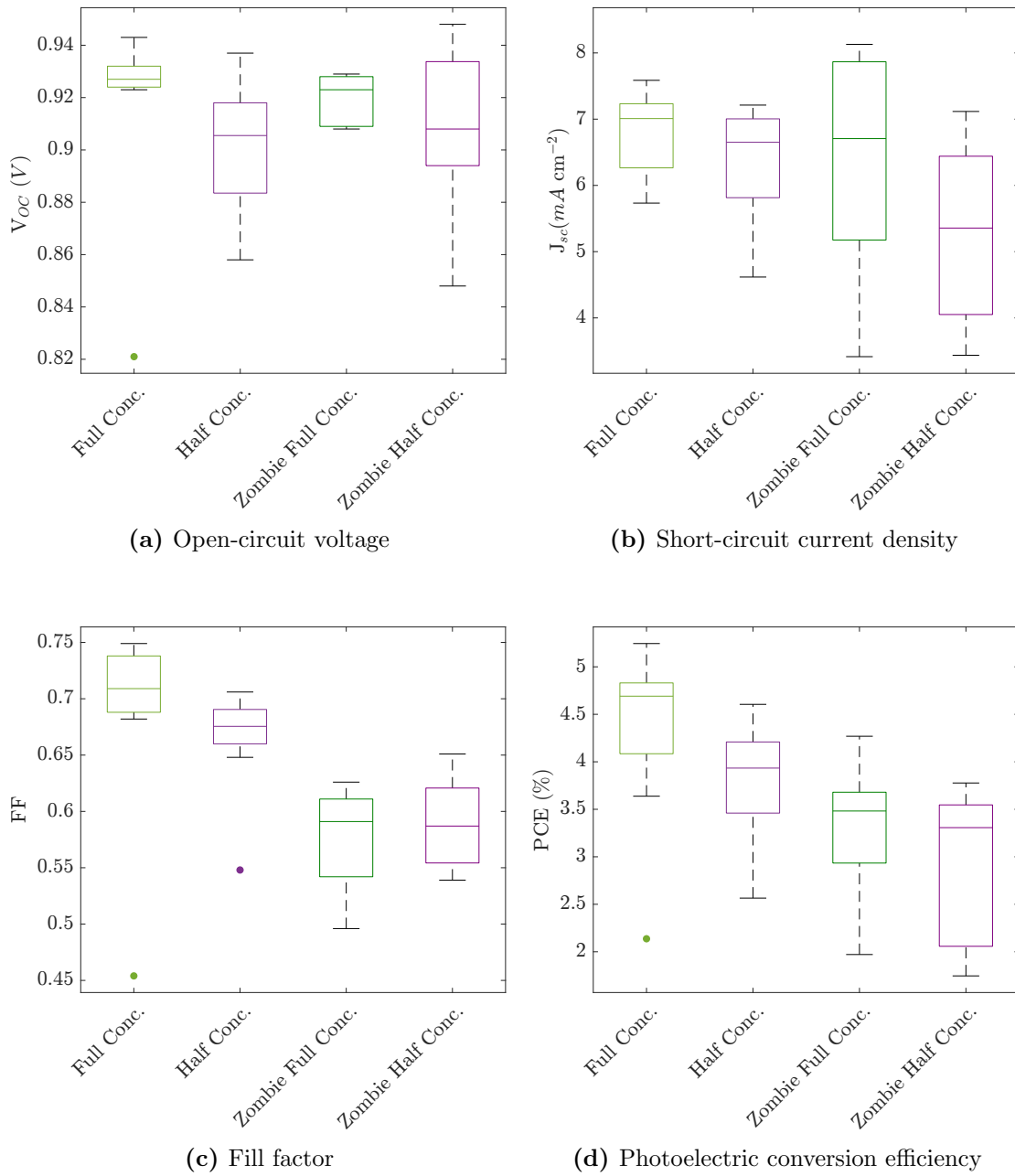


Figure 3.7: Shows that both the full concentration (numbered) and half concentration (lettered) of copper redox have dried

3.3.1.6.1 1 Sun

**Figure 3.8:** Zombie cell comparison at one sun

3.3.1.6.2 10,000 Lux

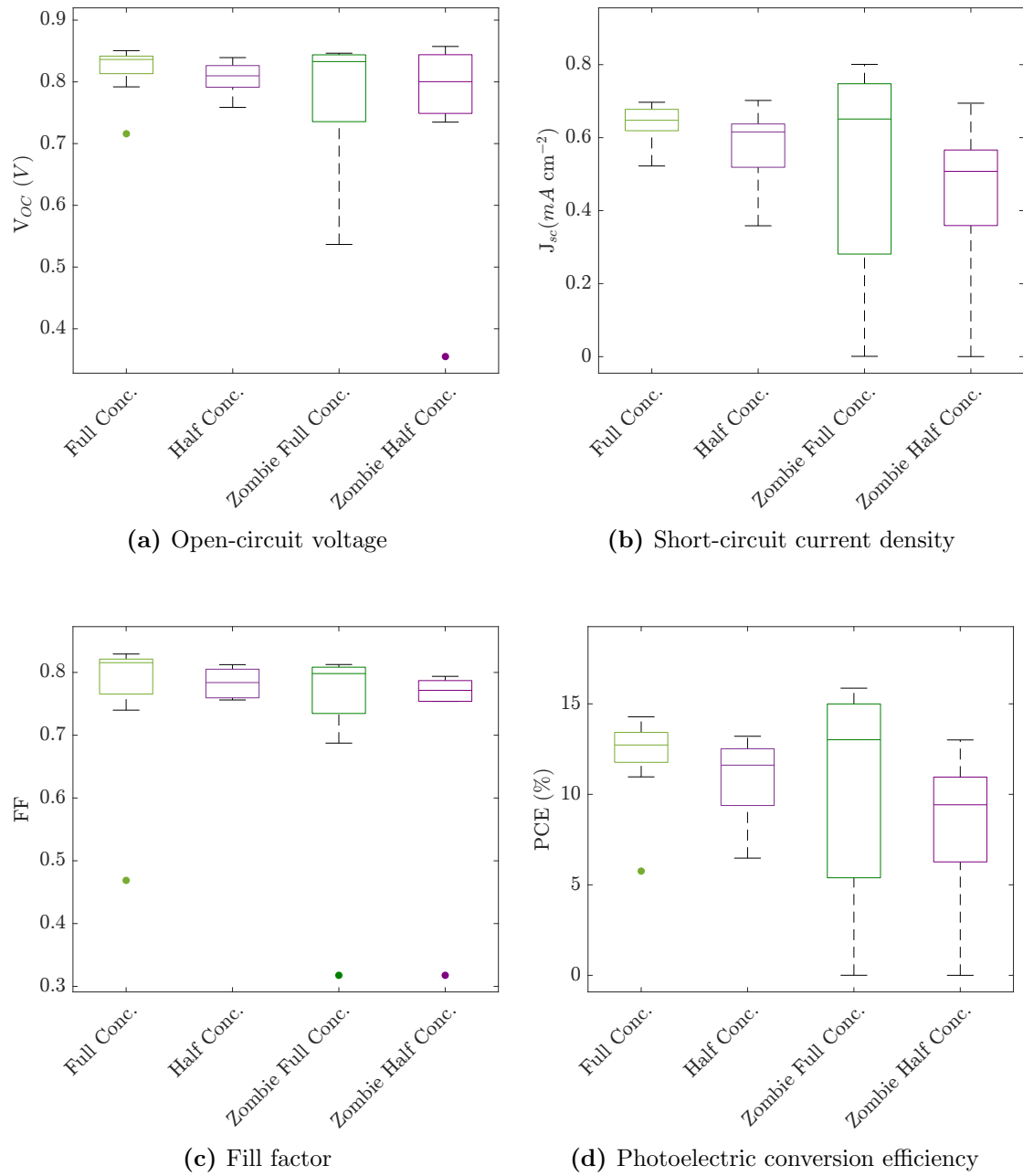
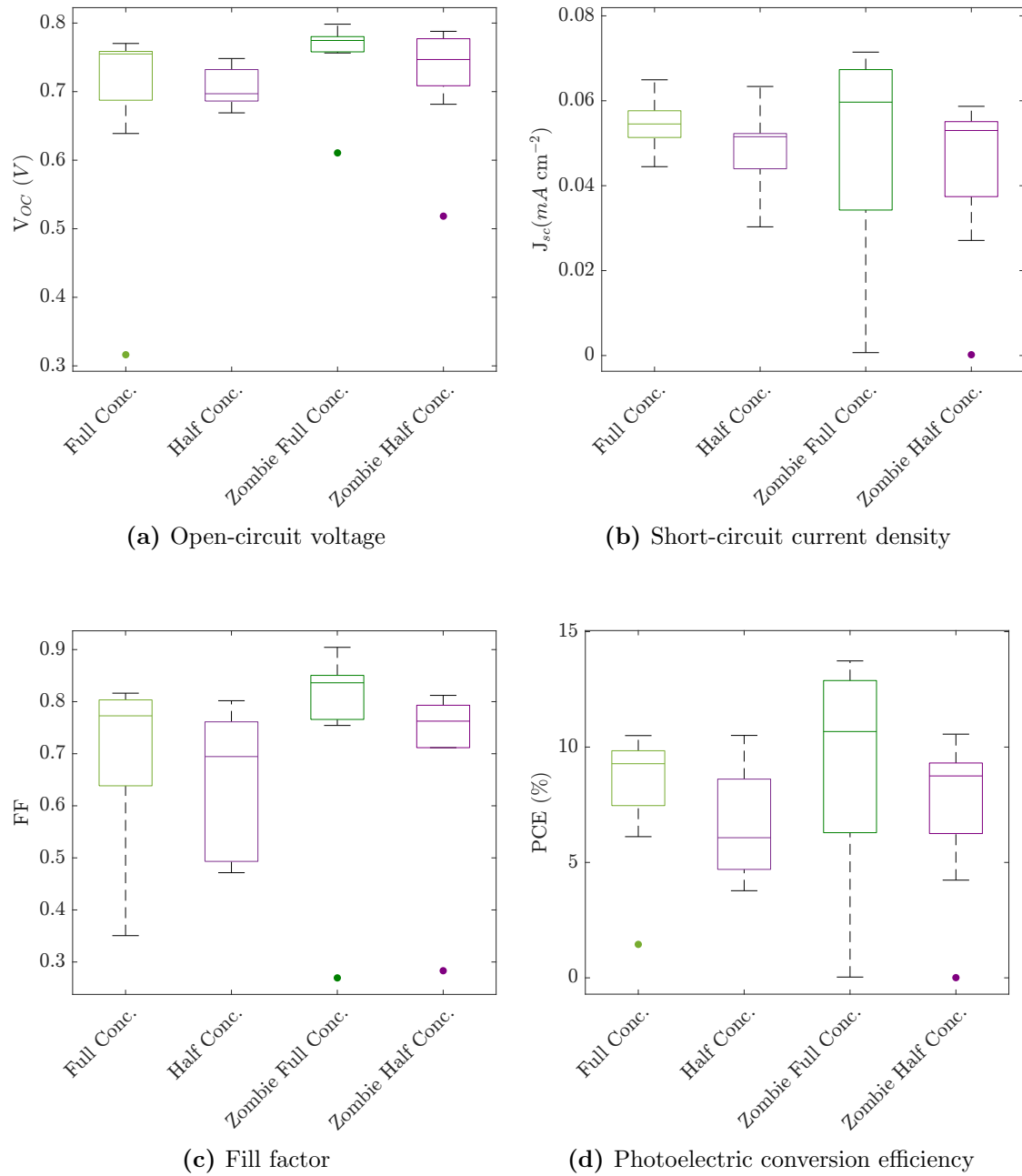
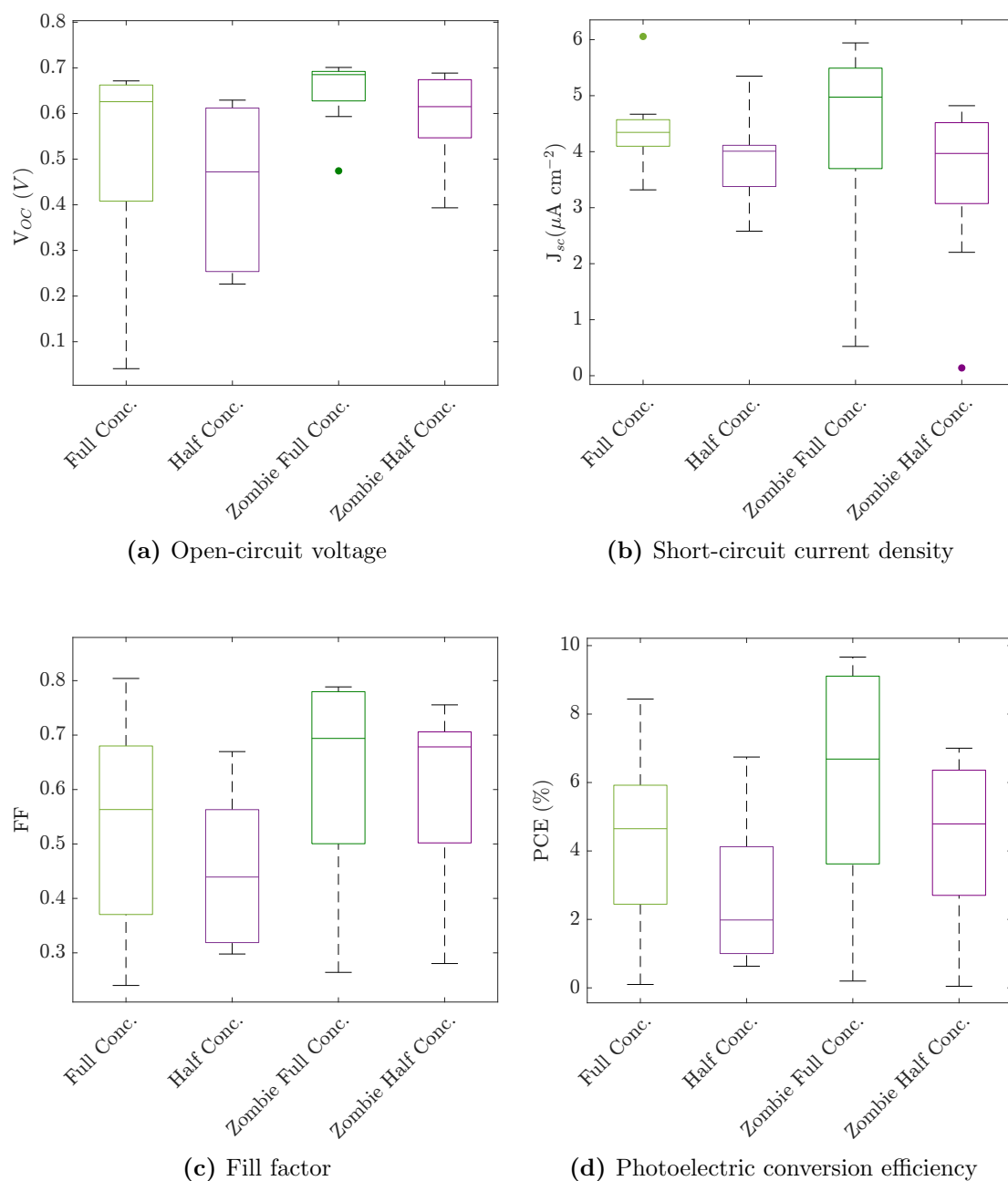


Figure 3.9: Zombie cell comparison at 10,000 Lux

3.3.1.6.3 1000 Lux

**Figure 3.10:** Zombie cell comparison at 1000 Lux

3.3.1.6.4 100 Lux

**Figure 3.11:** Zombie cell comparison at 100 Lux

The zombie cells, formed to a solid hole transport material, provides very interesting performance results. At 1 sun (in Figure 3.8), the performance of the pre-zombified cells is higher, with the FF of the zombified cells being lower. However, as the light intensity decreases, the PCE for the zombified full concentration copper redox is slightly higher at 10,000 Lux (Figure 3.9), 1,000 Lux (Figure 3.10), and at a 100 Lux (Figure 3.11). Nevertheless, the margin of error (between performing and underperforming cells) whilst producing a zombified cell does increase, shown by the larger whisker lengths. The half concentration of the copper redox also has a similar

trend when zombified but has a lower performance than the full copper concentration.

In concluding, based on the outcomes from the various measurements undertaken, the half copper concentration will not be further investigated, due to not having a substantial change in transparency, with worse performance compared to the full concentration copper. This is also the same for the I_3^-/I^- electrolyte, Z-50, performing the worst out of all types of DSSCs at low light intensities.

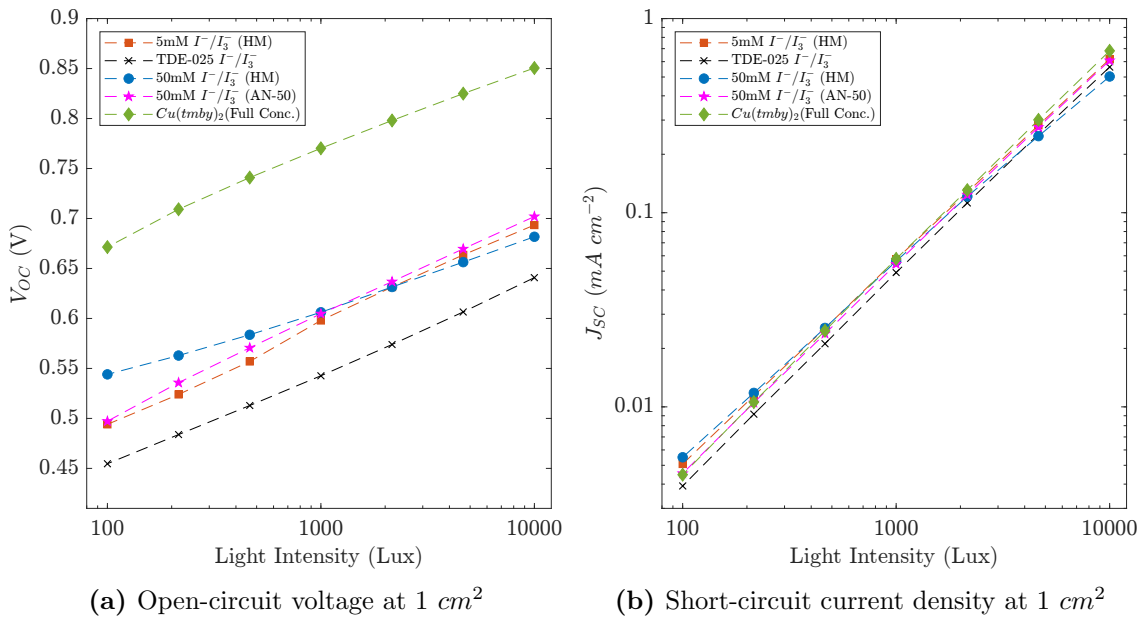
3.4 Performance of remaining DSSCs with different active area sizes

The performance of each type of DSSC is tested at various sizes, to determine a suitable size for a DSSC to integrate with an IoT node in indoor conditions. Four square-shaped, active area sizes were tested, being 1 cm^2 , 4 cm^2 , 16 cm^2 , and 64 cm^2 . Whilst 8 cells were tested and fabricated for 1 cm^2 , the best performing cells were chosen for further light intensity studies. However, due to large amount of material usage, especially the FTO substrate, the large active area cells were only fabricated once, to minimise material wastage and cost.

3.4.1 Results and discussion

3.4.1.1 Comparing different type of DSSCs at each active area size

3.4.1.1.1 1 cm^2



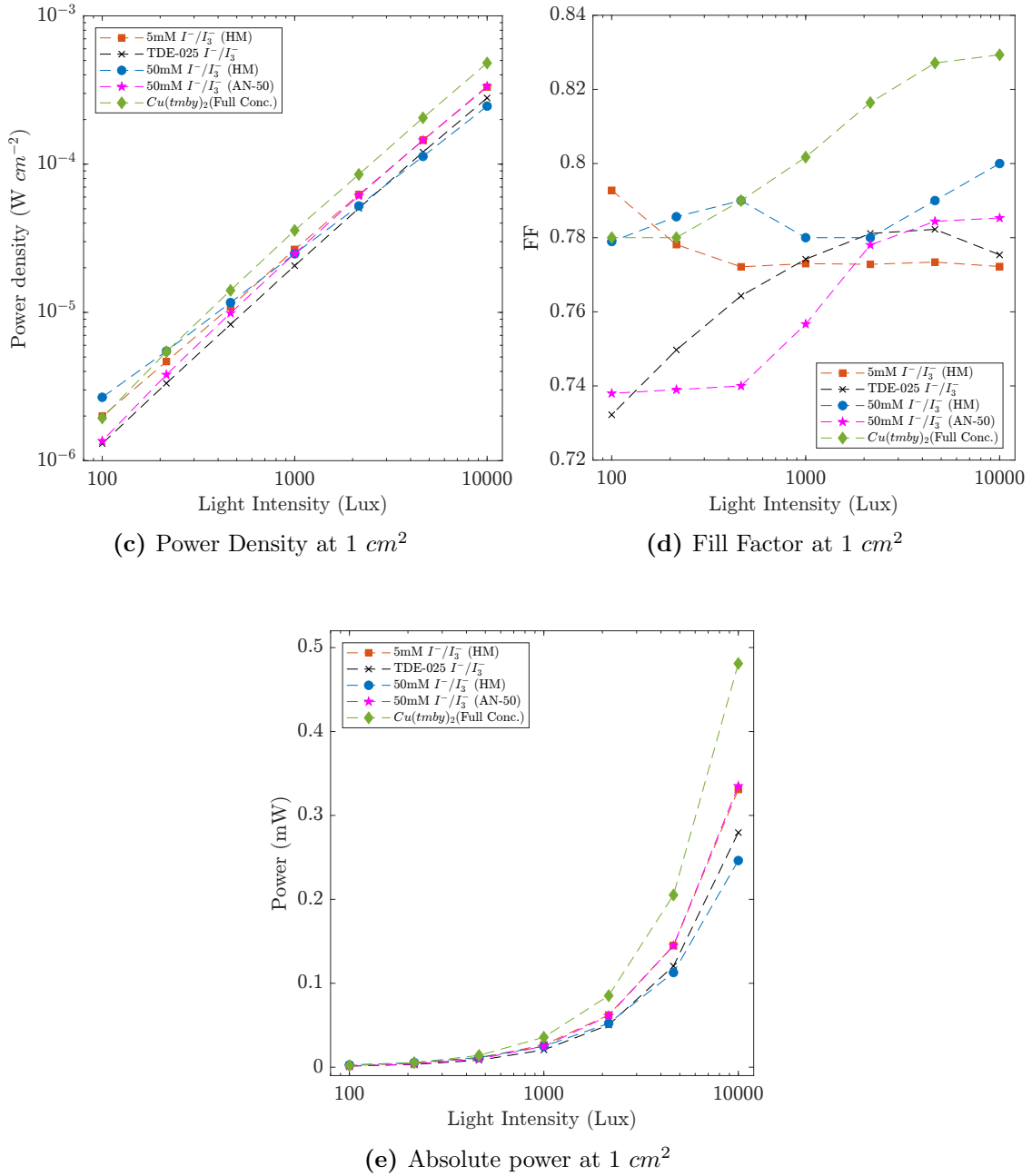
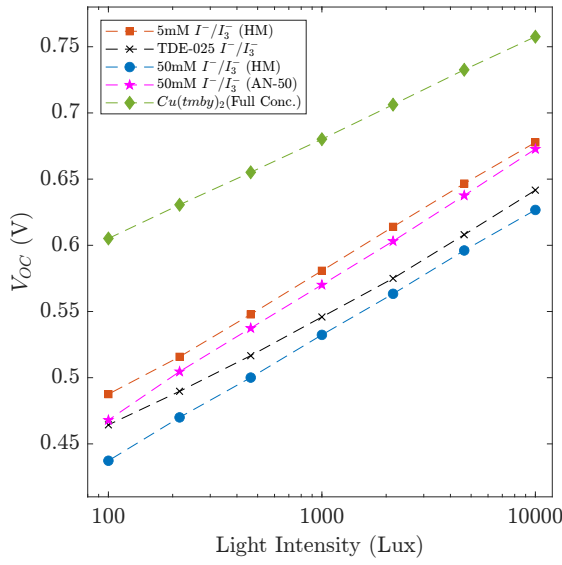
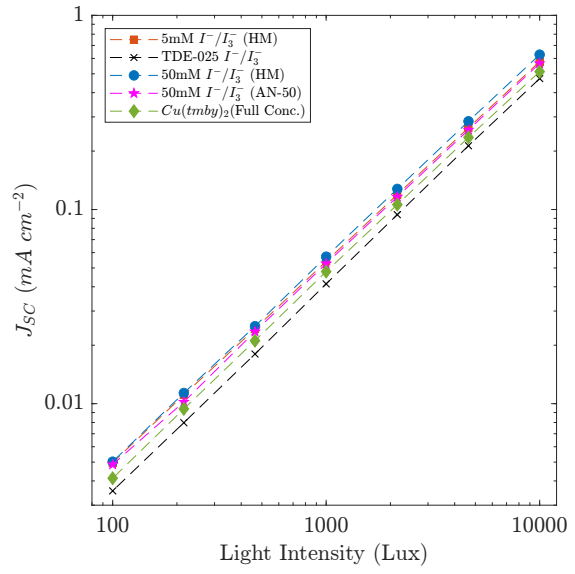
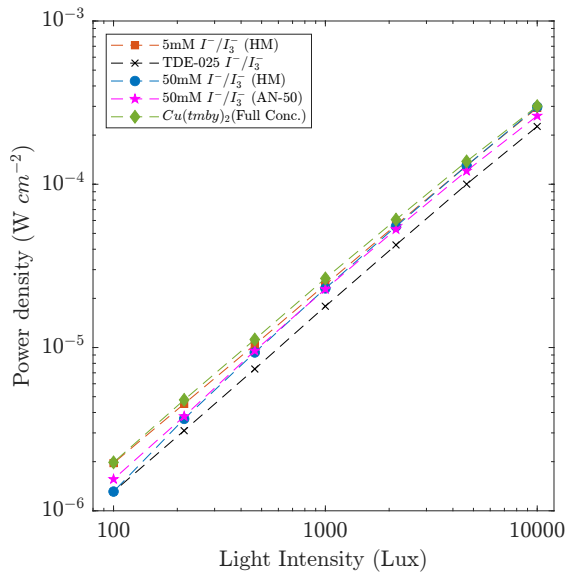
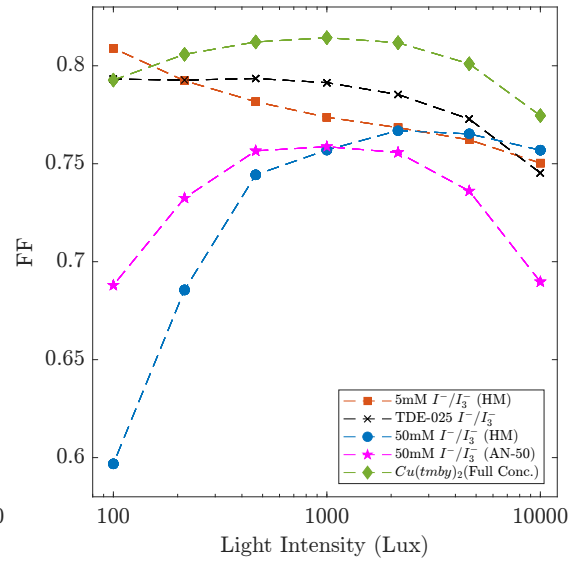
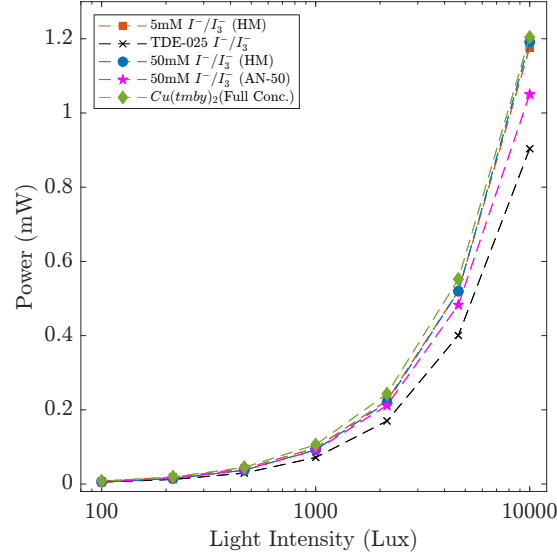


Figure 3.12: DSSC comparison at 1 cm^2

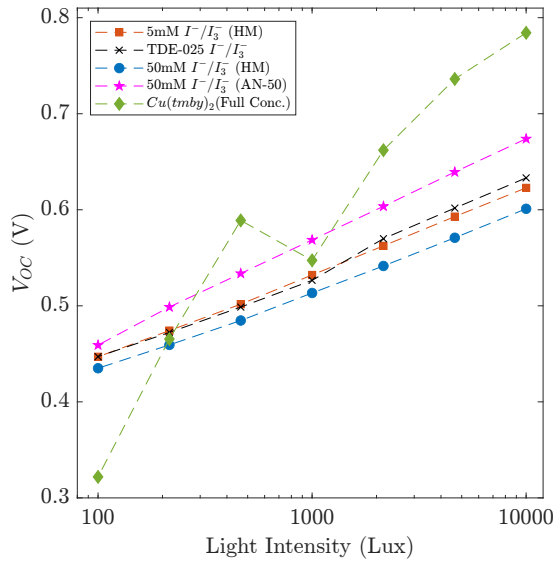
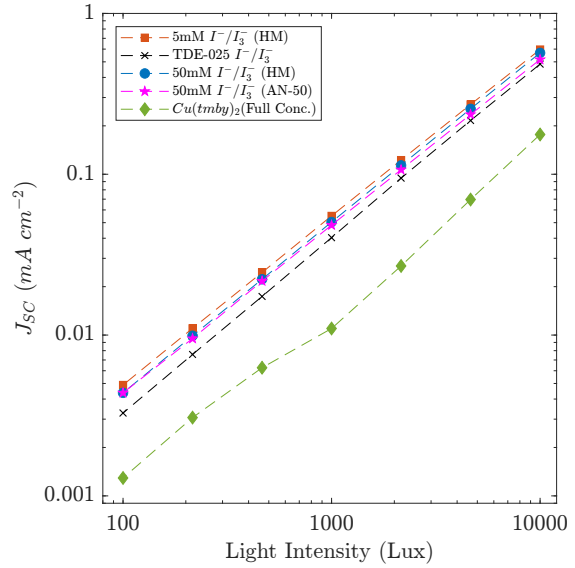
Previous results at 1 cm^2 are re-iterated in Figure 3.12, for each electrolyte type, with additional light intensities between 10,000 – 100 Lux. This concludes that the highest absolute power is outputted from the copper DSSC, due to its high V_{OC} . This observation is further reflected by the copper DSSC also having the highest power density, FF, and absolute power measurements.

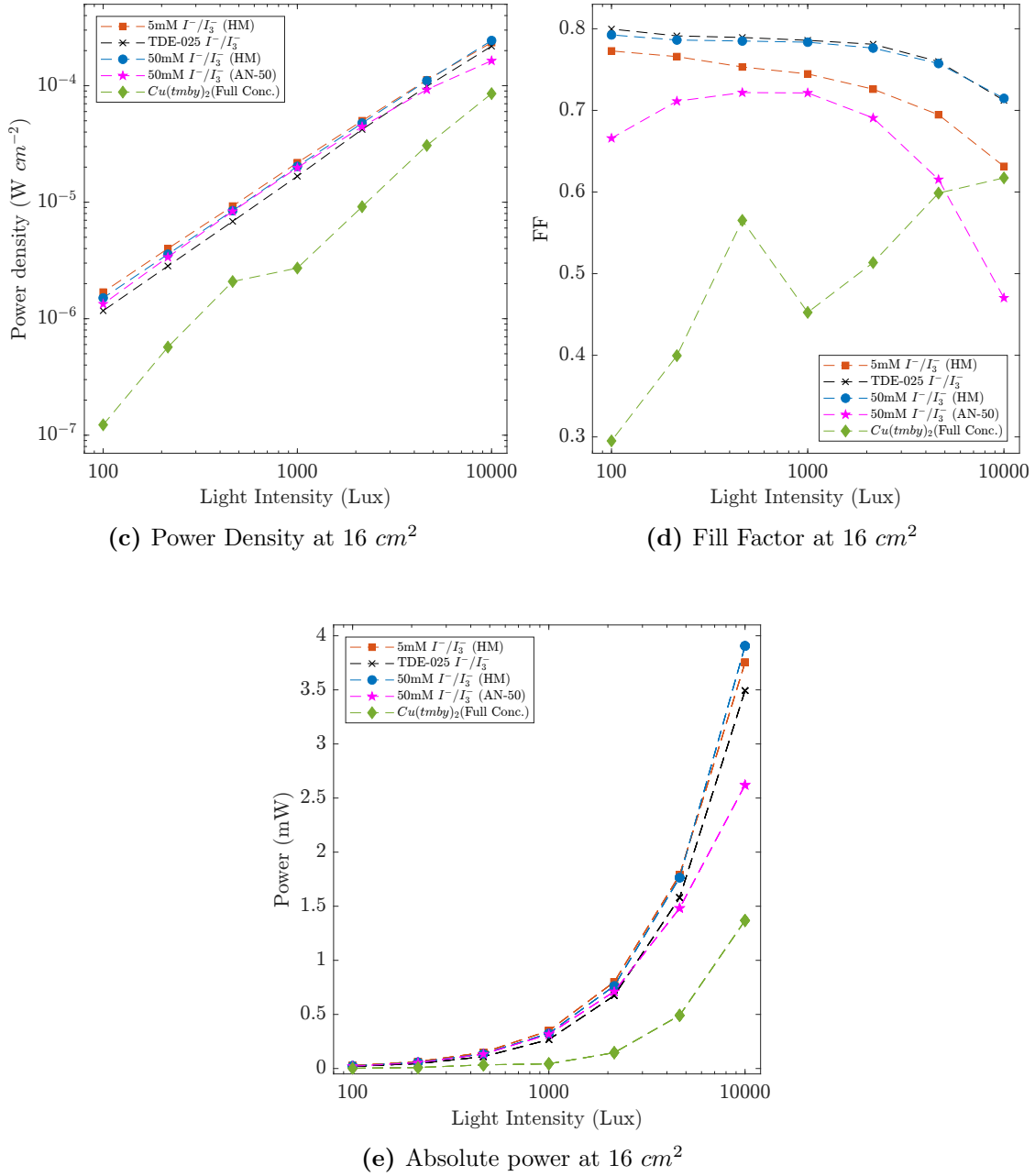
3.4.1.1.2 4 cm^2 (a) Open-circuit voltage at 4 cm^2 (b) Short-circuit current density at 4 cm^2 (c) Power Density at 4 cm^2 (d) Fill Factor at 4 cm^2

(e) Absolute power at 4 cm^2 **Figure 3.13:** DSSC comparison at 4 cm^2

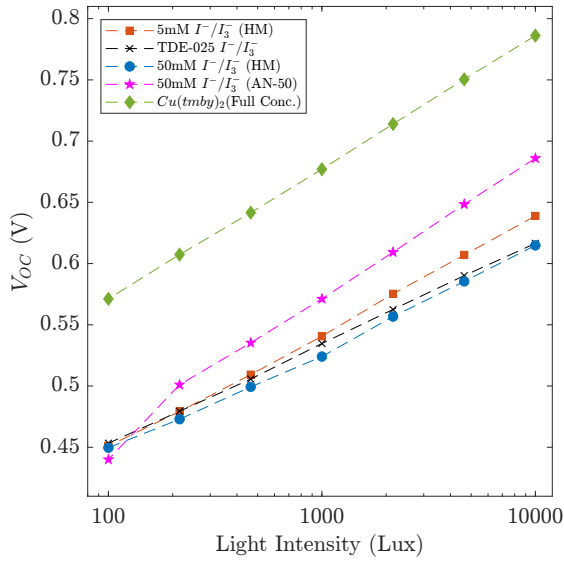
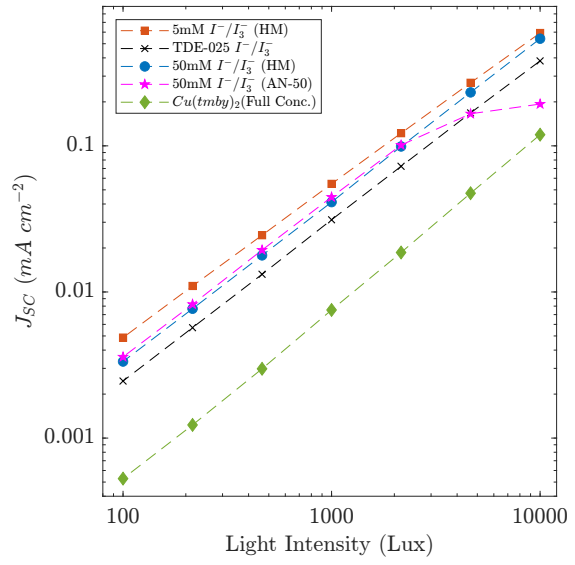
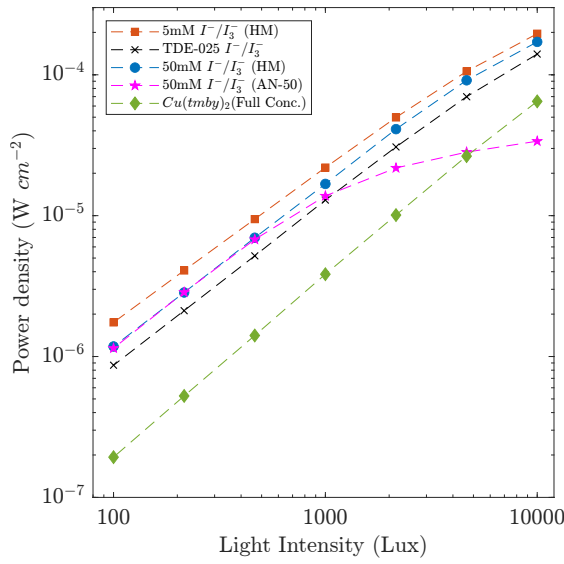
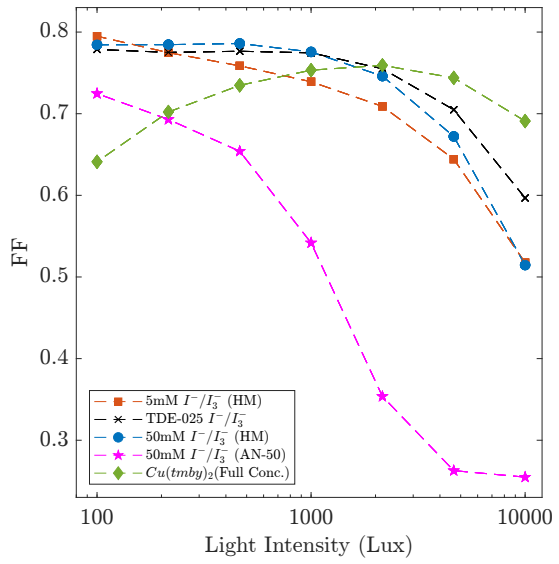
At 4 cm^2 , there is some reduced current density output (in Figure 3.13b) from the copper DSSC, resulting in the absolute power being slightly higher than the 5 mM HM and 50 mM HM DSSC.

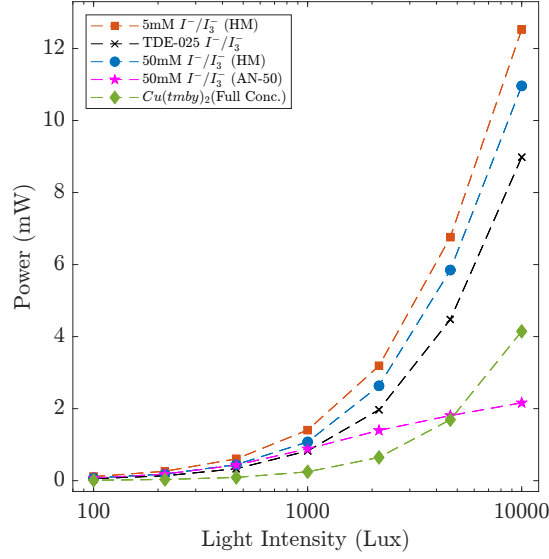
3.4.1.1.3 16 cm^2

(a) Open-circuit voltage at 16 cm^2 (b) Short-circuit current density at 16 cm^2

**Figure 3.14:** DSSC comparison at 16 cm^2

Unfortunately, at an active area of 16 cm^2 , the performance of the copper DSSC is uncharacteristically underperforming across all measurements, with a non-linear trend of the V_{OC} as the light intensity decreases. This could be due to several factors, including an uneven deposited BL or the PEDOT deposition for the CE. Both the HM triiodide electrolytes and the mosalyte TDE-025 perform well at 16 cm^2 under low light intensities, showing no additional problems with consistent FF.

3.4.1.1.4 64 cm^2 (a) Open-circuit voltage at 64 cm^2 (b) Short-circuit current density at 64 cm^2 (c) Power Density at 64 cm^2 (d) Fill Factor at 64 cm^2

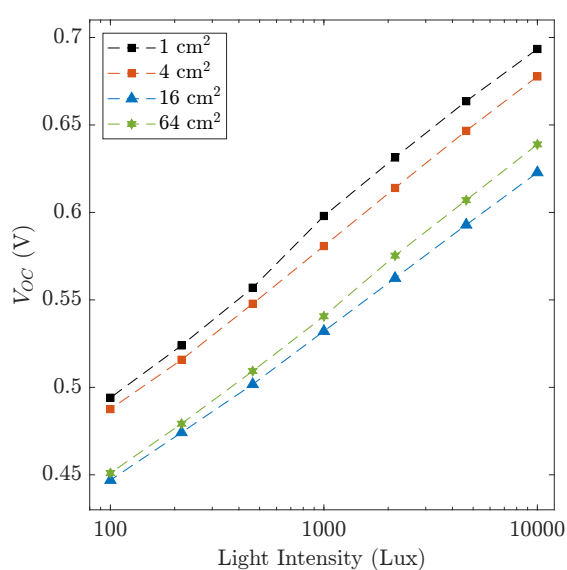
(e) Absolute power at 64 cm^2 **Figure 3.15:** DSSC comparison at 64 cm^2

At the largest active area tested, being 64 cm^2 , seen in Figure 3.15, the 5 mM HM electrolyte remarkably outperforms all other DSSC electrolyte types, with the highest power density outputs at all light intensities, and hence a higher absolute power. The 50 mM HM also performs well, with slightly lower V_{OC} and J_{SC} compared to the 5 mM HM. The J_{SC} is significantly lower for the full copper DSSC, resulting in a lower power output.

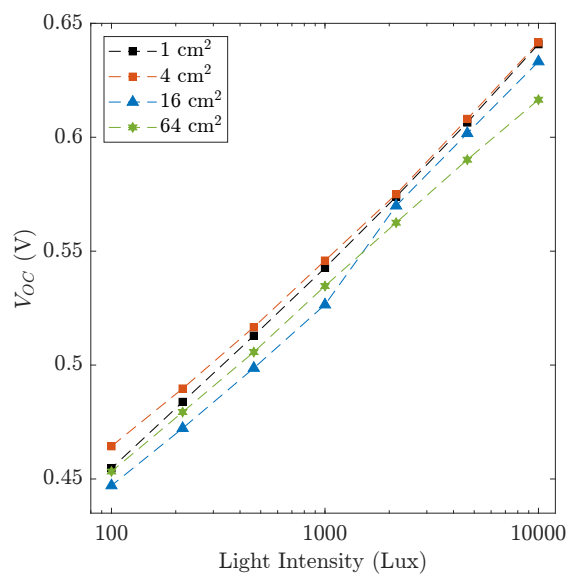
3.4.1.2 Comparing different active area sizes for each DSSC composition

This Section concentrates at each composition individually for every size tested. This allows analysis on the trend when increasing the active area size.

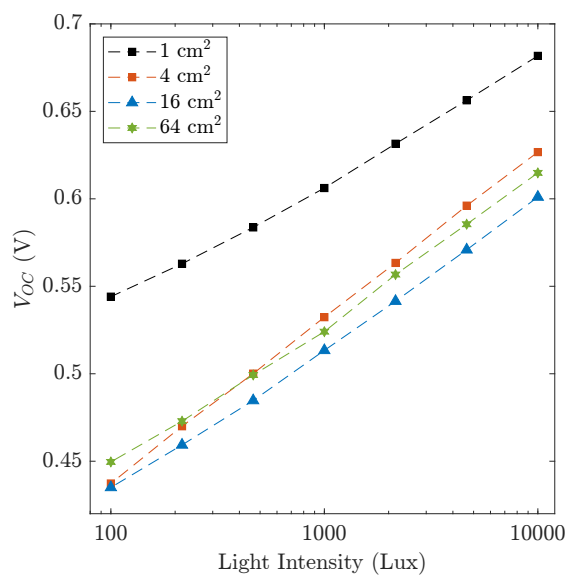
3.4.1.2.1 Open-circuit voltage (V_{OC})



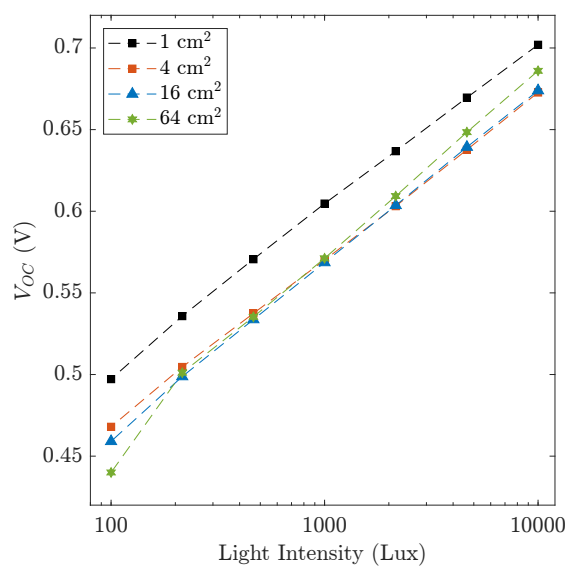
(a) 5 mM I^-/I_3^- (HM)



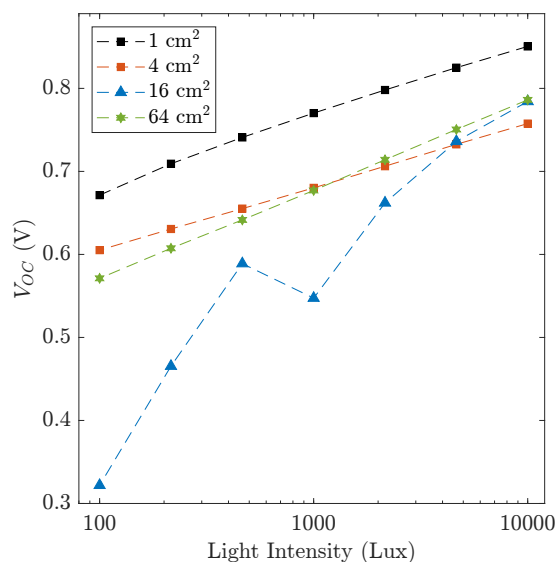
(b) TDE-025 I^-/I_3^-



(c) 50 mM I^-/I_3^- (HM)

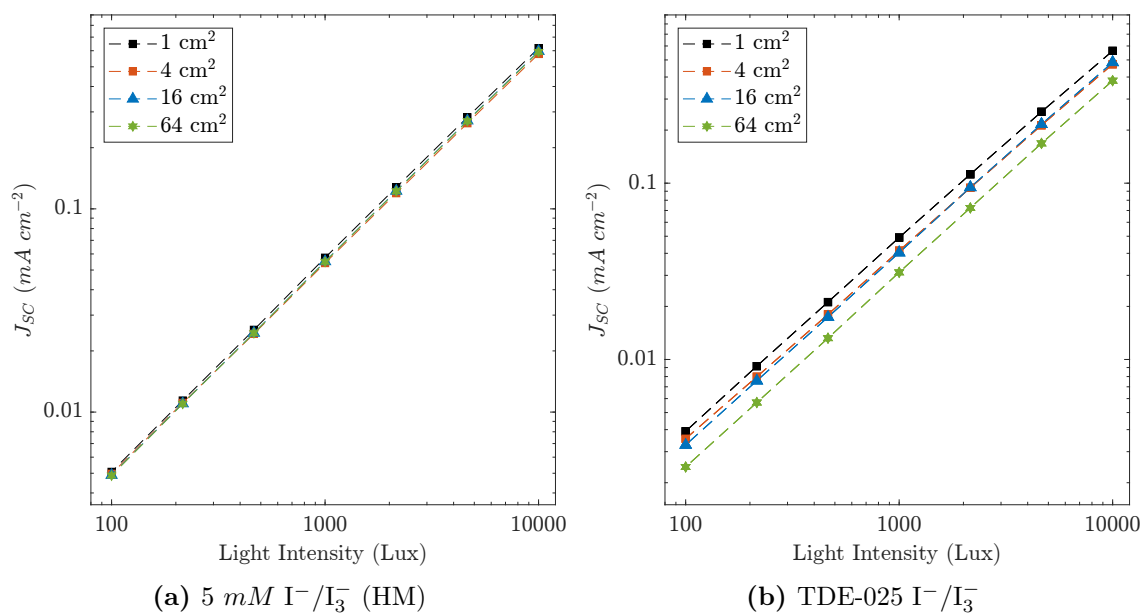


(d) 50 mM I^-/I_3^- (AN-50)

(e) Cu(tumby)₂ (Full Conc.)**Figure 3.16:** Open-circuit voltage at different active area sizes

The V_{OC} behaviour for each type of cell, seen in Figure 3.16, has a slight variation between each active area size, with the V_{OC} being marginally higher at a smaller active area size. Disregarding the 16 cm² copper DSSC (in Figure 3.16e), there is no obvious change in slope of V_{OC} to intensity relationship, meaning that there is a consistent recombination behaviour. It is seen that scaling up area doesn't have much impact on the V_{OC} , as series resistance doesn't impact on open-circuit voltage.

3.4.1.2.2 Short-circuit current density (J_{SC})

(a) 5 mM I⁻/I₃⁻ (HM)(b) TDE-025 I⁻/I₃⁻

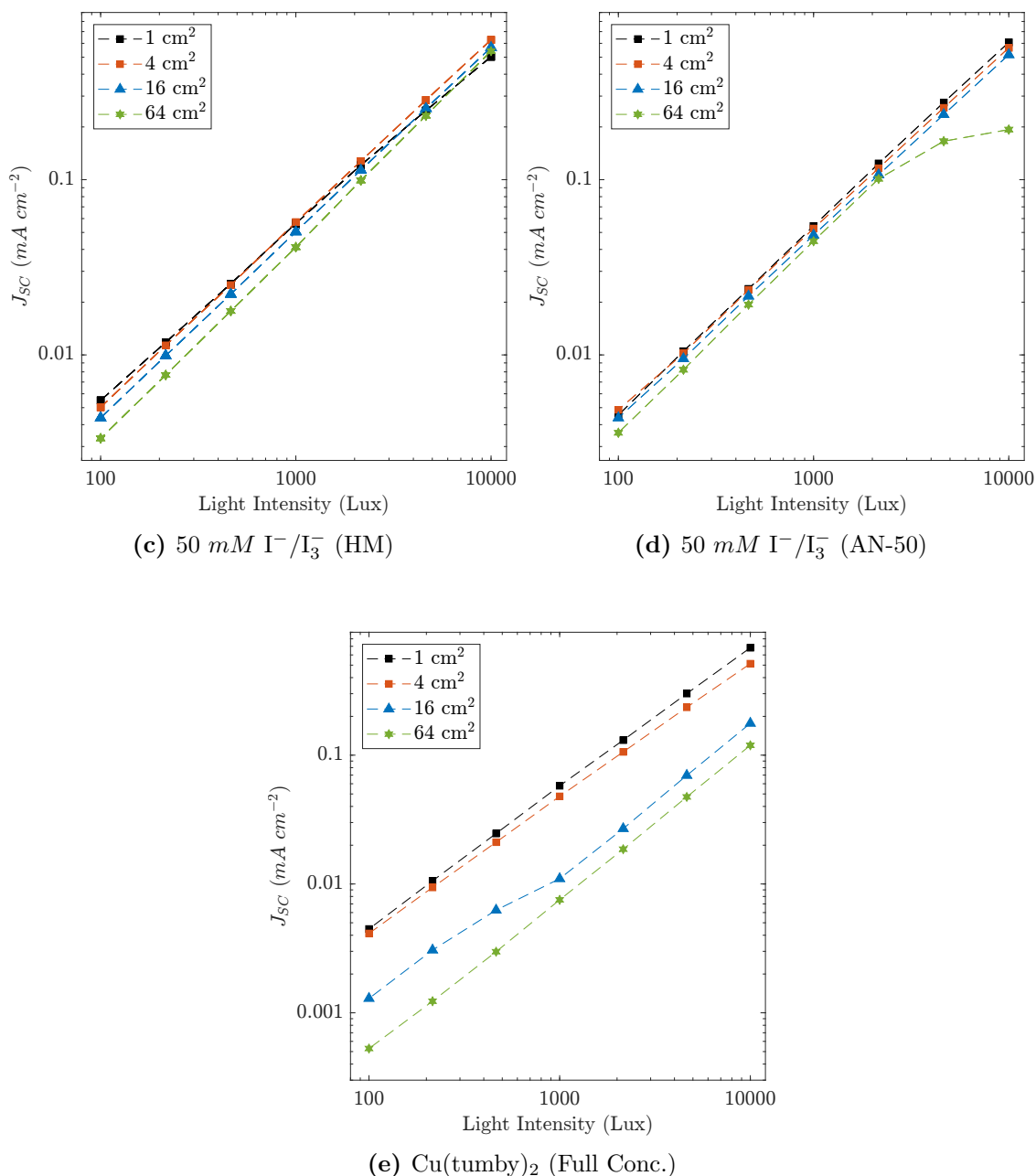
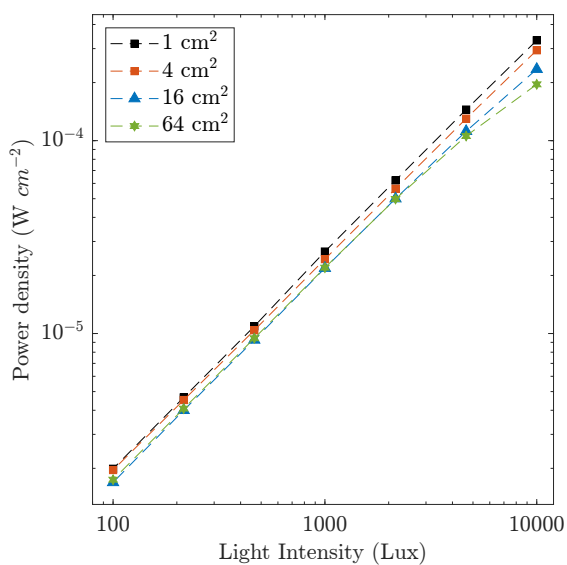
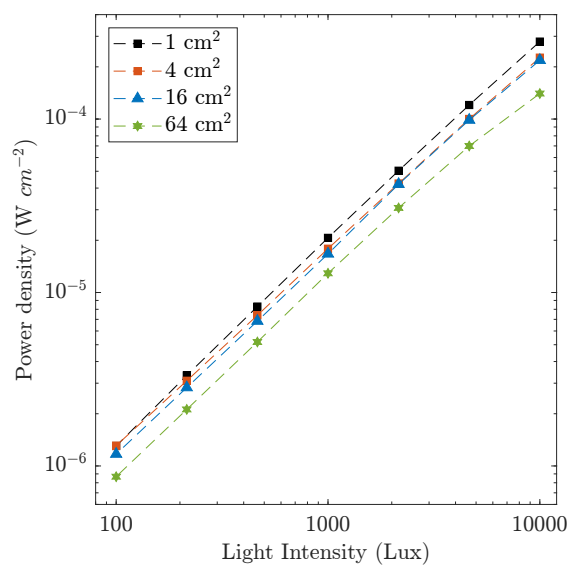
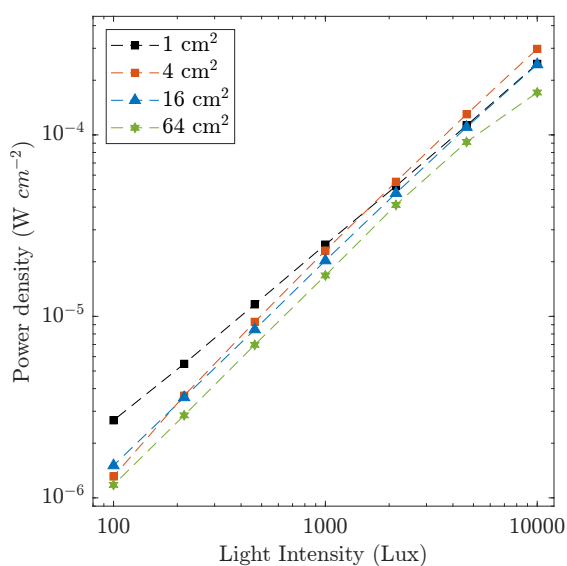
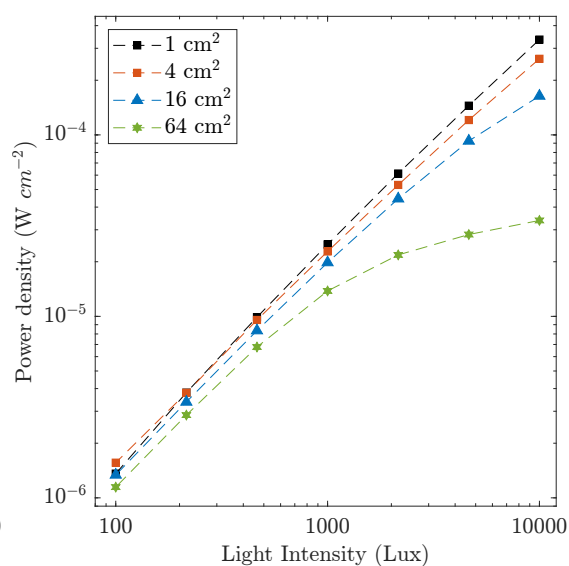
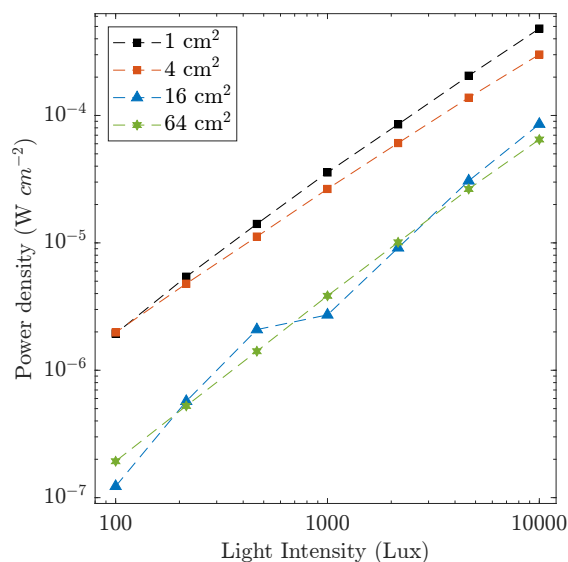


Figure 3.17: Short-circuit current density at different active area sizes

The short-circuit current density plots (Figure 3.17) are also generally linearly well behaved for each type of electrolyte. For AN-50 (Figure 3.17d), series resistance begins to limit the J_{SC} for the largest cell at higher light intensities. The J_{SC} is considerably lower for copper DSSC for the largest cell size, compared to the smaller cells. This might be due to high quantity of parasitic resistances affecting the larger cell.

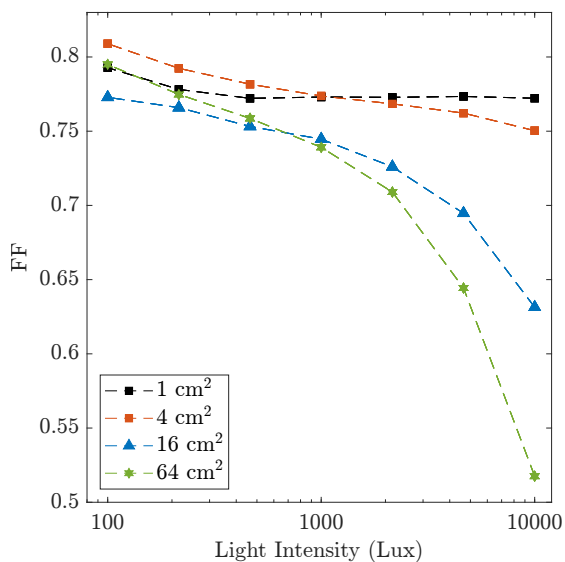
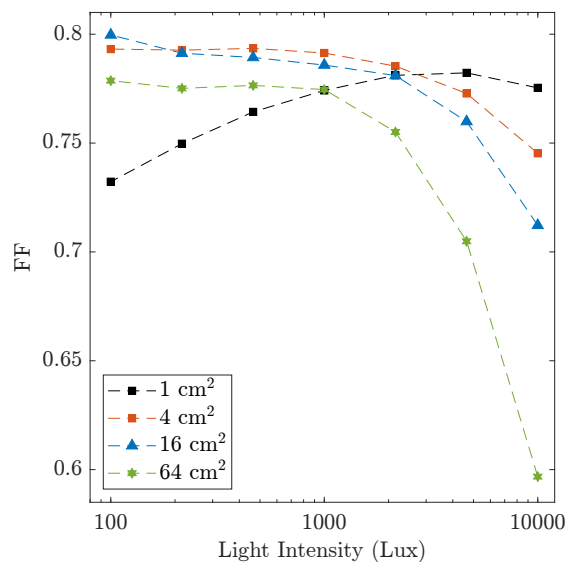
3.4.1.2.3 Power density

(a) 5 mM I^-/I_3^- (HM)(b) TDE-025 I^-/I_3^- (c) 50 mM I^-/I_3^- (HM)(d) 50 mM I^-/I_3^- (AN-50)

(e) $\text{Cu}(\text{tumbly})_2$ (Full Conc.)**Figure 3.18:** Power density at different active area sizes

The power density plots (Figure 3.18) provide similar results, with AN-50 having a limited power density at higher light intensities for larger cells, and copper having a significant power density decrease at the largest cell size.

3.4.1.2.4 Fill Factor (FF)

(a) $5 \text{ mM } \text{I}^-/\text{I}_3^-$ (HM)(b) TDE-025 I^-/I_3^-

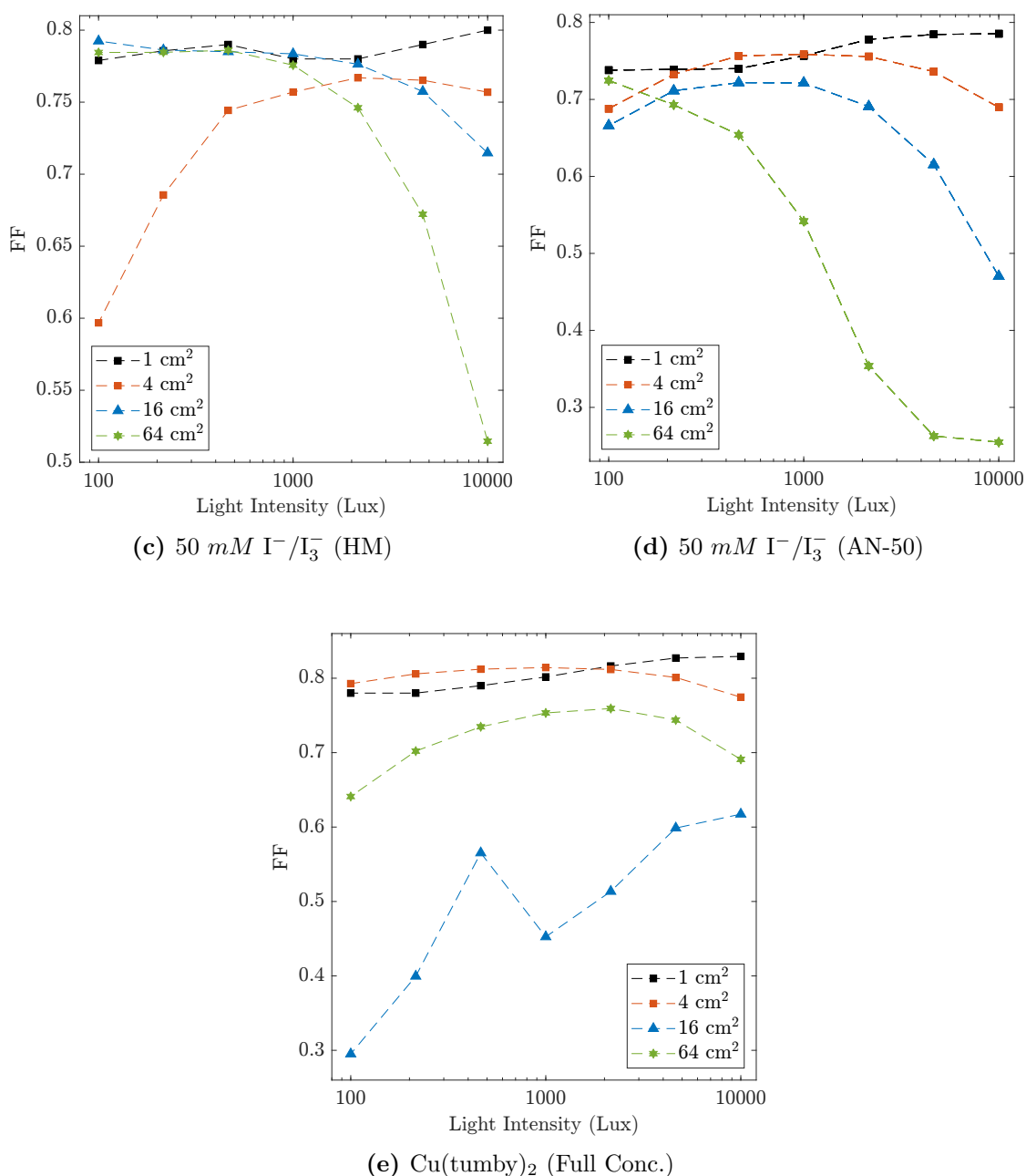
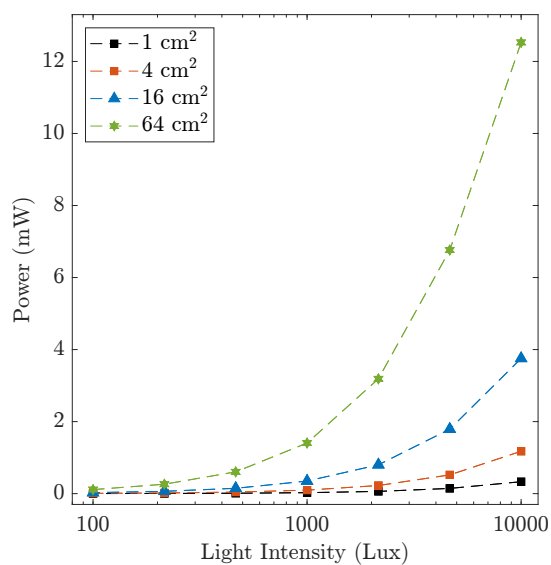


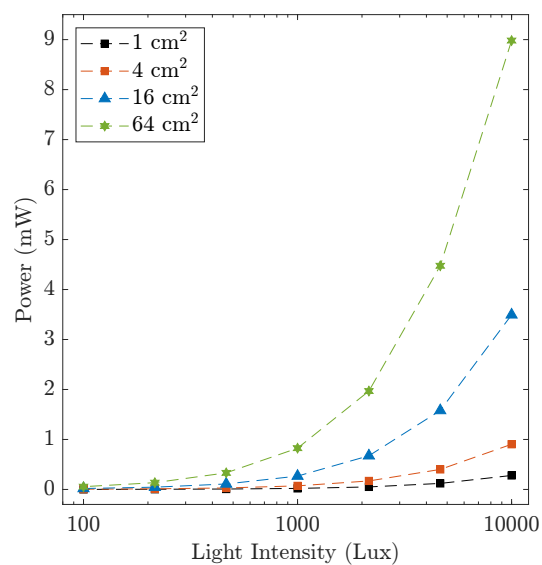
Figure 3.19: Fill factor at different active area sizes

Figure 3.19 provides the fill factor results. At higher intensities, the series resistance limits the FF, being significant for larger cells for all types of DSSC. At low light conditions, the FF is consistent for the 5 mM HM, TDE-025, 50 mM HM and AN-50. The two smallest areas (1 and 4 cm²) of the copper DSSC are providing consistent FF at low intensities; however, the largest cell (64 cm²) shows some decrease in FF, due to shunt resistant losses. This is also like the 4 cm² 50 mM HM DSSC. However, with consistent FF following larger cells, this is most likely due to a fabrication error, with potentially applying an uneven layer of BL.

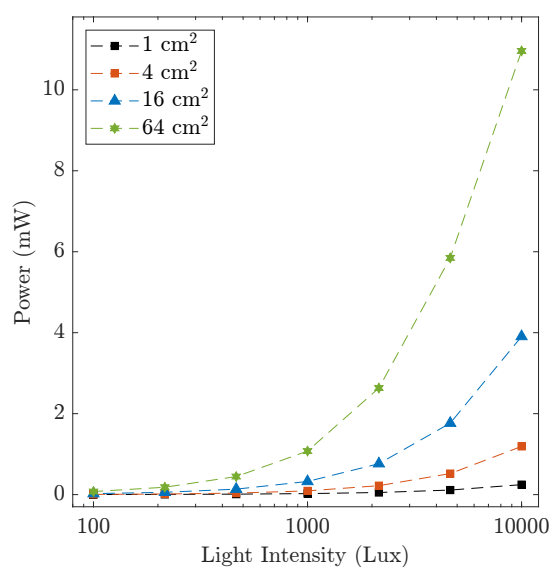
3.4.1.2.5 Absolute power



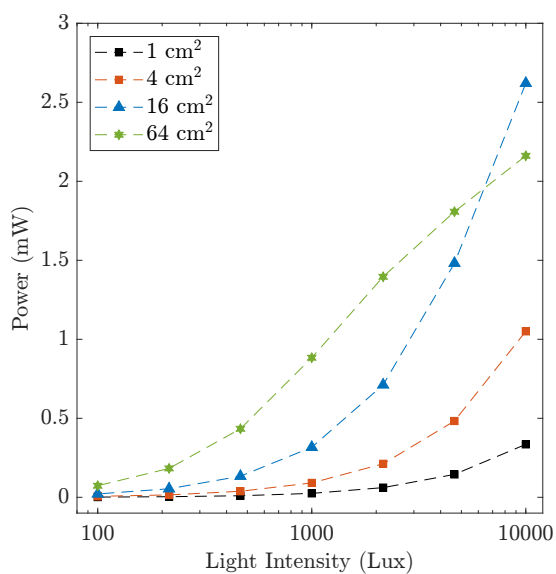
(a) 5mM I^-/I_3^- (HM)



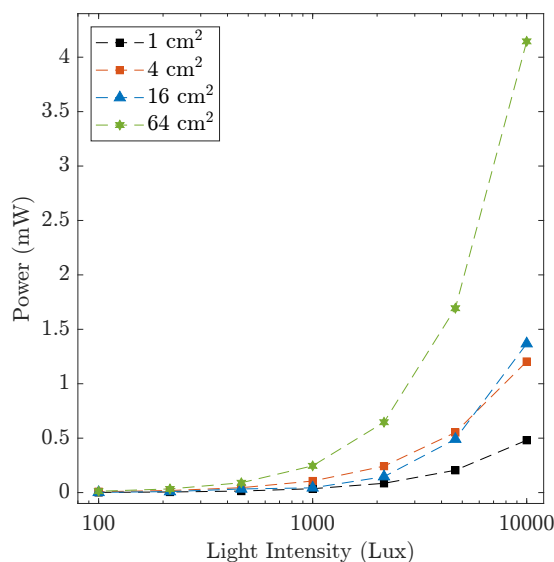
(b) TDE-025 I^-/I_3^-



(c) 50 mM I^-/I_3^- (HM)



(d) 50 mM I^-/I_3^- (AN-50)

(e) $\text{Cu}(\text{tumbly})_2$ (Full Conc.)**Figure 3.20:** Absolute Power at different active area sizes

Overall, despite the small drop in power density with an increase in size, the largest cells produce more power, with the 5 *mM* HM achieving the highest power output. Above 5000 Lux, the impact of the significant FF losses for the AN-50 64 cm^2 cell means it produces less power than the 16 cm^2 cell.

3.5 Conclusion

Table 3.1 below summarises the advantages and disadvantages of each electrolyte type tested throughout this Chapter.

The Chapter explores different electrolytes and DSSC fabrications to find the most appropriate type for indoor conditions, suitable for display integration behind the energy harvester. In doing so, this conclusion will review the outcomes against the two research questions as initially presented in Section 3.1.3. The research questions are as follows:

1. What type of transparent monolithic DSSC is best for indoor conditions, being feasibly assembled and suitable for integration with a display behind that leads to a balance of a good indoor power harvester and a visually appealing UI?
2. What is the best maximum/ optimal active area size, and type of monolithic DSSC in low light intensity conditions?

The results initially investigated 1 cm^2 DSSCs, with different I_3^-/I^- and copper concentrations. This concluded with promising PCE outputs for the full concentration copper redox, at low light levels. The transparent zombified transitions of these

Table 3.1: Advantages and disadvantages of each electrolyte tested

Electrolyte type	Advantages	Disadvantages
5mM (HM) (I_3^-/I^-)	Highest transmittance throughout each wavelength.	V_{OC} output and overall efficiency is lower at 1 cm^2 compared to Cu(tmby)_2 .
	Outperforms other electrolyte types within large active area sizes (64 cm^2).	
Mosalyte TDE-025 (I_3^-/I^-)	Good transmittance.	Poor performance at 1 sun.
	Non-volatile electrolyte.	Average performance withing larger monolithic cells.
50mM (HM) (I_3^-/I^-)	Good performance in larger monolithic cells.	Less transparent compared to mosalyte and 5mM.
50mM (Z-50) (I_3^-/I^-)	Semi-transparent electrolyte.	Poor performance at low light intensities (1 cm^2 cells)
50mM (AN-50) (I_3^-/I^-)	Good performance at low light intensities (1 cm^2).	Similar transparency to 50mM (HM) electrolyte.
		Poor performance in larger monolithic cells.
Cu(tmby)_2 (Full & half Conc.)	Outperformed other electrolyte types for 1 cm^2 active area size at 1 sun and low light intensities.	Poor performance in larger monolithic cells.
	Has good opportunities for ‘zombie cells’ transition.	Worst transmittance throughout each wavelength.

cells also showed encouraging result, which has a great advantage compared to liquid electrolytes, suffering from liquid evaporation, or leaking from the DSSC, which can drastically lower the performance over time. The downfall for the copper redox however, was its low transmittance levels, compared to the I_3^-/I^- electrolytes, especially the 5 mM HM (having low iodine levels). The results also show that lower iodine concentration performs well under low light conditions, which is in good agreement with the literature sources, mentioned in Section 3.1.2.1.2.

Additional experiments were conducted on increasing the active area size of the DSSC, under indoor lighting conditions. The results exhibited remarkable performance from the 5 mM HM electrolyte at 64 cm^2 DSSC, outperforming every other electrolyte tested.

In conclusion, whilst the opaque copper redox showed promising results under low light conditions, the transparent monolithic type does not achieve as high of a result when the active area is increased in comparison to the ‘common’ I_3^-/I^- electrolyte. This could be down to the complicated fabrication methods for assembling the copper DSSC, such as electropolymerization to form the PEDOT layer for the CE. The sealing using the UV curing glue could also have impacted on the performance of the cell. Nevertheless, the 5 mM HM electrolyte proved to be the superior electrolyte

type, achieving good transmission and performance in indoor conditions, suitable for indoor IoT node integration.

Bibliography

1. Dix A, Finlay J, Abowd GD, and Beale R. Human-computer interaction. Pearson Education, 2004
2. Karray F, Alemzadeh M, Abou Saleh J, and Arab MN. Human-computer interaction: Overview on state of the art. International journal on smart sensing and intelligent systems 2017; 1
3. Stone D, Jarrett C, Woodroffe M, and Minocha S. User interface design and evaluation. Elsevier, 2005 :273–4
4. Bissoli A, Lavino-Junior D, Sime M, Encarnação L, and Bastos-Filho T. A Human–Machine Interface Based on Eye Tracking for Controlling and Monitoring a Smart Home Using the Internet of Things. Sensors 2019; 19. DOI: 10.3390/s19040859. Available from: <https://www.mdpi.com/1424-8220/19/4/859>
5. Freitag M, Teuscher J, Saygili Y, Zhang X, Giordano F, Liska P, Hua J, Zakeeruddin SM, Moser JE, Grätzel M, et al. Dye-sensitized solar cells for efficient power generation under ambient lighting. Nature Photonics 2017; 11:372
6. Cao Y, Liu Y, Zakeeruddin SM, Hagfeldt A, and Grätzel M. Direct contact of selective charge extraction layers enables high-efficiency molecular photovoltaics. Joule 2018; 2:1108–17
7. Michaels H, Rinderle M, Freitag R, Benesperi I, Edvinsson T, Socher R, Gagliardi A, and Freitag M. Dye-sensitized solar cells under ambient light powering machine learning: towards autonomous smart sensors for the internet of things. Chem. Sci. 2020; 11:2895–906. DOI: 10.1039/C9SC06145B. Available from: <http://dx.doi.org/10.1039/C9SC06145B>
8. Zhang D, Stojanovic M, Ren Y, Cao Y, Eickemeyer FT, Socie E, Vlachopoulos N, Moser JE, Zakeeruddin SM, Hagfeldt A, et al. A molecular photosensitizer achieves a Voc of 1.24 V enabling highly efficient and stable dye-sensitized solar cells with copper (II/I)-based electrolyte. Nature communications 2021; 12:1–10

9. Selvaraj P, Baig H, Mallick TK, Siviter J, Montecucco A, Li W, Paul M, Sweet T, Gao M, Knox AR, and Sundaram S. Enhancing the efficiency of transparent dye-sensitized solar cells using concentrated light. *Solar Energy Materials and Solar Cells* 2018; 175:29–34. DOI: <https://doi.org/10.1016/j.solmat.2017.10.006>. Available from: <https://www.sciencedirect.com/science/article/pii/S0927024817305548>
10. Yoon S, Tak S, Kim J, Jun Y, Kang K, and Park J. Application of transparent dye-sensitized solar cells to building integrated photovoltaic systems. *Building and Environment* 2011; 46:1899–904. DOI: <https://doi.org/10.1016/j.buildenv.2011.03.010>. Available from: <https://www.sciencedirect.com/science/article/pii/S0360132311000886>
11. Zhang K, Qin C, Yang X, Islam A, Zhang S, Chen H, and Han L. High-performance, transparent, dye-sensitized solar cells for see-through photovoltaic windows. *Advanced energy materials* 2014; 4:1301966
12. Chalkias DA, Charalampopoulos C, Andreopoulou AK, Karavioti A, and Stathatos E. Spectral engineering of semi-transparent dye-sensitized solar cells using new triphenylamine-based dyes and an iodine-free electrolyte for greenhouse-oriented applications. *Journal of Power Sources* 2021; 496:229842. DOI: <https://doi.org/10.1016/j.jpowsour.2021.229842>. Available from: <https://www.sciencedirect.com/science/article/pii/S0378775321003815>
13. Grifoni F, Bonomo M, Naim W, Barbero N, Alnasser T, Dzeba I, Giordano M, Tsaturyan A, Urbani M, Torres T, et al. Toward Sustainable, Colorless, and Transparent Photovoltaics: State of the Art and Perspectives for the Development of Selective Near-Infrared Dye-Sensitized Solar Cells. *Advanced Energy Materials* 2021; 11:2101598
14. Roy P, Vats AK, Tang L, and Pandey SS. Implication of color of sensitizing dyes on transparency and efficiency of transparent dye-sensitized solar cells. *Solar Energy* 2021; 225:950–60. DOI: <https://doi.org/10.1016/j.solener.2021.08.014>. Available from: <https://www.sciencedirect.com/science/article/pii/S0038092X21006691>
15. Yu Z, Gorlov M, Nissfolk J, Boschloo G, and Kloo L. Investigation of iodine concentration effects in electrolytes for dye-sensitized solar cells. *Journal of Physical Chemistry C* 2010 Jun; 114:10612–20. DOI: 10.1021/JP1001918/SUPPL_FILE/JP1001918_SI_001.PDF. Available from: <https://pubs.acs.org/doi/full/10.1021/jp1001918>

16. De Rossi F, Pontecorvo T, and Brown TM. Characterization of photovoltaic devices for indoor light harvesting and customization of flexible dye solar cells to deliver superior efficiency under artificial lighting. *Applied Energy* 2015 Oct; 156:413–22. DOI: 10.1016/J.APENERGY.2015.07.031
17. Nakade S, Kanzaki T, Kubo W, Kitamura T, Wada Y, and Yanagida S. Role of electrolytes on charge recombination in dye-sensitized TiO₂ solar cell (1): The case of solar cells using the I⁻/I₃⁻ redox couple. *Journal of Physical Chemistry B* 2005 Mar; 109:3480–7. DOI: 10.1021/JP0460036/ASSET/IMAGES/LARGE/JP0460036F00010.JPEG. Available from: <https://pubs.acs.org/doi/full/10.1021/jp0460036>
18. Saeed MA, Yoo K, Kang HC, Shim JW, and Lee JJ. Recent developments in dye-sensitized photovoltaic cells under ambient illumination. *Dyes and Pigments* 2021 Oct; 194:109626. DOI: 10.1016/J.DYEPIG.2021.109626
19. Belessiotis GV, Antoniadou M, Ibrahim I, Karagianni CS, and Falaras P. Universal electrolyte for DSSC operation under both simulated solar and indoor fluorescent lighting. *Materials Chemistry and Physics* 2022; 277:125543. DOI: <https://doi.org/10.1016/j.matchemphys.2021.125543>. Available from: <https://www.sciencedirect.com/science/article/pii/S0254058421013262>
20. Lan JL, Wei TC, Feng SP, Wan CC, and Cao G. Effects of iodine content in the electrolyte on the charge transfer and power conversion efficiency of dye-sensitized solar cells under low light intensities. *The Journal of Physical Chemistry C* 2012; 116:25727–33

Chapter 4

Integrating a Monolithic DSSC for Hand Gesture Recognition

4.1 Introduction

4.1.1 Background

The primary driver in technology for HCI is the integrating commitment to value human activity and experience. This Chapter focuses on the physical connection between the user and the IoT node, achieving a suitable and easy-to-use user interface (UI). Most modern applications involve interaction through a touchscreen or physical mechanisms (such as remote controls, cell phones), allowing the user to directly interact with the display. However, this can hinder the natural interface between users and IoT devices, a key consideration for HCI.

Hand gesture recognition in IoT applications offers a compelling and intuitive way to interact with and control a wide range of connected devices. It can improve the users experience, mimicking real-world physical actions, making them easy to understand and accessible to people of various age groups and backgrounds. This includes individuals with physical disabilities, making it possible for them to control IoT devices and access technology that might otherwise be challenging. Hand gesture also allows the user to control IoT devices without physical contact, giving them the convenience of hands-free (such as if their hands are occupied or dirty), but also reduces the risk of contamination, which can be especially important in environments like healthcare, smart homes, and public spaces [1].

By integrating an energy harvesting module to harvest energy but to also act as a sensor to detect the user's gesture/interaction with the IoT node, would be an advantageous system to lower the overall energy consumption of the IoT node com-

pared to other gesture detection techniques [2][3][4].

There are two different types of hand gestures, being static and dynamic gestures. Static involves the motion of different hand shapes, whilst dynamic gestures are generally described according to hand movements. This Chapter will concentrate on dynamic gestures, as motion of hand is a more natural response when operating a smart device having a display.

4.1.2 Related work

What if the solar cell that is powering the IoT device can also recognise hand gestures, which would allow the user to naturally interact with the system? Previous methods to achieve this are mentioned below:

4.1.2.1 Photodiode array

Directional based gesture detection coinciding with energy harvesting has been achieved by attaching several photodiodes to the system 4.1 [4][5][6]. As the system knows the location of each photodiode; when a hand gestures over the device, the cast in shadow causes the photocurrent to be lowered. The pattern in photocurrent reduction (for each photodiode) can then be analysed to determine the hand direction, demonstrated below in Figure 4.1 [4][5][6].



Figure 4.1: Photodiode layout for IoT node applications. Adapted from [4][5]

Whilst this does allow efficient and reliable hand gesture recognition, due to each photodiode working independently, the set-up requires individual wiring to the system, resulting in a complex assembly and not as visually appealing UI.

4.1.2.2 SolarGest

Ma *et al.* [2] in 2019, demonstrated the feasibility of hand gesture recognition system from a photocurrent signal response of a monolithic opaque silicon cell, and two different transparencies (20.2% and 35.3%) of an organic cell (PBDB-T: ITIC). The layout and hand gestures implemented are shown in Figure 4.2. This achieved a

hand gesture recognition accuracy of 96%, by including signal pre-processing techniques, consisting of dynamic time warping (DTW) and Z-score transformation. The cleaned signal is then classified, from an extensive data-set, using machine learning (ML) techniques.

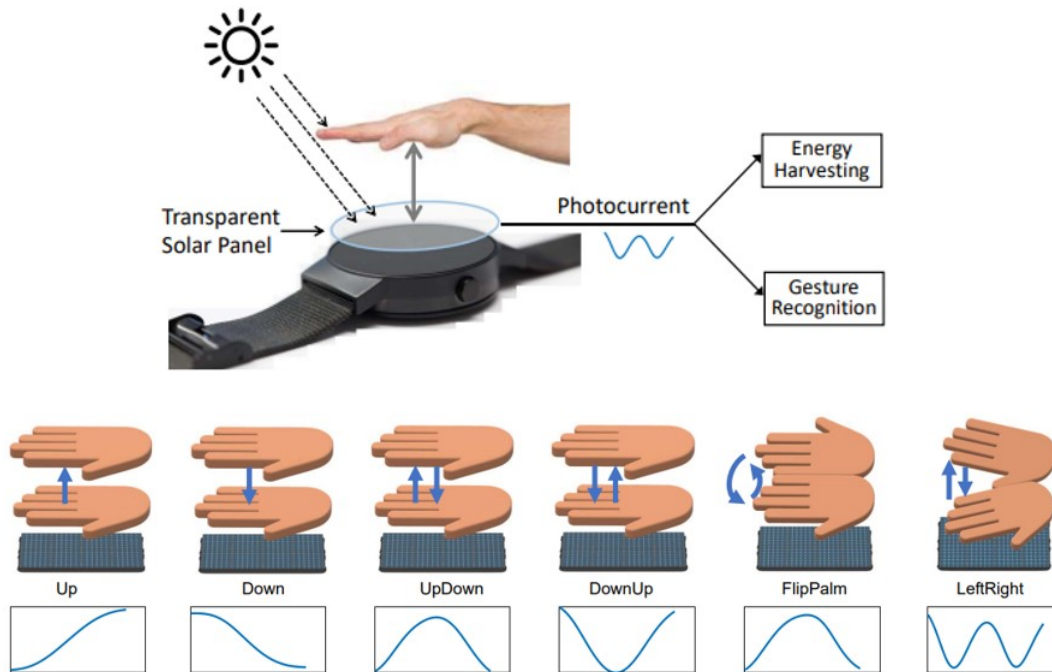


Figure 4.2: SolarGest layout and stored gestures used. Adapted from [2]

Whilst it seems that SolarGest has achieved a monolithic PV hand gesture recognition, there are some limitations with the device:

- Six different gestures were achieved; however, not directional based gestures. This means that this device cannot differentiate if the user is swiping right or swiping left over the cell due to the even layer of semiconductor material on the substrate; providing a constant photocurrent signal. This hinders the user from using a fully natural and comfortable hand gestures when using the IoT node.
- The pre-processing technique restricts further analysis on the device. Following the use of DTW, the author does this by using two signals of the same gesture. However, this cannot be achieved if the gesture is done during live gesture recognition; as the device cannot predict before what motion of the hand is accomplished.

4.1.3 Summary

Previous attempts to design an integrated PV hand gesture recognition device have involved either a complicated set-up with multiple PV cells, or gestures that are not

fully natural and comfortable to accomplish.

Therefore, the goal in this Chapter is to build a prototype, involving a monolithic DSSC, that can distinguish from basic hand gesture swipes (right, left, up, down) using the photocurrent output of the PV. DSSCs are used on the basis of the justification from Chapter 1, providing details on the ease of fabrication and their aesthetically pleasing appearance.

4.2 Materials and methods

4.2.1 DSSC design

4.2.1.1 Asymmetrical pattern

To achieve a different photocurrent signal for each directional gesture sweep, a possible DSSC active pattern could involve different active area sizes at each corner of the DSSC.

To initially test this principle, an 8 cm x 8 cm active area size transparent DSSC was fabricated, and covered with an asymmetrical cut-out cardboard, to mimic if there was no active area behind the material. A schematic of the layout is shown in Figure 4.3.

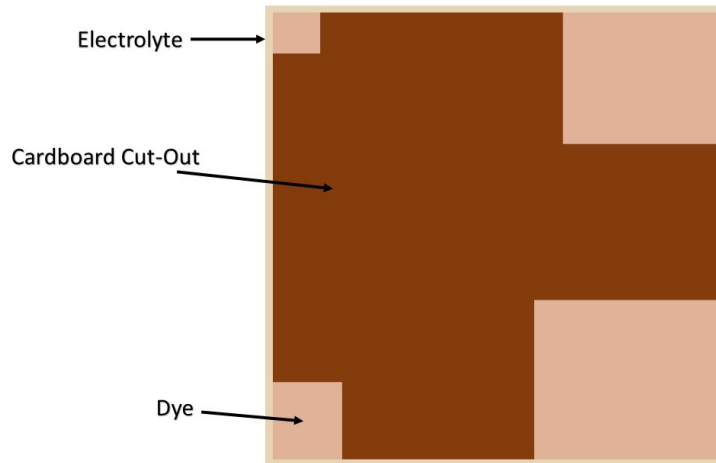


Figure 4.3: Schematic of initial DSSC testing

By covering each segment individually (at each corner in Figure 4.3), the photocurrent response, seen in Figure 4.4, can be clearly seen to change with amplitudes, depending on active area size.

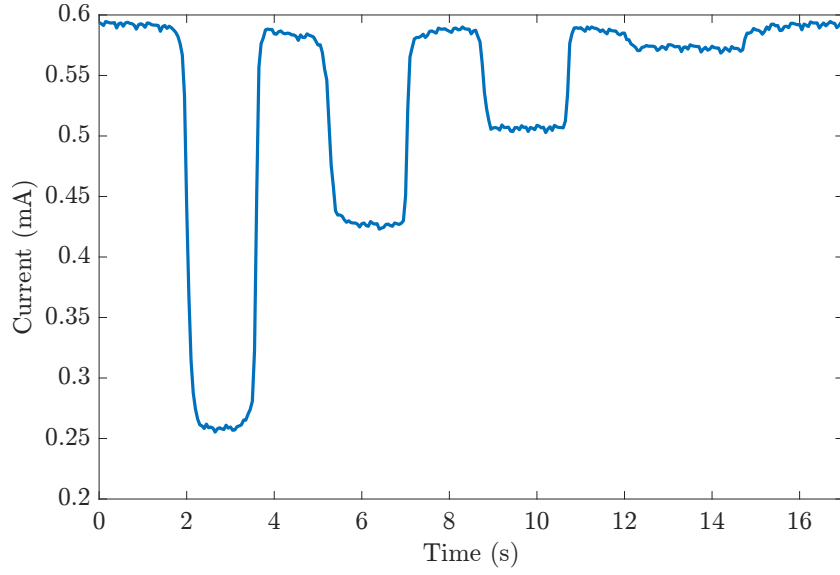


Figure 4.4: Photocurrent when individually covering from largest to smallest area

With that in mind, a flower pattern was designed (to demonstrate the capabilities screen printing can achieve) with different and randomised active area sizes at each corner (in Figure 4.5a), printed on a DSSC (8 cm x 8 cm), shown in Figure 4.5b.

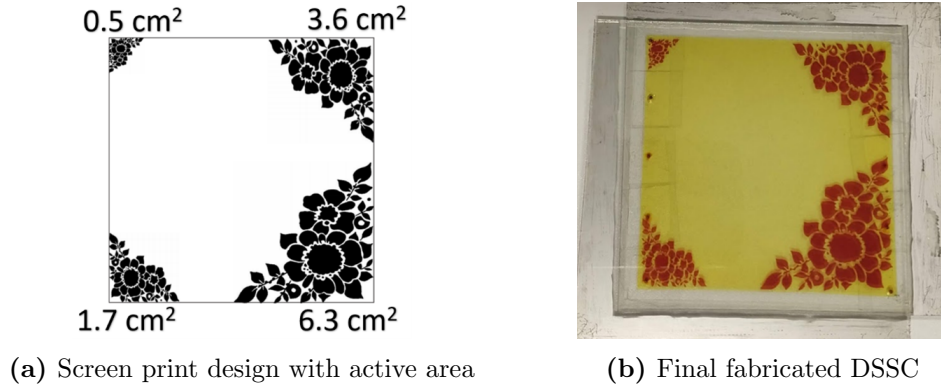


Figure 4.5: Asymmetrical pattern design

4.2.2 DSSC fabrication

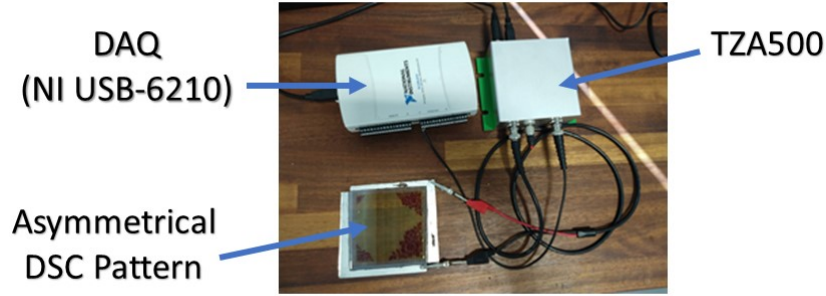
The composition of the preliminary DSSC (seen in Figure 4.5b) uses the I_3^-/I^- electrolyte and N719 dye. Whilst concluded in Chapter 3 that the best type of electrolyte for indoors is the 5 mM (HM), this Chapter was carried out simultaneously with 3, meaning that the resultant electrolyte was not used, but instead the AN-50.

4.2.3 Gesture Data collection

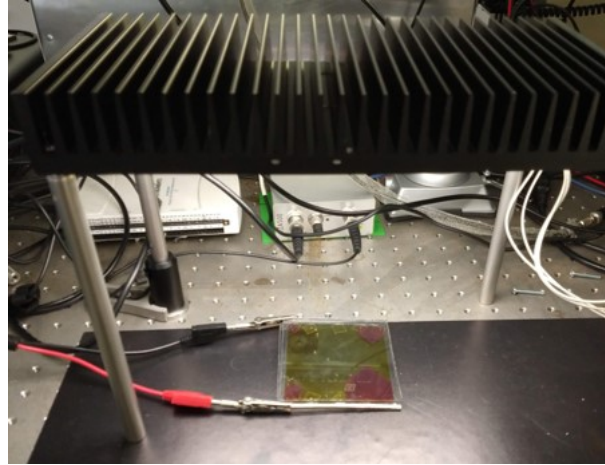
A large data-set is required in order to ensure a reliable system is built.

4.2.3.1 Data collection method

To initially discover if hand gesture recognition through a monolithic DSSC can be achieved, the instrumental power consumption for collecting/ reading the signals is not considered, but rather to obtain high data precision for increased chances of gesture recognition.



(a) Set-up for gesture data collection



(b) Light source set-up

Figure 4.6: Gesture data collection rig

The set-up for data collection method is shown in Figure 4.6 above. The DSSC is initially connected to a transimpedance amplifier TZA500. This converts the photocurrent to voltage, with a gain of 10, and bandwidth of 1 kHz ; a higher value of gain causes the instrument to overload and a high sampling rate was chosen to increase the chances of gesture recognition. The output of the transimpedance amplifier is connected to a data acquisition device (DAQ) (NI USB-6210) converting the analogue electrical signal to digital, through a 16-bit resolution. This instrument is mainly used due its compatibility with LabVIEW on the computer. A LED array is used as a consistent light source when collecting the gesture photocurrent signal.

An application created by Dr Adam Pockett (post-doctorate researcher at Swansea University) in LabVIEW, enables the user to capture a 2 second gesture multiple times, when the photocurrent goes below a set threshold, shown in Figure 4.7 below. This allows the ease of multiple gesture measurements without the need of resetting the device per gesture. After completing the number of gestures required for collection, the data can be all saved under one Excel document for further analysis using MATLAB.

The MATLAB codes assembled for each technique can be viewed through the storage file cloud [7], including the pre-processing and model training techniques.

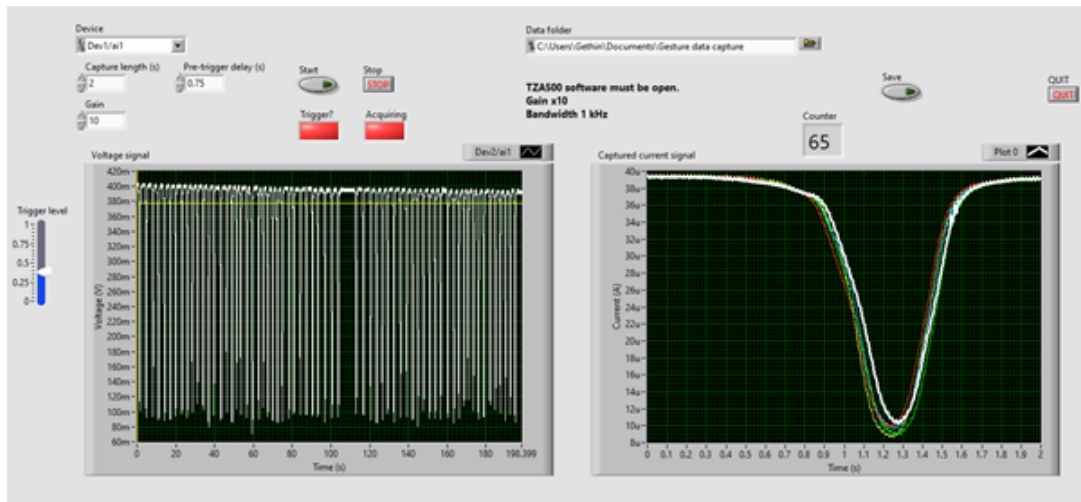


Figure 4.7: Gesture capture using LabVIEW

4.2.3.2 Gesture Signal Output

Following the gesture data collection method, the signal output of 4 hand gestures was collected. The photocurrent signal of each gesture shows some slight difference in the shape, seen in Figure 4.8 below.

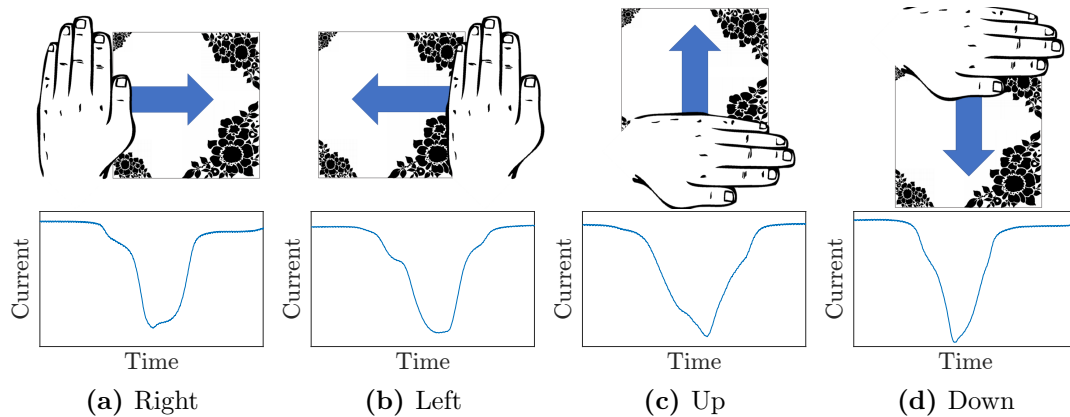


Figure 4.8: Sketches of the 4 hand gestures performed over the DSSC. The second row shows the photocurrent response for each gesture at 1000 Lux

120 samples of each gesture were collected under a light intensity of approximately 1000 and 2500 Lux. This was controlled by continuously placing a VEML7700 Lux meter connected to a display. The light source (seen in Figure 4.6b) can then be adjusted to the desired intensity using a power supply. The total data-set consisted of 960 gestures for analysis.

4.3 Gesture Detection Using Thresholding

4.3.1 Method

The proposed method of thresholding could possibly be successful in recognising the photocurrent response between different gesture sweeps. The method is simple to build, having a low computational cost.

Thresholding relies on extracting specific features that can differentiate each gesture photocurrent signal. The process manually goes through the ‘if’ loop process, using pre-defined values that have been selected at the start; and thereby separating each gesture. This evidently requires features that can be easily extracted and separated into different gestures.

4.3.1.1 Data pre-processing

There are several parameters that can affect the photocurrent signal of the same gesture, including: quality of DSSC fabrication (efficiency and fill factor); environmental conditions (light intensity); and user’s parameters (height from DSSC, speed of gesture, hand angle and size).

In this case, thresholding only requires the amplitude of each gesture signal to be normalised. This is achieved by using the ‘norm’ function in MATLAB, which uses Equation 4.1 below:

$$\| v \|_p = \left[\sum_{k=1}^N |v_k|^p \right]^{1/p} \quad (4.1)$$

where v is the vector and N is the number of elements. In this case p is 2, giving the vector magnitude or Euclidean length of the vector [8].

4.3.1.2 Data analysis

By collecting the gestures at a slightly higher light intensity of 2500 Lux, the output gesture photocurrent signal for each of the four gestures is amplified. Initially, the right and left gesture can be paired together during the selection process, as the direction of the gestures results in more active area being covered at once (two largest active area being covered simultaneously) (as seen in Figure 4.8 (see page 131)). These results in a lower photocurrent signal compared to the up and down gestures. Secondly, the initial trough values of the right and down gestures have a higher value of normalised current compared to the left and up gestures, which can also be grouped together. Therefore, with two different pairs matched together, a MATLAB code can be set-up to filter the correct gesture sweep.

To extract the relevant data from MATLAB, the method involves using the function ‘findpeaks’ and inverses the data values, which extracts the trough values instead. Additionally, the ‘smoothdata’ function in MATLAB is required; smoothing any noisy data, which otherwise would affect the true location of the initial trough value. The results can be seen in Figure 4.9, where a circle represents the first detection of the trough value (wherever the gradient of curve is 0) for each of the 4 gestures.

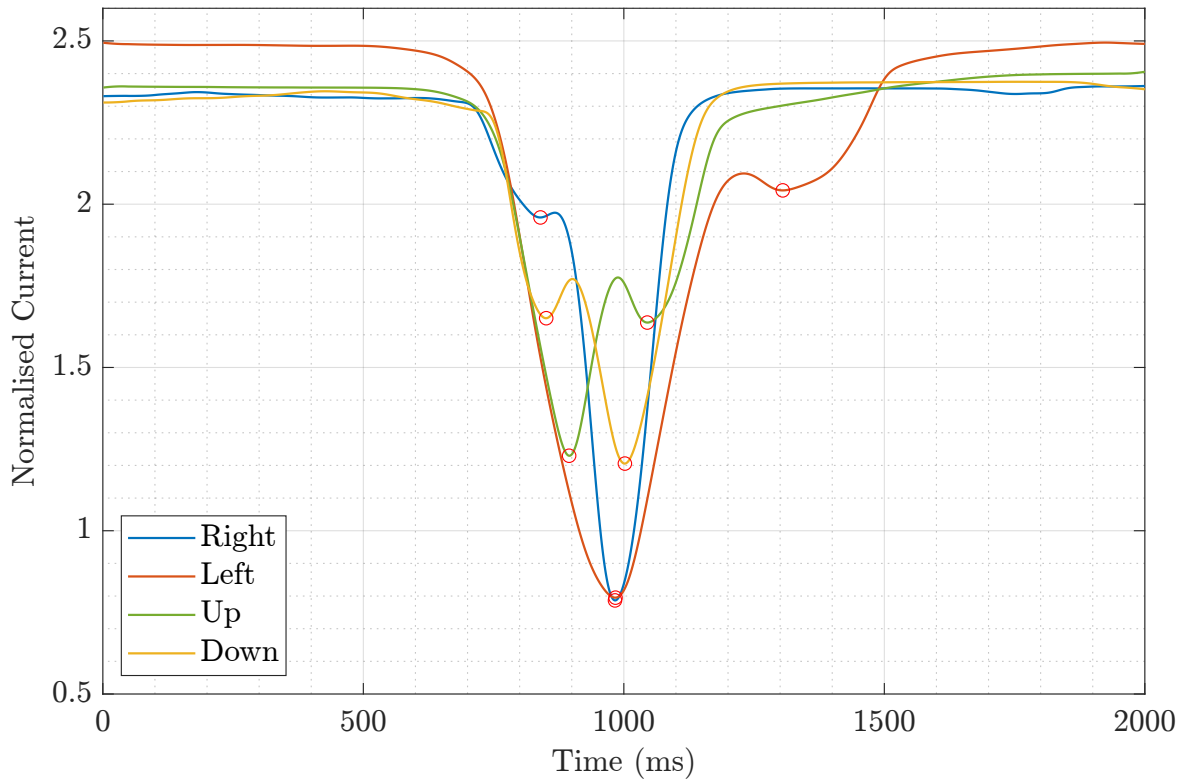


Figure 4.9: First Trough detection for each gesture photocurrent

4.3.2 Results and discussion

The threshold model combines both the minimum normalised current value and the initial trough value as the extracted features from a gestured photocurrent output signal. This is accomplished by using ‘if’ statements, to filter the minimum and initial trough value into one of the four gestures, using pre-defined (from the initial set-up) values.

The model undergoes rigorous testing, using both the data-set recorded at 1000 Lux and 2500 Lux, totalling 960 gestures, distributed equally for each gesture.

Table 4.1 below shows the confusion matrix of the threshold model prediction for each signal gesture tested. The table displays the predicted results (in each column) for every tested gesture signal, and also shows the true gesture class (in each row, which adds up to the amount of gestures for each direction used, in this case being 240) of that signal. Therefore, a perfect predicted model would show values only in the highlighted (in blue) diagonal sections, with every other non-highlighted area scoring 0. However, this is not the case, where Table 4.1 shows that there are many incorrect predictions, resulting in an unsuccessful application. The accuracy of correctly predicting the four directional sweeps from 960 gestures was $(\frac{0+3+103+0}{960}) = (106/960) \approx 11\%$, with the main confusion being incorrectly predicting the up sweep gesture (shown with the high predicted values in the up column of the confusion matrix), when not being its true gesture class.

Table 4.1: Confusion Matrix Using Threshold Detection

True Class	Right	0	14	226	0
	Left	2	3	200	35
	Up	17	97	103	23
	Down	0	128	112	0
		Right	Left	Up	Down
		Predicted Class			

Figure 4.10 shows that the light intensity not only affects the shape of the photocurrent signal, but also changes the normalised current of each signal, resulting in errors appearing whilst conducting the thresholding technique. The shape of the photocurrent signal at a lower light intensity becomes less distinctive, resulting in the right and down gestures losing the initial trough which should be located half way down the normalised current. This is the main reason as to why the accuracy from the confusion matrix is very low.

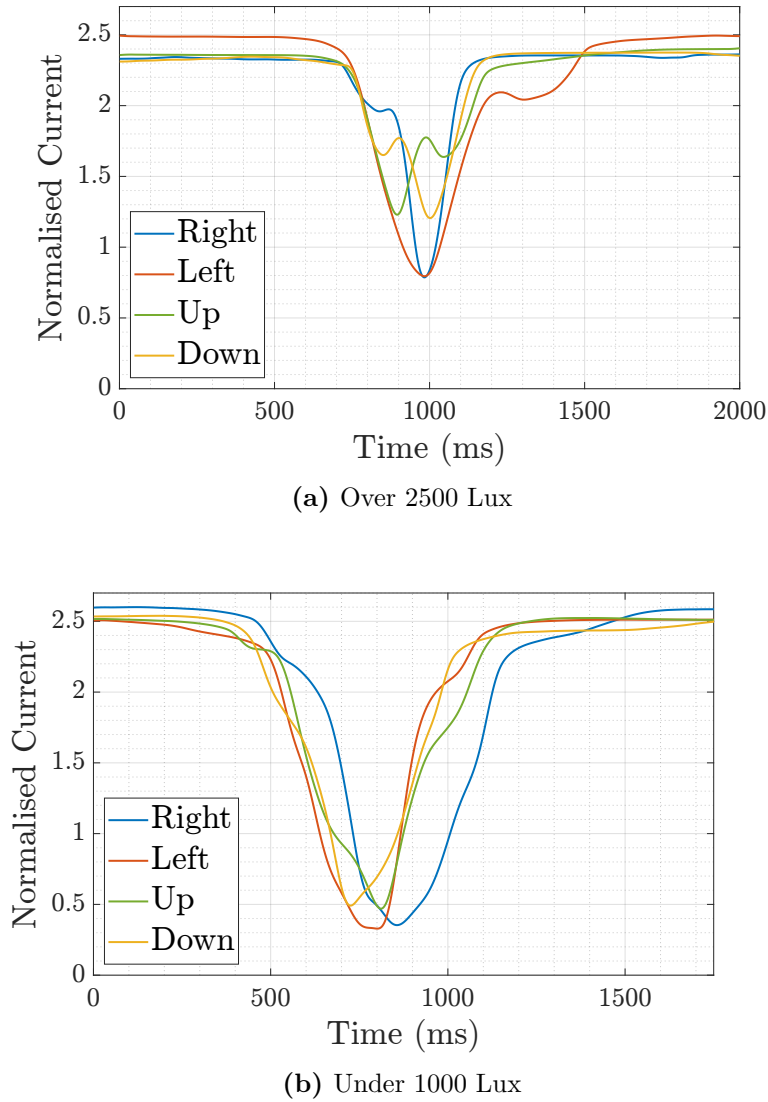


Figure 4.10: Comparing photocurrent signals under different light intensities

4.4 Gesture detection using machine learning (ML)

With the threshold technique being unfavourable, an alternative method which was also used by Ma *et al.* [2], is machine learning (ML). It is considered as the main recognition method amongst recently published papers that deal with self-powered hand gestures [2][4][9]. Supervised classification identifies which category (in this case, the four gesture sweeps) a new set of data belongs to, predicted from a training model built from another set of data that has already been categorised [10]. The general classification framework involves data pre-processing the photocurrent time series, extracting specific features, and finally training a classifier. MATLAB was used as the processing software for building the training model, and executing the trained model against a new set of data.

Figure 4.11 below shows a flow diagram of the machine learning process used for hand gesture recognition. The subsequent Sections describes each step in more detail.

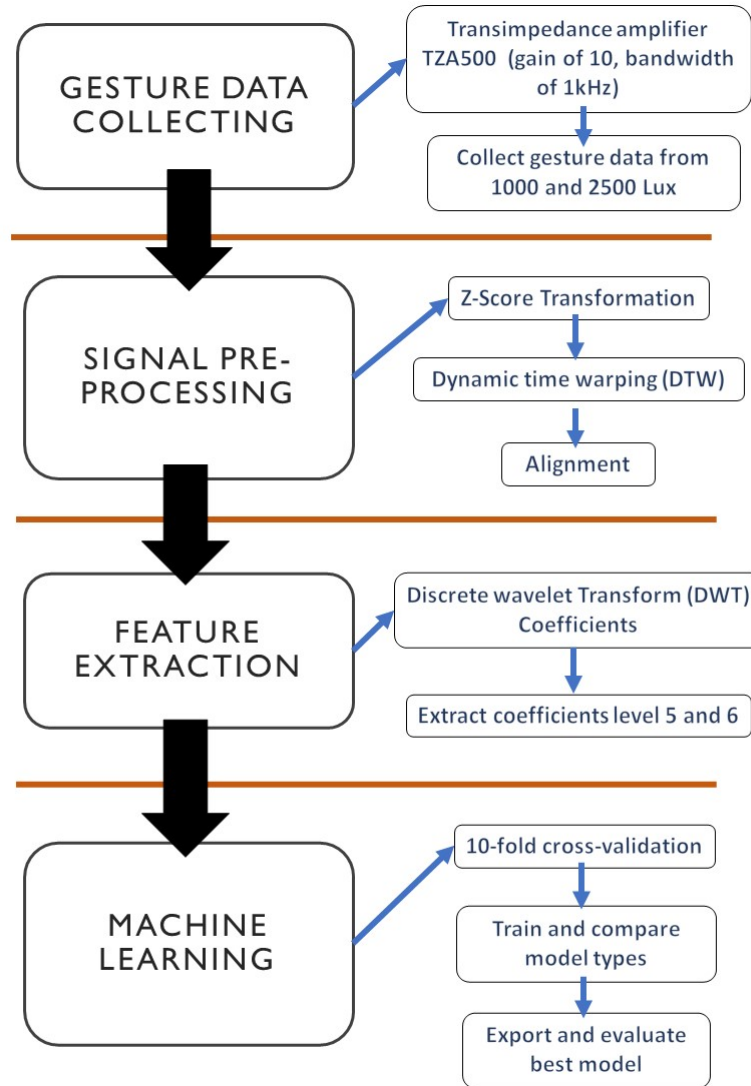


Figure 4.11: Flowchart of the machine learning process

4.4.1 Data Pre-Processing

4.4.1.1 Temporal and amplitude misalignment

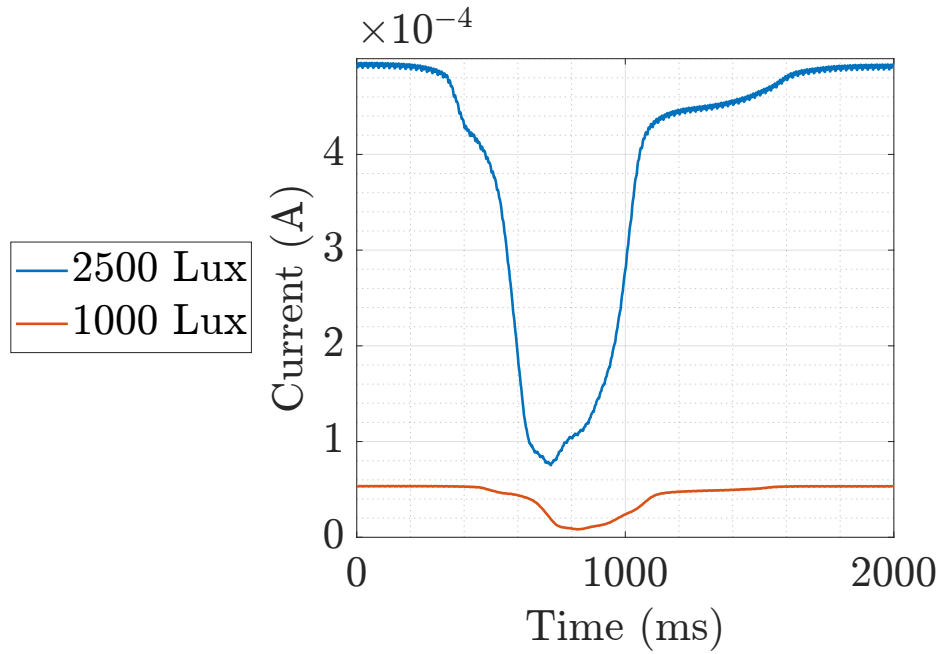
In the case of the thresholding technique, it is important to attempt to minimise the effect of external parameters mentioned in Section 4.3.1.1. The process closely follows the method applied by Ma *et al.* [2], which initially uses Z-score transformation to align the signal amplitudes, similar to the ‘norm’ function used during the thresholding technique. The Z-score transforms the signal into z-scores, mean of 0 and standard deviation of 1. Equation 4.2 for z-score is given below [11]:

$$z = \frac{(x - \bar{X})}{S} \quad (4.2)$$

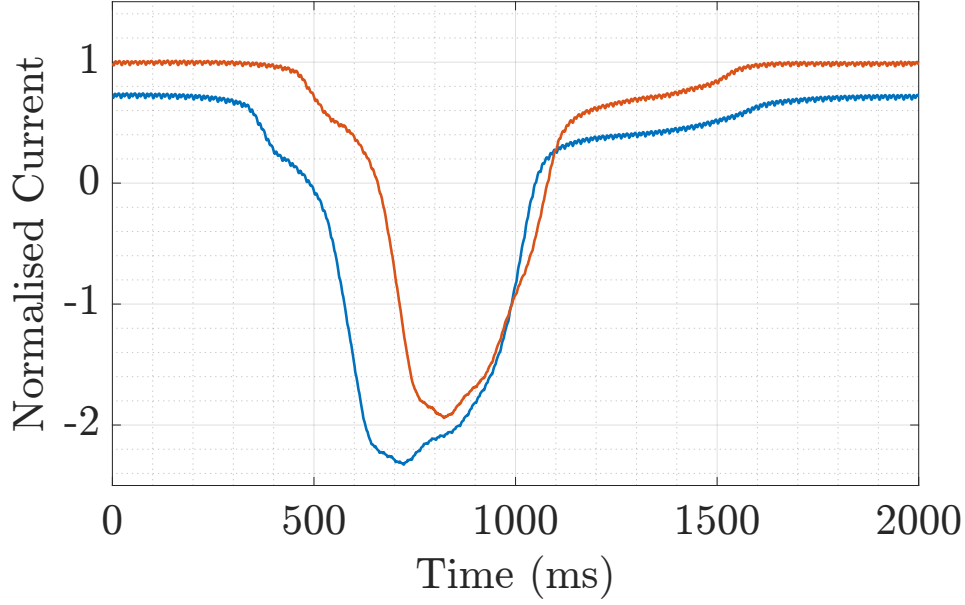
where \bar{X} is the data mean, S being the standard deviation and x being each data point. Standard deviation is given below in Equation 4.3:

$$S = \sqrt{\frac{\sum_{i=1}^n (x_i - \bar{X})^2}{n - 1}} \quad (4.3)$$

Where x_i is a data point value and n being the data sample length. Two photocurrent signals of the same gesture are seen in Figure 4.12a, collected at different light intensities (1000 and 2500 Lux). After Z-score transformation, both signals realign similarly to the same amplitude, seen in Figure 4.12b.



(a) Right gestures at different light intensities

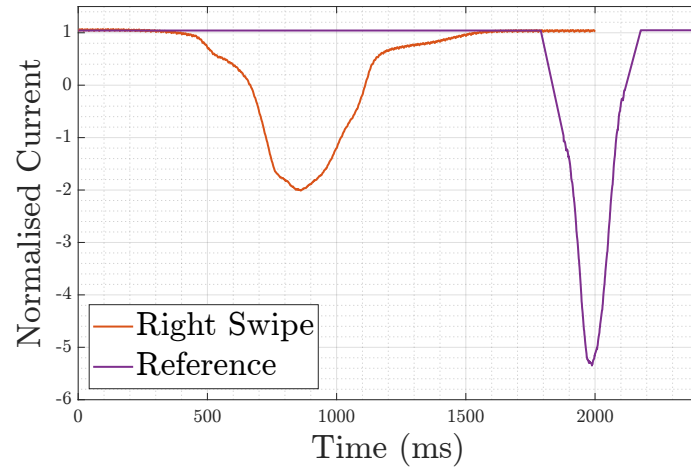


(b) Z-score transformation applied

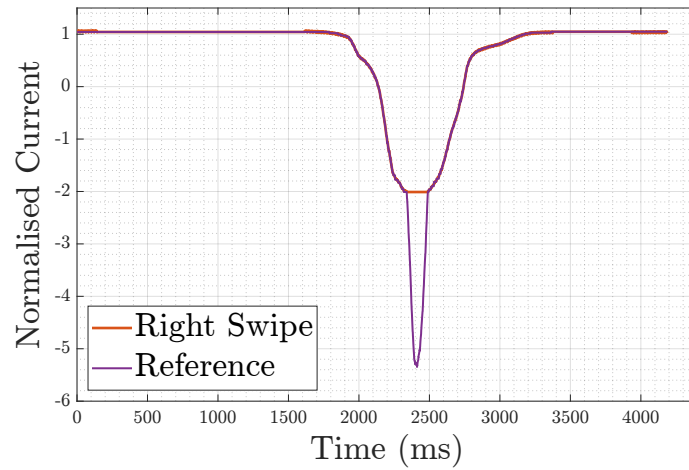
Figure 4.12: Amplitude alignment using Z-score transformation

Following on from Z-score transformation, Figure 4.12b indicates some temporal misalignment, which can be solved using dynamic time warping (DTW). SolarGest uses DTW to align two signals of the same gesture. It does this by distorting the duration of both data sets, to make them appear on a common time axis at the same location. The default distance metric is used, specified as ‘eculidean’ which is the root sum of squared differences [12].

However, as previously mentioned (in Section 4.1.2.2), this method of using two signals of the same gesture prevents any live data to be predicted, due to using another signal of the same gesture for DTW. To overcome this, a reference curve is used instead, which dynamic time warps the measured photocurrent signal to the reference curve. Figure 4.13a shows an example of DTW with one right swipe gesture and the reference curve.



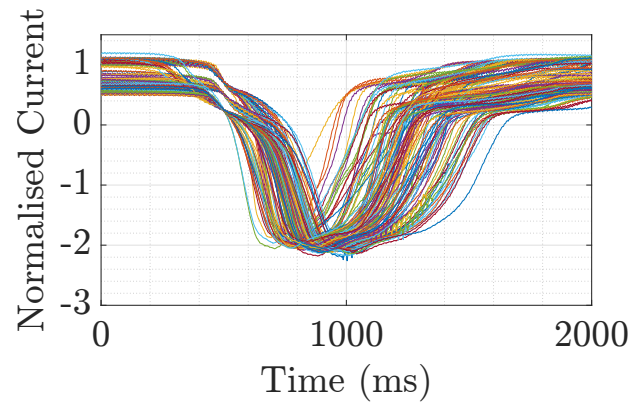
(a) Before DTW



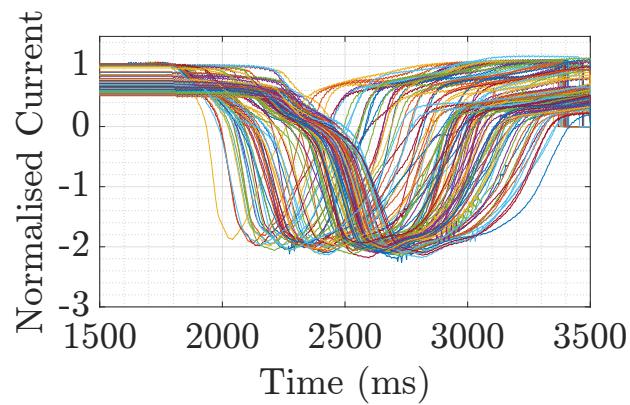
(b) After DTW

Figure 4.13: DTW technique using a reference curve

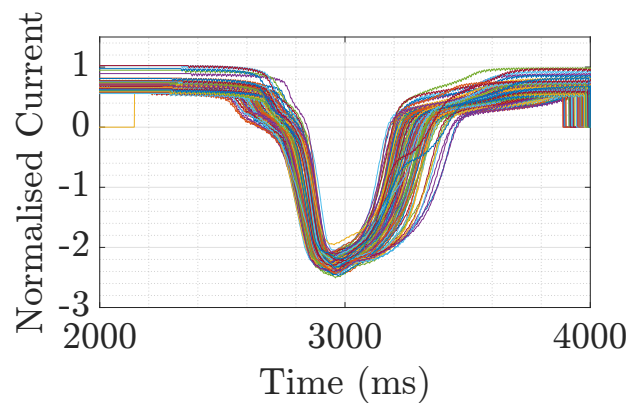
Initially, DTW seems to work very well with a reference curve, producing a new common time axis, as seen in Figure 4.13b. However, machine learning requires a substantial amount of gesture data-set for a robust gesture recognition framework. Figure 4.14a shows 120 gestures (from the same user hand) of a right sweep after Z-score transformation and before DTW. However, after DTW shown in Figure 4.14b, using the same reference curve for each gesture, not every gesture is temporally aligned with one another, with some nearly 1s apart. This is mainly down to the user's parameters affecting the initial position of each gesture, due to the difference in speed and height from the DSSC.



(a) After Z-score transformation



(b) After Z-score transformation and DTW



(c) Using aligning tool before and after DTW

Figure 4.14: Alterations to the pre-processing technique

To overcome this, a function called ‘alignsignals’ in MATLAB is used before and after DTW, as seen in Figure 4.14c, successfully realigning each gesture to the reference curve. Compared to DTW, this technique only delays the earliest signal, in this case the gesture signal, to have the same starting point as the reference curve [13]. DTW is currently used between the aligning tools, due to it slightly shrinking the trough width of the gesture signal towards the reference curve. A study in this

Chapter was undertaken (see Section 4.4.2.2) to investigate if DTW is required or not in the pre-processing method alongside the other aligning tool, by comparing the accuracy of the trained models.

4.4.1.2 Feature extraction

After pre-processing the data, feature selection extracts specific values that reduce the number of values of each gesture. By selecting a small subset from the original data, it tends to lead towards an increased trained model performance, better data interpretability and lowering the computational cost [10].

Ma *et al.* [2] compares two set of features, statistical and Discrete Wavelet Transform (DWT) coefficients. The results discovered that DWT coefficients had higher prediction accuracy by 11%. Nonetheless, both features will be extracted and analysed separately from the photocurrent of the preliminary design.

4.4.1.2.1 Statistical features

Time domain features are extracted, including basic statistics (mean, standard deviation, root mean square and shape factor), higher-order statistics (kurtosis and skewness) and impulsive metrics (peak value, impulse factor, crest factor and clearance factor).

The best method found for extracting these statistical features was through an application on MATLAB called Diagnostic Feature Designer [14]. The application is designed for estimating the remaining life and the monitoring of rotating machines; however, it can be used to extract statistical features from the gesture data set with ease. An ensemble file with all the collected pre-processed gesture data set can be imported into the application, making sure that each variable name inside the main table is identical.

After re-organising into a multimember ensemble data-set, the application can generate the statistical features. The application can rank the features by assessing how effectively it separates the data into different gestures. The statistical method used in this case is One-Way ANOVA, and the results are seen in Figure 4.15 below. The greater the one-way Anova value is, the better the extracted feature is to determine the correct gesture sweep performed.

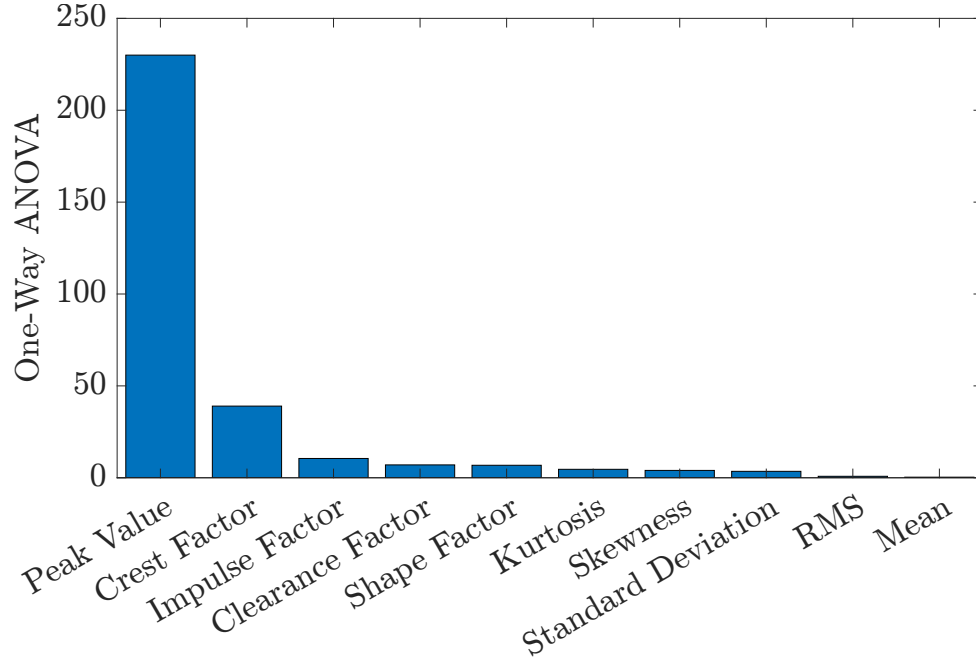


Figure 4.15: Statistical Features Ranked Through One-Way ANOVA

Only one feature has a significant impact of differentiating between each gesture, being peak value. This might affect the overall gesture recognition accuracy when it comes to the ML stage, due to only having one distinguishable feature to separate the four gestures.

4.4.1.2.2 Discrete Wavelet Transform (DWT) coefficients

This technique decomposes a signal at various resolutions and different frequency domain, capturing both temporal and frequency information [15].

The detail coefficients are extracted on the selected coefficient level used. Ma *et al.* [2] does this by halving the sampling rate, to obtain the highest frequency contained in the signal, following Nyquist Theorem. In this case the sampling rate is $1kHz$, therefore 500 Hz is the contained highest frequency. The fast Fourier transform (FFT) graph seen below in Figure 4.16, shows that the frequency right swipe gesture lies below 5 Hz . Therefore, the level 6 DWT is required, as it covers the gesture frequency, as the range is $[0, 500/2^6]\text{ Hz} = [0, 7.8]\text{ Hz}$. Level 5 detail coefficients are also collected, to compare if a larger frequency range is beneficial or not for machine learning.

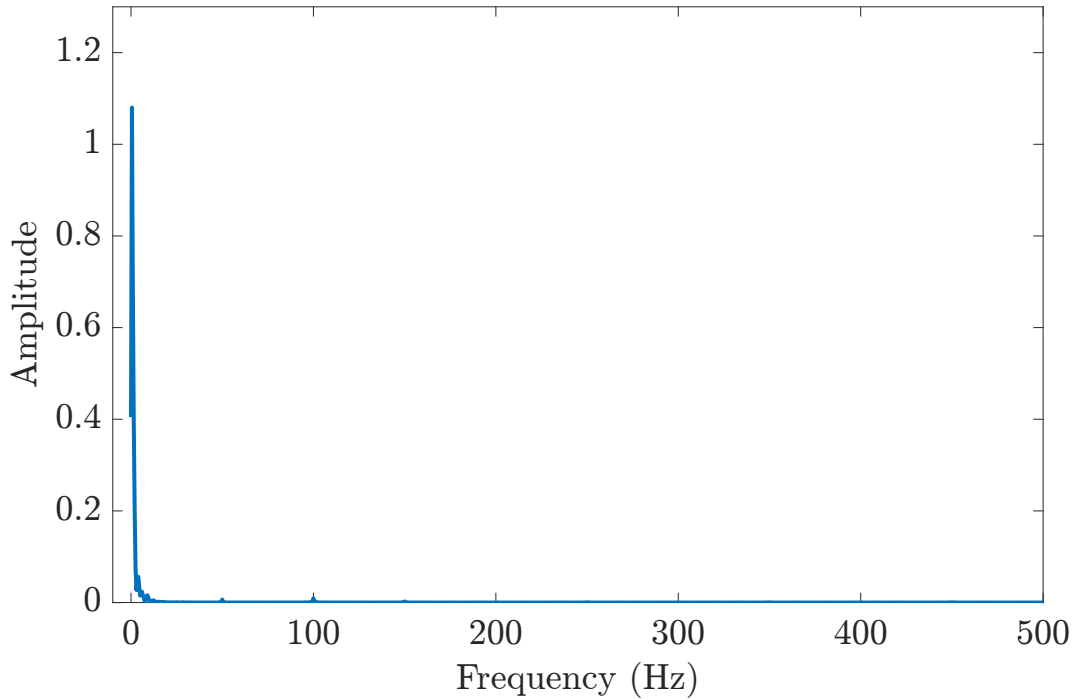


Figure 4.16: FFT analysis of a single photocurrent signal

Ma *et al.* [2] also uses this technique to denoise the raw photocurrent signal, before data pre-processing. This involved soft thresholding the detail coefficients, then reconstructing with the unmodified coefficient approximations, a method called inverse DWT [16]. It was mainly required due to the noise from the ‘minor imperfections in the micro-controller of the Arduino’. However, in this case there is less noise created from the transimpedance amplifier and DAQ in indoor conditions, as seen in Figure 4.16 above; meaning that this step is not required.

There are several different types of wavelets available to use, with MATLAB capable of using these wavelet families: Daubechies, Coiflets, Symlets, Fejér-Korovkin, Discrete Meyer, Biorthogonal, and Reverse Biorthogonal. Ma *et al.* [2] undertook a wavelet analysis comparing five different wavelets: Haar(haar), Daubechies1(db1), Daubechies2(db2), Daubechies4(db4), and Coiflet2(coif2), with db2 having a slightly higher recognition accuracy. These five different wavelets will be investigated during machine learning.

Figure 4.17 below shows the DWT process, halving the amount of detail coefficient points as the wavelet level increase to 6, also showing the approximation coefficients at level 6. The example below extracts the detail coefficients of a single right gesture through Daubechies2 (db2) wavelet.

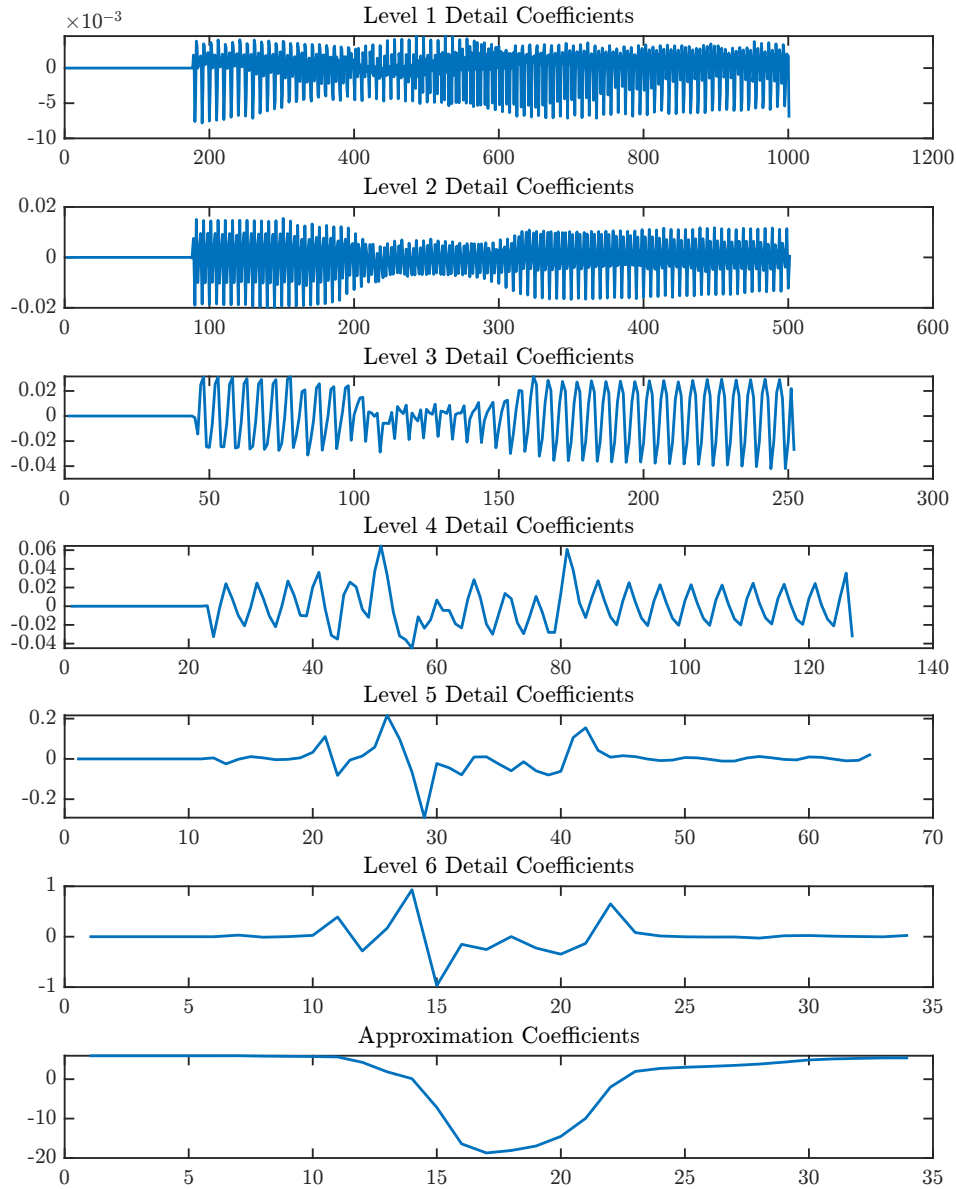


Figure 4.17: DWT detail coefficients up to level 6 with approximation coefficients level 6

4.4.1.2.3 Classification

Slightly different to the threshold technique set-up, half of the data from the 1000 Lux and 2500 Lux (done randomly but an equal amount for each gesture and light intensity) are placed in one file for classification; totalling 480 photocurrent signals (120 for each gesture). The data follows the pre-processing technique, involving Z-transformation and DTW (including the alignment function), leading to certain features being extracted including both statistical and detail coefficients.

After this, the machine learning classifiers are trained for gesture recognition. This is done through the MATLAB application called classification learner [17]. As there is uncertainty as to which classifier model is best, all models are trained on MAT-

LAB to find the best accuracy, these include: Decision Tree (Fine, Medium, and Coarse); Discriminant Analysis (Linear and Quadratic Discriminant); Naïve Bayes Classifiers (Gaussian and Kernel); Support Vector Machines (Linear, Quadratic, Cubic, Fine Gaussian, Medium Gaussian and Coarse Gaussian); Nearest Neighbour Classifiers (Fine, Medium, Coarse, Cosine, Cubic and Weighted); and Ensemble Classifiers (Boosted Trees, Bagged Trees, Subspace Discriminant, Subspace KNN, RUSBoosted Trees).

There are different statistical methods of estimating the accuracy of the trained model, with the main two being cross-validation and hold-out. The hold-out method involves separating the data into a training set (where the model is trained) and a hold-out set (measuring its performance). The cross-validation method involves dividing the data randomly into equally sized folds (k), where k is defined by the user. One of the folds is used as the test set with all the other folds being used as the training set. This is repeated for each unique fold, averaging the observed errors to form the k -fold estimate. K -fold cross-validation is found to have a better generalisation of error compared to hold-out, giving a better indication on unseen data [18]. A 10-fold cross-validation is selected, following the same validation method used by Ma *et al.* [2].

4.4.2 Gesture Recognition Results and Discussion

4.4.2.1 Performance of complete pre-processing technique

Table 4.2 (see page 146) shows the accuracy of the trained models from machine learning at different wavelets features of coefficient level 5 and 6, and statistical features.

The trained model accuracy from the preliminary design shows great potential in recognising the different photocurrent signals for the four gestures (right, left, up and down). An accuracy of 99% (highlighted in red) was achieved from the coefficient level 6 and wavelet Haar, under the Quadratic SVM classifier. There are also several 99% accuracy trained models, mainly from the SVM and Ensemble classifiers, for the feature selection Haar, Db1 and Db2. Statistical features also show promising results, however, scoring slightly lower on average compared to the DWT Features.

The highest accuracy trained model from each feature selection was saved for every single model type (Decision Tree, Discriminant Analysis, Naïve Bayes Classifiers, Support Vector Machines, Nearest Neighbour Classifiers and Ensemble Classifiers). To additionally validate the trained model, an unseen data-set (data in which the

Table 4.2 Trained model accuracy for wavelet and statistical features

		Model Type Accuracy (%)																						
Level	Feature Selection	Tree			Linear Discriminant	Naive Bayes		SVM					KNN					Ensemble						
		Fine	Medium	Coarse		Gaussian	Kernel	Linear	Quadratic	Cubic	Fine Gaussian	Medium Gaussian	Course Gaussian	Fine	Medium	Coarse	Cosine	Cubic	Weighted	Boosted Trees	Bagged Trees	Subspace Discriminant	Subspace KNN	RUSBoosted Trees
5	Coif2	85	85	82	93	69	33	93	94	93	48	92	80	78	84	67	85	72	84	90	96	94	72	85
6		93	93	89	93	68	46	94	97	97	68	94	88	89	88	81	88	83	90	73	95	91	93	72
5	Haar	92	92	90	95	25	93	47	97	98	99	66	98	98	98	88	97	93	98	25	99	98	99	25
6		94	95	90	93	25	94	58	98	99	99	68	98	97	97	87	96	95	97	25	99	97	99	25
5	db1	93	93	91	94	25	93	47	97	98	98	60	98	97	98	88	97	94	98	25	99	97	98	25
6		96	96	91	94	25	92	61	98	99	99	68	98	98	97	87	97	96	97	25	99	97	99	25
5	db2	94	94	93	97	95	88	38	98	99	99	47	98	95	99	90	96	90	98	25	99	97	93	25
6		94	94	94	94	96	93	52	96	98	98	63	97	97	93	88	94	89	95	25	98	95	97	25
5	db4	88	88	83	94	85	70	30	92	94	93	44	92	83	84	75	86	78	86	92	96	94	68	88
6		91	91	84	92	91	68	42	93	95	95	64	93	86	88	75	88	82	88	94	96	91	92	91
	Statistical Features	75	73	60	89	53	70	88	91	88	79	80	63	77	79	61	78	78	79	77	81	80	78	73

trained model has not seen) consisting of another 480 gestures (being the other half of the gestures not used during classification, at 1000 and 2500 Lux) was used to test the trained model. Each trained model predicts the gesture for each unseen photocurrent signal, with the accuracy of success being recorded, shown in Table 4.3 below.

Table 4.3 Evaluated accuracy from each trained model classifier type

Level	Feature Selection	Evaluated Accuracy of the Trained Model (%)					
		Tree	Discriminant Analysis	Naïve Bayes	SVM	KNN	Ensemble
5	Coif2	79 (Medium)	88 (Linear)	40 (Gaussian)	84 (Quad)	68 (Cosine)	79 (BaggedTrees)
6		61 (Fine)	62 (Linear)	40 (Gaussian)	74 (Quad)	56 (Weighted)	68 (Bagged Trees)
5	Haar	76 (Fine)	76 (Linear)	92 (Gaussian)	93 (Cubic)	98 (Weighted)	97 (Subspace KNN)
6		80 (Fine)	76 (Linear)	91 (Gaussian)	94 (Cubic)	96 (Fine)	95 (Subspace KNN)
5	Db1	76 (Fine)	76 (Linear)	92 (Gaussian)	93 (Cubic)	98 (Weighted)	93 (Bagged Trees)
6		80 (Fine)	78 (Linear)	91 (Gaussian)	94 (Cubic)	96 (Fine)	95 (Subspace KNN)
5	Db2	77 (Fine)	91 (Linear)	83 (Gaussian)	91 (Cubic)	97 (Med)	90 (BaggedTrees)
6		77 (Coarse)	77 (Quad)	69 (Gaussian)	89 (Cubic)	84 (Fine)	76 (BaggedTrees)
5	Db4	68 (Fine)	84 (Linear)	43 (Gaussian)	81 (Quad)	72 (Cosine)	81 (BaggedTree)
6		55 (Fine)	82 (Linear)	58 (Gaussian)	88 (Cubic)	75 (Cosine)	79 (BaggedTrees)
	Statistical Features	25 (Fine)	25 (Quad)	25 (Kernal)	25 (Quad)	25 (Weighted)	25 (BaggedTrees)

The best model after evaluation was found to be the level 5, wavelet feature Db1 and Haar, under the classifier KNN (weighted) and Haar, both achieving 98%. Statistical Features had poor success accuracy, with all classifiers only achieving 25%. The low accuracy is mainly down to the lack of feature variation between each gesture, resulting in the trained model only recognising one directional gesture during the evaluation, hence why the accuracy being $\frac{1}{4}$. Overall, level 5 showed a higher success rate in predicting the 480 unseen gestures, with the best level 6 coefficient being the Fine KNN classifier for the wavelet feature Haar and Db1, with an accuracy of 96%.

Table 4.4: Confusion Matrix of best evaluated model

True Class	Right	115	2	0	3
	Left	0	118	2	0
	Up	1	1	116	2
	Down	0	0	0	120
		Right	Left	Up	Down
		Predicted Class			

Table 4.4 above shows the confusion matrix for the highest evaluation accuracy from the best scored trained model (which achieved 98%). The matrix shows that the down gesture was predicted with 100% accuracy, with right gesture having the lowest accuracy of 96% correct, predicting incorrectly three of the gestures down, and the other two signals as left.

The highest accuracy trained model before evaluation as mentioned previously was the level 6 Haar wavelet of 99% from the quadratic SVM classifier. This model was used to predict the gesture direction of each 480 gestures, resulting in an accuracy of correct predictions being 91%. It was found that the trained model of the Cubic SVM classifier of the same level and wavelet had a higher success rate of 94% as seen in Table 4.3, with its trained model accuracy following the 10-fold cross-validation being slightly less, with 99%. This example is portrayed several times in Table 4.3, being that a high accuracy trained model from Table 4.2 does not always result in better predicted success accuracy.

4.4.2.2 Performance without the pre-processing tool DTW

Haar, Db1 and Db2 wavelets, of level 5 were selected to train 480 gestures, without the pre-processing step of DTW, to investigate if this affects the overall accuracy of the model. These features were selected due to its high accuracy from the previous results, with the 3 best classifier models being collected, SVM, KNN and Ensemble.

Table 4.5 below shows the accuracy results of each trained model following the 10-fold cross validation without the DTW pre-processing technique. Initially the results are very similar to the previous results shown in Table 4.2, with the highest accuracy being 99% (highlighted in red), from the Cubic SVM on coefficient level 5, Haar.

Table 4.5 Trained model accuracy for selected wavelet features without DTW

		Model Type Accuracy %																
Level	Feature Selection	SVM						KNN						Ensemble				
		Linear	Quadratic	Cubic	Fine Gaussian	Medium Gaussian	Course Gaussian	Fine	Medium	Coarse	Cosine	Cubic	Weighted	Boosted Trees	Bagged Trees	Subspace Discriminant	Subspace KNN	RUS Boosted Trees
5	Haar	98	99	99	62	98	97	99	97	85	97	94	97	25	99	98	99	25
6		97	99	99	71	99	97	99	96	85	96	93	97	25	99	95	99	25
5	db1	98	99	99	60	98	97	99	97	87	97	95	98	25	99	98	98	25
6		97	98	98	70	98	96	99	96	84	96	93	97	25	99	99	99	25
5	db2	98	98	98	48	96	96	95	95	84	96	88	95	25	99	99	92	25
6		96	98	98	64	96	94	95	93	83	94	88	94	25	97	97	97	25

However, the results after evaluating the best trained models with unseen data show a decrease in accuracy, seen in Table 4.6. The highest accuracy reached was 95% from the weighted KNN, level5 Db1. This is a decrease of 3% from the best model which included the DTW pre-processing technique. Other classifiers are also significantly lower compared to the results with DTW, from Table 4.3. This implies including DTW for the pre-processing stage does improve the gesture recognition model, as previously mentioned, closely matching the trough width of the gesture signal towards the reference curve. Henceforth, this pre-processing technique will be kept alongside the alignment function.

Table 4.6 Evaluated accuracy from each trained model classifier type without DTW technique

Level	Feature Selection	Evaluated Accuracy of the Trained Model (%)		
		SVM	KNN	Ensemble
5	Haar	84 (Cubic)	89 (Fine)	89 (Subspace KNN)
6		76 (Cubic)	79 (Fine)	79 (Subspace KNN)
5	Db1	84 (Cubic)	95 (Weighted)	85 (Subspace KNN)
6		77 (Quad)	80 (Weighted)	81 (Bagged Trees)
5	Db2	79 (Quad)	93 (Cosine)	88 (Bagged Trees)
6		84 (Cubic)	83 (Weighted)	87 (Bagged Trees)

4.5 Additional Gestures with Machine Learning

Machine learning has shown to be a technique for gesture recognition, achieving 98% (see Table 4.4) after evaluating using unseen data. Additional gestures alongside the

original gestures can be tested and analysed, finding the ML capabilities and limits.

Four diagonal directional gestures were added, as seen below in Figure 4.18, with the photocurrent response shown on the second row.

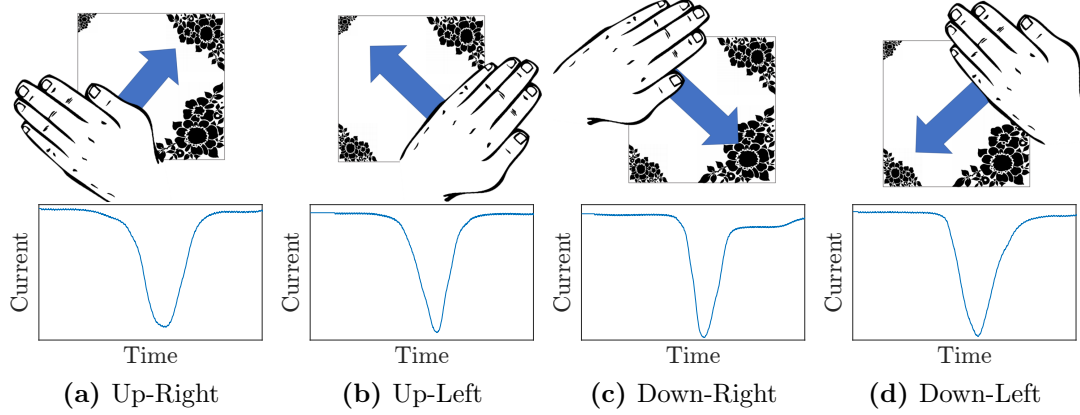


Figure 4.18: Sketches of the 4 additional hand gestures performed over the DSSC. The second row shows the photocurrent response for each gesture at 1000 Lux

Initial comparison between the four diagonal gestures shows similarities in the shape of the photocurrent signal. This might impede on predicting the correct gestures whilst evaluating the trained model.

4.5.1 Results and discussion

Like the method used to ML the initial 4 gestures, all 8 gestures are collected (120 data set of each) at 1000 and 2500 Lux (separated equally), and undergo the finalised pre-processing technique of Z-score transformation, DTW and alignment with the reference curve. Following on from previous results, Haar, Db1 and Db2 wavelet features of level 5 and 6 detail coefficients were selected, with the SVM, KNN and Ensemble trained model classifiers being collected, due to high accuracies from previous results.

Table 4.7 below shows the accuracy results of each trained model following the 10-fold cross validation of the 8 gestures.

Table 4.7 Trained model accuracy for 8 gestures

		Model Type Accuracy %																
Level	Feature Selection	SVM						KNN						Ensemble				
		Linear	Quadratic	Cubic	Fine Gaussian	Medium Gaussian	Course Gaussian	Fine	Medium	Coarse	Cosine	Cubic	Weighted	Boosted Trees	Bagged Trees	Subspace Discriminant	Subspace KNN	RUS Boosted Trees
5	Haar	94	96	96	56	95	88	94	91	75	90	88	93	92	95	90	96	84
6		94	97	96	58	96	89	95	93	75	93	91	94	90	96	88	97	83
5	db1	94	96	96	57	94	89	94	91	74	90	88	93	92	96	91	96	83
6		94	96	96	60	95	89	95	93	74	93	91	94	89	95	87	97	83
5	db2	90	93	93	33	93	82	91	87	62	89	80	90	88	96	85	93	82
6		86	92	92	57	92	81	91	88	65	89	84	90	84	94	80	94	73

The best trained model achieved under the 10-fold cross validation seen in Table 4.7 is 97% (highlighted in red), being 2% lower than the best trained model under 4 gestures. This promisingly shows only a small negative impact in the accuracy, whilst adding an additional 4 gestures to train. However, as seen previously, evaluating the model with unseen data establishes its true accuracy.

Table 4.8 Evaluated accuracy from the best trained model classifier type

		Evaluated Accuracy of the Trained Model (%)		
Level	Feature Selection	SVM	KNN	Ensemble
5	Haar	47 (Cubic)	52 (Fine)	60 (Subspace KNN)
6		47 (Cubic)	51 (Fine)	52 (Subspace KNN)
5	Db1	47 (Cubic)	52 (Weighted)	60 (Subspace KNN)
6		47 (Quad)	51 (Weighted)	51 (Bagged Trees)
5	Db2	50 (Quad)	55 (Cosine)	50 (Bagged Trees)
6		50 (Cubic)	56 (Weighted)	57 (Bagged Trees)

Table 4.8 above shows a significant decrease in accuracy after evaluating the best trained models for each classifier type with unseen data; achieving the highest accuracy of 60% under the Subspace Ensemble classifier, with the level 5, Db1 feature. The confusion matrix of the 60% model in Table 4.9 below clarifies where the prediction errors occur.

Table 4.9 Confusion Matrix of best evaluated model for 8 Gestures

True Class	Right	119	0	0	0	0	0	0	1
	Left	0	117	0	0	0	3	0	0
	Up	0	0	68	0	0	52	0	0
	Down	0	0	0	39	0	8	0	73
	Up-Right	3	2	21	3	7	4	70	10
	Up-Left	1	4	6	1	4	92	11	1
	Down-Right	5	0	0	17	11	0	2	85
	Down-Left	24	6	0	1	35	0	51	3
		Right	Left	Up	Down	Up-Right	Up-Left	Down-Right	Down-Left
		Predicted Class							

It is seen in Table 4.9 that the errors accumulate between the confusion of up and down gestures with the new additional gestures of up-left and down-left respectively. Also, the model predicts the down-right gesture as down-left and vice versa. It seems that the photocurrent signal does not differentiate enough between each gesture, resulting in these predicting errors shown in Table 4.9.

4.6 Conclusion

With HCI being an important factor when designing an IoT node, this Chapter investigates if a system can be designed to include a monolithic DSSC that not only harvests energy but also acts as a hand gesture recognition sensor.

Initial experimental studies found that using threshold detection as a suitable method for hand gesture recognition was unsuccessful, achieving a low accuracy of 11% (from 960 gestures). The reasoning behind such a low accuracy is down to the amplitude change under different light intensities, with normalising the data not being enough to accurately pre-define both the universal thresholding values. Therefore, the amplitude values scatters in an unexpected larger range, resulting in errors during thresholding. Also, the shape under lower light intensities of a 1000 Lux, seen in Figure 4.10 becomes less distinctive, resulting in the loss of the initial troughs that separate the right and down gestures with left and up gestures.

An alternative method of using ML to train classifiers results in a substantial improvement in the prediction accuracy of four directional hand gestures, achieving 98% (from the level 5 detail coefficient, wavelet feature Db1, under the classifier KNN (weighted)) from an unseen data-set. Analysis on reducing the computational

cost was also investigated, exploring if DTW was required alongside the alignment function. The results found that whilst including DTW, the model accuracy from evaluation was 3% greater than without.

Four additional gestures were also added, to find its success rate combined with the original gestures. With machine learning having a high success rate with the original four gestures, this technique was used to investigate if it could possibly predict up to 8 gestures. The additional gestures included the diagonal motion on the DSSC pattern, further exploring the linear directional hand gesture capabilities. The best model after evaluation with unseen data only achieved 60%, this time from the level 5 detail coefficient, wavelet feature Db1, under the classifier Ensemble (Subspace). This error in gesture prediction can be explained by the similarities in the shape of the photocurrent signal of the additional gestures with the original two gestures of up and down. This can be seen from the confusion matrix in Table 4.9.

This Chapter demonstrates that by monitoring the photocurrent output of an asymmetrical patterned monolithic (i.e., single cell) DSSC, and using machine learning, it can recognise simple hand gestures (right, left, up, and down), achieving an accuracy prediction of 98%. However, further optimisations can be investigated, looking into reducing the computational cost and power; and by reducing the sampling rate and data collection equipment. Additionally, it would be interesting to find the optimised active area pattern to recognise 8 gestures, with alternative DSSC fabrication layout, with the goal of re-producing similar photocurrent signal output.

Bibliography

1. Oudah M, Al-Naji A, and Chahl J. Hand Gesture Recognition Based on Computer Vision: A Review of Techniques. *Journal of Imaging* 2020; 6. DOI: 10.3390/jimaging6080073. Available from: <https://www.mdpi.com/2313-433X/6/8/73>
2. Ma D, Lan G, Hassan M, Hu W, Upama MB, Uddin A, and Youssef M. SolarGest: Ubiquitous and Battery-Free Gesture Recognition Using Solar Cells. *The 25th Annual International Conference on Mobile Computing and Networking*. MobiCom '19. New York, NY, USA: Association for Computing Machinery, 2019. DOI: 10.1145/3300061.3300129. Available from: <https://doi.org/10.1145/3300061.3300129>
3. Varshney A, Soleiman A, Mottola L, and Voigt T. Battery-Free Visible Light Sensing. *Proceedings of the 4th ACM Workshop on Visible Light Communication Systems*. VLCS '17. New York, NY, USA: Association for Computing Machinery, 2017 :3–8. DOI: 10.1145/3129881.3129890. Available from: <https://doi.org/10.1145/3129881.3129890>
4. Li Y, Li T, Patel RA, Yang XD, and Zhou X. Self-Powered Gesture Recognition with Ambient Light. *Proceedings of the 31st Annual ACM Symposium on User Interface Software and Technology*. UIST '18. New York, NY, USA: Association for Computing Machinery, 2018 :595–608. DOI: 10.1145/3242587.3242635. Available from: <https://doi.org/10.1145/3242587.3242635>
5. Duan H, Huang M, Yang Y, Hao J, and Chen L. Ambient Light Based Hand Gesture Recognition Enabled by Recurrent Neural Network. *IEEE Access* 2020; 8:7303–12. DOI: 10.1109/ACCESS.2019.2963440
6. Meena YK, Seunarine K, Sahoo DR, Robinson S, Pearson J, Zhang C, Carnie M, Pockett A, Prescott A, Thomas SK, Lee HKH, and Jones M. PV-Tiles: Towards Closely-Coupled Photovoltaic and Digital Materials for Useful, Beautiful and Sustainable Interactive Surfaces. *Proceedings of the 2020 CHI Conference on Human Factors in Computing Systems*. CHI '20. Honolulu, HI, USA: Association for Computing Machinery, 2020 :1–12. DOI: 10.1145/3313831.3376368. Available from: <https://doi.org/10.1145/3313831.3376368>

7. Thomas G. Shared Content - Matlab Codes for Gesture Detection. Available from: https://drive.google.com/drive/folders/1kug4AyVRtBWQpapsPx_eCAgNM2PnAb7?usp=sharing
8. MATLAB. normalize. Available from: https://uk.mathworks.com/help/matlab/ref/double.normalize.html#mw_a45727ad-ed25-4720-91fc-c47d5cd792d1 [Accessed on: 2021 Sep 29]
9. Ma D, Lan G, Hassan M, Hu W, Upama MB, Uddin A, and Youssef M. Gesture Recognition with Transparent Solar Cells: A Feasibility Study. *Proceedings of the 12th International Workshop on Wireless Network Testbeds, Experimental Evaluation & Characterization*. WiNTECH '18. New York, NY, USA: Association for Computing Machinery, 2018 :79–88. DOI: 10.1145/3267204.3267209. Available from: <https://doi.org/10.1145/3267204.3267209>
10. Tang J, Alelyani S, and Liu H. Feature selection for classification: A review. *Data classification: Algorithms and applications* 2014 :37
11. MATLAB. zscore. Available from: <https://uk.mathworks.com/help/stats/zscore.html> [Accessed on: 2021 Jul 29]
12. MATLAB. dtw. Available from: <https://uk.mathworks.com/help/signal/ref/dtw.html>
13. MATLAB. alignsignals. Available from: <https://uk.mathworks.com/help/signal/ref/alignsignals.html#buvrt30-1-Xa> [Accessed on: 2021 Aug 2]
14. MATLAB. Diagnostic Feature Designer. Available from: <https://uk.mathworks.com/help/predmaint/ref/diagnosticfeaturedesigner-app.html> [Accessed on: 2021 Aug 12]
15. MATLAB. wavedec. Available from: <https://uk.mathworks.com/help/wavelet/ref/wavedec.html#d123e91376> [Accessed on: 2021 Aug 10]
16. MATLAB. idwt. Available from: <https://uk.mathworks.com/help/wavelet/ref/idwt.html> [Accessed on: 2021 Aug 9]
17. MATLAB. Classification Learner. Available from: <https://uk.mathworks.com/help/stats/classificationlearner-app.html> [Accessed on: 2021 Aug 13]
18. Blum A, Kalai A, and Langford J. Beating the hold-out: Bounds for k-fold and progressive cross-validation. *Proceedings of the twelfth annual conference on Computational learning theory*. 1999 :203–8

Chapter 5

Optimising the Active Area Pattern of a Monolithic DSSC for Hand Gesture Recognition

5.1 Introduction

Chapter 4 provided a novel method of measuring and detecting four directional hand gestures (right, left, up, and down), from a monolithic DSSC with an asymmetrical active area pattern. This Chapter persists with the investigation of hand gesture recognition, aiming to expand the limits of using a monolithic DSSC and other photocurrent data capturing technologies.

Optimising the asymmetrical active area pattern would increase the number of hand gestures that the DSSC can recognise. The Chapter explores the computational optimisation of the active area pattern to achieve eight directional hand gesture recognition with high accuracy prediction, when previously only achieved an accuracy prediction of 60% in Chapter 4. Expanding the number of gestures recognised would enhance the interaction, allowing users to interact with devices in a more nuanced and expressive manner. It would also provide a richer user experience and increased functionality, by enabling the device to perform a wider array of functions. Overall, by increasing the number of recognised hand gestures by a DSSC offers a more versatile, user-friendly, and adaptable gesture recognition experience. This Chapter also introduces alternative DSSC fabrication and data capturing methods, attempting to increase the overall output power of the DSSC and reducing the computational cost.

5.2 Computational modelling of different patterns for gesture optimisation

This Section attempts to produce an optimised active area pattern on the monolithic DSSC. By modelling different active areas on the DSSC, this increases throughput of the results outcome but also substantially reduces the material usage and cost, as no DSSCs are fabricated until the final design. The goal is to improve the gesture recognition accuracy for 8 direction hand gestures, being the original four (right, left, up, and down)(see Section 4.2.3.2), and the four additional diagonal directional gestures, introduced in Section 4.5.

5.2.1 Computer model set-up

A model on LabVIEW was created by Dr Adam Pockett (post-doctorate researcher at Swansea University), shown in Figure 5.1, outputs the photocurrent signals of each gesture swipe using different active area patterns designed for optimisation. There are some factors which are not considered in the model, these include: light intensity; and the user's parameters (such as the speed and height of the hand), except for hand size. The hand size parameter can be controlled by altering the width size of the scanning area bar, with Figure 5.1 showing an example of the scanning bar (in red) being a ratio of 0.2 of the bed width.

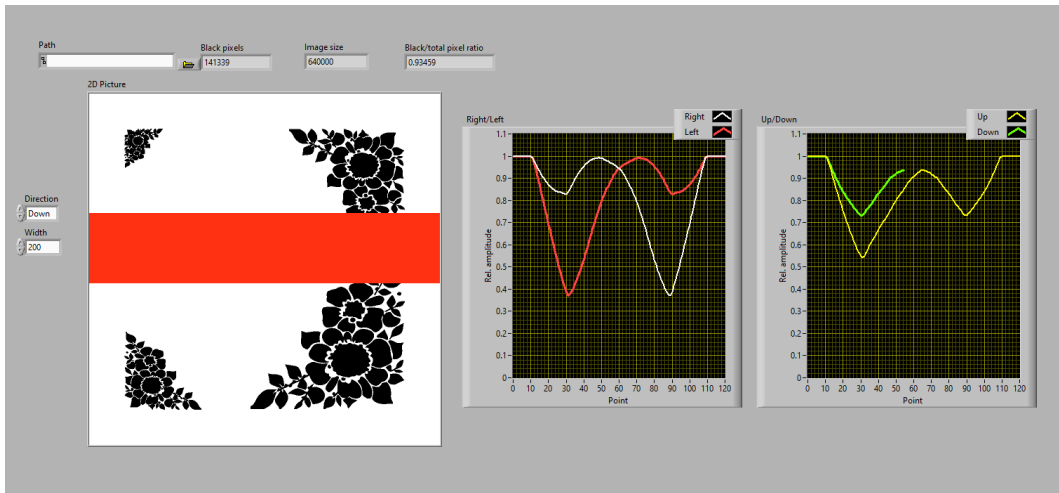


Figure 5.1: Example of the Model in LabVIEW, with a bar width ratio of 0.2

5.2.1.1 Signal comparison and optimisation

The computer model can be applied to discover patterns that might achieve a higher recognition accuracy compared to the initial design. Prior to undertaking this, the model outputs must be verified with the original signal outputs from the DSSC.

This is done by scanning the preliminary design using the model and comparing this with the DSSC signal outputs from the previous Chapter, replicating the signals as best as possible by adjusting the scanning width bar, mimicking the user's hand. The width bar value can be set to a ratio of the scanning bed, meaning that a value of 1 is the maximum width of the bed.

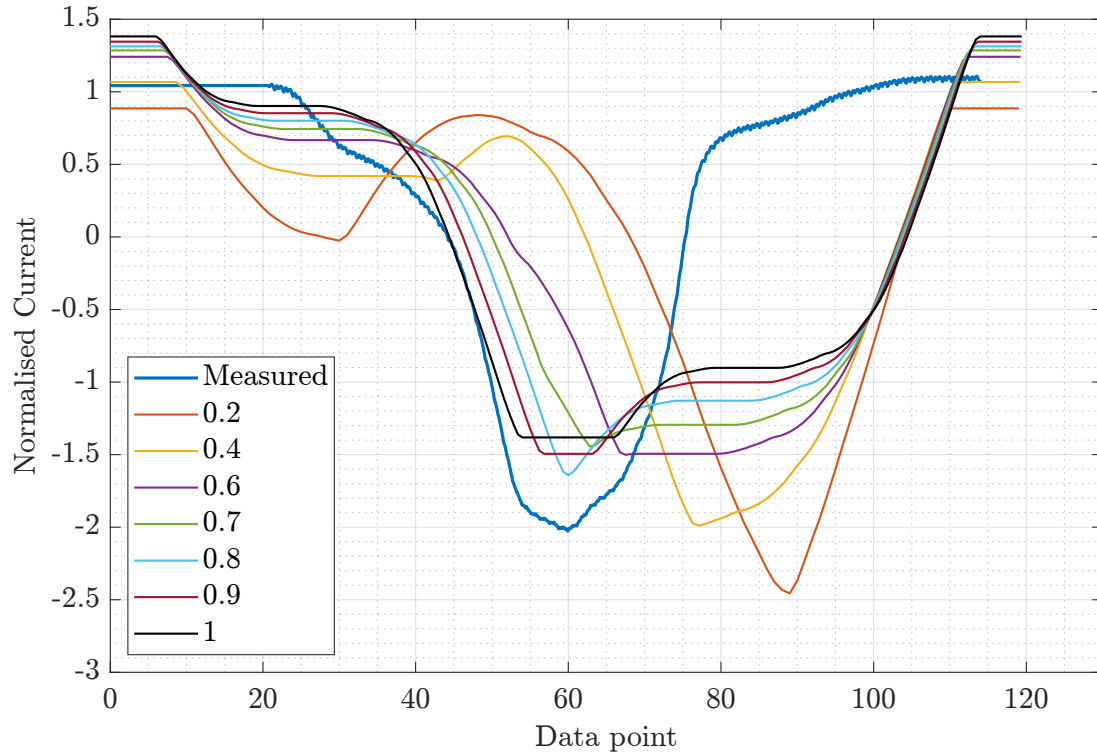


Figure 5.2: Right Swipe Gesture model output using different width bar sizes compared to DSSC measured data at 1000 Lux

Figure 5.2 above compares the modelling right gesture sweep output at different bar width ratios with a measured normalised photocurrent signal. The results show some differences when comparing the model data with the measured data, including:

- The model does not consider the speed of the user's hand, resulting in all photocurrent models having a longer signal affect compared to the measured signal (the true data in this case has been measured with a higher hand velocity).
- When the width bar is increased from a ratio of 0.2 to 1, the largest trough (being in the normalised current range of -1.5 to -2.5) can be seen to shift to the left, with a decrease in gradient of the signal towards 0.

A ratio of 0.8 seems to be the curve that has the most resemblance to the measured photocurrent signal. Whilst not having the same minimum normalised current amplitude, the shape of the trough at -1.6 normalised current is very similar to the

trough of the measured data, compared with a ratio of 0.6 and 0.9 having a lower gradient. A ratio of 0.4 has the best similarities in amplitude, however, a peak is formed at data point 52, similarly with the 0.2 signal, which does not replicate the signal output from the DSSC. This is due to the scanning bar not covering enough of the active area whilst swiping towards the two largest areas of 3.6 cm^2 and 6.3 cm^2 .

A band width ratio of 0.8 is selected as the bar for the computational model due to its similarities with the true photocurrent output. Figure 5.3 below shows the output of the solar cell for each gesture compared to the model output at the selected width ratio of 0.8.

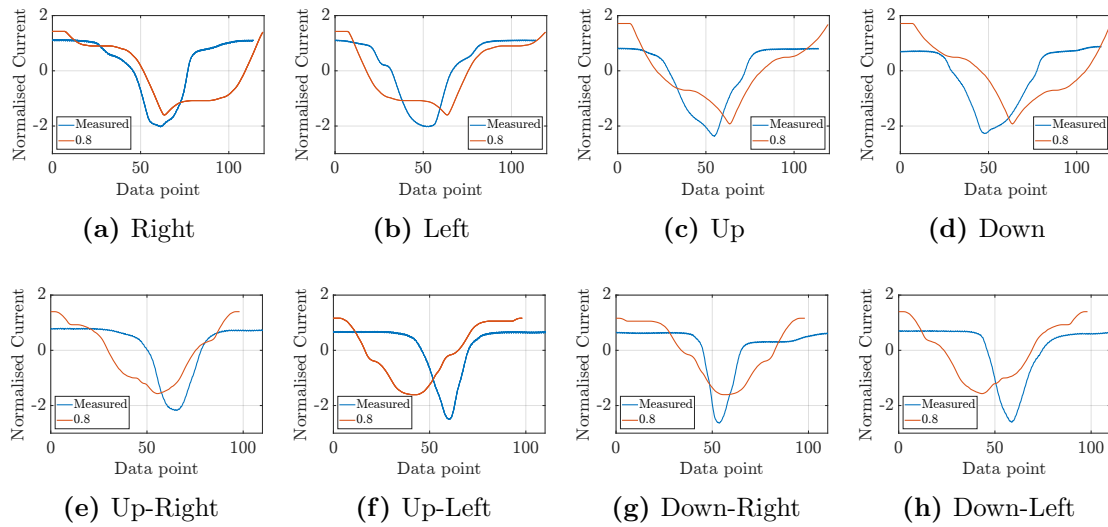


Figure 5.3: Comparing all eight gesture photocurrent outputs with the model outputs at a width bar ratio of 0.8

Disregarding that there is a large temporal misalignment, due to the computer model from LabVIEW not considering the user's hand speed, the results shown in Figure 5.3 have some promising resemblance between the model and the measured data from the DSSC for each gesture. There are some slight differences between both, such as the signals of the diagonal gestures from the model have a slight decrease in gradient before and after the main trough, not shown in the true measured data. However, the four diagonal model signals still show close similarities between each other, like what is portrayed from the measured data, which is why the resultant prediction accuracy was low (being 60%) in Chapter 4.

5.2.2 Active area optimisation

Before designing new patterns for gesture optimisation, there are some factors to consider, these include:

- The total active area, as this will reflect on the maximum power that can be harvested from the solar cell;
- The active area being too far apart, not allowing the user to cover the required pattern for gesture recognition;
- Initially concentrating on the signal output, therefore not considering how the pattern appears aesthetically (This can be altered when the desired signal output has been achieved);
- The DSSC size should be kept the same as the initial preliminary design in Chapter 4, being $8 \times 8 \text{ cm}$;
- Consider how the signal pre-processing technique for machine learning re-aligns each signal using the largest trough as its central point;
- From comparing the original cell data and the modelling data from Figure 5.3, keep in mind that the signal shape is less pronounced from the fabricated cell.

5.2.2.1 Pattern design and development

Twenty four different black and white patterns are explored in Appendix A.1. Each design was created in bitmap form, through the design software CorelDRAW, of 800 x 800 black (representing the active area) and white (representing no active area) pixels, with the output signals exported from the LabView Model for each of the eight gestures. Some initial ideas for new patterns revolved around the preliminary design (flower pattern), which achieved a remarkable 98% for the four directional gestures. Other new designs were created randomly with a mixture of different shapes to explore the output photocurrent signal.

Design idea 2,3,4 and 5 are like the original pattern, seen in Figure 5.4, having the same area in each corner (6.3 cm^2 , 3.6 cm^2 , 1.7 cm^2 and 0.5 cm^2) but using different shapes.

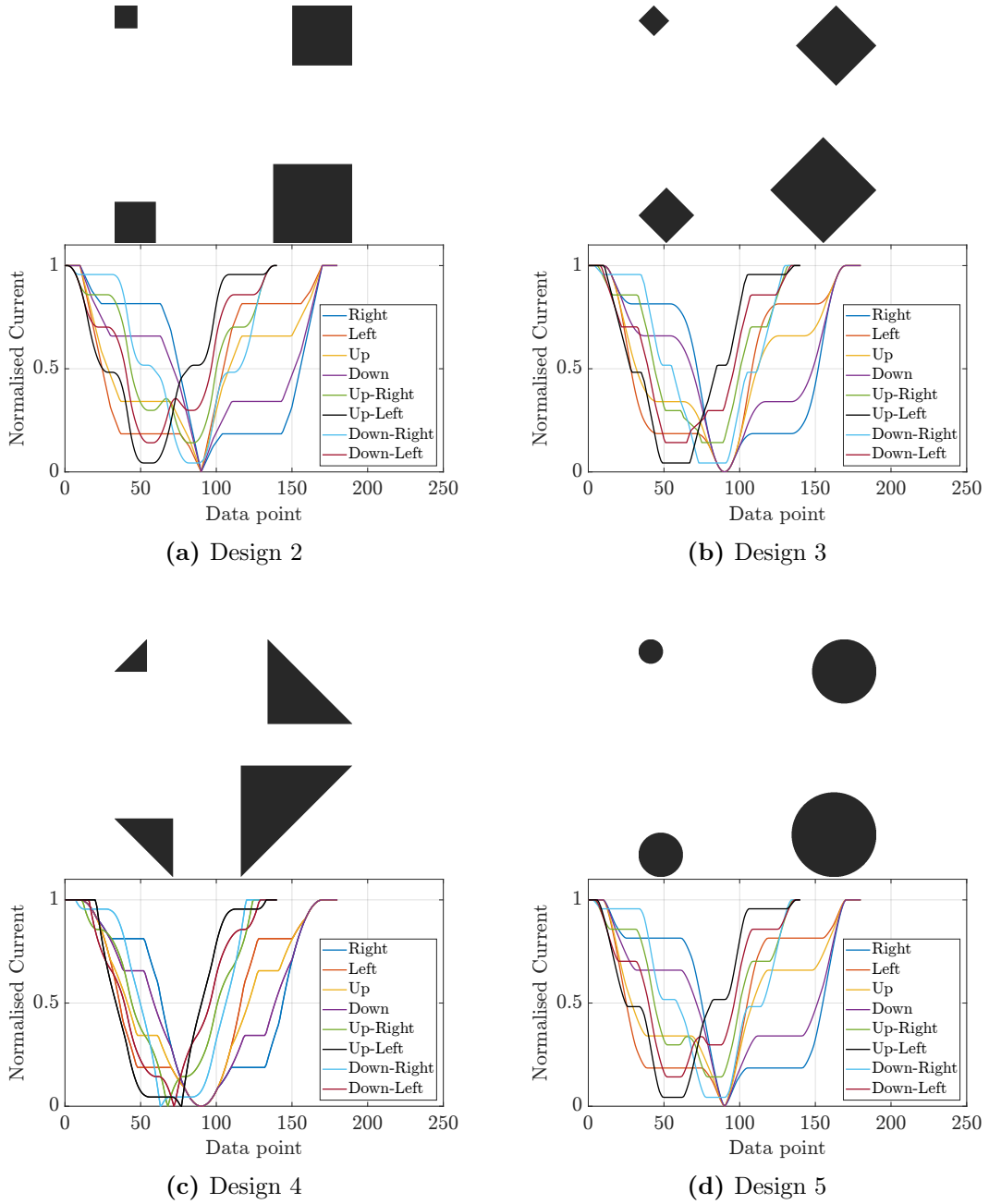


Figure 5.4: Adaption designs from the original flower pattern using same active area

Designs 2 and 5 show good differentiation between each gesture, with a peak forming with gesture up-right and down-left, with the signal being sharper using the circles. This can be seen to slightly disappear in design 3 and completely disappear in design 4, resulting in similarities between each gesture signal.

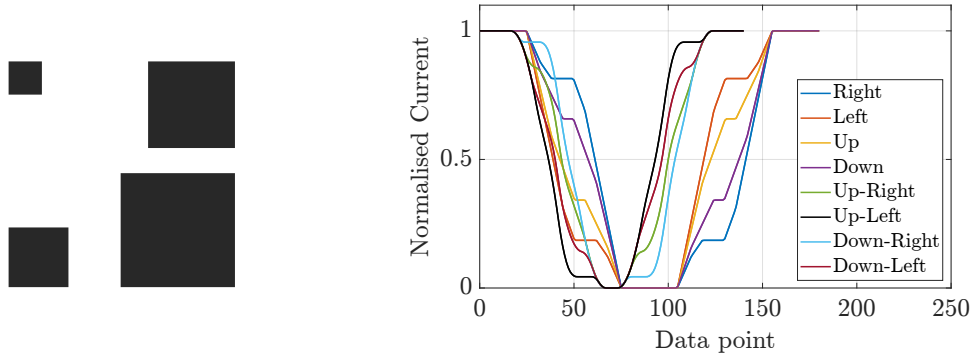


Figure 5.5: Design idea 6

Design 6 in Figure 5.5 above has the squares moved closer to the centre compared to design 2. The signal output becomes less distinct compared to the signal output in design 2, because of the shapes being too close to each other, reducing the time for the bar to swipe from one shape to another, ‘blocking’ any photocurrent to be produced.

Other patterns explored the combination of using different size geometries in each corner, with additional shapes in the centre. Design 16 seen in Figure 5.6 below showed some promising signal differences between each gesture, evolving from design 3 but reducing the areas and adding two additional squares asymmetrically in the centre.

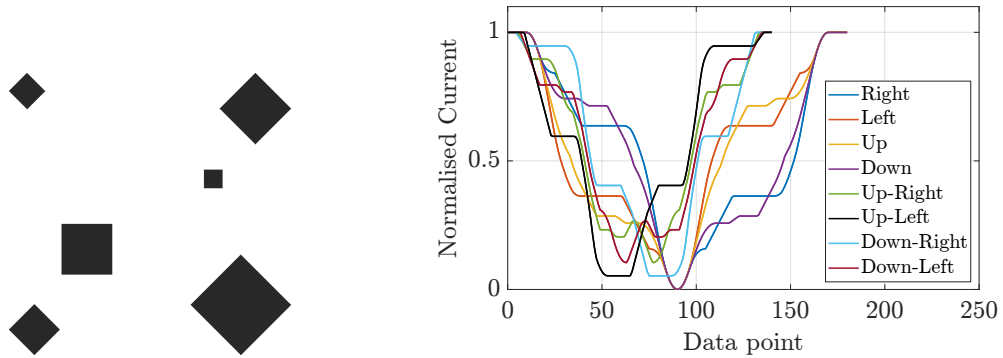


Figure 5.6: Idea Pattern 16

Triangular, rectangular, and curvature-based geometries were also explored, however, these all resulted in the output signals for each gesture being too identical to one another and therefore being disregarded. The conclusion following the initial pattern testing from Appendix A.1, is that designs 5 and 16 have the most distinct differences in the signal output of the horizontal, vertical, and diagonal gestures. Both patterns can be further investigated to find the optimised output signals.

5.2.2.2 Pattern optimisation and final selection

The optimisation begins by improving the signal outputs from design 5. Currently, the signal between the up-left and down-right signals are very similar, which might lead to confusion by the trained model. Appendix A.2 covers the optimisation process, detailing further on how the geometry change affects the signal outputs. The results concluded that step 4 has the best pattern design outcomes seen in Figure 5.7, having the largest difference in photocurrent signal between each directional gestures.

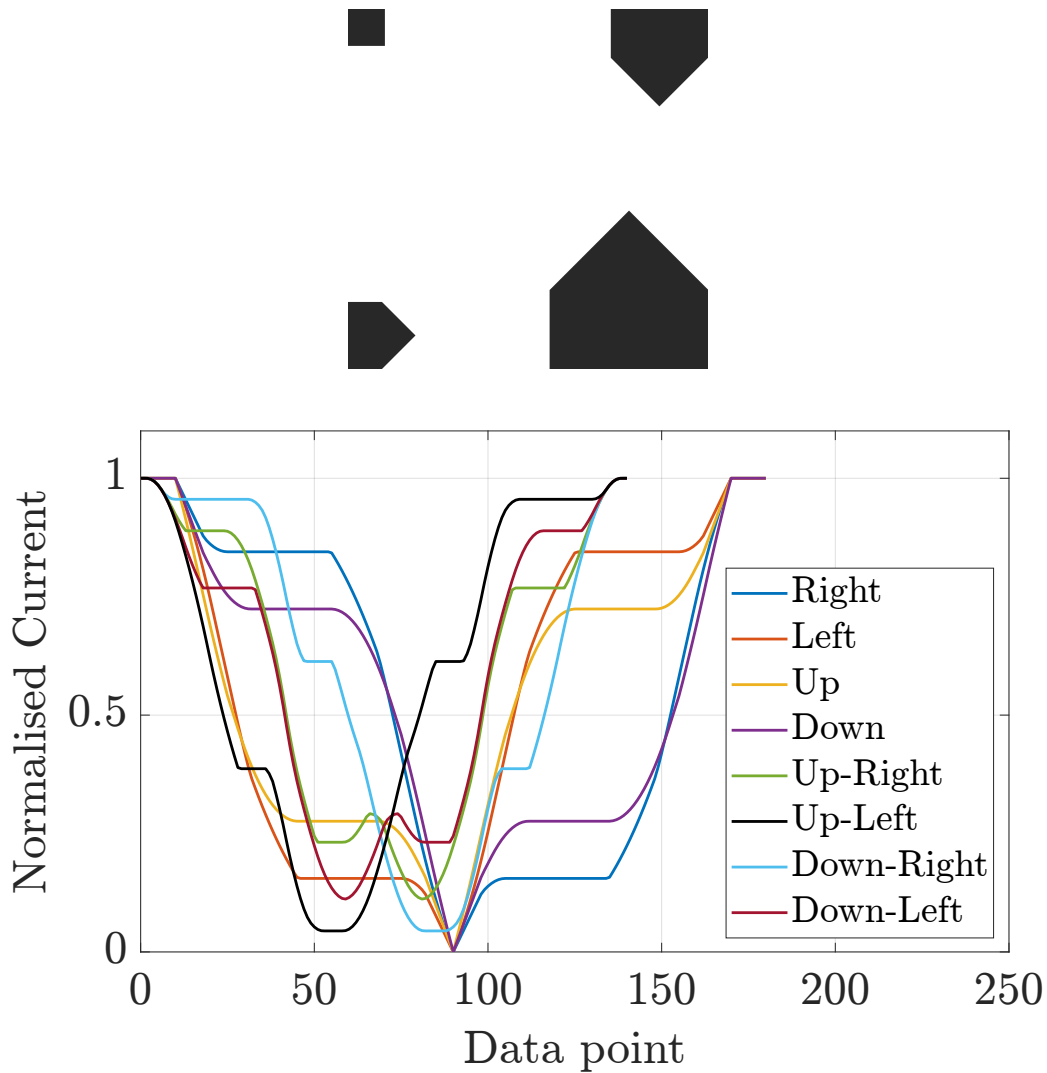


Figure 5.7: Step. 4

The design from Figure 5.7 can now be further optimised by integrating with design 16. This way it can increase the total active area of the DSSC, increasing its final power output. The pattern in step 8, shown in Figure 5.8 below demonstrates that the only possible location that the new shapes can appear is in the red circle box, otherwise, it can impact on the shape of the signals previously optimised after part 1.

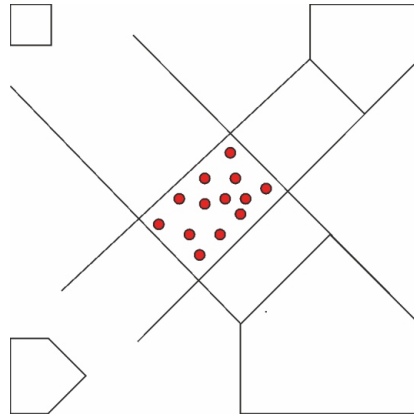


Figure 5.8: Geometry restriction

Several different iterations were attempted, with step 13 achieving the best signal differences with the additional active area, shown in Figure 5.9.

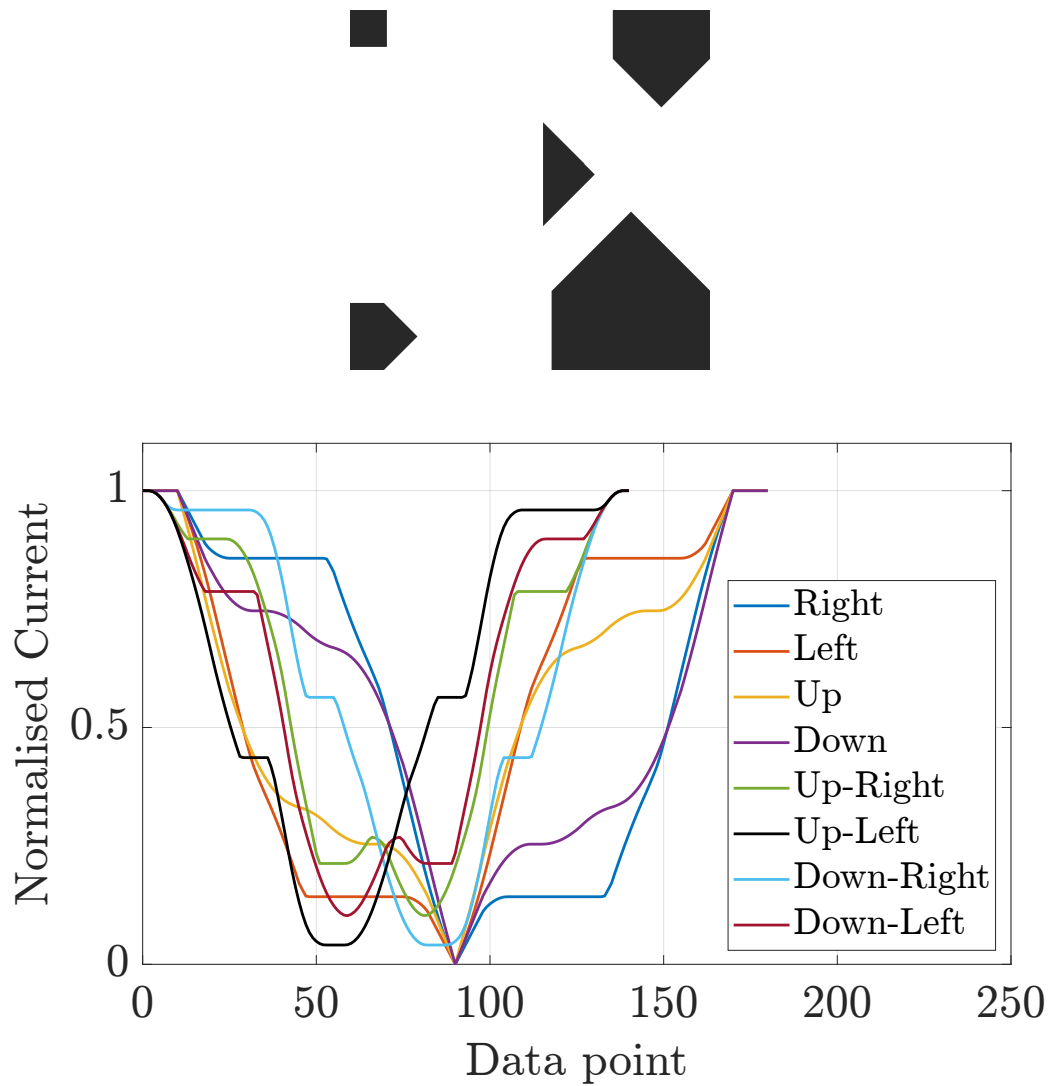


Figure 5.9: Step. 13

A further and final attempt of increasing the active area was achieved by adding an

additional background to the whole solar cell. Different spacing and shape area sizes were modelled, with the best signal output (step 20) being the 1.5 mm diameter circles, 10 mm apart, seen in Figure 5.10.

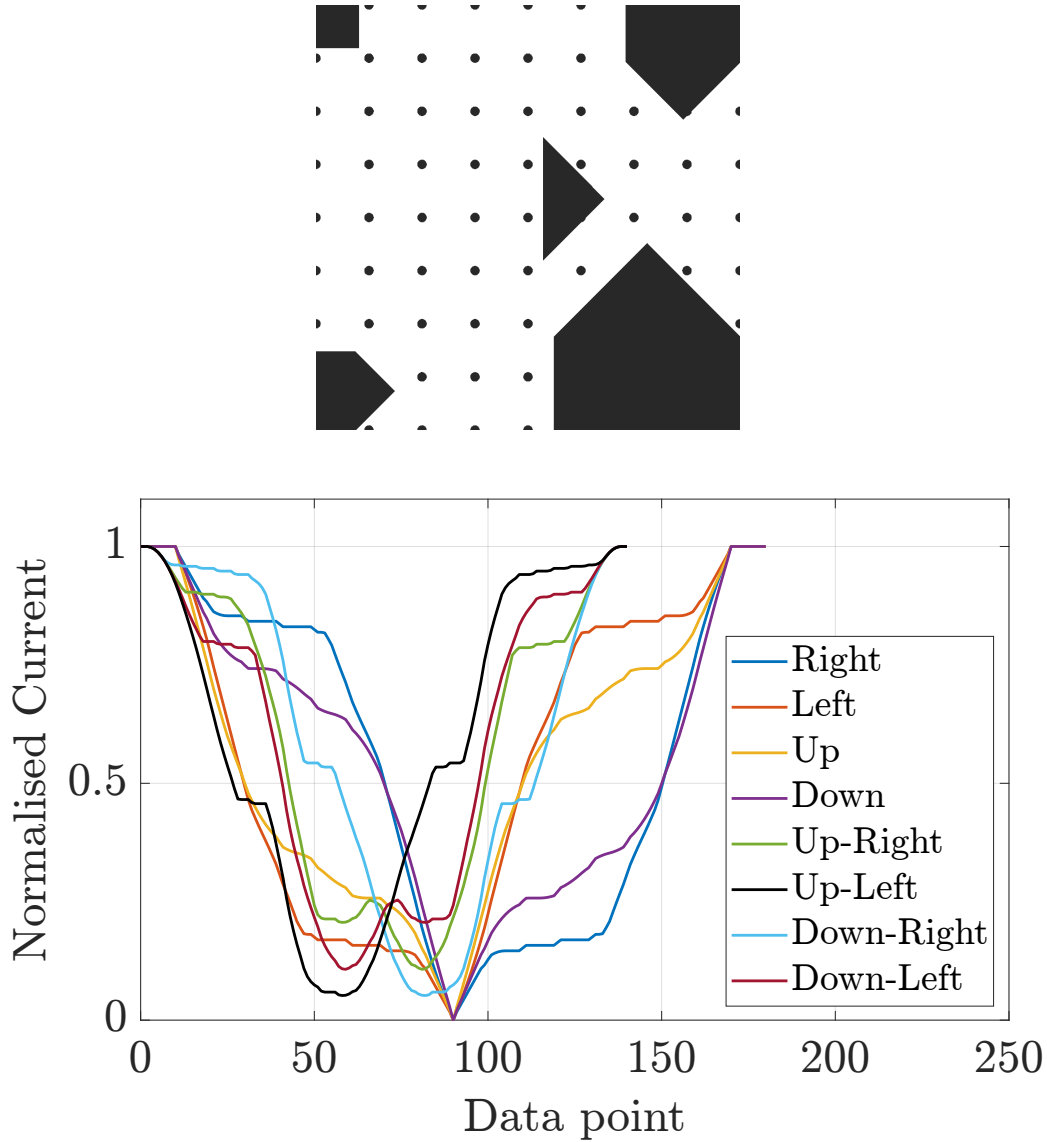


Figure 5.10: Step. 20

5.2.3 Results and discussion

The three optimised design patterns from Figure 5.7, Figure 5.9, and Figure 5.10 are fabricated and tested following the same machine learning steps achieved in the previous Chapter. The only difference is the electrolyte used compared to the flower pattern DSSC in Chapter 4. The previous Chapter used the AN-50 electrolyte, whilst this Chapter uses the 50 mM (HM) solution fabricated from Chapter 3. Whilst it would have been ideal to use the same electrolyte as the flower pattern, difficulties arose due to internal ordering issues with international suppliers. As

investigation of Chapter 3 was conducted alongside this Chapter, initial evidence showed that the 50 *mM* (HM) was adequate as an alternative electrolyte. Other materials used such as the dye and CE materials are the same.

A justification summary for using different electrolytes in various Chapters are shown below in Table 5.1

Table 5.1 Justification for the use of different electrolytes in various Chapters

Chapter	Investigation	Electrolyte used	Justification for use
3	Determining the best electrolyte for indoor use	5 mM (HM)	Resulted in the best output performance in indoor conditions for small and large active areas. Due to COVID restrictions and lockdowns, the timescale of this Chapter was undertaken throughout Chapters 4, 5 and 6.
4	Initial flower pattern design	AN-50	This Chapter was worked alongside Chapter 3; therefore, the optimum was not established, with the AN-50 being a readily available electrolyte to use.
5	Optimised DSSCs, being pattern 1, 2 and 3. This also includes the etched FTO DSSC.	50 mM (HM)	Due to internal ordering barriers to obtain additional AN-50, the 50 mM (HM) electrolyte was used instead. Initial evidence from Chapter 3 showed promising results as an alternative electrolyte.
6	PV-PIX and light-based prototypes	AN-50	Again, this electrolyte was used due to being readily available, with the optimum not established.
6	Optimised Moiré pattern	5 mM (HM)	The optimal electrolyte from Chapter 3 was discovered and implemented into the optimised Moiré pattern DSSC.

The ML analysis steps for each DSSC pattern include:

1. Data collection of 120 swipes for each of the 8 gestures, under light intensity of 1000 and 2500 Lux.
2. Pre-processing and feature extraction for half of the data collected at a 1000 and 2500 Lux. This involves Z-score transformation and DTW for amplitude and temporal misalignment. The best performing features have been carefully selected from the previous Chapter, being levels 5 and 6 detail coefficients of wavelets Haar, Db1 and Db2.
3. Classifiers are trained through MATLAB, again from the best performed classifiers investigated in Chapter 4, being support vector machines (SVM), nearest neighbour classifiers (KNN), and ensemble classifiers, following the 10-fold cross validation.

- The trained models are finally used to validate unseen data-set (the other half of the data-set not trained at a 1000 and 2500 Lux), to find the best performed classifier and DSSC active area pattern.

5.2.3.1 Fabricated DSSCs

The three DSSCs are presented below in Figure 5.11, with pattern 1 being the initial optimised design to pattern 3, having the increased active area applied.

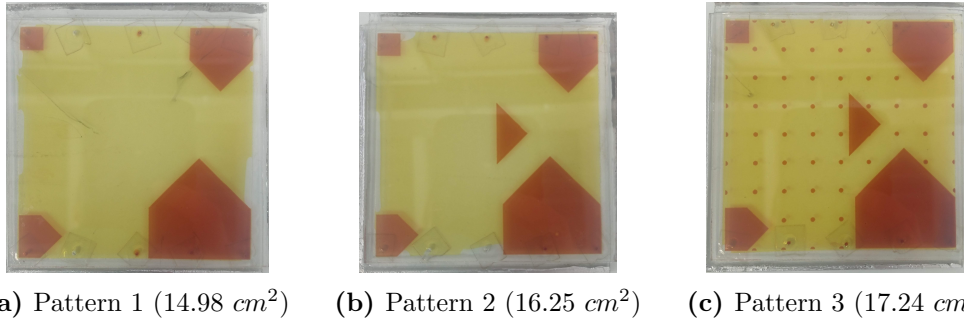


Figure 5.11: Fabricated 3 Cells from the optimised steps progression in Appendix A.2

5.2.3.2 Machine learning outcome

Each cell undertakes the vigorous pre-processing techniques and feature extraction, prior to undergoing training, where the accuracy results from the 10-cross validation for 8 gestures are shown in Appendix C.1. However, as previously discovered in Chapter 4, the values do not resemble the true accuracy of the trained models.

The true accuracy can be explored by running the trained models with the unseen data-set. Table 5.2, 5.3, and 5.4 show the evaluated accuracy of the 3 optimised patterned cells, with the best in each highlighted in red.

Table 5.2 Trained model accuracy for pattern 1 (14.08 cm^2)

		Model Type Accuracy %																
Level	Feature Selection	SVM						KNN						Ensemble				
		Linear	Quadratic	Cubic	Fine Gaussian	Medium Gaussian	Course Gaussian	Fine	Medium	Coarse	Cosine	Cubic	Weighted	Boosted Trees	Bagged Trees	Subspace Discriminant	Subspace KNN	RUS Boosted Trees
5	Haar	55	60	62	16	54	48	59	47	37	46	45	51	41	48	53	53	39
6		54	60	61	15	55	50	56	45	36	46	45	49	39	47	46	50	25
5	db1	55	60	62	16	54	48	59	47	37	46	45	51	41	54	52	53	39
6		54	60	61	15	55	50	56	45	36	46	45	49	39	49	46	40	25
5	db2	52	53	54	14	49	44	48	42	40	44	40	44	41	45	49	49	38
6		52	57	59	13	55	44	51	46	37	46	44	48	43	48	45	54	33

Table 5.3 Trained model accuracy for pattern 2 (16.25 cm^2)

		Model Type Accuracy %																
Level	Feature Selection	SVM						KNN						Ensemble				
		Linear	Quadratic	Cubic	Fine Gaussian	Medium Gaussian	Course Gaussian	Fine	Medium	Coarse	Cosine	Cubic	Weighted	Boosted Trees	Bagged Trees	Subspace Discriminant	Subspace KNN	RUS Boosted Trees
5	Haar	39	46	46	13	47	32	36	30	23	31	30	32	37	42	48	43	30
6		43	47	43	13	45	31	36	30	23	31	28	32	31	38	43	39	28
5	db1	39	46	46	13	47	32	36	30	23	31	30	32	37	46	48	44	30
6		42	47	43	13	45	31	36	30	23	31	28	32	31	36	44	41	28
5	db2	49	54	54	13	45	50	57	55	40	54	54	57	49	46	48	57	48
6		46	50	50	13	45	46	51	45	33	43	46	47	40	49	47	55	37

Table 5.4 Trained model accuracy for pattern 3 (17.24 cm^2)

		Model Type Accuracy %																
Level	Feature Selection	SVM						KNN						Ensemble				
		Linear	Quadratic	Cubic	Fine Gaussian	Medium Gaussian	Course Gaussian	Fine	Medium	Coarse	Cosine	Cubic	Weighted	Boosted Trees	Bagged Trees	Subspace Discriminant	Subspace KNN	RUS Boosted Trees
5	Haar	82	79	77	17	72	76	72	76	71	75	72	76	69	75	80	80	52
6		81	76	71	20	70	75	72	72	68	73	69	73	72	73	78	78	71
5	db1	82	79	77	17	72	76	72	76	71	75	72	76	69	74	81	80	52
6		81	76	71	20	70	75	72	72	68	73	69	73	73	67	78	79	71
5	db2	80	83	83	17	74	79	69	71	57	77	68	72	66	80	75	75	57
6		81	82	82	14	70	78	75	75	68	74	71	75	78	79	74	78	71

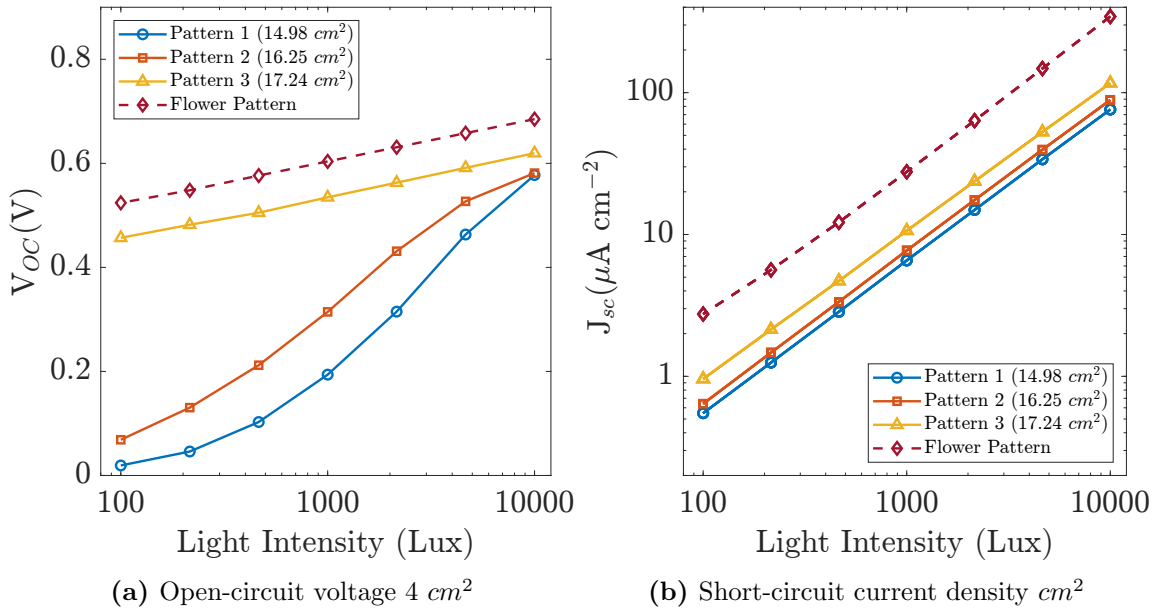
Initial results from pattern 1 in Table 5.2 indicates a similar trend experienced in Chapter 4, Section 4.5.1, with the best trained model achieving 62%, like the flower pattern design achieving 60% (Table 4.8). Pattern 2 also has similar poor results, only achieving a maximum value of 57%. Remarkably, the third pattern, optimised for additional active area achieved an accuracy prediction of 83%. Illustrated below is the confusion matrix (Figure 5.5) of the best evaluated model from pattern 3. The largest confusion error was between incorrectly predicting the up-left gesture with up, leading to a correct accuracy prediction of 63% for the up-left sweep.

Table 5.5 Confusion Matrix of best evaluated model from pattern 3 (17.24 cm^2)

True Class	Right	116	1	0	0	2	1	0	0
	Left	0	116	0	0	0	3	1	0
	Up	0	0	95	6	2	14	3	0
	Down	0	0	13	83	13	2	2	7
	Up-Right	0	4	1	0	104	6	5	0
	Up-Left	0	2	36	1	1	75	5	0
	Down-Right	2	0	0	0	0	1	114	3
	Down-Left	0	0	4	18	0	2	0	96
		Right	Left	Up	Down	Up-Right	Up-Left	Down-Right	Down-Left
		Predicted Class							

5.2.3.3 DSSC performance for each pattern

The performance characteristics of each pattern is measured below in Figure 5.12 under low light conditions, and compared against the flower pattern design (which involves the AN-50 electrolyte) fabricated in Chapter 4.



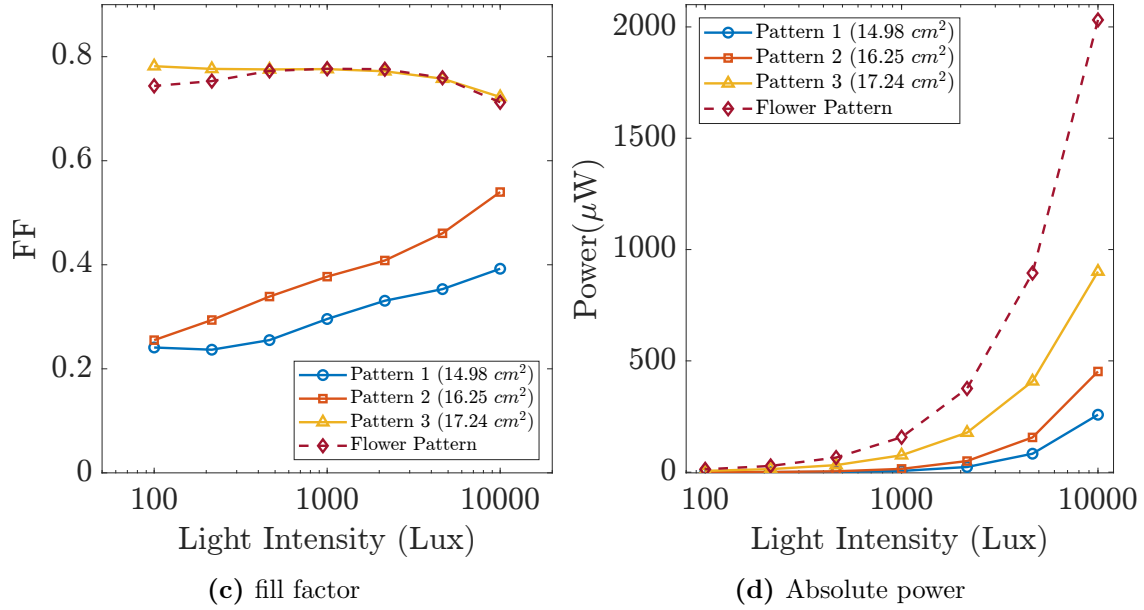


Figure 5.12: DSSC design pattern comparison

The results in Figure 5.12 immediately show that the best performing cell is from the flower pattern DSSC compared to three optimised patterns, with a larger power output seen in Figure 5.12d. The three pattern DSSCs has a lower short current density and open circuit voltage output at each light intensity compared to the flower pattern DSSC. This is most likely due to the change in electrolyte used, where Chapter 3 demonstrates that the AN-50, used in the flower pattern, does perform better compared to the 50 mM (HM) for small to medium sized active area cells, where the outcome showed a larger V_{OC} and J_{SC} values (see Section 3.3.1.2).

Patterns 1 and 2 under-performed compared to pattern 3 (achieving 83% accuracy), with only a slight increase in active area between them. The V_{OC} for patterns 1 and 2 significantly drops between 5000 and 100 Lux, with a change in slope of V_{OC} to intensity relationship. This is the probable cause for the poor accuracy predictions from the design patterns 1 and 2, only achieving 60% and 57%, as the data capturing method involves measuring the voltage difference between a known resistor, in order to measure the current. If there is a lower voltage output, then the differential before and after will be lower, reducing the photocurrent output accuracy and hence reduce the amplification of the shape of the curve.

A possible reasoning behind such a drop in V_{OC} for patterns 1 and 2 could be because of the electrolyte void in the centre, with no additional active area, increasing the recombination rate of electrons at lower light intensities. In order to prove this, a further experiment is required in order to visualise the performance of DSSCs with different electrolyte void sizes involving the homemade electrolyte solution.

5.2.3.4 Testing different void areas

The schematic set-up layout to investigate the effect of changing the space between the dyed active area and only electrolyte is shown below in Figure 5.13 that involves testing three different areas of 4 cm^2 , 9 cm^2 , and 25 cm^2 . In all cases the active area in the centre is maintained at 1 cm^2 .

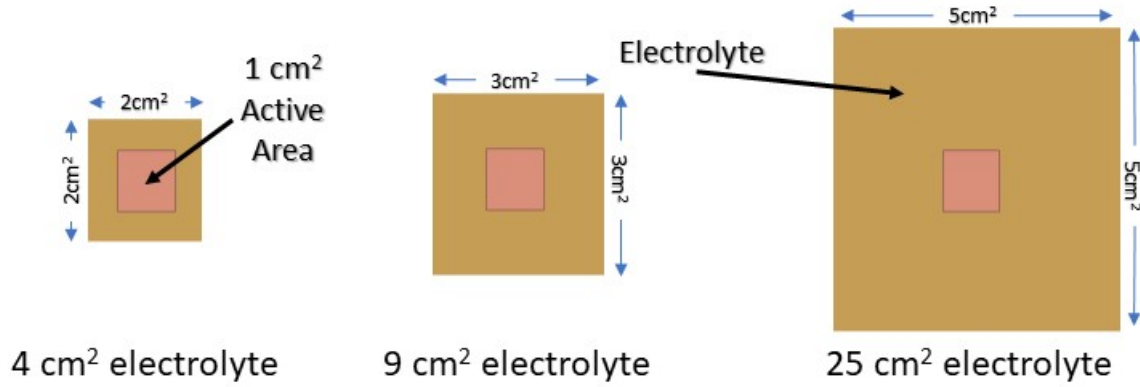
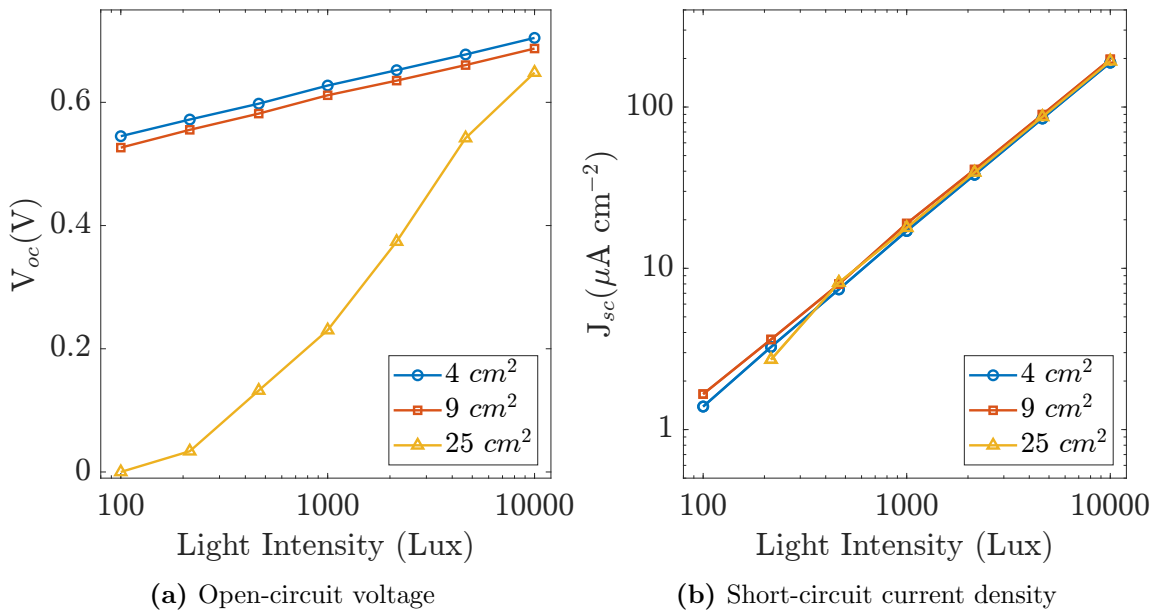


Figure 5.13: Changing the electrolyte area around a 1 cm^2 active area

The performance results are shown below for the 50 mM (HM) solution in Figure 5.14, with the 5 mM (HM) also tested and shown in Appendix B.



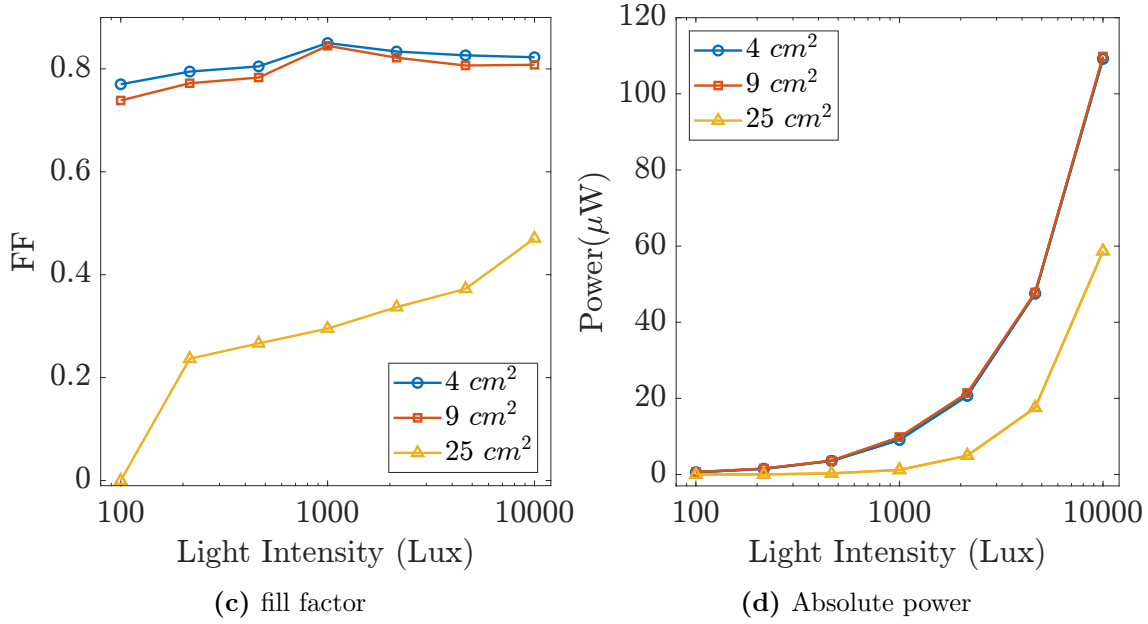


Figure 5.14: 50 mM (HM) DSSC performance characteristics of changing the electrolyte area around a 1 cm^2 active area

By comparing the results from Figure 5.12 and Figure 5.14, there is a clear resemblance between the V_{OC} of patterns 1 and 2 (see Figure 5.12a) with the V_{OC} of the 25 cm^2 electrolyte area DSSC (see Figure 5.14a), having a slope below 5000 Lux. Generally, the J_{SC} is well behaved for each void size, agreeing with the results in Figure 5.12, showing no limits due to series resistance. Overall, Figure 5.14 provides the additional evidence to show that an increase in the electrolyte void (over 20 mm away from the centre 1 cm^2 active area) and low light intensity, will cause the V_{OC} and FF to decrease significantly due to charge recombination. This relationship is also the same for the 5 mM (HM) electrolyte, presented in Appendix B, concluding that the HM electrolytes are susceptible to an increase in the rate of charge recombination, if the electrolyte void is too large.

This also provides the reasoning as to why the pattern 3 characteristic performance (see Figure 5.12d) was better, due to the additional active area circles plotted over the entire DSSC (10 mm apart), reducing the gap between the electrolyte and the active areas (see Figure 5.11c).

5.2.3.5 Changing the active area appearance

The optimised active area design, being pattern 3, is not very aesthetically pleasing, with random geometric shapes scattered on the DSSC. An example of an aesthetically pleasing design, which is still in the constraints of pattern 3 (shown with dotted red lines) is shown below, in Figure 5.15, with Figure 5.16 demonstrating how detailed the images can be printed on a DSSC.



Figure 5.15: Re-design of pattern 3, showing the constraints



Figure 5.16: Re-designed detailed pattern on a DSSC

5.3 Invisible gesture detection

5.3.1 Introduction

With a successful optimisation of detecting 8 gestures on a patterned monolithic DSSC, further experimental changes on the DSSC fabrication method could result in a better visually appearing cell, ideal for HCI.

A good visual appearance of the cell would be one without the distinct pattern of the active area, which previously was required to generate the distinct photocurrent outcome. A potential alternative method for this would be to etch the FTO layer from the working electrode, whilst screen printing a uniform TiO_2 layer. This will

result in an appearance of a normal DSSC cell, however, the asymmetrical etched FTO on the working electrode allows for a distinguishable difference in the photocurrent output for each directional hand gesture.

The FTO can be etched by using zinc oxide and 4 *M* of hydrochloric acid (HCL). The effect of the etched FTO layer areas can be assumed that there is no electron transfer taking place, similar to the yellow void of electrolyte seen in Figure 5.11.

To simplify the process and to initially demonstrate that this method is feasible, the flower pattern is used to detect the 4 basic gestures (horizontal and vertical directions), such as in the previous Chapter. This pattern needs to be fully simplified into solid triangles, as etching the flower pattern would require a high precision laser cutter to complete this.

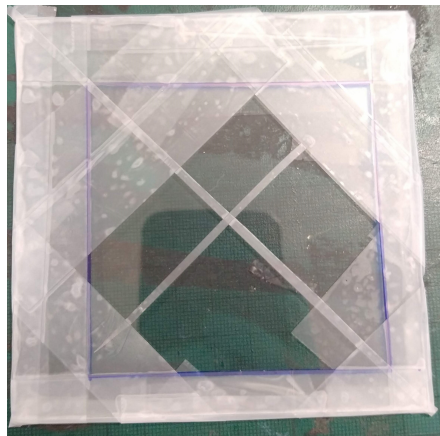


Figure 5.17: Masking the active area before etching

Figure 5.17 above demonstrates the initial step of etching the FTO, before applying the BL. To make sure that the charge transport was not affected between each corner, a thin pathway was also created in the centre, to allow for an efficient response of the photocurrent. The zinc oxide powder can now be applied on the FTO side, dropping the HCL onto the powder and scrubbing the layer away. Once this is completed, the process is identical to the normal process of fabricating a DSSC, with the blocking layer being the next step then screen printing the TiO_2 layer. The dyed working electrode can be seen in Figure 5.18a below, where the etched FTO can be faintly seen. The completed cell seen in Figure 5.18c shows its transparency, with no real sign of the FTO being etched.

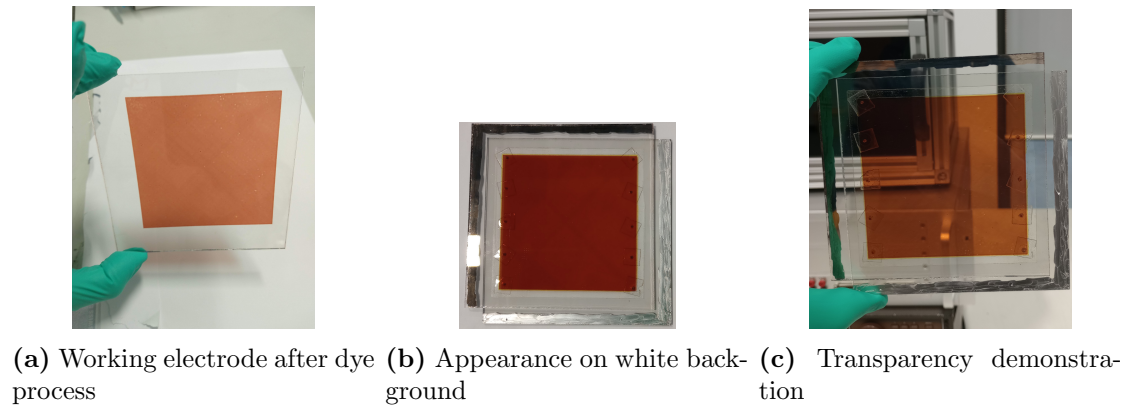


Figure 5.18: Final fabricated appearance of the etched FTO DSSC

Figure 5.19 shows the photocurrent output signal of the 4 gestures. There are good similarities between signals right and left, and up and down gestures, being nearly mirrored to one another. There is also a good signal difference between each gesture, meaning that the asymmetrically etched FTO has been successful. The active area will be adopted as the area with FTO underneath the TiO_2 layer. However, the area calculated will be an assumption that all the FTO was correctly etched from the correct areas.

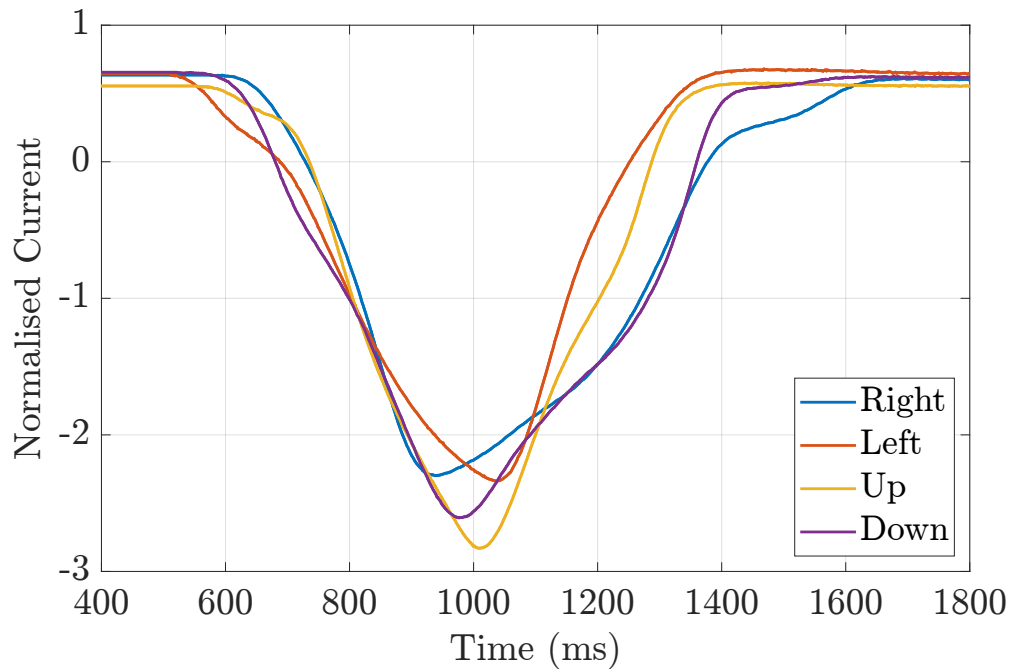


Figure 5.19: Photocurrent signal output for Etched FTO DSSC

5.3.2 Results and discussion

5.3.2.1 Machine learning outcome

Once again, a large data-set of gestures is collected, of 120 swipes per gesture, at a light intensity of 1000 and 2500 Lux. The trained models produced from using half

of the 1000 and 2500 Lux data-set is shown in the Appendix C.2, with the evaluated trained model on the unseen data-set on the other half of the 1000 and 2500 Lux data-set is shown below in Table 5.6.

Table 5.6 Evaluated trained model accuracy for etched FTO DSSC

		Model Type Accuracy %																
Level	Feature Selection	SVM						KNN						Ensemble				
		Linear	Quadratic	Cubic	Fine Gaussian	Medium Gaussian	Course Gaussian	Fine	Medium	Coarse	Cosine	Cubic	Weighted	Boosted Trees	Bagged Trees	Subspace Discriminant	Subspace KNN	RUS Boosted Trees
5	Haar	98	98	98	45	98	98	97	98	88	87	96	98	25	99	99	99	25
6		98	99	99	41	99	98	98	98	87	97	97	98	25	97	99	99	25
5	db1	98	98	98	45	98	98	97	98	89	97	96	98	25	99	99	99	25
6		98	99	99	41	99	98	98	98	87	97	97	98	25	99	99	99	25
5	db2	99	99	99	45	98	98	97	97	89	99	96	97	25	99	99	94	25
6		99	100	100	48	98	99	98	99	84	99	97	99	25	99	99	99	25

Table 5.6 shows exceptional high predication accuracy, with the highest percentage highlighted in red, achieving an approximated accuracy of 100%. The confusion matrix of one of the best evaluated model types, SVM Quadratic, at a DWT of level 6 is shown below, in Table 5.7. The matrix shows that only one gesture was predicted incorrectly (from a 480 gestures), being the right gesture mistakenly predicted as left.

Table 5.7: Confusion Matrix of best evaluated model with 100% accuracy

True Class	Right	119	1	0	0
	Left	0	120	0	0
	Up	0	0	120	0
	Down	0	0	0	120
		Right	Left	Up	Down
		Predicted Class			

5.3.2.2 Etched DSSC performance compared to other pattern design DSSCs

The cell characteristics of the etched FTO compared to the pattern 3 DSSC and the flower pattern DSSC are shown below.

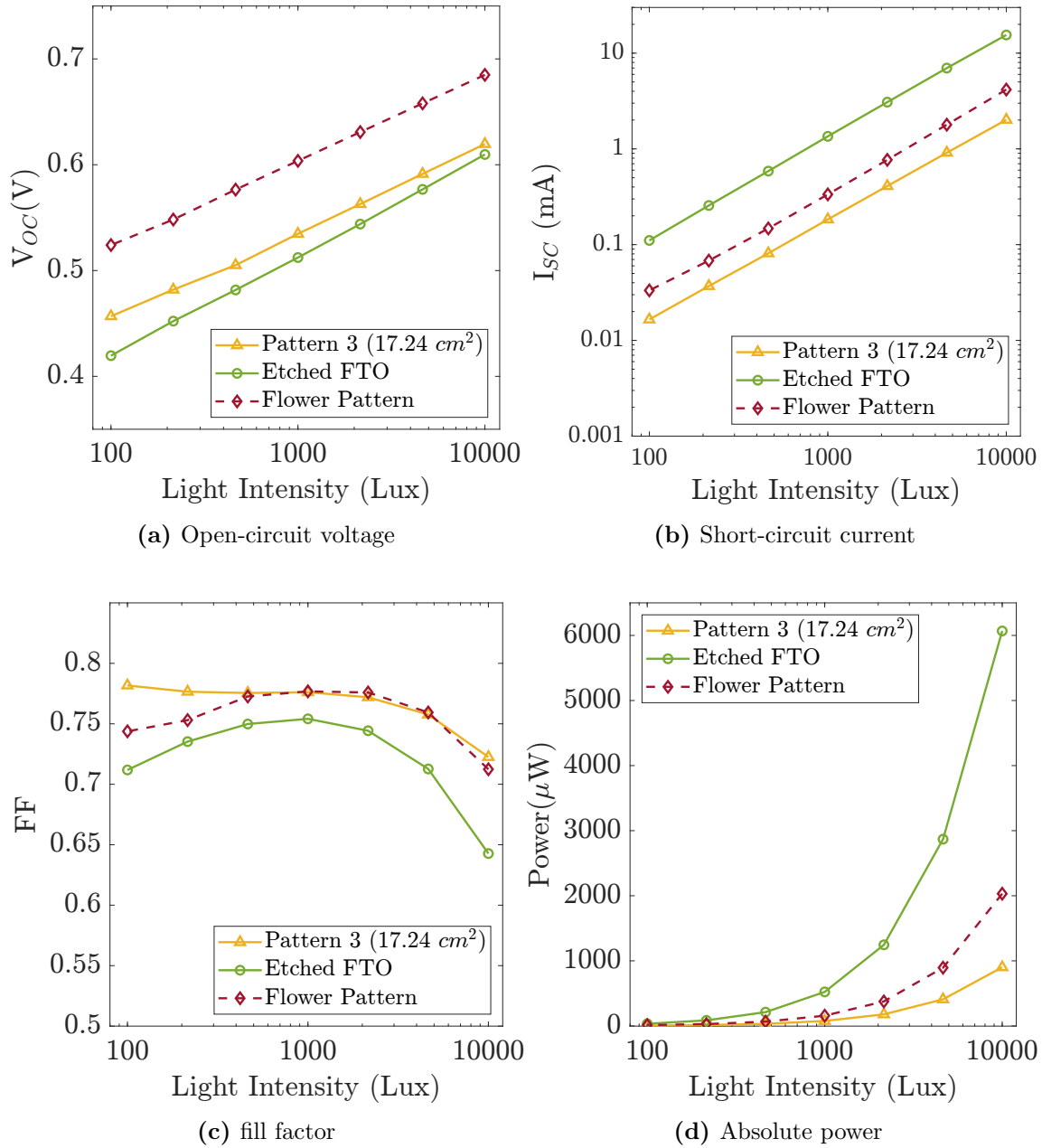


Figure 5.20: Etched DSSC performance characteristics compared to pattern design 3 and the original flower pattern DSSC

Figure 5.20 shows that the etched DSSC does not only provide a great invisible hand gesture recognition method, but also outputs higher power values (in Figure 5.20d) compared to the pattern 3 design and the flower pattern DSSC at different light intensities.

As it was uncertain to the amount of active area was available after etching the FTO, instead, the short-circuit current (I_{sc}) is presented in Figure 5.20b. This showed that the etched FTO produced a higher short-circuit current compared to the flower and the design pattern 3, most likely due to a larger active area present.

The FF in Figure 5.20c at higher light intensities shows a slight decrease due to series resistance losses. There are also some signs of shunt resistance losses for the flower pattern and design pattern 3, indicated by the curved drop at the lower light intensities.

5.4 Alternative low power data collection method

Following successful data collection of the photocurrent from the DSSC using the transimpedance amplifier and DAQ, demonstrated by the high hand gesture prediction accuracy from various trained models, a low power and simplistic method can be investigated, to achieve a more realistic goal of embedding this technique for indoor IoT nodes.

5.4.1 Set-up

The ADS1115 device can be an ideal alternative for an analogue-to-digital converter (ADC), as it is a 16-bit programmable gain amplifier, I2C-compatible low power module. This module can be used as a differential to find the voltage between a known resistor, in order to calculate the photocurrent output of the DSSC [1].

The schematic in Figure 5.21 below shows the set-up required to measure the live photocurrent response of different hand gestures directions.

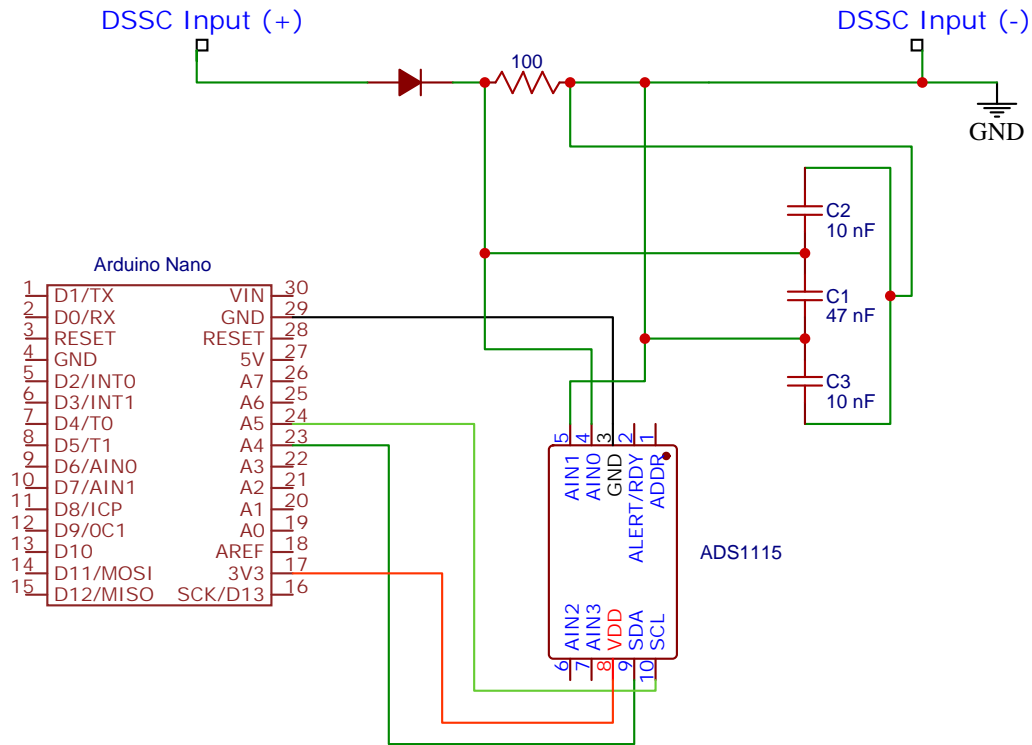


Figure 5.21: Schematic diagram of ADS1115 Set-up

5.4.1.1 Comparing Capture Rate

The rate of capture can also be altered, with the maximum being close to 860 samples per second (SPS). Figure 5.22 below shows the accuracy of the signal at different capture rates, after Z-score transformation and the alignment function.

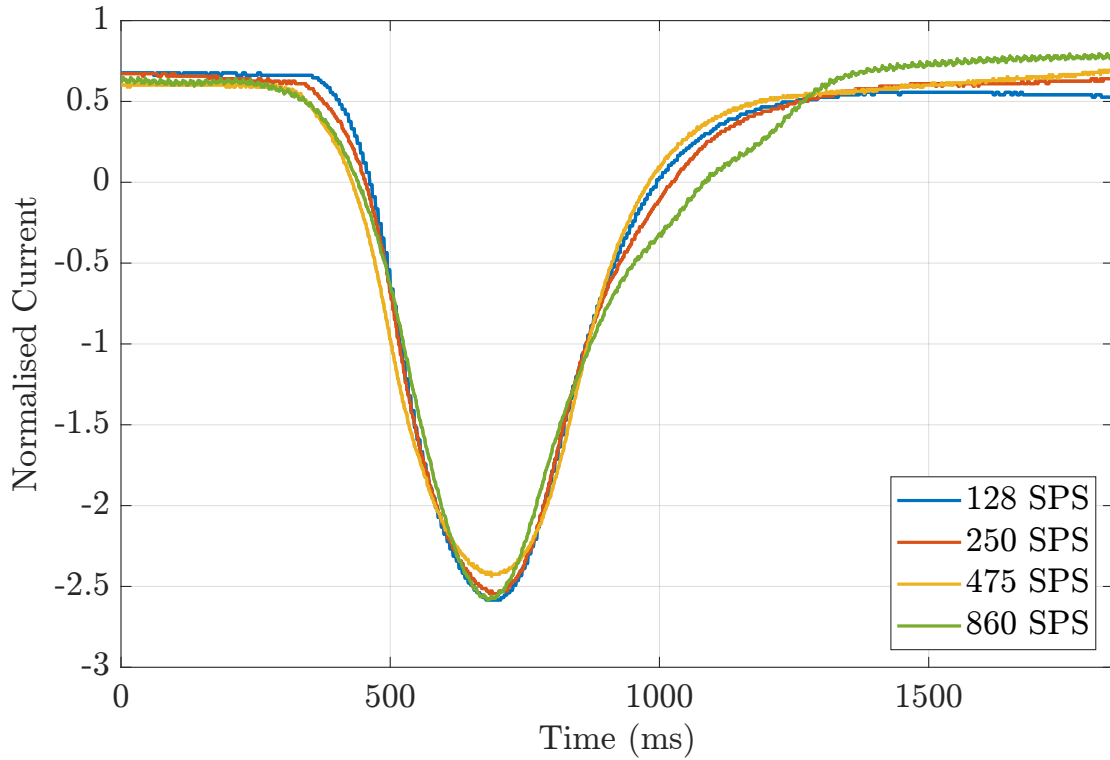


Figure 5.22: Comparing capture rate speeds of the ADS1115 with the Right swipe

The shape from the highest capture rate speed of 860 SPS shows a defined shape of the curve compared to the lower rates, which have a basic trough shape with no defined features, which would result in a failed trained model. Therefore, the sample rate at 860 SPS will be used to capture the data for each gesture direction.

5.4.2 Results and discussion

To test the performance of this method, four gestures are captured and analysed the same way as previous tests, using the etched FTO DSSC. The trained model efficiency are shown in the Appendix C.3, with the evaluated efficiency of the predicted models seen below in Table 5.8.

Table 5.8 Evaluated trained model accuracy for low power alternative data capturing method

		Model Type Accuracy %																
Level	Feature Selection	SVM						KNN						Ensemble				
		Linear	Quadratic	Cubic	Fine Gaussian	Medium Gaussian	Course Gaussian	Fine	Medium	Coarse	Cosine	Cubic	Weighted	Boosted Trees	Bagged Trees	Subspace Discriminant	Subspace KNN	RUS Boosted Trees
5	Haar	48	62	63	25	37	45	60	48	43	45	51	49	25	52	55	64	25
6		51	60	67	25	33	43	59	43	45	41	42	44	25	33	46	59	25
5	db1	48	62	63	25	37	45	60	48	43	45	51	49	25	30	56	62	25
6		51	60	67	25	33	43	59	43	45	41	42	44	25	33	50	51	25
5	db2	70	76	78	25	67	65	80	66	59	70	70	68	25	60	62	71	25
6		69	71	72	25	54	66	71	61	50	63	61	64	25	64	51	74	25

The maximum efficiency achieved was 80%, from KNN Fine, at a DWT of level 5, 20% less than the efficiency of the etched FTO captured using the transimpedance amplifier. The confusion matrix of the best trained model is shown below, in Figure 5.9. The main error can be seen between similarities of the down gestures being predicted incorrectly as the left gestures.

Table 5.9: Confusion matrix of best evaluated model with 80% accuracy

True Class	Right	90	20	9	1
	Left	6	112	0	2
	Up	1	0	119	0
	Down	6	48	4	62
		Right	Left	Up	Down
		Predicted Class			

A factor for the decrease in level of success can be down to the lower sampling rate of the ADC. The transimpedance amplifier achieved a rate of 1 kHz , whilst the ADS1115 has a maximum of 860 Hz , which in practical reality can be lower than this, due to the rate of the microcontroller can receive and transmit.

Live hand gesture recognition was attempted by using the threshold gesture algorithm (which performs well under higher light intensity, with a simple feature extraction method, see Section 4.3) to demonstrate that instantaneous detection can be achieved through the ADS1115. By placing the flower pattern DSSC near a window to provide a higher light intensity (≈ 4000 Lux), the hand gesture data was transferred from the ADS1115 to the MATLAB code on the computer, predicting the gesture direction. A video demonstrating successful live gesture detection

is shown on the file cloud storage [2]. To achieve this with the optimised machine learning algorithm, it would require a larger data-set of different hand gesture parameters (height from the cell, light intensities, hand size, and gesture speed) in order to increase the likelihood of live hand gesture recognition.

5.5 Conclusion

This Chapter optimises the active area pattern on a monolithic DSSC in order to increase the hand gesture recognition accuracy for eight directional hand gestures, through a sweep gesture computer simulation model. The best active area pattern was achieved by pattern design 3 (seen in Figure 5.11c on page 167), where the evaluated trained model achieved an accuracy prediction of 83%; and increase of 23% compared to the flower pattern DSSC from Chapter 4. It was also discovered that the homemade (HM) electrolytes of 5 *mM* and 50 *mM* concentration of iodine were susceptible of charge recombination at low light intensities, if the distance between the active area and the electrolyte (without any active area underneath) was at least 20 *mm* apart, causing the V_{OC} and FF to significantly decrease, resulting in less power being outputted.

An alternative DSSC fabrication method was also achieved by etching the FTO layer at specific areas to copy the outline of a simplistic version from the flower pattern active area design. This resulted in a normal appearance DSSC, with no patterned active areas to detect the hand gesture direction. Instead, the etched FTO provided an invisible hand gesture recognition method which achieved a evaluated accuracy of 100% for detecting the basic four directional sweeps (right, left, up and down). This method can be a suitable option for IoT node applications which require a subtle appearance for the user, which harvests decent amount of energy from indoor lighting (more than pattern 3 and the flower pattern) but can also successfully recognise four gestures.

Finally, a low powered method of collecting photocurrent outputs for gesture recognition was also achieved, by integrating an ADS1115 ADC having a high accuracy (860 samples/second) through a 16-bit programmable gain amplifier. Beforehand, data was initially collected using the transimpedance amplifier, which required to be powered from a power source of 230 *V*. This alternative method can be powered using a microcontroller with an output voltage to the ADC as low as 2.0 *V*, with also a lower current consumption of 150 μA . The evaluated accuracy from the best trained model however achieved a slightly lower accuracy of 80% due to the lower sampling rate of the ADC compared to the transimpedance amplifier, reducing the

distinguishable features required for ML to predict the correct gesture direction.

Bibliography

1. Chaudhari KG. Windmill Monitoring System Using Internet of Things with Raspberry Pi. SSRN Electronic Journal 2019 Nov. DOI: 10.2139/SSRN.3729041. Available from: <https://papers.ssrn.com/abstract=3729041>
2. Thomas G. Shared Content - Live Gesture Detection through Thresholding. Available from: <https://drive.google.com/drive/folders/1kxPuLiLGNG3D1n8fKg0dUBwGDusp=sharing>

Chapter 6

Human Computer Interaction Prototyping and Contribution

Throughout the thesis, there have been several contributions by the author of this PhD to facilitate prototypes for different HCI projects involving PV technologies. These contributions to design prototyping and material selection were submitted as part of the joint paper submissions to CHI conferences in 2021 [1], and 2022 [2]. This Chapter delves into the design challenges faced during prototyping, developing unique and self-powered methods for HCI devices.

There were many challenges faced when integrating DSSC's into indoor IoT nodes, especially when working on an initial low-fidelity prototype. These included:

Low light intensity - Indoor lighting conditions can vary greatly, providing a lower light intensity compared to natural sunlight using various lighting sources, such as LED or fluorescent lighting. The intermittent energy generation of DSSCs due to this may struggle to meet the energy requirements of IoT nodes, whilst dealing with the user potentially expecting an IoT node that works effortlessly and without interruptions.

Cost and weight – Another challenge when facing with tight budget constraints was balancing cost-effectiveness with energy harvesting performance. The large weight of the DSSCs was another challenge faced, especially when integrating with IoT nodes which required the DSSC itself to rotate, requiring larger amount of energy to power the actuators. This is mainly from fabricating large DSSCs, with most of the weight coming from the two FTO coated glass substrates.

6.1 PV-Pix: Deformable smart messaging material prototypes

Throughout this project [1], two PV-Pix concepts, being the FabricOn and TiltTile, were explored for inter-home connections in communities where there are unreliable and underdeveloped energy infrastructures. The concepts provide a self-powered method through PV materials, to power IoT nodes, transmitting messages between homes.

Rendered diagrams of each prototype is initially required for clarity, with working examples constructed from the support of the computer aided design (CAD) drawings. The design developments and construction of both concepts are discussed in detail below.

6.1.1 FabricOn prototypes

6.1.1.1 Configuration

This prototype involved the concept of rolling an array of individual panels to convey a message to another home. As it only requires a small footprint for each IoT node, a commercially available flexible organic photovoltaic (OPV) was used instead of a DSSC, which can be scrolled up into a housing. An exploded view of the rendered design is shown in Figure 6.1, using the CAD software SolidWorks.

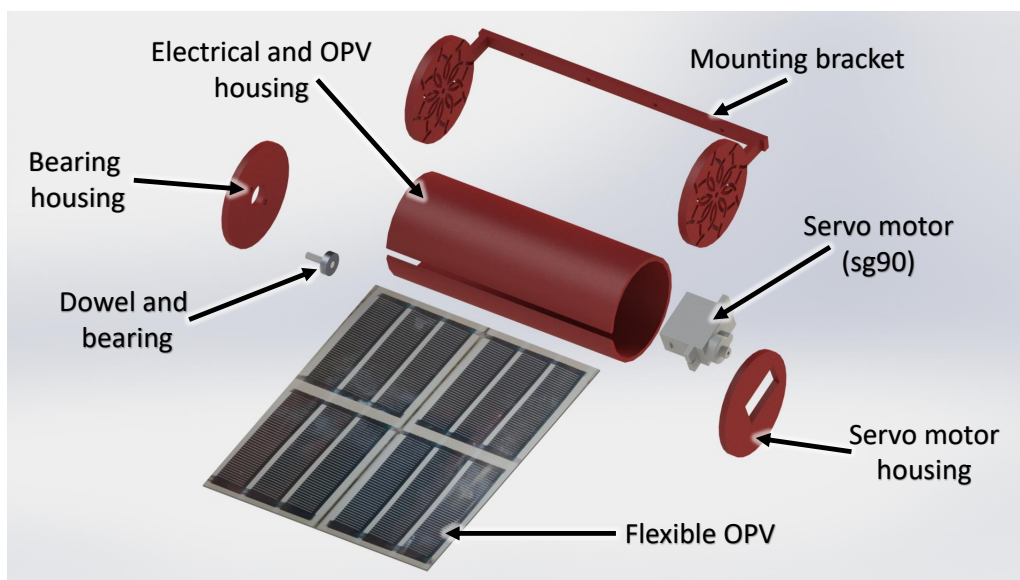


Figure 6.1: Exploded view of the rendered FabricOn design

Figure 6.2a shows the assembled design rolled up, being in its closed state (orange arrow displaying the motion direction to open), and Figure 6.2b, showing the open

state, through the rotation of the SG-90 servo motor (blue arrow representing the motion direction to close). Smaller servo motors were also trialled, however, due to the requirement of rotating the whole housing, these servo motors struggled to close the OPV, when in open state.

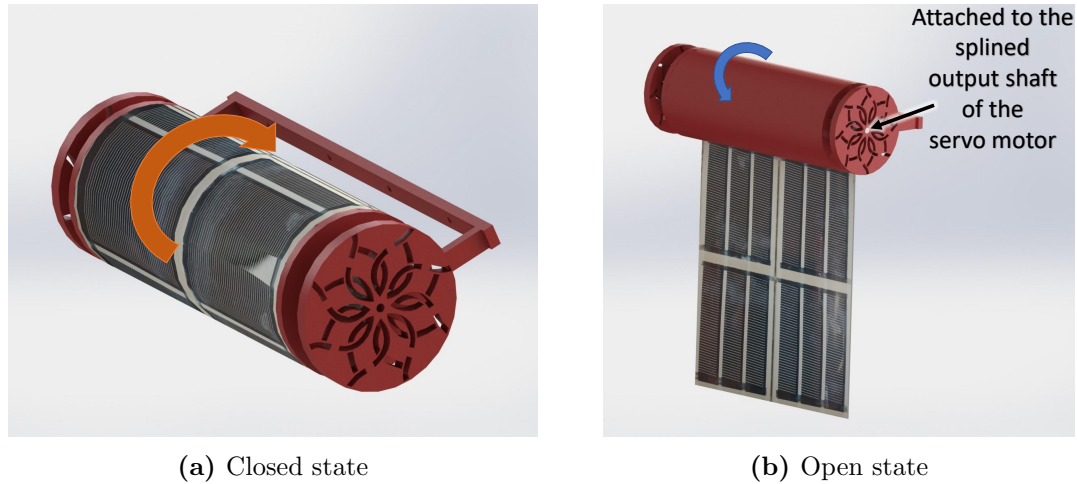


Figure 6.2: Rendered operation of the FabricOn

A video of the working example assembled from using the design in Figure 6.2 is shown on the cloud storage [3], demonstrating the FabricOn prototype opening and closing. A still image of this is shown below in Figure 6.3.

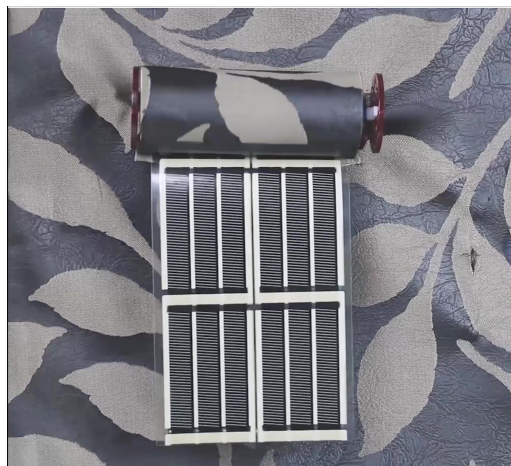


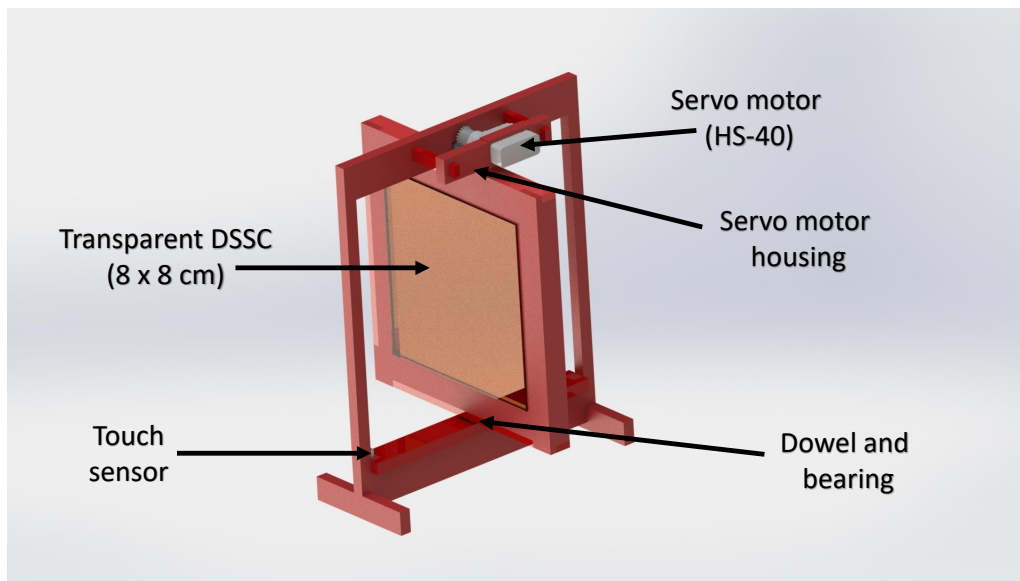
Figure 6.3: Working example of the FabricOn in open state

6.1.2 TiltTile module prototype

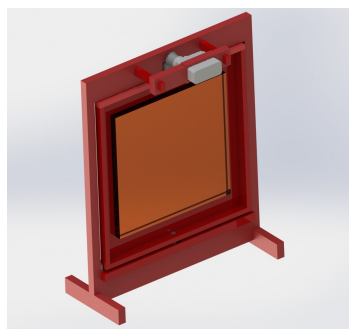
An alternative method of providing messages between households was through the TiltTile module, tilting 90° to either show the full face of the tile, or facing sideways. The tile itself contained an $8 \times 8 \text{ cm}$ DSSC, to harvest energy to power the IoT node and actuator, but also acts as the tile itself.

6.1.2.1 Configuration

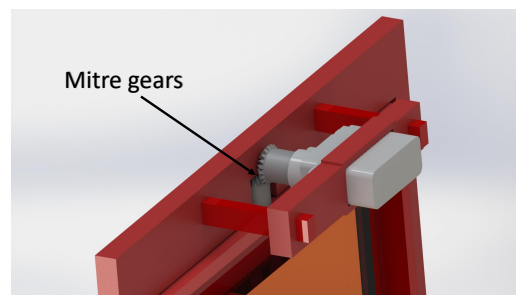
Initially rendered concepts are shown below in Figure 6.4a and Figure 6.4b, for a single tile to demonstrate the operation of the actuator opening and closing the tile. To minimise the frame of the TiltTile, a small servo motor was used, being the HS-40, and mounted horizontally. As a consequence of this, to move the tile, it requires mitre gears (having a gear ratio of 1:1) to change the direction of the power transmitted by the servo motor, which is shown in Figure 6.4c. A touch sensor is also included to enable the user to automatically open or close the tile.



(a) Open state



(b) Closed state



(c) Close-up of the mitre gears

Figure 6.4: Initial prototype of the TiltTile module

A working example of the initial TiltTile module is shown below in Figure 6.5 with a video stored online [4] showing the tile open and close. Several other rendered designs of the 2 x 2 and 7 x 7 array are also stored on the online file cloud [4].

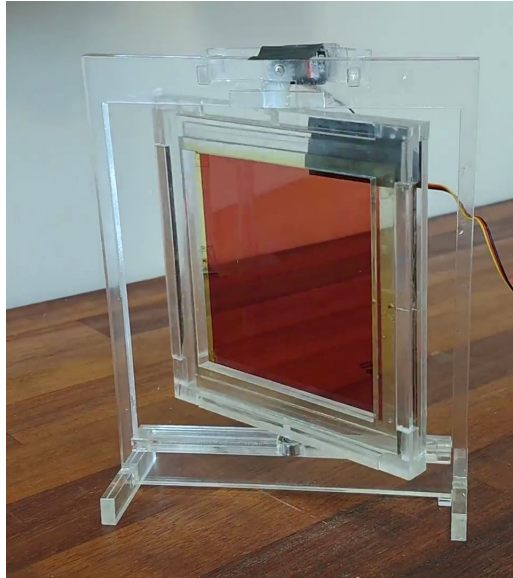
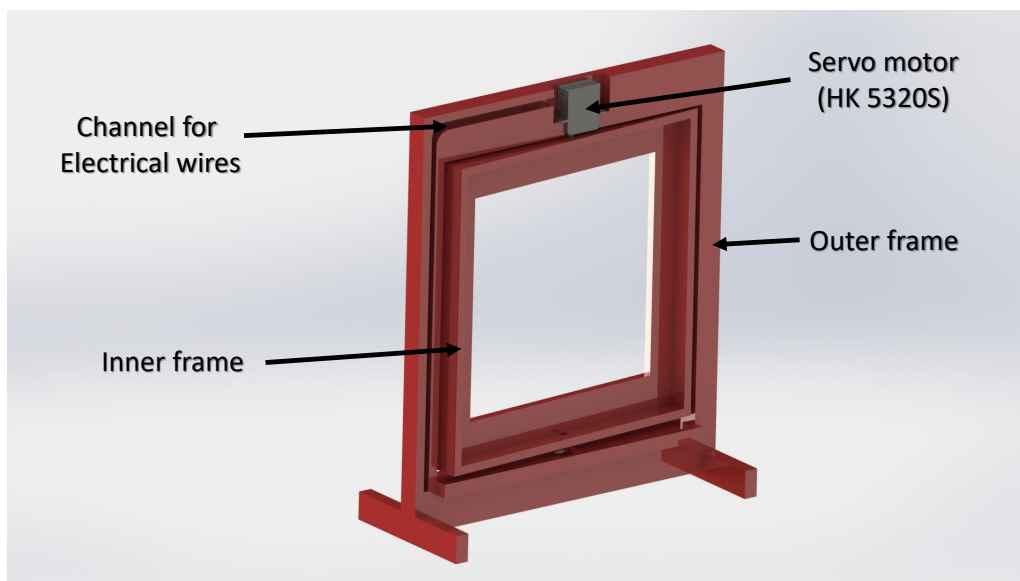
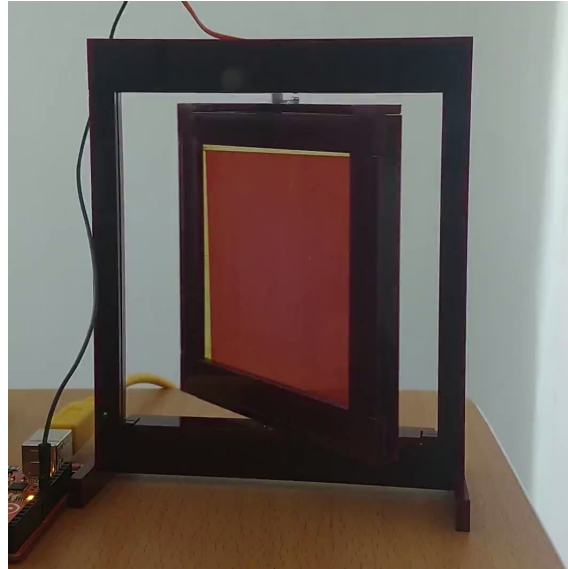


Figure 6.5: Working example of the initial prototype

Whilst the initial prototype was successful in turning the tile from open to close; assembling the mitre gears accurately was difficult to achieve, with several attempts leading to the gears slipping, resulting in the incorrect positioning of the tile. To rectify this, a smaller servo motor (HK 5320S) was used to directly drive the tile, meaning that the overall outer frame will be slightly thicker, but results in a more reliable mechanical system. The design of the optimised single TiltTile is shown below in Figure 6.6, alongside the working example. Again, additional designs including a video of the TiltTile operating is stored on the file cloud [5], with additional rendered designs of 2 x 2 array TiltTile.



(a) Rendered optimised design



(b) Optimised working example

Figure 6.6: Final optimised concept design of the TiltTile

6.2 Light-based concept prototypes

Light-based concepts were explored in [2], to harvest sunlight or indoor lighting to provide a self-powered method of communicating or for entertainment in areas where there are unreliable energy networks. The paper [2] concentrates on three different avenues of design. These included SolarPix (using reflections from mirrors to display pixellated patterns), GlowBoard (communication devices through glow board and UV laser), and ShadMo (shadow animation through Moiré pattern). The design contributions for the SolarPix and ShadMo are presented below, with no contributions required for the GlowBoard, due to only integrating an external PV cells for energy harvesting.

6.2.1 SolarPix prototype designs

The SolarPix involves mirrors to selectively reflect sunlight on a surface, displaying a customised pixellated pattern. The SolarPix can also be self-powered, with either the PV cells attached onto the mirror or placed separately, by the side. This application can be installed in particularly poor lit alleyways which are usually densely packed with businesses, stores, and workshops. SolarPix would enable additional lighting to these poorly lit areas, but also can allow the community to share graphical messages and directions.

6.2.1.1 Configuration

The SolarPix required concept designs and prototype development to demonstrate the operation of the device. SolidWorks is used, being CAD software, to initially create designs before building the prototypes.

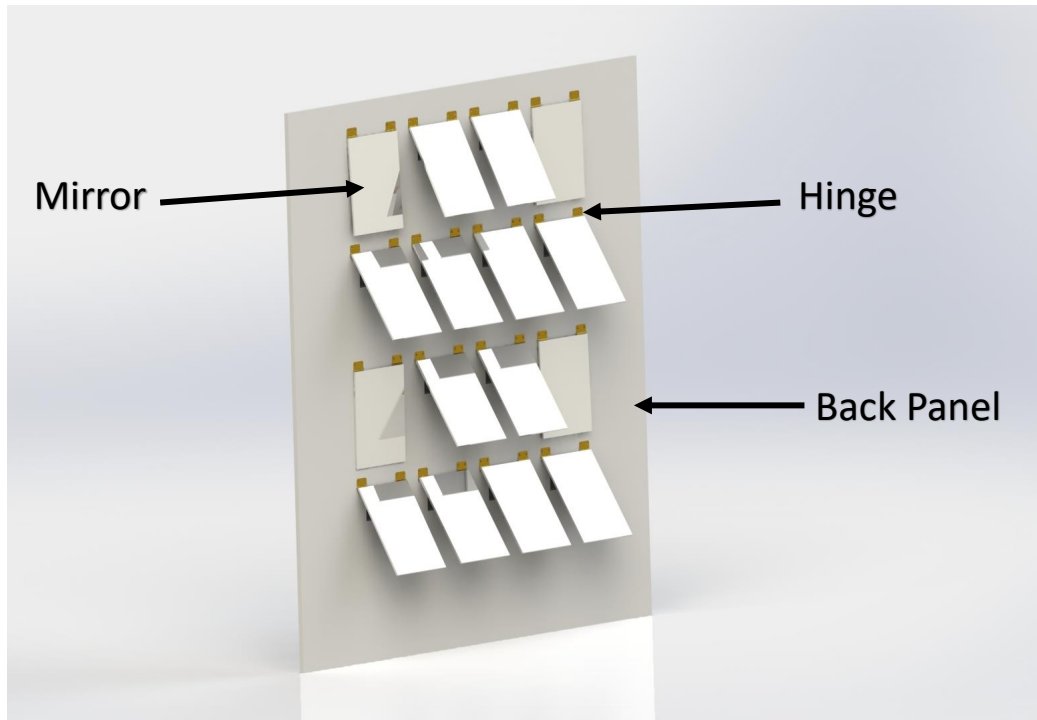


Figure 6.7: Rendered design of the SolarPix

Figure 6.7 demonstrates how the SolarPix works, with an array of mirrors, which can be tilted up by using an HS-40 servo motor, which is placed behind the back panel, shown in Figure 6.8.

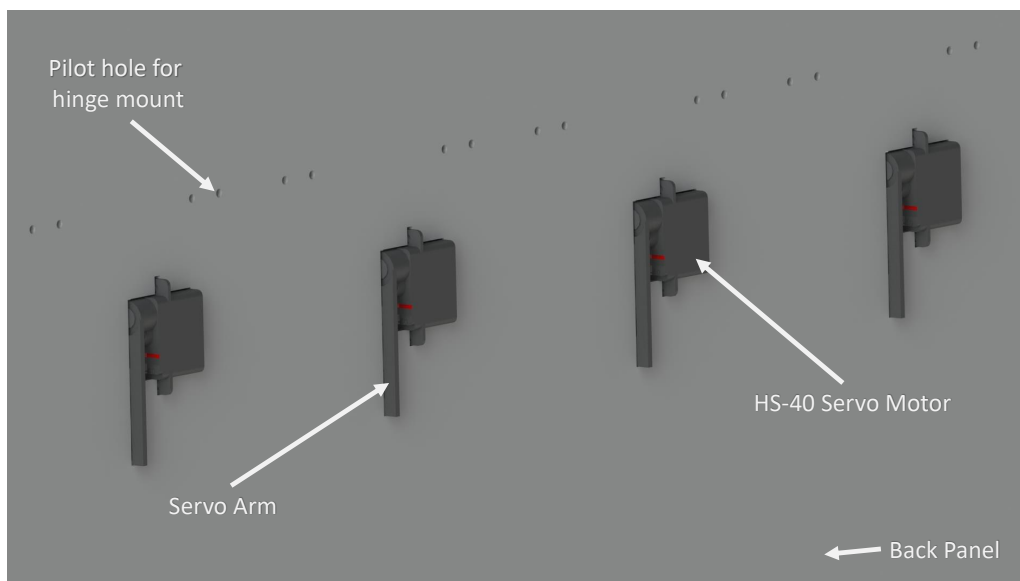


Figure 6.8: Back view of the SolarPIx

Each mirror is individually tilted with the use of a servo arm, as seen in Figure 6.9 below, where the directional motion is shown with a blue arrow. Additionally, DSSCs can potentially be placed above the mirror to harvest energy to power the servo motors. These design concepts were used to construct the prototype shown in the light-based concepts paper [2].

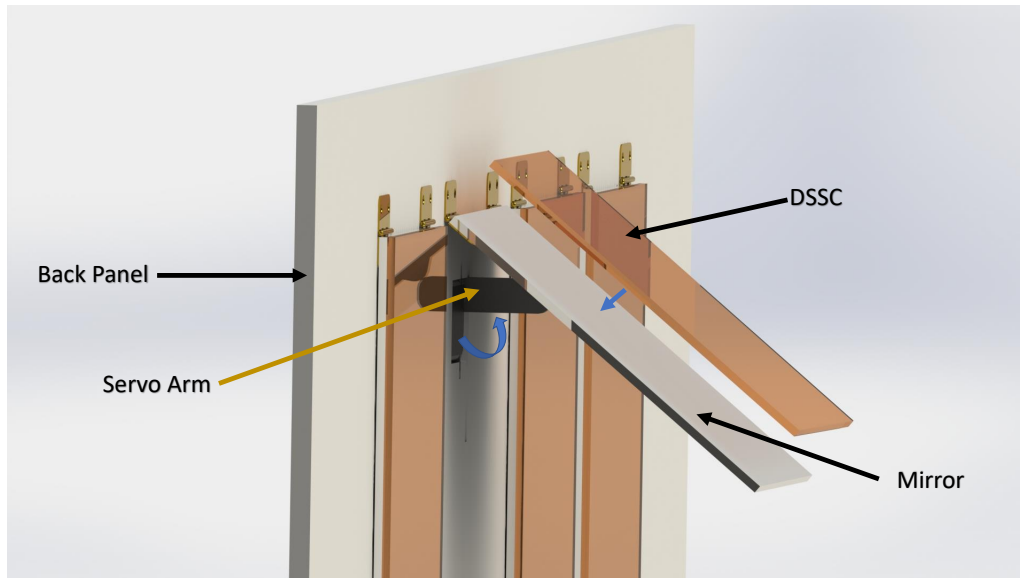


Figure 6.9: Side view of SolarPix, with the addition of DSSCs

6.2.2 Self-powered Moiré pattern shadow motion (ShadMo)

This Section concentrates on the design developments and iterations of the ShadMo, which creates shadows (under light from the table or sunlight) to portray a moving animation through a Moiré pattern. ShadMo's concept is to provide a sense of entertainment or to change the user's experience of a location, producing shadows of different sizes (by moving the light source closer or further away from the prototype) of animated images through a Moiré pattern onto the wall.

By superposing two transparent layers, which contain correlated opaque Moiré lines, a Moiré pattern is formed. An example is shown below in Figure 6.10, where the revealing layer (in this case at the front, which must be transparent in between the Moiré lines) stays stationary, and a base layer (situated behind the revealing layer, where the gaps between the opaque Moiré lines can be opaque or transparent), in this case being a butterfly pattern positioned behind [2]. By moving the base layer linearly behind the revealing layer, an animation illusion is created, showing the butterfly flapping its wings as seen in Figure 6.11. Illuminating this motion can project the animation as a shadow on a wall, either by providing a lamp source or sunlight if positioned by the window.

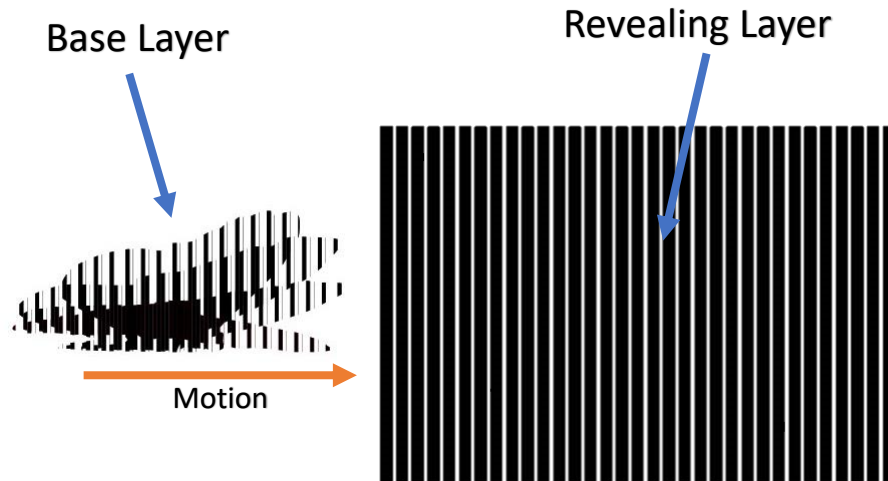


Figure 6.10: Base layer moving under the revealing layer

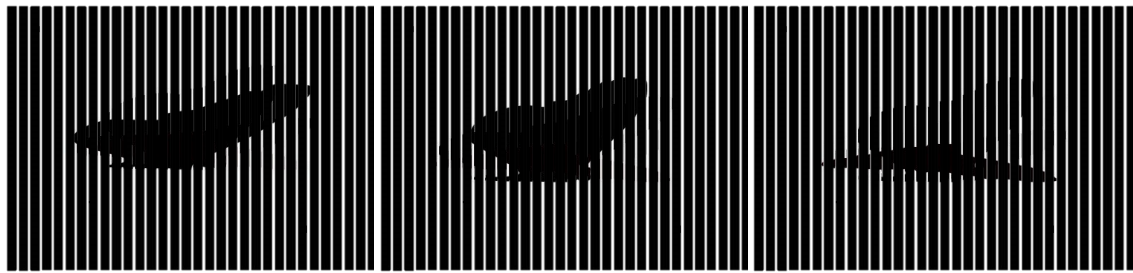


Figure 6.11: Demonstrating the effect of the base layer under the revealing layer at different linear movements

6.2.2.1 Initial design concept

As there is a stationary (revealing layer) and moving layer (base layer), difficulties arise in integrating both layers as light energy harvesters, especially the external moving part. Therefore, the initial design only includes one PV monolithic cell, being placed as the revealing layer, to simplify the mechanics and assembly of the prototype. A monolithic DSSC is used based on the justifications from Chapters 1 and 3 with regards to the ease of fabrication as well as the best DSSC composition for indoor environment.

As the DSSC will be fabricated as the revealing layer, the black strips shown in Figure 6.10 will represent the active area, whilst the white strips in between will only contain the electrolyte. This is why it's important that the electrolyte used has a good transmittance for the base layer to be clearly seen underneath. Consequently, the best electrolyte was deemed to be the 5 *mM* (HM), as justified in Chapter 3, providing good indoor performance and great (or high) transmittance. An additional step mentioned in Section 2.2.2 (Chapter 2), is to provide an opaque layer of TiO_2 ,

which is important for the Moiré pattern effect to work. By applying this opaque layer on the active area, it also increases the power output from the DSSC. As the light initially enters the DSSC, some of the light exiting the cell becomes reflected back into the DSSC by this opaque layer, increasing the photocurrent output.

6.2.2.1.1 Configuration

Prototypes were initially designed through SolidWorks, where the initial rendered designs are shown below in Figure 6.12. Before introducing the DSSC pattern and actuator to the design, it is important to make sure the initial concept works, having the correct measurements between the revealing and base layers. The movement of the base layer is achieved through a linear bearing sliding on a rail.

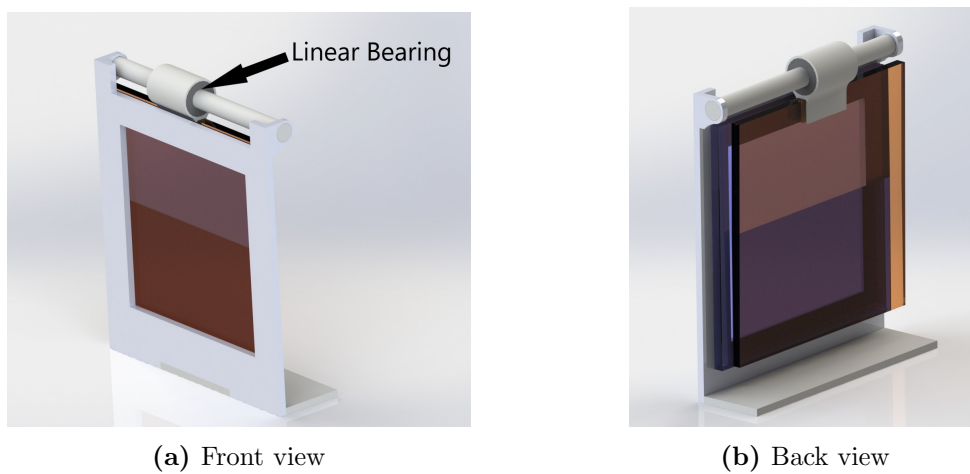


Figure 6.12: Initial rendered design of the Moiré pattern mount

The concept shown in Figure 6.12 was fabricated using a laser cutter (for 3 mm acrylic sheets) and a 3D printer (to fabricate the linear bearing sheath); using super glue to attach the base and face mount together. The results are shown below in Figure 6.13, where both the base (in this case being a beating heart) and revealing layers are printed on an acetate sheet, with an additional orange tinted acetate sheet at the front to represent the DSSC colour produced from the N719 dye.

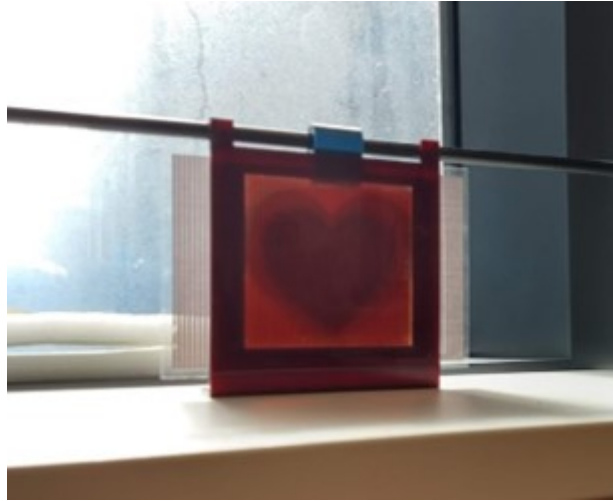
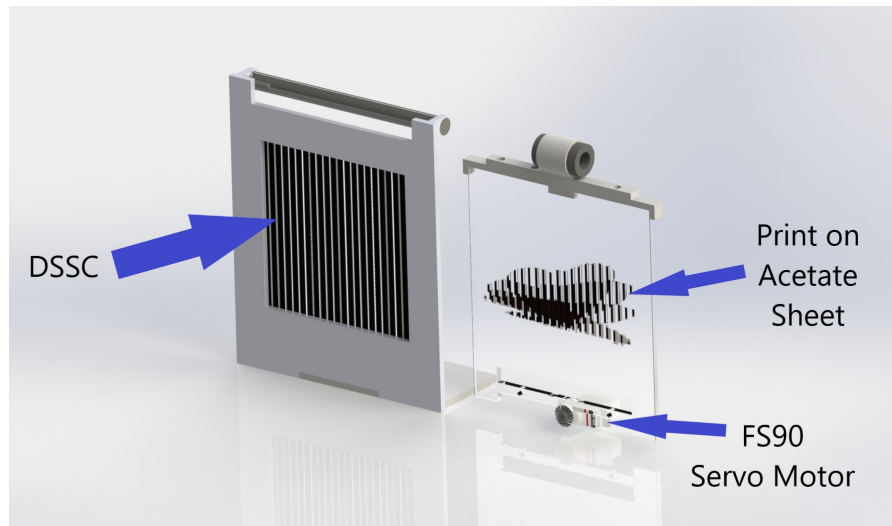


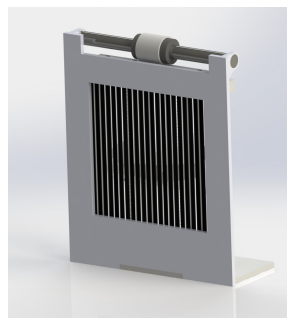
Figure 6.13: Moiré pattern of a beating heart using acetate sheets

Figure 6.13 displays the beating heart, with a video showing the Moiré pattern movement, stored on the cloud [6]. It shows that there is some misalignment with the base and revealing layer, which can be seen from the multiple faint shapes of the heart. This demonstrated the difficulties that arise in aligning both layers together, being the Moiré lines of both layers being parallel to one another, meaning that precise care must be taken when assembling the prototype.

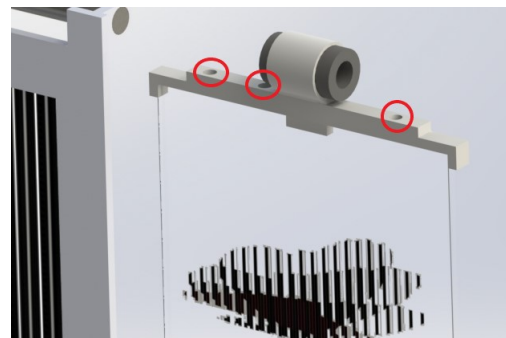
As the initial prototype was successful, a second iteration including the actuator mount was designed to move the base layer, as shown in Figure 6.14. Initially, a 1.5 g micro linear actuator servo was attached to the bottom of the base layer and fixed onto the face of the mount. However, this method resulted in slow and twitchy movements from the base layer, causing the Moiré pattern to have an uneven motion. This is most likely due to the small teeth on the worm drive gear. An alternative and better method was to attach the Kitronik linear actuator kit, which includes the FS90 servo motor, as seen in Figure 6.14a. The base layer assembled onto the bearing rail is shown in Figure 6.14b.



(a) Showing the base and revealing layer separately



(b) The base layer assembled behind of the revealing layer



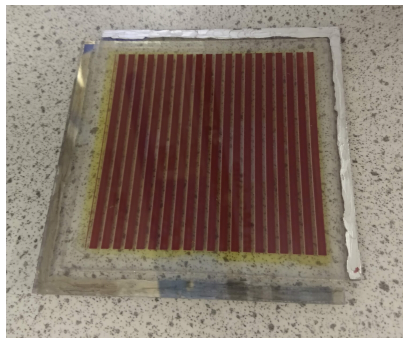
(c) Close up of the magnetic mount

Figure 6.14: Rendered schematic design of the second iteration with an actuator and DSSC

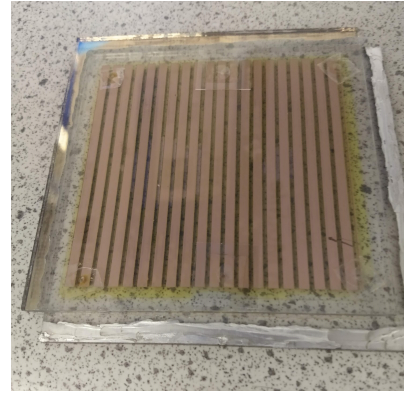
To ensure that the base layer is sturdy enough, the Moiré lines printed on the acetate sheet is held onto a thin sheet of clear acrylic, for the servo motor and linear bearing to be also assembled on the layer. Modularity is also added to this design, with magnets (slots circled in red) used to allow a swift change of the base layer to provide different Moiré patterns, as seen in Figure 6.14c, permitting the linear bearing to be constantly fixed on the bearing rail.

6.2.2.1.2 Results and discussion

The revealing layer, being vertical straight lines was fabricated onto a monolithic DSSC, by screen printing the lines of the transparent and opaque TiO_2 . This is shown in Figure 6.15 below, presenting the difference in appearance of the front of the DSSC (facing towards the light source), and the back of the DSSC, showing a thicker layer of TiO_2 , where less dye molecules have attached onto the semiconductor (hence having the paler colour).



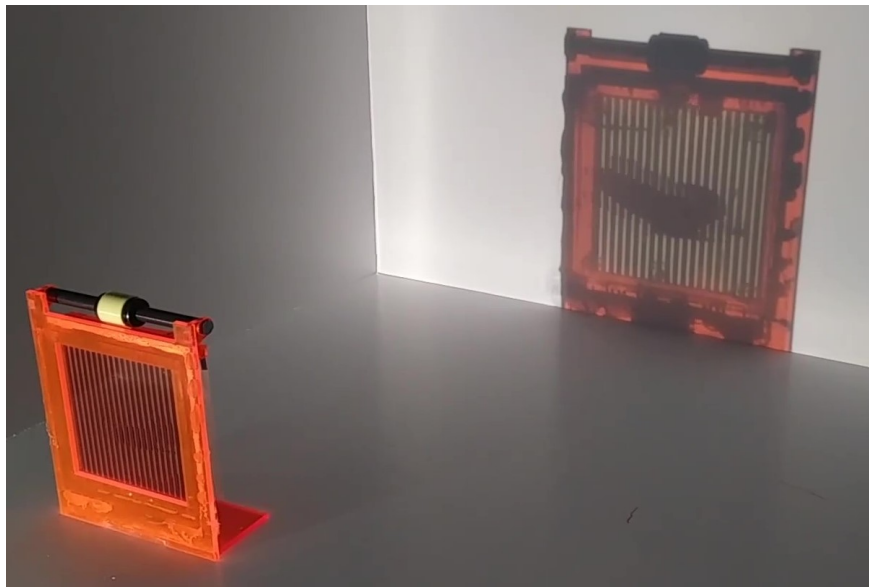
(a) Front facing DSSC Moiré lines



(b) Back facing DSSC Moiré lines

Figure 6.15: Resultant fabrication of DSSC with Moiré line for revealing layer

By following the design in Figure 6.14, the prototype is shown below in Figure 6.16, demonstrating the shadow cast from the Moiré pattern, caused by the linear motion of the base layer (actuated by the Kitronik kit). This prototype is being self-powered by the DSSC acting as the light energy harvester but also as the revealing layer.

**Figure 6.16:** Assembled Moiré pattern design using a DSSC as the revealing layer

A video can also be viewed on the stored file cloud [6], showing the actuator moving the base layer creating an animation of a flying butterfly. Whilst initial results show some promising advancements with displaying a Moiré pattern through a monolithic DSSC, limitations arise considering the power consumption.

By requiring a powerful servo motor (FS90) rather than using a low powered micro linear actuator servo, the input power required is too much of a demand from a single monolithic DSSC. The input voltage required to power the servo motor is 4.8 V, with a current consumption ranging between a 100 to 550 mA. Depending on

the intensity of the light, the maximum voltage when the power is at its maximum varies between 0.3 to 0.4 V. This is considerably less than the servo motor requirements. Therefore, an energy harvester module is required to increase the output voltage of the DSSC, which consequently charges an energy storage, such as LIBs. Nevertheless, by including the energy harvesting module and storage to the system, the operation time of the device is very small, being only 5 minutes of operation from 12 hours at high light intensities in indoor conditions (5,000 to 10,000 Lux), or 34 minutes of operation under 24-hour period under direct sunlight.

The initial design concept provides the sufficient requirements to produce the Moiré pattern. However, whilst being described as ‘self-powered’, the operation time performance of this design is poor, with further improvements to consider.

6.2.2.2 Moiré Pattern advancement to achieve self-power

Whilst the conference research paper [2] is based on the design results shown in Figure 6.16, additional advancement attempts to optimise the Moiré pattern continues in this Section, by attempting to reduce the overall power consumption of the system, and hence increasing the operational time of the Moiré pattern movement.

6.2.2.2.1 Configuration

Low energy movement has already been achieved with other devices, such as the solar dancing flower. An example of a solar dancing flower is shown below in Figure 6.17, annotating the inside mechanics on how the solar dancer works.

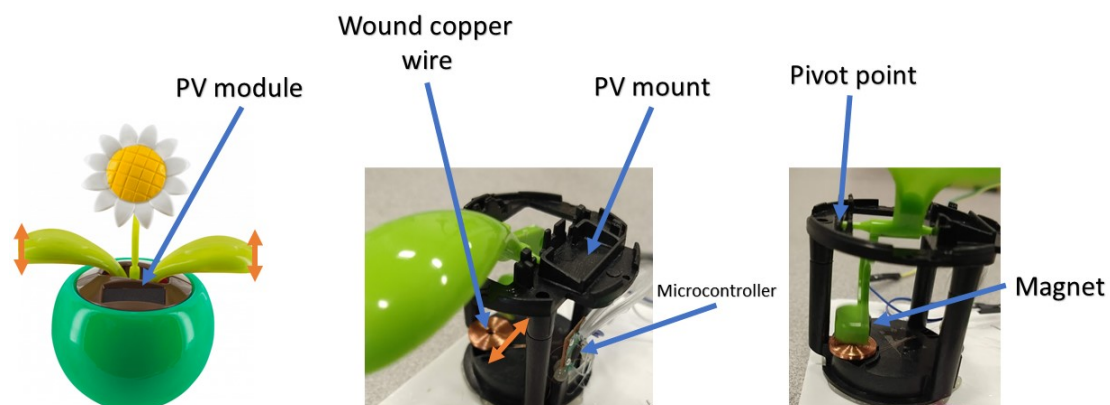


Figure 6.17: Example of a solar dancing flower [7] showing the inside mechanic. The arrows in orange represent the motion direction

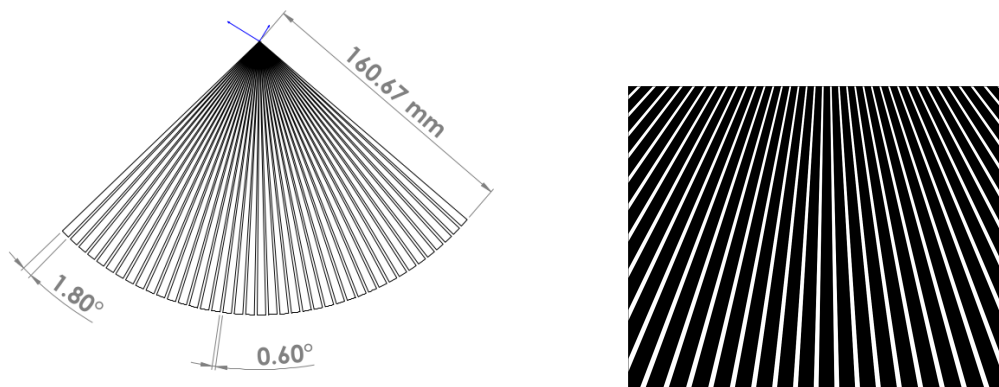
A silicon-based PV module is used as the input power for movement propulsion. A capacitor (not visible in the image) is also included, to provide constant voltage to the electronic board. The solar dancing flower works by using a pendulum motion around a pivot point. When light is projected at the PV module, electrical current

is pulsed (timed from the microcontroller) through the copper wire, causing a magnetic field along the axis of the copper coil. The magnet (located at the bottom of the swinging part) is then pulled towards the coil, causing the pendulum rig to swing the flower design. This method could be re-purposed to move the base layer instead.

Difficulties arise in integrating a Moiré pattern through a pendulum motion rather than a linear motion as previously designed. Previous literature on a Moiré pattern created on a circular arc has been very limited. However, Gabrielyan *et al.* [8] details the specific design requirements in order to superimpose circular patterns, in a pendulum motion.

6.2.2.2.2 Progress of altering linear to radial motion of Moiré pattern

The initial step was to design the revealing layer, to provide the required spacing to design and alter the butterfly Moiré lines on the base layer. To achieve this, SolidWorks is used to precisely measure the spacing between each opaque area and curvature, which can be seen in Figure 6.18a. Each transparent gap (0.6°) is a third of the size of the opaque Moiré line (1.8°). The design is then sent to CoralDraw to snip a square area of $8 \times 8 \text{ cm}$, and shaded in the areas to be opaque, displayed in Figure 6.18b.

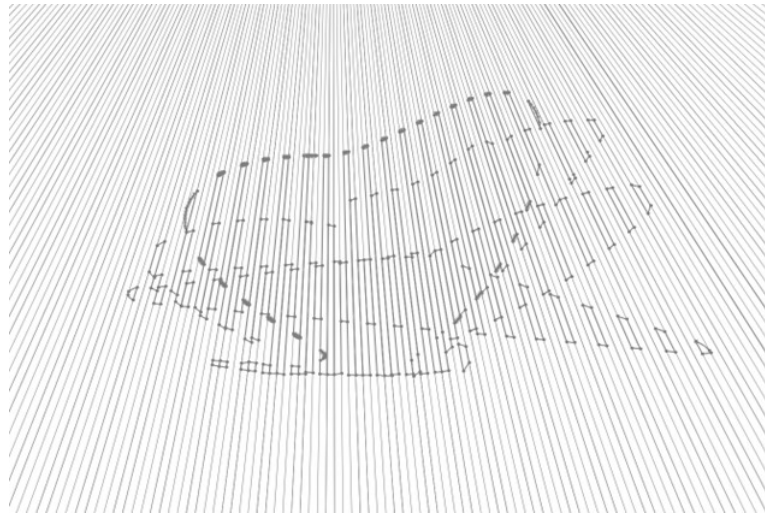


(a) Design measurements for the revealing layer (b) Final revealing layer design for deployment

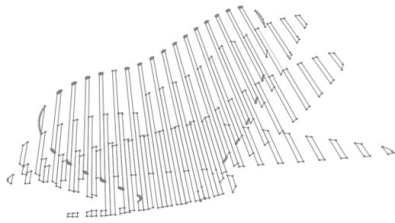
Figure 6.18: Design alteration of the revealing layer for radial movement by the base layer

The butterfly shape can then be overlaid (drawn freely on Solidworks) at a specific location on the revealing layer, as seen in Figure 6.19a. This allows certainty that the butterfly pattern will be compatible with the revealing layer, matching the angle and thickness of each Moiré line. The butterfly is drawn in four segments, meaning the animation of the butterfly has four individual still pictures which after one another animates the butterfly flapping its wings. The Moiré lines for each segment of the butterfly is accurately positioned by sectioning each opaque lines of the revealing

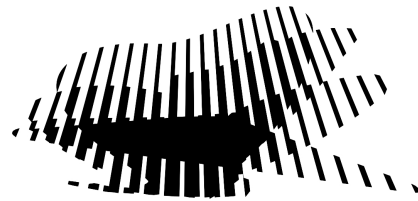
layer into thirds. This means that overall, a single segment is a window to display the butterfly (transparent/in white) and the other three segments (being the opaque part/in black) hides the Moiré lines of the base layer. When there is a movement from the base layer, a different part of the segment is then displayed in the window, creating the Moiré pattern effect of the butterfly flapping its wings. The Moiré lines without the revealing layer are shown in Figure 6.19b, with the complete base layer after using CoralDraw seen in Figure 6.19c.



(a) Sketching the base layer on the revealing layer



(b) Removing the revealing layer



(c) Final base layer design

Figure 6.19: Design alteration of the base layer for radial movement

The superimposed revealing and base layers are shown below in Figure 6.20, with now a radial motion direction introducing a new Moiré pattern.

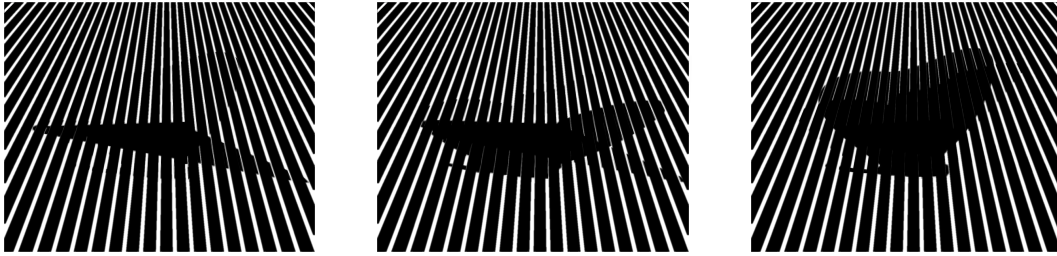


Figure 6.20: Motion of the base layer underneath the revealing layer, showing different segments of the butterfly

The location as to where the base layer is positioned behind the revealing layer is important to display the correct Moiré pattern, as the base layer was set at a specific height as shown in Figure 6.19a. The misalignment results are shown below in Figure 6.21, where if the positioning is incorrect, in this case being lower behind the revealing layer, then it produces a disfigured pattern. Therefore, extreme precision is required when initially superimposing the layers together.



Figure 6.21: Disfigured pattern when the base layer is positioned lower behind the revealing layer

6.2.2.2.2.1 Mount design

Changes to the mount design are required to allow the base layer, having an acetate print of the butterfly pattern, to move in a pendulum motion. Figure 6.22 below (see page 202) shows the updated design to achieve a pendulum motion (shown with an orange arrow) Moiré pattern, where the electronic configurations are taken from a solar dancing flower, having already been programmed to pulse current through the coil.

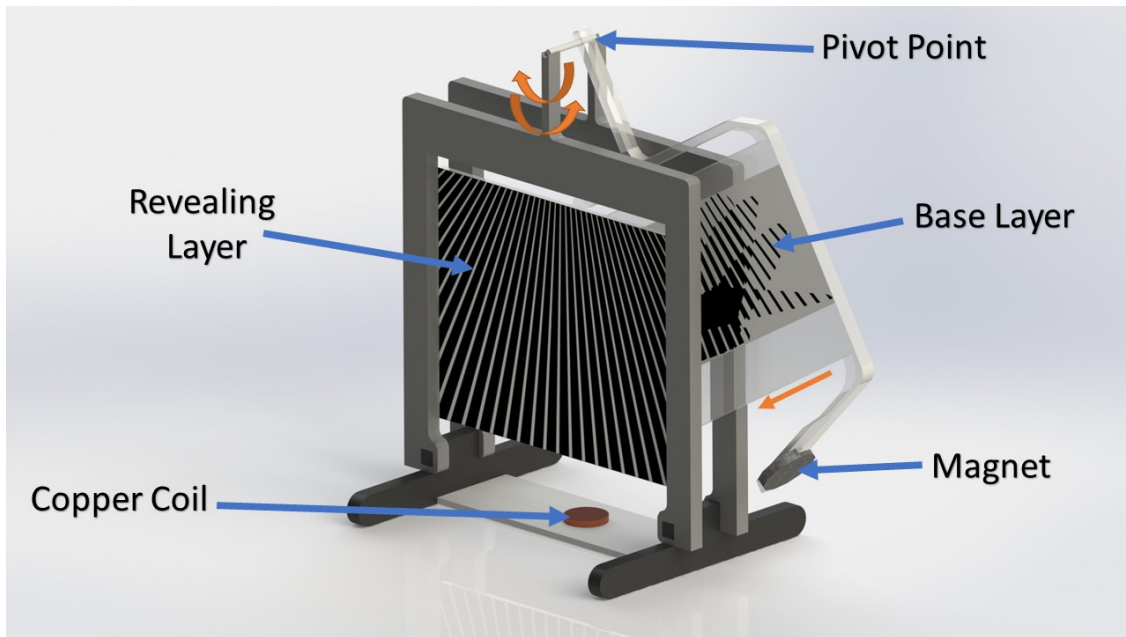
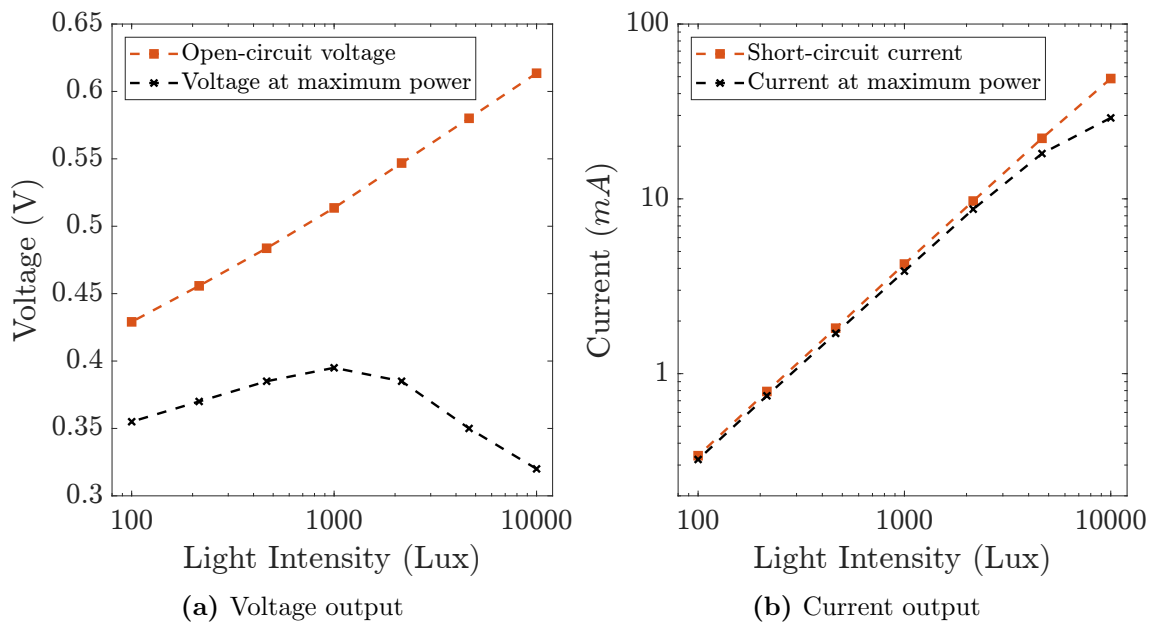


Figure 6.22: Labelled set-up of the pendulum Moiré pattern

6.2.2.2.3 Results and discussion

6.2.2.2.3.1 Power consumption

The updated Moiré lines on the revealing layer were printed onto a monolithic DSSC, which uses the same materials as before, being the N719 dye, the opaque layer (Ti-Nanoxide D/SP), and the 5 mM (HM) triiodide electrolyte. The DSSC was assembled onto the pendulum mount design as shown in Figure 6.22, with the performance characteristics of the DSSC shown below in Figure 6.23.



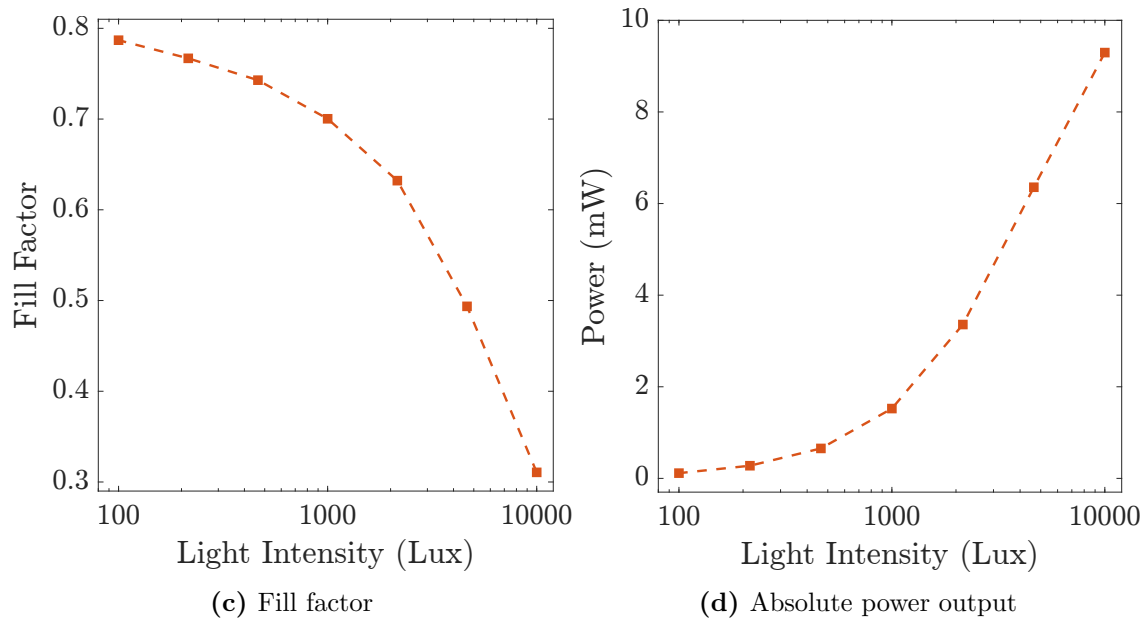


Figure 6.23: Performance characteristics of the DSSC (revealing layer)

The voltage and current outputs in Figure 6.23a and Figure 6.23b also include the values at maximum power for each light intensity tested. This especially shows in Figure 6.23a that the difference in output value at maximum power (V_{MP}) (0.3 – 0.4 V) compared to the V_{OC} (0.4-0.6 V) is considerably lower. The V_{MP} is lower at 10,000 Lux than at a 1,000 Lux, due to the decrease in FF (seen in Figure 6.23c) at higher light intensities, limited by the increase in series resistance. The I_{SC} and the current at maximum power (I_{MP}) in Figure 6.23b is generally well behaved at high and low light intensities.

The solar dancing flower seen previously in Figure 6.17 was powered from a PV module with an overall output voltage of 1.2 V. Therefore, approximately 1.2 V is required to operate the microcontroller, to pulse current into the copper coil. The amount of current used to power the microcontroller and coil is shown below in Figure 6.24.

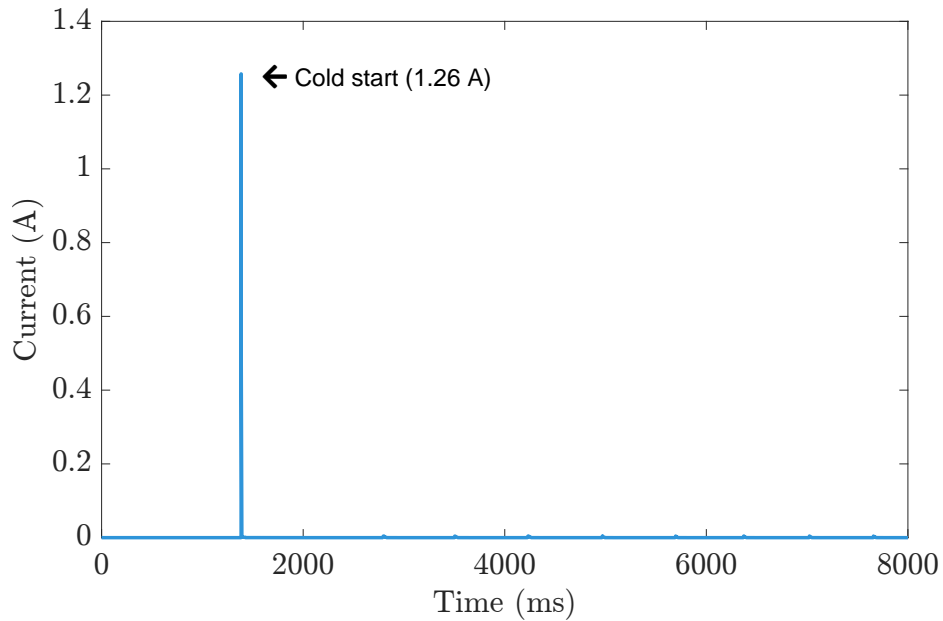


Figure 6.24: Current consumption of the microcontroller

Figure 6.24 shows a large peak of current usage of just over 1.2 mA , lasting approximately 2 ms . This is considered as the cold start requirements of the microcontroller, following which there is a significant lowering of the current consumption. The current consumption of each pulse is shown below in Figure 6.25, which consumes approximately 4.4 mA , lasting around 34 ms . The rate of pulse can also be gathered as approximately 675.4 ms per pulse.

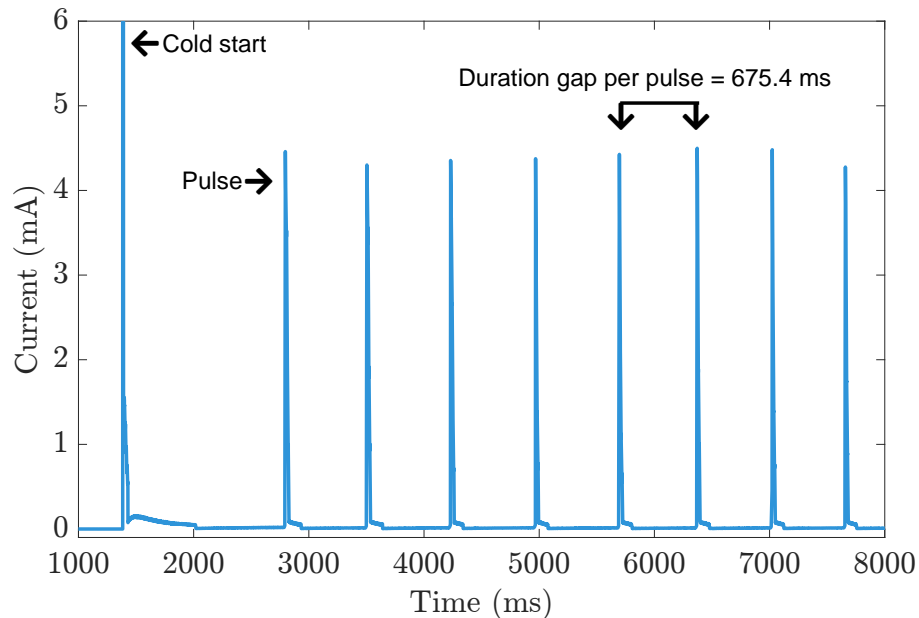


Figure 6.25: Current consumption after the cold start of the microcontroller

Over 13 s of data was captured, with an average power consumption to operate the microcontroller and pulsing the copper coil of 0.203 mW , which includes the initial

cold start. At 215.44 Lux and 100 Lux, the output power from the DSSC was 0.276 *mW* and 0.115 *mW* respectively, meaning that just over a light intensity of a 100 Lux will fully self-power the pendulum motion, to create the Moiré pattern.

To increase the voltage output from the DSSC to the microcontroller, the power is first transferred into an energy harvester, consisting of the AEM10941 chip. This has a unique low cold start voltage of 380 *mV*, and 3 μW of input power, being an ideal harvester for a monolithic DSSC (having low voltage outputs). The harvesting device stores the energy from the DSSC into a lithium-ion supercapacitor, which previously mentioned to be an ideal power storage method (see Section 1.1.3.2 on page 24). The harvester can then output the required 1.2 *V* (being adjustable) to power the microcontroller for current pulsing.

6.2.2.2.3.2 Final assembled prototype

The final pendulum prototype can be seen below in Figure 6.26, showing the Moiré pattern form a radial motion of the base layer. A video can also be viewed on the file stored cloud [6] (labelled, Optimised - Pendulum for low powered movement), showing the full motion of the Moiré butterfly pattern.



Figure 6.26: Moiré pattern powered through a low powered pendulum mechanism

Figure 6.26 shows a successful assembly from the concept design in Figure 6.22; using a magnetic field to propel a magnet, causing the base layer to swing on the pivot point, creating a Moiré pattern. With a depleted battery and in an office

environment, having low light intensity (100-300 Lux), the pendulum motion begins in a couple of minutes, to initially power the cold start, then maintains a stable radial movement until there is no light projected at the DSSC. This demonstrates a fully self-powered mechanism to display the Moiré pattern.

This final prototype provides a unique method of conveying information using a Moiré pattern, having the capabilities of functioning under very low light conditions. These displays could be implemented in communities where there are unreliable energy networks, especially in alleyways where there are limited sunlight coming through. They could be used by businesses as a way of displaying directions or advertisement for customers, such as having the name of business with an arrow increasing in size. Alternatively, they could be used in homes as a source of entertainment or a customisable visually appealing device for users.

Figure 6.26 illustrates some improvements that can be made to the base layer arm, which currently is in display behind the revealing layer. The swinging speed of the base layer can also be further adjusted with different materials used as the rod for the pivot point, such as, a spongy material will absorb some of the radial force, retarding the movement of the base layer arm.

6.3 Conclusion

This Chapter provides a detailed summary of the contributions involving design concept progression and the assembly of working prototypes, towards the CHI joint conference papers. The Chapter demonstrates the design evolution of the PV-Pix, from initial prototyping of the FabricOn and TiltTile module to working examples, alongside rendered diagrams created through SolidWorks for clarity.

Light based concept prototypes were also achieved, including the SolarPix and ShadMo. Additional optimisation of the ShadMo concept was accomplished by altering the actuator from a servo motor to an electromagnetic force, drastically increasing the lifetime and operation of the ShadMo under low light intensities (≈ 200 Lux). This required a re-design of the Moiré lines for the base and revealing layers, including the mounting for the layers, to allow the base layer to exhibit a pendulum motion.

The addition of DSSCs to these prototypes can offer several potential economic benefits, especially when considering the unique requirements and operational characteristics of indoor IoT applications. It does this by lowering the overall cost of

the IoT node, by either extending or replacing batteries altogether, reducing the maintenance and operational interruptions. This allows IoT devices to be placed in hard-to-reach or remote indoor locations. The addition of a DSSCs also aligns with the sustainable and environmentally friendly practices (by reducing the reliance with traditional batteries and providing renewable energy), which can appeal to customers, potentially increasing sales of the IoT node.

Bibliography

1. Raju DK, Seunarine K, Reitmaier T, Thomas G, Meena YK, Zhang C, Pockett A, Pearson J, Robinson S, Carnie M, Sahoo DR, and Jones M. PV-Pix: Slum Community Co-Design of Self-Powered Deformable Smart Messaging Materials. *Proceedings of the 2021 CHI Conference on Human Factors in Computing Systems*. CHI '21. New York, NY, USA: Association for Computing Machinery, 2021. DOI: 10.1145/3411764.3445661. Available from: <https://doi.org/10.1145/3411764.3445661>
2. Seunarine K, Kalarikalayil Raju D, Thomas G, Thomas SK, Pockett A, Reitmaier T, Steer C, Owen T, Meena YK, Robinson S, Pearson J, Carnie M, Sahoo DR, and Jones M. Light-In-Light-Out (Li-Lo) Displays: Harvesting and Manipulating Light to Provide Novel Forms of Communication. *Proceedings of the 2022 CHI Conference on Human Factors in Computing Systems*. CHI '22. New York, NY, USA: Association for Computing Machinery, 2022. DOI: 10.1145/3491102.3517730. Available from: <https://doi.org/10.1145/3491102.3517730>
3. Thomas G. Shared Content - FabricOn. Available from: <https://drive.google.com/drive/folders/1ithBlHwkKDJC9SI3P6VN8rhdFA0i3HE7?usp=sharing>
4. Thomas G. Shared Content - Initial Prototype TiltTile. Available from: <https://drive.google.com/drive/folders/1jMYM8qGtBzFJvhPnV4QjvmVPkr-xQoqA?usp=sharing>
5. Thomas G. Shared Content - Optimised TiltTile. Available from: <https://drive.google.com/drive/folders/1jWXaMhLN5EU6Z3b0hmTtgYzdNRCCfQOK?usp=sharing>
6. Thomas G. Shared Content - ShadMo. Available from: https://drive.google.com/drive/folders/1cE0mYnpsi8qcaF5rQDPnGdfCFM2_gRgy?usp=sharing

7. Pylones. Solar-powered - Dancing Flowers. Available from: <https://www.pylones.com/en/flowers-and-plants/2155-solar-powered-dancing-flowers-marguerite-vert.html>
8. Gabrielyan E. THE BASICS OF LINE MOIRÉ PATTERNS AND OPTICAL SPEEDUP

Chapter 7

Conclusion

IoT nodes contribute significantly to the ecosystem, capturing and storing real-time data in a wide range of applications. With the increased number of deployed IoT nodes, there has been a significant rise in security attacks, incapable of defending due to their insufficient power and storage to include the required memory and processing capabilities to tackle security threats. Furthermore, to be fully dependent on relying solely on primary or secondary batteries to power IoT nodes, is economically and environmentally unsustainable.

This PhD thesis investigates a solution of providing additional power for indoor IoT nodes, through energy harvesting, prolonging the lifespan of these nodes. Chapter 1 presents recent advancements, highlighting both benefits and limitations of the available indoor energy harvesters, focusing on two different types of energy, being ambient (naturally occurring energy) and external (mechanical or human energy) sources. Chapter 1 evaluates various indoor energy sources, using the Pugh matrix, with the best technique being light harvesting through a PV. The Chapter ends by exploring different types of indoor PV, with the conclusion that DSSC is the ideal type, having the design flexibility and performance to be implemented in indoor applications.

HCI is an important field to consider when designing IoT nodes, needing to be aesthetically pleasing and valuable to the user. Otherwise, having energy harvesters (without considering their appearance) to only sufficiently power indoor IoT nodes might not be as an attractive reason for users to integrate into their homes. Chapter 3 delves into the performance metrics of different types and active area sizes of transparent monolithic DSSCs in indoor lighting conditions, to find the best type to be integrated with an IoT node. The Chapter mainly compares the highest-performing electrolyte as referenced in [1], being the Cu(II/I)(tmby) (for opaque DSSCs) with the commonly explored electrolyte composition of the I_3^-/I^- . The study revealed

that by reducing the iodine levels of the I_3^-/I^- electrolyte not only improves the transparency of the DSSC, but also shows good performance at low light intensities, strongly supporting other published studies [2] [3] [4] [5] [6] on the reduction of iodine concentrations; concluding that the I_3^-/I^- electrolyte with 5 mM of iodine concentration proved to be the superior type for indoor DSSCs. This Chapter also investigates the effects of increasing the active area of different electrolyte based monolithic DSSCs in indoor lighting conditions, not fully explored in previous research. The findings found that the power density was considerably consistent as the active area increased to 64 cm², for the 5 mM iodine concentration. In contrast, other electrolyte types showed slight decrease in power density as the active area increased, with the Copper redox mediator having the worst performance consistency.

Some applications involving IoT nodes require several sensors, actuators and displays to provide its functionality; increasing the energy consumption demand of the IoT node. Chapters 4 and 5 investigate a method of integrating a monolithic DSSC to not only harvest energy but also self-power its interactive features. Chapter 4 demonstrates that by monitoring the photocurrent output of an asymmetrically patterned monolithic (i.e., single cell) DSSC, and using machine learning, it can recognise simple hand gestures (four linear directions), achieving a prediction accuracy of 98%. Compared with previous self-powered hand gesture recognition research, this method provides a simpler and visually appealing UI, as opposed to attaching several individual photodiodes/ PV cells to the system [7][8][9]. Chapter 5 optimises the asymmetrical active area pattern of the DSSC through computational modelling, achieving an accuracy prediction of 83% for eight different hand directional gestures. This DSSC pattern was also modified to demonstrate the capabilities of providing an aesthetically pleasing environment, alongside also detecting hand gestures. The alternative fabrication method of etching the FTO was also successful in detecting hand gestures. Compared to SolarGest by Ma *et al.* [10], being the only other previous research that achieved hand gesture recognition through a monolithic PV cell; this work provides several natural hand gestures recognised through a machine learning system that can also achieve live gesture recognition, not achievable with SolarGest.

The penultimate Chapter 6 showcases various functional examples of integrating monolithic DSSCs and other types of PV technology, to self-power different IoT node applications. Chapter 6 shows the design challenges and solutions to achieve autonomous power, exhibiting a novel method of displaying a Moiré pattern in low light conditions. Whilst this prototype is not fully considered as an IoT node, due to no wireless communication or data storage, the Moiré prototype demonstrates

the capabilities that a monolithic DSSC can achieve.

This thesis demonstrates that DSSCs are the perfect choice for self-powered interactive technologies, both in terms of powering IoT nodes in ambient light conditions and having aesthetic qualities that are prioritised by users. As well as powering interactive technologies, they can also provide a means of interactive control, as discussed in the subsequent section on future work.

7.1 Future prospects

- It would be interesting to learn more about the stability of larger monolithic DSSCs, conducting characterisation tests under continuous lighting or saved lighting scenarios. This can be compared with DSSC modules with the same active area, to find the limitations of both DSSC types. It is also important to carry out further experiments on the indoor lighting stability of the reduced iodine concentrated DSSCs. A method of investigating the stability is through tracking the maximum power point at different light intensities. An example is using the Candlelight MPPT, to track the performance of the cell. Stored light intensities from real world scenarios (such as from an office environment) can also be captured and outputted as the light source when measuring the MPP, measuring the performance for a set number of days/weeks.
- An interesting avenue is to optimise the efficiency of Cu(II/I)(tmby) redox mediators for larger active areas, having proved to be a good performing type for small active areas.
- Whilst in this thesis (Chapter 3), the primary parameter was the electrolyte, different dyes and TiO_2 thicknesses can also be investigated, to improve the transparency of the DSSC.
- Increasing the transparency of the copper redox mediator, and still able to achieve a zombie cell would significantly increase the durability of the DSSC, prolonging the DSSC life, as there is no risk of the electrolyte leaking. This would be a suitable DSSC type to be integrated as the base layer of the Moiré design.
- Additional work can be carried out to integrate the optimised asymmetrical active area pattern for live gesture recognition. This will require a substantial amount of data to be recorded for machine learning, collecting several different hand parameters and at different light intensities, to accurately achieve this.

Bibliography

1. Zhang D, Stojanovic M, Ren Y, Cao Y, Eickemeyer FT, Socie E, Vlachopoulos N, Moser JE, Zakeeruddin SM, Hagfeldt A, et al. A molecular photosensitizer achieves a Voc of 1.24 V enabling highly efficient and stable dye-sensitized solar cells with copper (II/I)-based electrolyte. *Nature communications* 2021; 12:1–10
2. Yu Z, Gorlov M, Nissfolk J, Boschloo G, and Kloo L. Investigation of iodine concentration effects in electrolytes for dye-sensitized solar cells. *Journal of Physical Chemistry C* 2010 Jun; 114:10612–20. DOI: 10.1021/JP1001918/SUPPL_FILE/JP1001918_SI_001.PDF. Available from: <https://pubs.acs.org/doi/full/10.1021/jp1001918>
3. De Rossi F, Pontecorvo T, and Brown TM. Characterization of photovoltaic devices for indoor light harvesting and customization of flexible dye solar cells to deliver superior efficiency under artificial lighting. *Applied Energy* 2015 Oct; 156:413–22. DOI: 10.1016/J.APENERGY.2015.07.031
4. Nakade S, Kanzaki T, Kubo W, Kitamura T, Wada Y, and Yanagida S. Role of electrolytes on charge recombination in dye-sensitized TiO₂ solar cell (1): The case of solar cells using the I⁻/I₃⁻ redox couple. *Journal of Physical Chemistry B* 2005 Mar; 109:3480–7. DOI: 10.1021/JP0460036/ASSET/IMAGES/LARGE/JP0460036F00010.JPEG. Available from: <https://pubs.acs.org/doi/full/10.1021/jp0460036>
5. Saeed MA, Yoo K, Kang HC, Shim JW, and Lee JJ. Recent developments in dye-sensitized photovoltaic cells under ambient illumination. *Dyes and Pigments* 2021 Oct; 194:109626. DOI: 10.1016/J.DYEPIG.2021.109626
6. Belessiotis GV, Antoniadou M, Ibrahim I, Karagianni CS, and Falaras P. Universal electrolyte for DSSC operation under both simulated solar and indoor fluorescent lighting. *Materials Chemistry and Physics* 2022; 277:125543. DOI: <https://doi.org/10.1016/j.matchemphys.2021.125543>. Available from: <https://www.sciencedirect.com/science/article/pii/S0254058421013262>

7. Li Y, Li T, Patel RA, Yang XD, and Zhou X. Self-Powered Gesture Recognition with Ambient Light. *Proceedings of the 31st Annual ACM Symposium on User Interface Software and Technology*. UIST '18. New York, NY, USA: Association for Computing Machinery, 2018 :595–608. DOI: 10.1145/3242587.3242635. Available from: <https://doi.org/10.1145/3242587.3242635>
8. Duan H, Huang M, Yang Y, Hao J, and Chen L. Ambient Light Based Hand Gesture Recognition Enabled by Recurrent Neural Network. *IEEE Access* 2020; 8:7303–12. DOI: 10.1109/ACCESS.2019.2963440
9. Meena YK, Seunarine K, Sahoo DR, Robinson S, Pearson J, Zhang C, Carnie M, Pockett A, Prescott A, Thomas SK, Lee HKH, and Jones M. PV-Tiles: Towards Closely-Coupled Photovoltaic and Digital Materials for Useful, Beautiful and Sustainable Interactive Surfaces. *Proceedings of the 2020 CHI Conference on Human Factors in Computing Systems*. CHI '20. Honolulu, HI, USA: Association for Computing Machinery, 2020 :1–12. DOI: 10.1145/3313831.3376368. Available from: <https://doi.org/10.1145/3313831.3376368>
10. Ma D, Lan G, Hassan M, Hu W, Upama MB, Uddin A, and Youssef M. SolarGest: Ubiquitous and Battery-Free Gesture Recognition Using Solar Cells. *The 25th Annual International Conference on Mobile Computing and Networking*. MobiCom '19. New York, NY, USA: Association for Computing Machinery, 2019. DOI: 10.1145/3300061.3300129. Available from: <https://doi.org/10.1145/3300061.3300129>

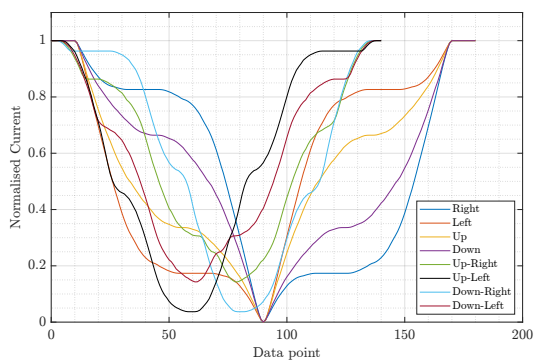
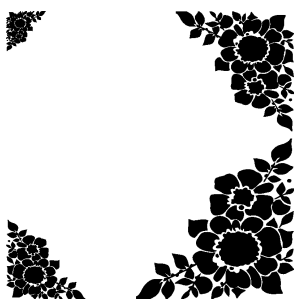
Appendices

Appendix A

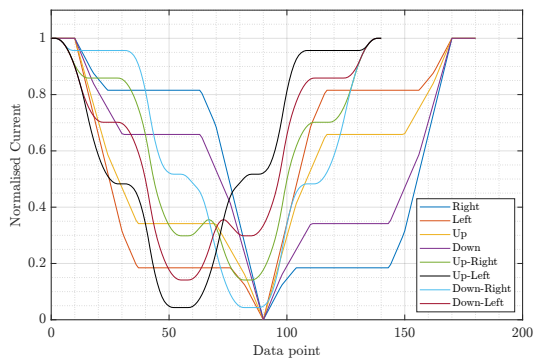
Initial Pattern Exploration and Optimisation

A.1 Initial Pattern Exploration

1. Original Design

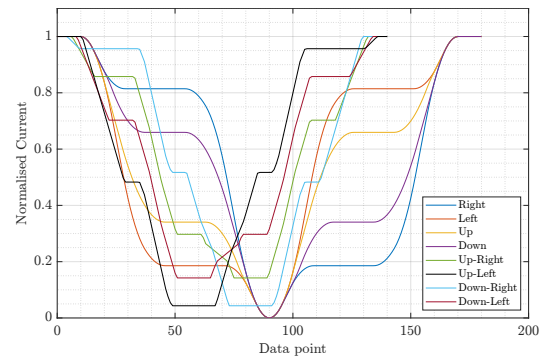
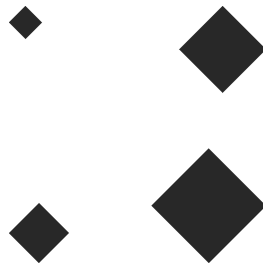


2.

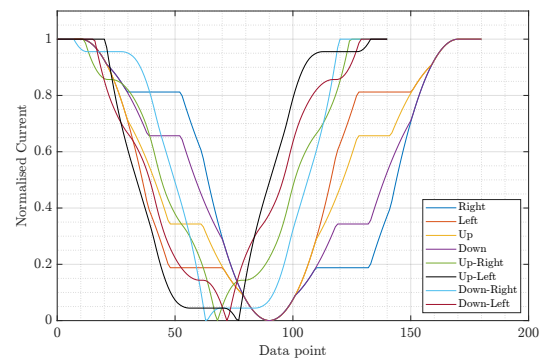
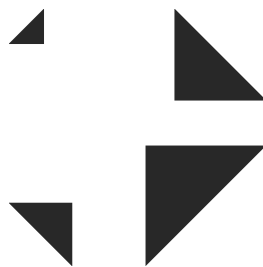


3.

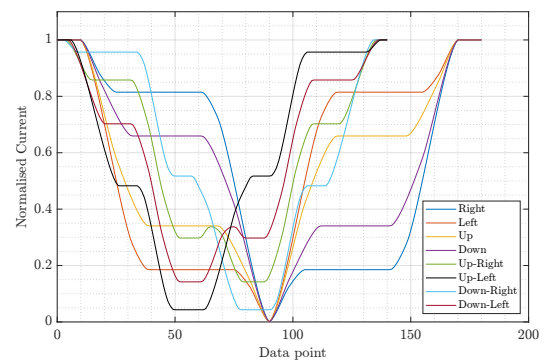
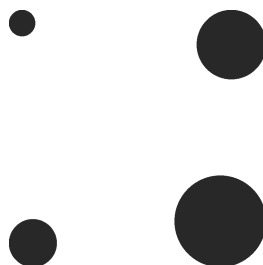
4.



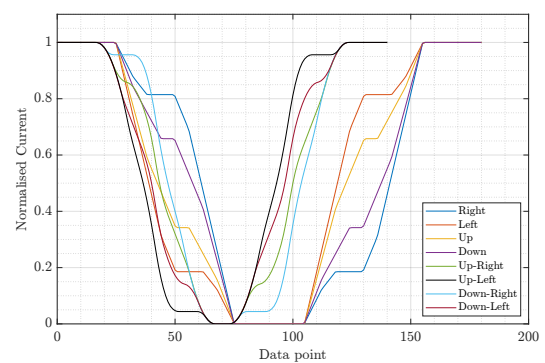
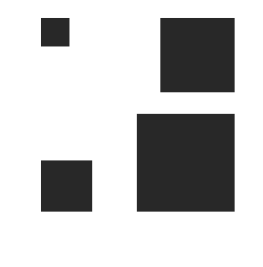
5.



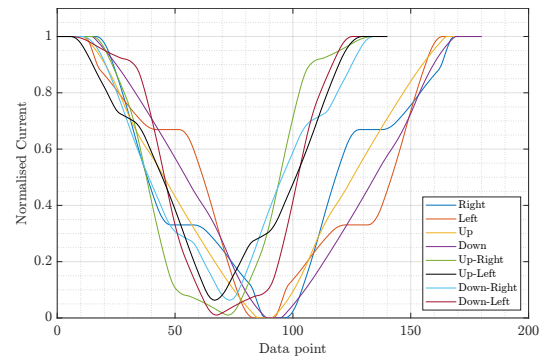
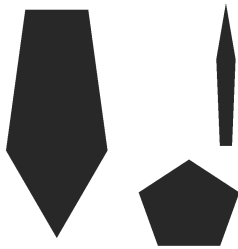
6.



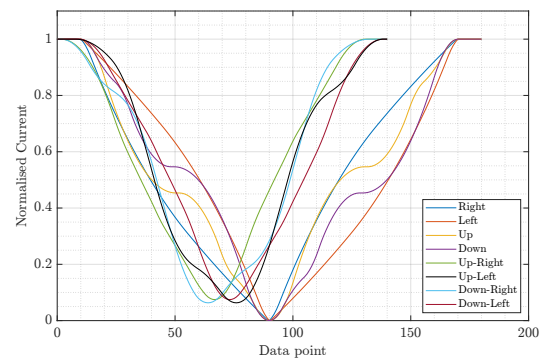
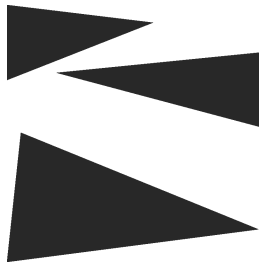
7.



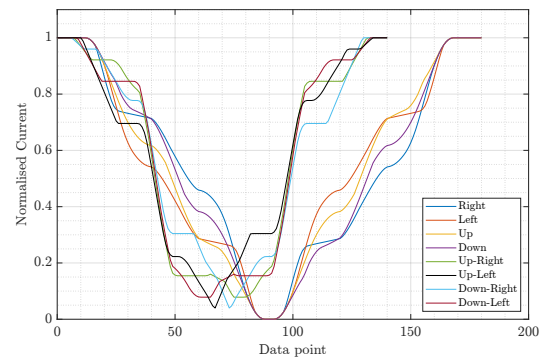
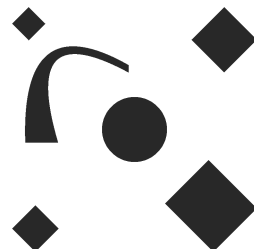
8.



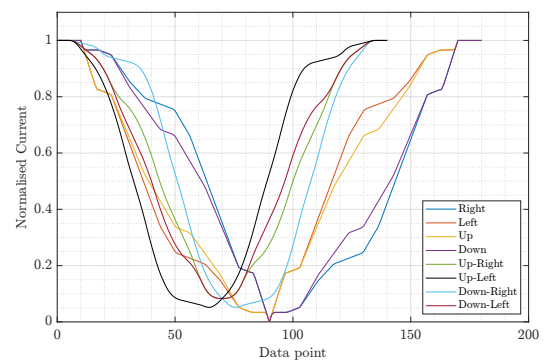
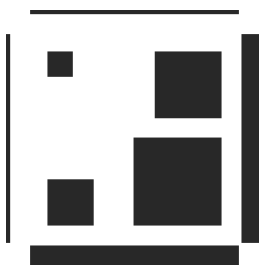
9.

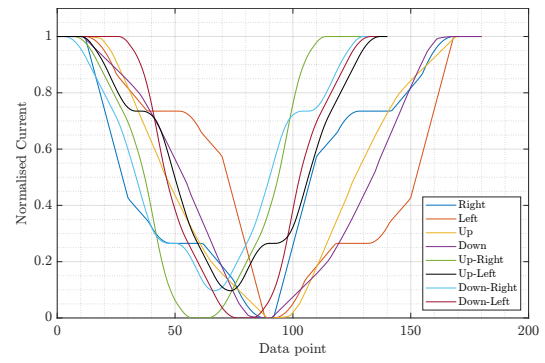
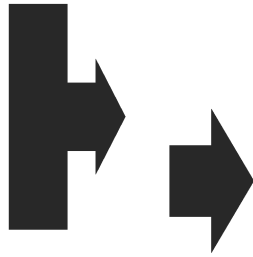


10.

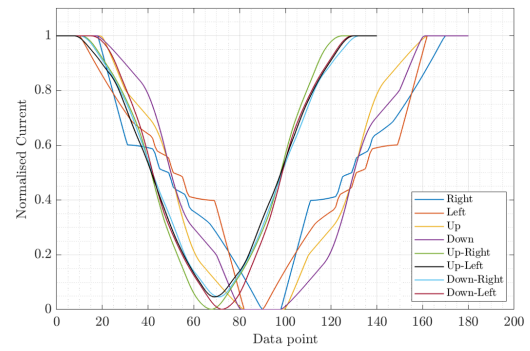
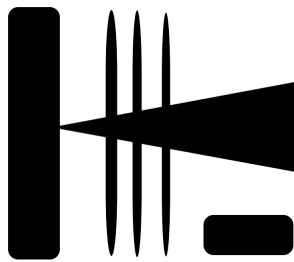


11.

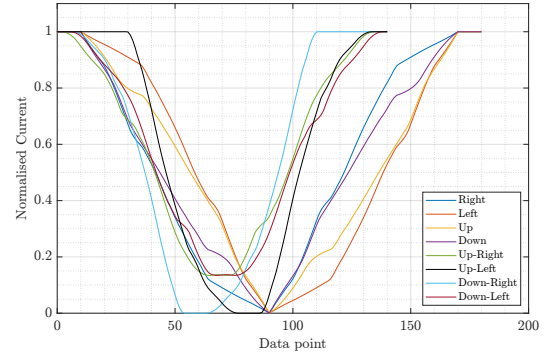




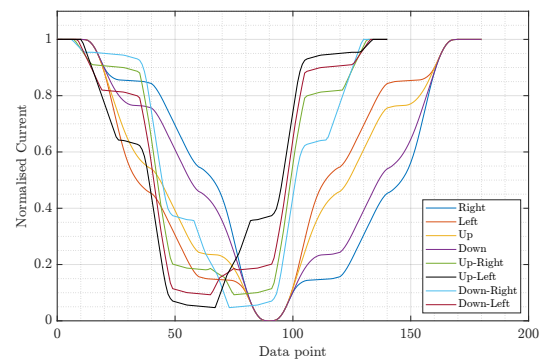
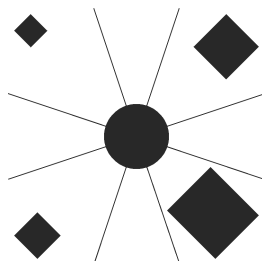
12.



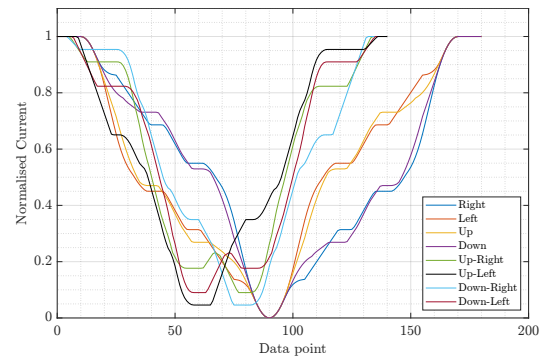
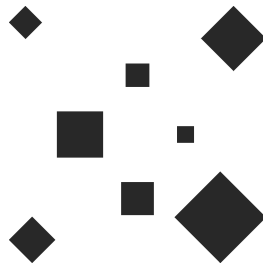
13.



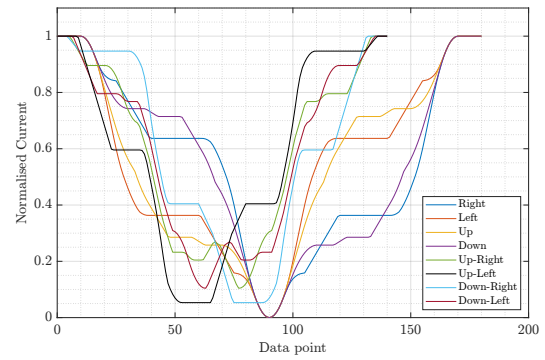
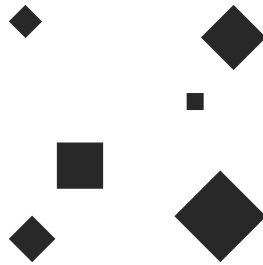
14.



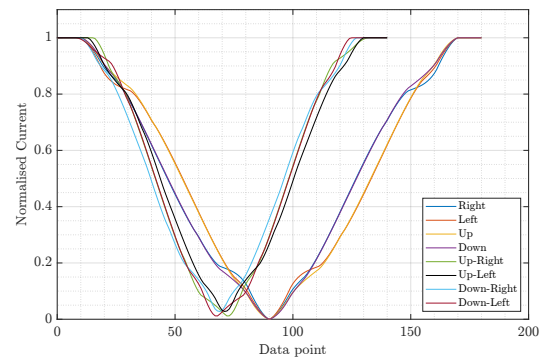
15.



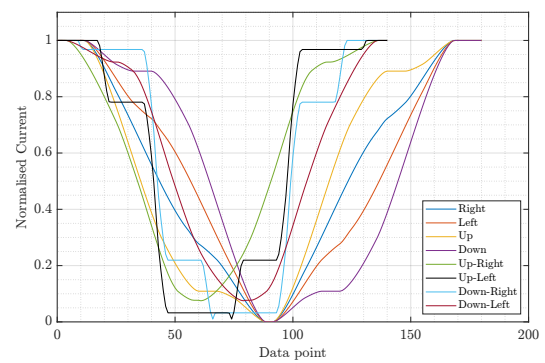
16.



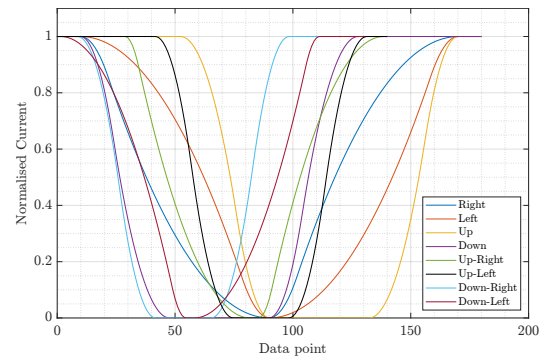
17.



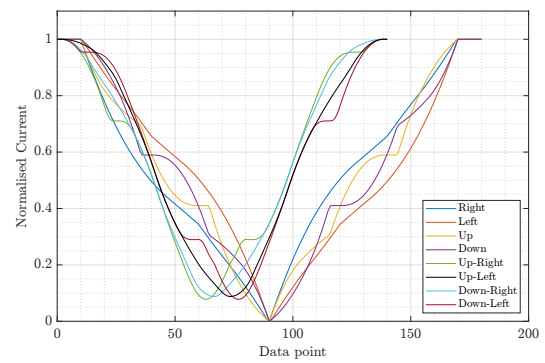
18.



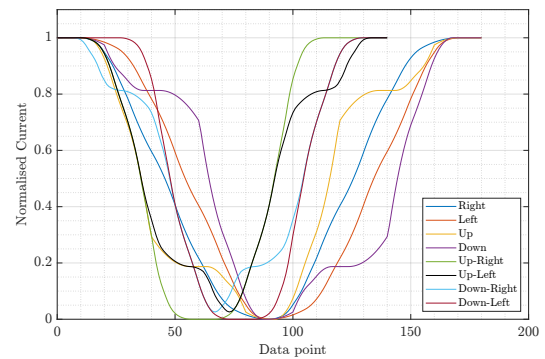
19.



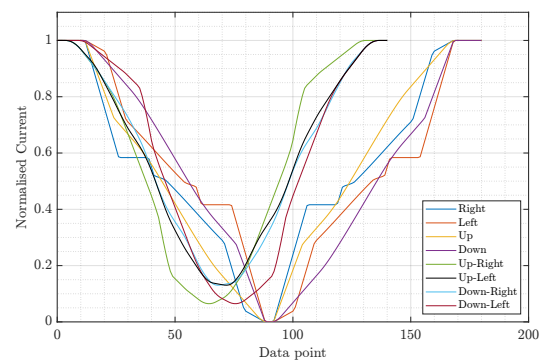
20.



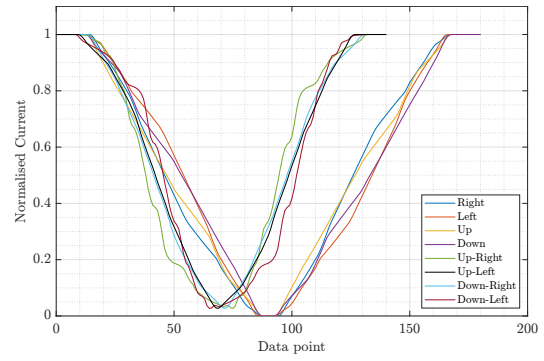
21.



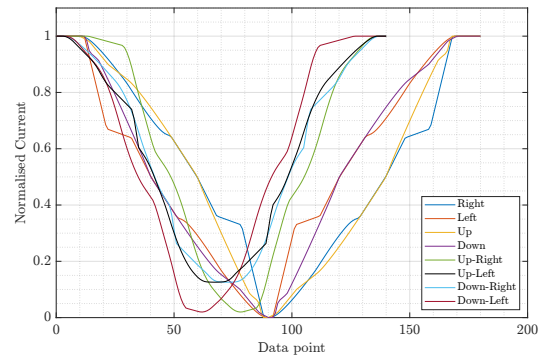
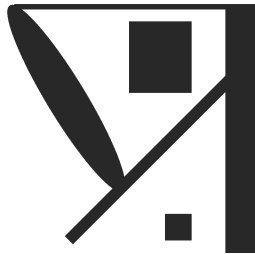
22.



23.



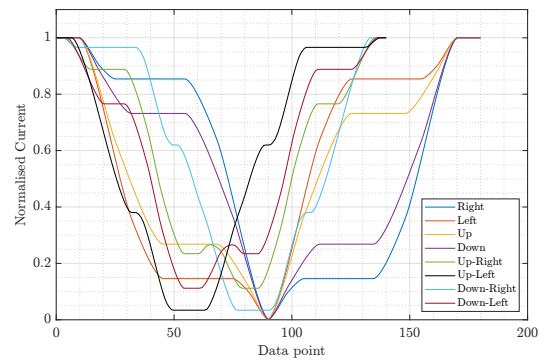
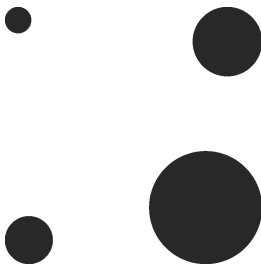
24.



A.2 Optimisation

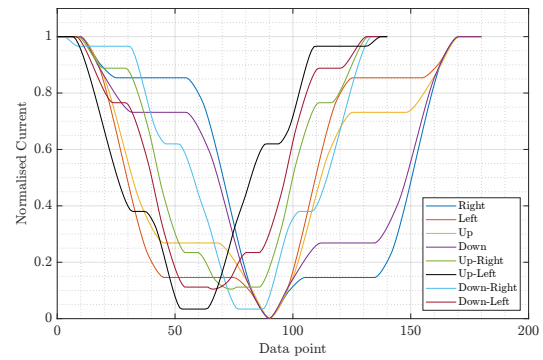
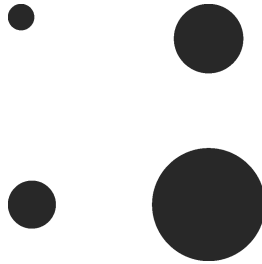
Step 1.

By increasing the area of the largest circle from design 5, the signal differences between up-left and down-right improves, however, this reduces the curve feature.



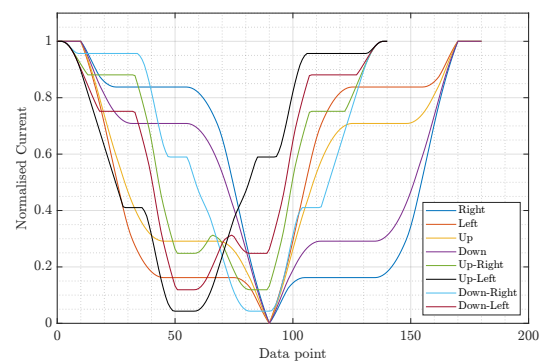
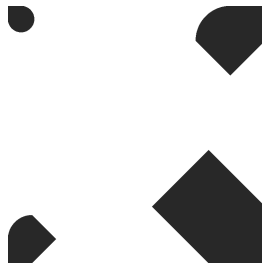
Step 2.

By shifting the two medium area circles towards the smallest, this increases the 0 gradient for up-left and down-right, but now eliminates the distinct peak for up-right and down-left.



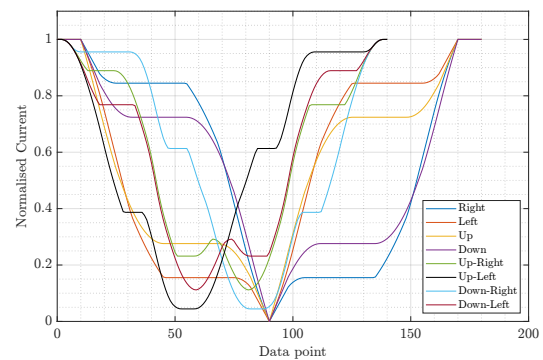
Step 3.

The peaks are restored through squaring the circle edges.



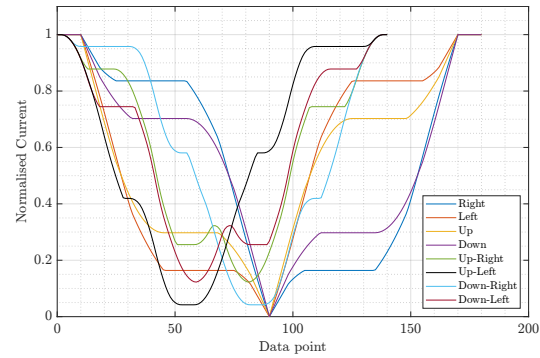
Step 4.

Increasing the overall area. Weakens the signal slightly, but not enough to make a significant difference. The goal is to now make a larger difference signal between the pairs (down and right) and (left and up).



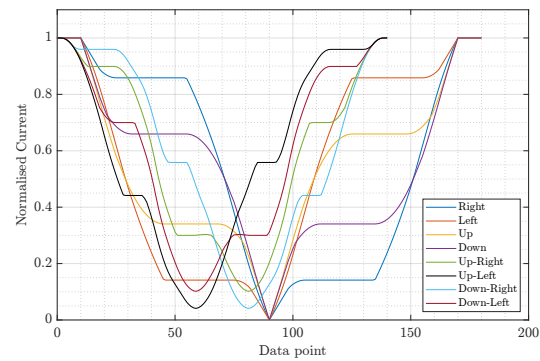
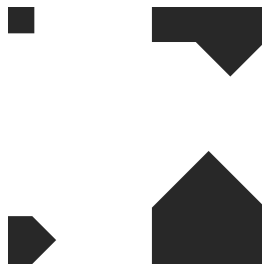
Step 5.

By squaring the edges of the two medium areas, this weakened the Up-Left and Down-right signal.



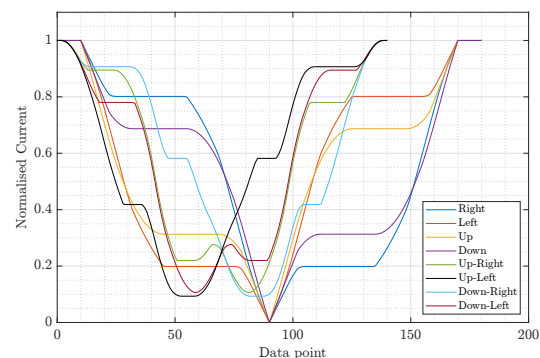
Step 6.

Altering pattern 4, increasing the top right corners shape area results in a larger difference between the two signals pairs mentioned in pattern 4, however has now weakened the peaks.



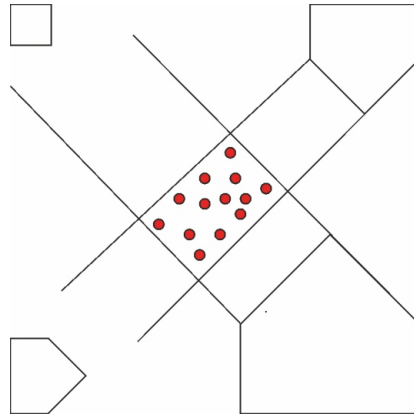
Step 7.

Increasing the area of the smallest square results in the lowest troughs of all diagonal gestures becoming similar, compared to pattern 4.

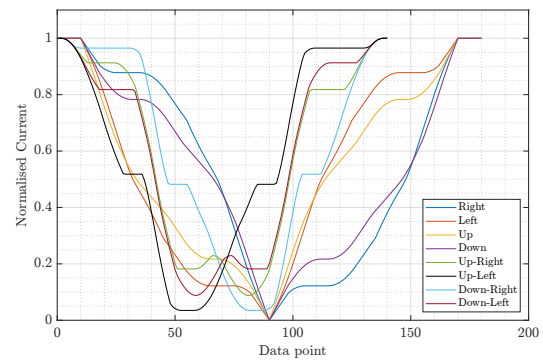


Step 8.

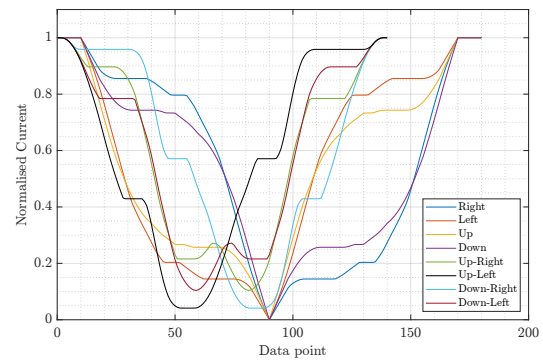
Step 4 seems to be the optimised pattern following design 5. This pattern now integrates part 2 for signal optimisation. The pattern below explains that the only possible location that the new shapes can appear is in the red circle box, otherwise, it can affect the shape of the signals previously optimised.

**Step 9.**

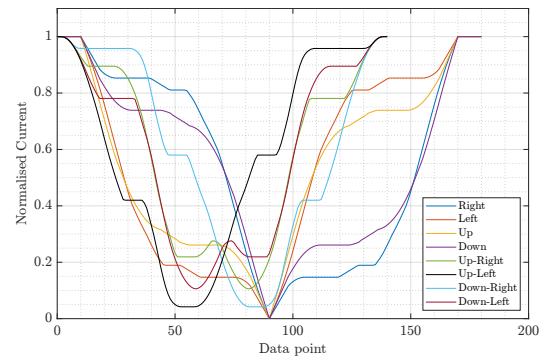
By fully filling the area, it is seen that the up-left and down-right are too similar.

**Step 10.**

Breaking the centre rectangular into two parts of different sizes weakens the horizontal and vertical gesture signals.

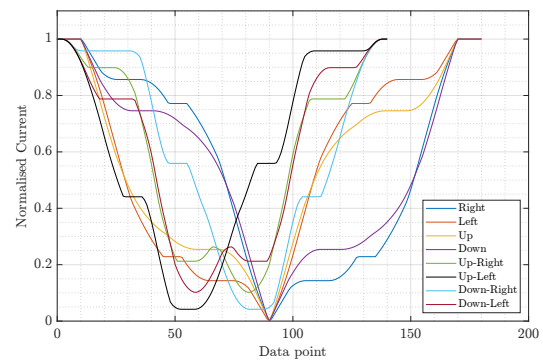
**Step 11.**

The squares have a larger effect on the horizontal motion; however, it slightly weakens the vertical signal gestures.



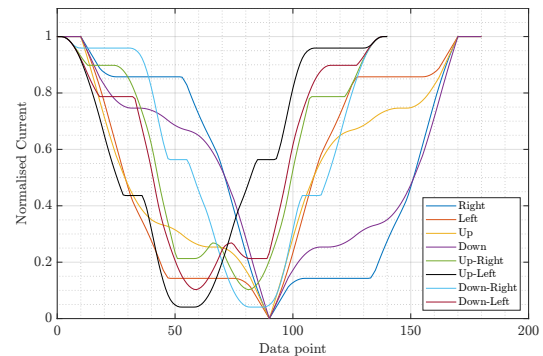
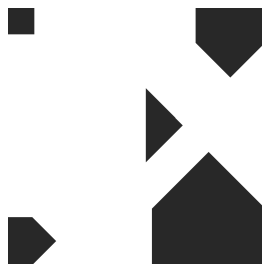
Step 12.

The photocurrent signal gap of the left/up and down/right signal has decreased.



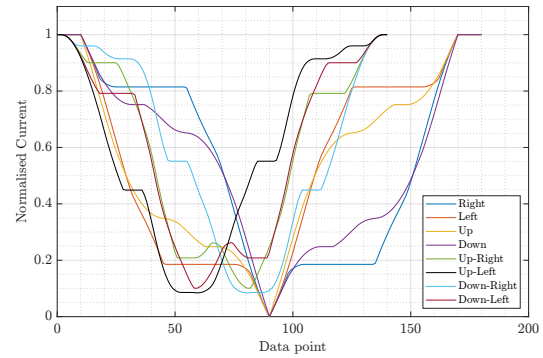
Step 13.

This is an improvement from step 12, with a greater differential between the signals.



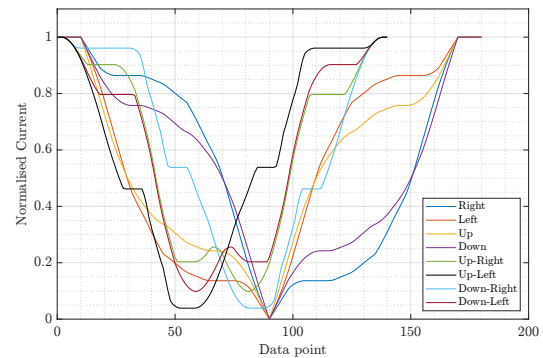
Step 14.

This decreases the right and left 0 gradient signal pattern, which becomes too similar to the up/down gesture.



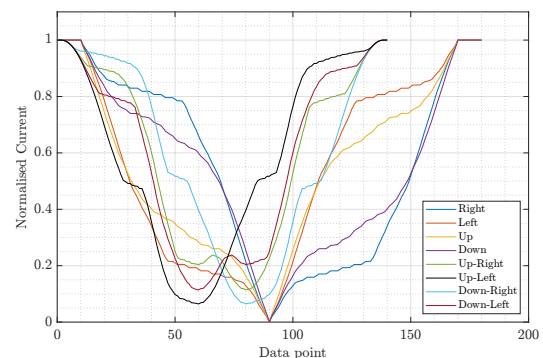
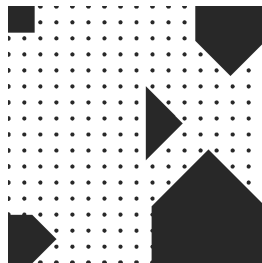
Step 15.

This again is a deterioration from the step 13 signal output. Overall, it is seen that step 13 is best following the addition of part 2.



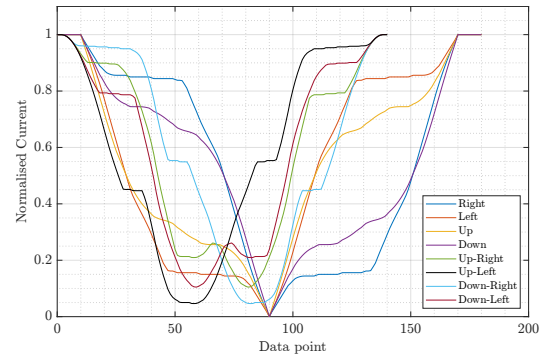
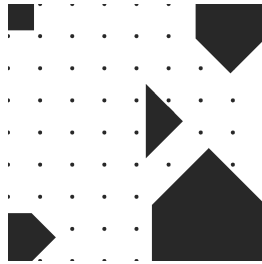
Step 16.

To further optimise the pattern design. A background can be added to slightly increase the active area of the solar cell. 1 mm diameter circles showed some promising response, however, the signal between up-left and down-right are too similar.



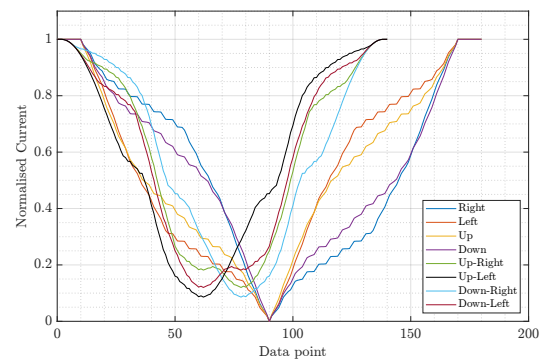
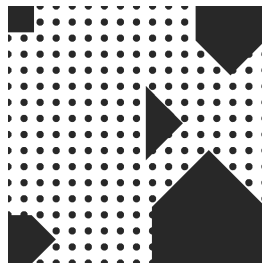
Step 17.

Spacing the 1 mm diameter circles resulted in a better deviation between the signals mentioned in step 16.



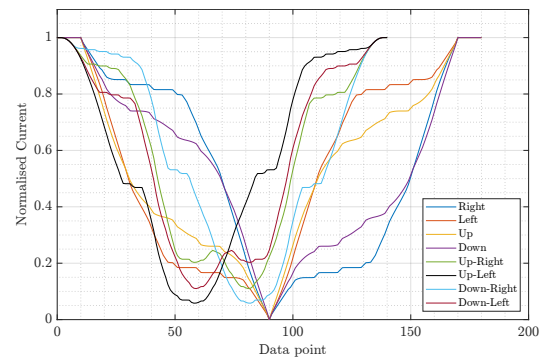
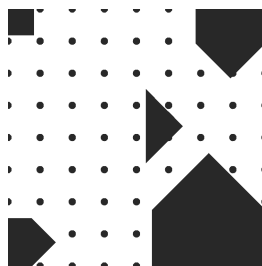
Step 18.

A larger diameter circle of 2 mm weakens the signal greatly.



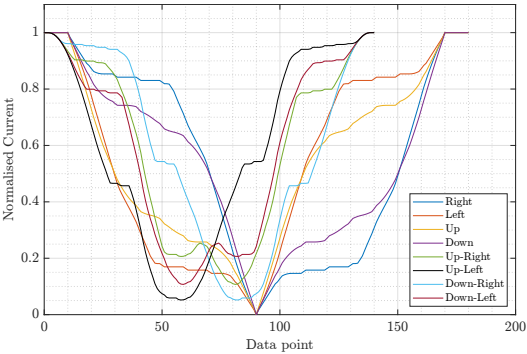
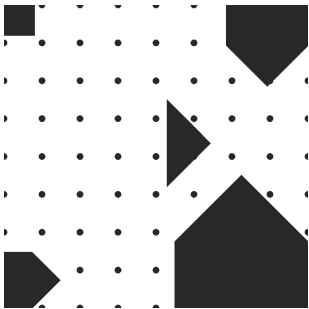
Step 19.

This is an improvement from step 18, however signals up-left and down-right are too similar.



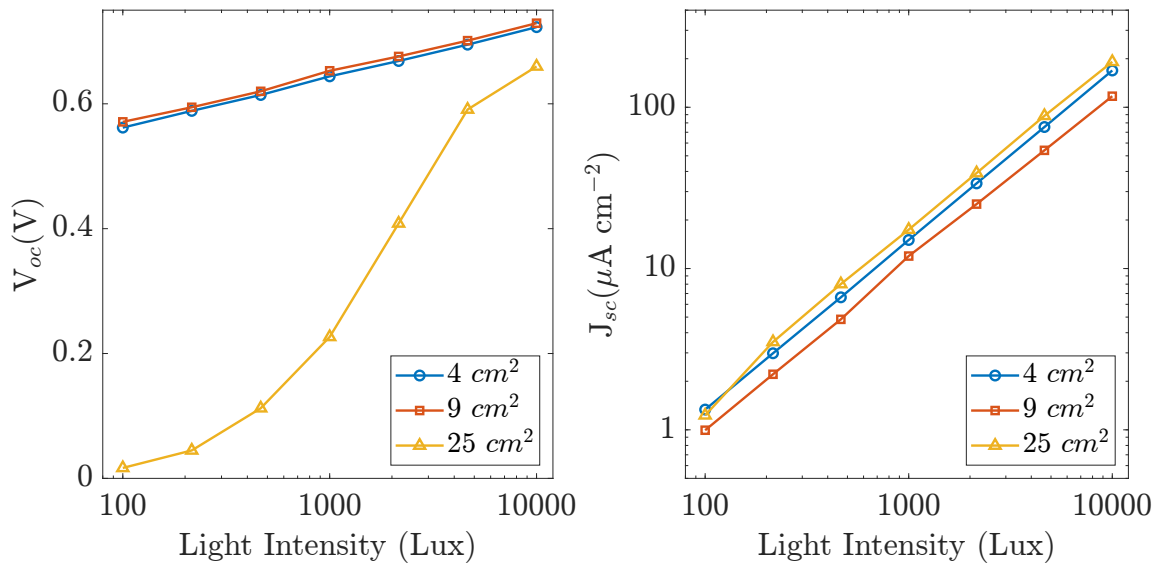
Step 20.

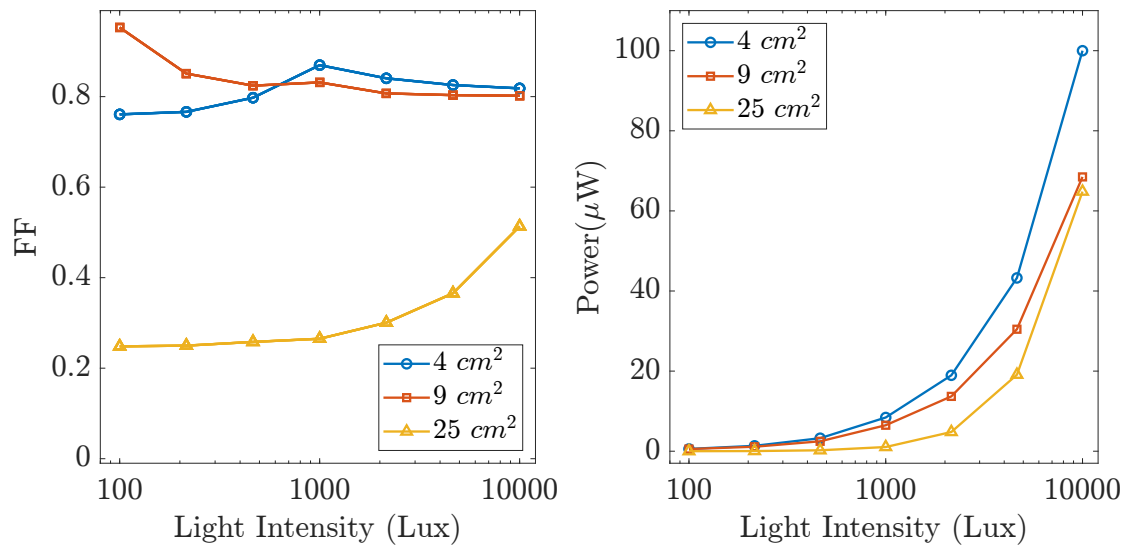
This is the best compromise between increasing the circles area and signal differential output. The circle diameter is 1.5 mm, with a good signal output like step 17.



Appendix B

Additional results from 5 mM (HM) electrolyte area void change





5 mM (HM) DSSC performance characteristics of changing the electrolyte area around a 1 cm² active area

Appendix C

Additional Results from Optimised and FTO etched Cells

C.1 Trained Model Results of the 3 Optimised Cells

Trained model accuracy for pattern 1 (14.98 cm^2)

		Model Type Accuracy %																
Level	Feature Selection	SVM						KNN						Ensemble				
		Linear	Quadratic	Cubic	Fine Gaussian	Medium Gaussian	Course Gaussian	Fine	Medium	Coarse	Cosine	Cubic	Weighted	Boosted Trees	Bagged Trees	Subspace Discriminant	Subspace KNN	RUS Boosted Trees
5	Haar	91.6	96.1	95.7	64.9	93.9	82.3	93.0	86.9	62.7	85.5	81.4	90.1	88.4	95.1	83.1	94.4	71.6
6		93.2	97.0	97.4	69.4	95.7	82.9	94.3	89.5	64.2	87.7	85.2	91.7	89.5	96.9	81.9	96.8	74.7
5	db1	92.3	96.6	95.9	65.0	94.0	82.4	92.3	87.0	63.1	85.7	82.1	90.2	89.6	95.3	83.7	93.8	70.3
6		92.9	97.3	97.3	70.7	95.2	82.9	94.4	88.2	62.4	87.6	85.6	92.6	90.0	96.0	81.9	96.0	73.3
5	db2	88.9	93.8	94.4	37.0	91.1	82.9	85.4	74.3	45.0	77.8	69.1	78.3	85.7	92.9	80.3	83.5	73.1
6		90.4	95.1	95.2	55.1	94.2	81.7	91.0	80.9	51.6	82.8	77.0	87.6	88.5	94.4	77.5	92.6	78.2

Trained model accuracy for pattern 2 (16.25 cm^2)

		Model Type Accuracy %																
Level	Feature Selection	SVM						KNN						Ensemble				
		Linear	Quadratic	Cubic	Fine Gaussian	Medium Gaussian	Course Gaussian	Fine	Medium	Coarse	Cosine	Cubic	Weighted	Boosted Trees	Bagged Trees	Subspace Discriminant	Subspace KNN	RUS Boosted Trees
5	Haar	94.5	97.1	95.7	50.6	94.5	86.7	89.8	85.5	68.4	87.7	81.1	87.7	87.0	93.4	91.5	95.8	81.8
6		94.9	96.4	96.0	54.7	94.7	87.8	90.8	85.2	71.6	86.3	83.3	87.8	86.5	94.3	87.9	95.6	80.1
5	db1	94.2	96.0	96.8	52.2	94.4	86.1	90.2	86.7	68.2	87.2	81.8	88.2	86.5	94.4	91.6	95.8	81.0
6		94.1	96.6	96.1	54.8	94.5	87.2	90.4	86.0	70.8	86.6	83.1	87.8	87.4	92.9	88.0	95.1	81.4
5	db2	91.9	94.6	94.9	29.6	92.9	85.1	88.5	83.2	58.0	87.2	78.0	85.5	88.6	94.6	85.7	94.6	75.9
6		92.0	96.7	96.0	51.7	93.9	85.4	91.1	85.4	65.5	87.4	81.6	87.8	87.9	95.2	84.8	95.0	75.7

Trained model accuracy for pattern 3 (17.24 cm^2)

		Model Type Accuracy %																
Level	Feature Selection	SVM						KNN						Ensemble				
		Linear	Quadratic	Cubic	Fine Gaussian	Medium Gaussian	Course Gaussian	Fine	Medium	Coarse	Cosine	Cubic	Weighted	Boosted Trees	Bagged Trees	Subspace Discriminant	Subspace KNN	RUS Boosted Trees
5	Haar	92.8	95.3	94.6	40.8	91.7	85.7	87.2	87.7	74.9	86.8	79.3	89.0	88.2	93.4	89.5	95.7	78.4
6		94.0	96.6	96.3	62.7	93.1	87.0	91.6	86.5	73.1	87.5	83.3	89.2	86.5	92.6	89.0	95.8	73.7
5	db1	92.9	96.1	95.1	40.8	92.7	85.5	88.1	87.8	75.0	86.6	79.3	88.4	88.5	93.8	89.7	95.8	80.0
6		93.8	96.5	96.3	62.1	93.4	87.1	90.9	87.1	72.5	87.6	83.9	89.7	86.9	92.9	88.5	95.5	77.6
5	db2	87.5	89.6	89.2	28.1	87.8	80.9	75.5	71.0	56.9	82.8	64.3	72.5	79.4	91.5	83.7	89.1	68.2
6		91.6	94.9	94.2	43.4	92.7	84.7	89.5	87.5	68.4	87.7	82.9	88.3	86.8	94.1	86.3	94.0	77.4

C.2 Trained Model Results for Etched FTO Cell

Trained model accuracy for etched FTO Cell

		Model Type Accuracy %																
Level	Feature Selection	SVM						KNN						Ensemble				
		Linear	Quadratic	Cubic	Fine Gaussian	Medium Gaussian	Course Gaussian	Fine	Medium	Coarse	Cosine	Cubic	Weighted	Boosted Trees	Bagged Trees	Subspace Discriminant	Subspace KNN	RUS Boosted Trees
5	Haar	99.0	99.6	99.4	58.1	98.1	98.8	97.7	98.1	91.5	96.5	95.4	98.1	25.0	99.4	99.8	99.6	25.0
6		99.2	99.2	99.6	68.1	98.8	99.0	98.5	97.1	91.9	96.0	94.8	98.3	25.0	99.6	99.6	100.0	25.0
5	db1	98.8	99.6	99.4	58.3	97.9	98.8	97.9	97.5	90.8	96.7	95.0	98.3	25.0	99.6	99.6	99.4	25.0
6		99.2	99.8	99.8	68.1	98.5	99.0	99.0	96.9	92.1	96.5	95.4	98.1	25.0	99.8	99.4	100.0	25.0
5	db2	99.4	99.6	100.0	54.8	98.5	98.5	97.3	97.9	90.2	97.7	94.8	98.3	25.0	99.4	99.2	98.5	25.0
6		99.8	99.6	99.4	67.1	97.9	99.6	97.7	98.1	90.4	98.3	96.3	98.5	25.0	99.6	99.2	100.0	25.0

C.3 Low Power Alternative Method

Trained model accuracy for low power alternative

		Model Type Accuracy %																
Level	Feature Selection	SVM						KNN						Ensemble				
		Linear	Quadratic	Cubic	Fine Gaussian	Medium Gaussian	Course Gaussian	Fine	Medium	Coarse	Cosine	Cubic	Weighted	Boosted Trees	Bagged Trees	Subspace Discriminant	Subspace KNN	RUS Boosted Trees
5	Haar	99.6	100.0	99.6	51.5	97.9	99.4	98.1	98.1	94.4	98.5	94.2	98.5	25.0	99.8	100.0	98.8	25.0
6		99.0	99.8	100.0	56.2	99.0	99.6	99.0	97.9	95.6	98.1	95.6	98.5	25.0	99.0	99.4	99.2	25.0
5	db1	99.6	99.8	99.8	49.6	97.9	99.6	98.5	98.1	94.8	98.8	93.5	98.8	25.0	99.4	99.8	99.4	25.0
6		99.2	100.0	100.0	53.7	99.0	99.8	98.1	98.3	95.4	97.7	95.4	98.5	25.0	99.0	99.6	99.4	25.0
5	db2	99.0	99.4	99.4	39.2	97.3	99.4	96.9	98.3	96.3	98.3	93.1	98.5	25.0	98.8	99.8	88.3	25.0
6		100.0	99.6	99.8	51.7	97.3	99.6	96.7	97.7	97.9	96.7	94.2	97.7	25.0	100.0	100.0	95.8	25.0